PURDUE UNIVERSITY
GRADUATE SCHOOL
Thesis/Dissertation Acceptance

This is to certify that the thesis/dissertation prepared

By TIRTHANKAR ROY

Entitled STUDY OF TWO-PHASE FLOWS IN REDUCED GRAVITY

For the degree of DOCTOR OF PHILOSOPHY

Is approved by the final examining committee:

PROF. MAMORU ISHII

_____
Chair

PROF. TAKASHI HIBIKI

PROF. MARTIN LOPEZ-DE-BERTODANO

PROF. SURESH GARIMELLA

To the best of my knowledge and as understood by the student in the *Research Integrity and Copyright Disclaimer (Graduate School Form 20)*, this thesis/dissertation adheres to the provisions of Purdue University's "Policy on Integrity in Research" and the use of copyrighted material.

Approved by Major Professor(s): PROF. MAMORU ISHII

Approved by: PROF. AHMED HASSANEIN   09/16/2010
              Head of the Graduate Program   Date

PURDUE UNIVERSITY
GRADUATE SCHOOL

Research Integrity and Copyright Disclaimer

Title of Thesis/Dissertation:

STUDY OF TWO-PHASE FLOWS IN REDUCED GRAVITY

For the degree of DOCTOR OF PHILOSOPHY

I certify that in the preparation of this thesis, I have observed the provisions of *Purdue University Teaching, Research, and Outreach Policy on Research Misconduct (VIII.3.1)*, October 1, 2008.*

Further, I certify that this work is free of plagiarism and all materials appearing in this thesis/dissertation have been properly quoted and attributed.

I certify that all copyrighted material incorporated into this thesis/dissertation is in compliance with the United States' copyright law and that I have received written permission from the copyright owners for my use of their work, which is beyond the scope of the law. I agree to indemnify and save harmless Purdue University from any and all claims that may be asserted or that may arise from any copyright violation.

TIRTHANKAR ROY
_____
Printed Name and Signature of Candidate

09/16/2010
_____
Date (month/day/year)

*Located at http://www.purdue.edu/policies/pages/teach_res_outreach/viii_3_1.html

STUDY OF TWO-PHASE FLOWS IN REDUCED GRAVITY

A Dissertation

Submitted to the Faculty

of

Purdue University

by

Tirthankar Roy

In Partial Fulfillment of the

Requirements for the Degree

of

Doctor of Philosophy

December, 2010

Purdue University

West Lafayette, Indiana

UMI Number: 3453362

UMI

Dissertation Publishing

ProQuest®

ProQuest LLC
789 East Eisenhower Parkway
P.O. Box 1346
Ann Arbor, MI 48106-1346

ACKNOWLEDGEMENTS

TABLE OF CONTENTS

LIST OF TABLES

Table   Page

LIST OF FIGURES

Figure   Page

Figure   Page

Figure   Page

Figure   Page

NOMENCLATURE

t	Time
$\vec{v}_k$	Velocity of k phase
$\vec{g}$	Acceleration due to gravity
$\vec{v}_{ki}$	Velocity of k phase at interface
$\vec{M}_{ik}$	Generalized interfacial drag
i_k	Enthalpy of k phase
$\overline{\overline{q}}_k$	Conduction heat flux of k phase
q_k^t	Turbulent heat flux of k phase
i_{ki}	Enthalpy of k phase at interface
a_i	Interfacial area per unit volume
q_{ki}''	Interfacial heat flux into k phase
L	Height of the test section
D_h	Hydraulic diameter of the test section

Greek Symbols

α_k	Local void fraction of k phase
ρ_k	Density of k phase
Γ_k	Mass source for k phase
p_k	Pressure of k phase

$\overline{\overline{\tau}}_k$	Average viscous stress for k phase
τ_k^t	Turbulent stress for k phase
$\overline{\overline{\tau}}_{ki}$	Mean interfacial shear stress
ϕ_k	Energy dissipation
ϕ_j	Rate of change of interfacial area concentration due to jth interaction mechanism
ϕ_{ph}	Rate of change of interfacial area concentration due to phase change
η_{ph}	Void fraction source/sink rate due to nucleation/condensation

ABSTRACT

Roy, Tirthankar. Ph.D., Purdue University, December 2010. Study of two-phase flows in reduced gravity. Major Professor: Mamoru Ishii.

Study of gas-liquid two-phase flows under reduced gravity conditions is extremely important. One of the major applications of gas-liquid two-phase flows under reduced gravity conditions is in the design of active thermal control systems for future space applications. Previous space crafts were characterized by low heat generation within the spacecraft which needed to be redistributed within the craft or rejected to space. This task could easily have been accomplished by pumped single-phase loops or passive systems such as heat pipes and so on. However with increase in heat generation within the space craft as predicted for future missions, pumped boiling two-phase flows are being considered. This is because of higher heat transfer co-efficients associated with boiling heat transfer among other advantages. Two-phase flows under reduced gravity conditions also find important applications in space propulsion as in space nuclear power reactors as well as in many other life support systems of space crafts.

Two-fluid model along with Interfacial Area Transport Equation (IATE) is a useful tool available to predict the behavior of gas-liquid two-phase flows under reduced gravity conditions. It should be noted that considerable differences exist between two-phase flows under reduced and normal gravity conditions especially for low inertia flows. This is because due to suppression of the gravity field the gas-liquid two-phase flows take a considerable time to develop under reduced gravity conditions as compared to normal gravity conditions. Hence other common methods of analysis applicable for fully developed gas-liquid two-phase flows under normal gravity conditions, like flow regimes

and flow regime transition criteria, will not be applicable to gas-liquid two-phase flows under reduced gravity conditions.

However the two-fluid model and the IATE need to be evaluated first against detailed experimental data obtained under reduced gravity conditions. Although lot of studies have been done in the past to understand the global structure of gas-liquid two-phase flows under reduced gravity conditions, using experimental setups aboard drop towers or aircrafts flying parabolic flights, detailed data on local structure of such two-phase flows are extremely rare.

Hence experiments were carried out in a 304 mm inner diameter (ID) test facility on earth. Keeping in mind the detailed experimental data base that needs to be generated to evaluate two-fluid model along with IATE, ground based simulations provide the only economic path. Here the reduced gravity condition is simulated using two-liquids of similar densities (water and Therminol 59 ® in the present case). Only adiabatic two-phase flows were concentrated on at this initial stage. Such a large diameter test section was chosen to study the development of drops to their full extent (it is to be noted that under reduced gravity conditions the stable bubble size in gas-liquid two-phase flows is much larger than that at normal gravity conditions). Twelve flow conditions were chosen around predicted bubbly flow to cap-bubbly flow transition region. Detailed local data was obtained at ten radial locations for each of three axial locations using state-of-the art multi-sensor conductivity probes. The results are presented and discussed. Also one-group as well as two-group, steady state, one-dimensional IATE was evaluated against data obtained here and by other researchers, and the results presented and discussed.

1. INTRODUCTION

Gas–liquid (or vapor–liquid) two-phase flows are commonly found in many industrial processes, engineering applications, and in ordinary life. Due to their important applications in chemical engineering processes, nuclear reactors, air conditioning and refrigeration systems, and heat exchangers, two-phase flows have been actively investigated for several decades. Valuable experimental data were collected on-ground for different flow orientations and flow passage geometries. Theories and correlations were developed to predict the engineering parameters of gas–liquid flows in conduits like flow pattern transitions, pressure drops, void fraction, heat-transfer rates, etc. However, due to the complexity of the flow, predictions were largely in terms of empirical or semi-empirical correlations, which were for the most part based on specific test conditions; e.g., conduit size and shape, adiabatic or boiling flows, method of heating or gas injection, etc. [1]. Extrapolation of these correlations to other conditions would not be valid, particularly when gravity is significantly reduced.

One of the major applications of two-phase flow at microgravity conditions is the design and maintenance of active thermal control systems for future space stations and high-power communications satellites [2, 3 and 4]. Past thermal management requirements for satellites and orbiting spacecraft have been characterized by low power (< 25 kW) and short lifetime (< 3 years). These modest requirements can usually be satisfied by passive devices, such as heat pipes, or by pumped single-phase fluid cooling systems. The performance of passive devices is mostly independent of gravity. Knowledge gained of the performance of such systems on-ground can be directly used in the design of the space systems [2]. Two-phase flow systems (capillary or mechanically driven) have been chosen as potential candidates for the design of future thermal subsystems [2, 5, 6, 7, 8 and 9]. There are several characteristics that make two-phase

flows more desirable than single-phase flow for heat transfer purposes. First, the heat transfer coefficient in two-phase flow with phase change can be several orders of magnitude higher than that in single-phase flow due to the large latent heat of vaporization of the liquid. This results in a physically smaller system that can carry as much heat as a single-phase system with much larger size. Secondly, heat can be transferred to the fluid while maintaining a constant surface temperature. This is a highly desirable feature since many advanced instruments onboard payloads require an isothermal environment.

Another important application of two-phase flow is in the design of space nuclear power systems [2 and 4]. Such systems have been proposed to meet escalating power needs.

Two-phase flow phenomena also occur in many life-support systems in space stations and space labs. For example, the environmental conditions inside a space station (e.g., level of O_2, humidity, etc.) have to be maintained at comfortable levels. Water used for personal hygiene or other purposes, in many instances, has to be collected and processed for reuse. Two-phase flow is also prevalent in material processing in space, cryogenic transfer and storage, and many other enabling technologies.

Studies of two-phase flow under microgravity conditions are also of great interest to better understand the behavior of terrestrial flows. Since gravity force plays an overwhelming role on-ground, the microgravity conditions provide an ideal environment to study the influence of other less dominant forces such as those due to surface tension, lift force, and turbulence.

Prediction of two-phase flow and its evolution is made difficult by the existence of the dispersed phase and its numerous interfaces. The phenomena involved in two-phase flow are numerous and interrelated. Generally these flows are categorized based on the geometric orientations of the dispersed phase which are termed as flow patterns. These flow patterns influence the transfer of mass, momentum and energy between the phases. Moreover, the dispersed phase (in the form of bubbles or drops) interacts with each other causing the flow patterns to change which in turn influence the interaction mechanisms.

Due to this, the prediction of two-phase flow behavior remains a challenge, despite a lot of research into the area. Two-phase flow prediction in reduced-gravity condition is also far from being accomplished. Prediction of two-phase flows has evolved beginning with purely empirical relations. Over the years a number of models have been developed to better predict two-phase flow. Among these models, the drift-flux model and the two-fluid model are the most widely used. The drift-flux model is a semi-empirical approach based on the governing equations for mass, momentum and energy transfer and utilize well-established empirical correlations to describe the interaction between the phases. It has enjoyed wide spread use in part due to its ease of implementation. The drift-flux model works very well in cases where the two phases involved in the flow are strongly coupled [1]. Over the years, the two-fluid model has been established as the most detailed model to describe two-phase flow problems. The two-fluid model uses six equations (three for each phase, Equations 1.1 – 1.3) to describe the flow and uses interaction terms to describe the interaction between the phases. It has been widely used to predict multi-dimensional and transient two-phase flow. It has also proved to be very useful in cases where the flow changes significantly due to interactions within the dispersed phase.

Continuity equation:

$$\frac{\partial \alpha_k \rho_k}{\partial t} + \nabla \cdot (\alpha_k \rho_k \vec{v_k}) = \Gamma_k \tag{1.1}$$

Momentum equation:

$$\frac{\partial \alpha_k \rho_k \vec{v}_k}{\partial t} + \nabla \cdot (\alpha_k \rho_k \vec{v}_k \vec{v}_k)$$
$$= -\alpha_k \nabla p_k + \overline{M}_{ik} + \nabla \alpha_k (\overline{\overline{\tau}} + \tau_k^t) + \alpha_k \rho_k \vec{g} + v_{ki} \Gamma_k + \tau_{ik} - \nabla \alpha_k \cdot \overline{\overline{\tau}}_{ki} \tag{1.2}$$

Energy equation:

$$\frac{\partial \alpha_k \rho_k i_k}{\partial t} + \nabla \cdot (\alpha_k \rho_k i_k v_k)$$
$$= -\nabla \cdot \alpha_k (\overline{\overline{q}}_k + q_k^t) + \alpha_k \frac{D_k p_k}{Dt} + i_{ki} \Gamma_k + q_i^{''}_{ki} + \phi_k \tag{1.3}$$

It can be found that several interfacial transfer terms arise on the right hand side of the mass, momentum and energy equations above (generalized interfacial drag $\overline{M}_{ik}$, interfacial

mass transfer Γ_k and interfacial heat flux $q_{ki}^{"}$). These interaction terms can be expressed as a product of the interfacial area concentration and the driving force for the transfer. Hence, the predictive capability of the two-fluid model can be said to rest on the accurate determination of the interfacial area concentration since the driving force for the transfer is usually known. The interfacial area concentration, a_i, is defined as

$$a_i = \frac{1}{L_s} = \frac{\text{total interfacial area}}{\text{mixture volume}} \tag{1.1}$$

where, L_s represents the length scale at the interface. Thus, the physical meaning of the interfacial area concentration, a_i, is the interfacial area per unit mixture volume [1]. Traditionally, the interfacial area concentration has been specified using flow regime based correlations/models. The flow regime transition criteria are based on the assumptions of steady-state and fully-developed flows, which do not dynamically represent the changes in the interfacial structure. Moreover, under reduced-gravity condition, two-phase flow may not reach a steady-state condition and the interfacial structure may not reach an equilibrium configuration, particularly at low flow rates. Therefore, the use of flow regime dependent closure relations for interfacial area concentration may cause significant error, in particular for reduced-gravity two-phase flows. Moreover, their use represents a paradoxical situation in which a dynamic model is coupled with static correlations.

In case of normal gravity two-phase flows, a novel approach that takes into account the dynamic changes of the structure of two-phase flow has been adopted by introducing the interfacial area transport equation. The interfacial area transport equation (IATE) is formulated by mechanistically modeling the physical processes that govern the creation and destruction of interfacial area. The "1-group" IATE [1] is given by

$$\frac{\partial a_i}{\partial t} + \nabla \cdot \left(a_i \vec{v}_i \right) - \frac{2}{3} \left(\frac{a_i}{\alpha_g} \right) \left(\frac{\partial \alpha_g}{\partial t} + \nabla \cdot \left(\alpha_g \vec{v}_g \right) - \eta_{ph} \right) = \sum_j \phi_j + \phi_{ph} \tag{1.5}$$

where, $a_i(\vec{x}, t)$ is the average interfacial area concentration of all-sized particles at location $\vec{x}$ and $\vec{v}_i(\vec{x}, t)$ is the interfacial velocity. The ϕ_j and ϕ_{ph} in the RHS of Equation 1.5 represent the rate of change in the interfacial area concentration due to fluid particle interactions, such as breakup and coalescence, and due to evaporation or condensation

processes, respectively. Therefore, the IATE dynamically models the changes in the flow structure and can, potentially, significantly improve the predictions. The IATE has been successfully developed for normal gravity conditions [1]. It has been demonstrated that by using the IATE, the evolution of interfacial structures can be dynamically predicted for a flow field.

The objective of the present research was to develop IATE applicable to reduced-gravity two-phase flows. To that purpose, a detailed ground-based experimental study has been carried out since 2004 to investigate two-phase flow structure under reduced-gravity conditions, and to establish a reliable database of local two-phase flow parameters. In the study, reduced-gravity condition was simulated using two immiscible liquids of similar densities. The detailed two-phase flow parameters were measured by state-of-the-art global and local two-phase flow measurement techniques, including advanced image processing, multi-sensor impedance void-meter, and local double- and four-sensor conductivity probes. In the previous phase of this research program extensive global and local two phase flow measurements were performed in a small diameter (25 mm inner diameter or ID) test section for a large number of flow conditions. "One-group" IATE applicable was evaluated against the obtained data. All these results were reported in earlier reports [10, 11, 12 and 13]. The current phase of the research program concentrated on experiments performed in a large diameter (304 mm ID) test section. Experiments ranged from rise velocity experiments to local two-phase flow measurements. The results of rise velocity experiments were also reported in an earlier report [14].

A detailed literature review of previous work to investigate structure of two-phase flows under reduced gravity conditions is presented in the next Chapter. Chapter 3 presents the rationale behind performing ground based simulations to study gas-liquid to-phase flows under reduced gravity environments. This chapter also presents the details of the experimental facility, instrumentation and other related information. Chapter 4 presents the results of local two-phase flow measurements performed in the large diameter test facility and discuss it. In Chapter 5 both 1-group and 2-group IATE is evaluated against data obtained by several researchers and the results discussed. Chapter

6 summarizes and concludes the report and also suggests possible directions of future work.

2. LITERATURE REVIEW

Researchers have long been interested in the mechanisms of boiling heat-transfer, condensation and adiabatic two-phase flows in the absence of Earth's gravity. This curiosity was turned into an urgent need as space missions and skylabs were emerging in the 1960s and 1970s. As spacecrafts increased in size and power demands, active methods of transporting heat along a spacecraft were pursued. A two-phase system was considered an attractive alternative to the conventional single-phase systems for handling large energy levels and also providing them at uniform temperatures. It was, therefore, recommended in the early eighties that two-phase heat transport systems for thermal management in space be developed and demonstrated from initial ground feasibility tests through on-orbit demonstration of actual zero-gravity performance. Some work has been done in this regard and two-phase systems were designed and underwent ground testing with anticipation of similar performance on-orbit under actual zero-gravity conditions. Fundamental research of the influence of gravity on two-phase flow system parameters is still far from complete. Since initially we are more concerned with the structure of adiabatic two-phase flows under reduced gravity environments, previous relevant work was reviewed in detail and observations noted in the following.

Many studies have been done to understand global flow patterns and their transitions for gas-liquid flows under reduced gravity conditions. The pioneering study was done by Hepner et al. [15] in 1975. C-135 trajectories were used to collect data on flow patterns for air-water flow in a 2.54 cm diameter tube having an L/D_h of 20. Obviously the test section length was small and consequently there were lots of discrepancies between duplicate tests. Dukler et al. [16] performed experiments in two facilities. The first one was 9.52 mm diameter Plexiglass tube which was 0.457 m long. For experiments in this facility reduced gravity was generated using a drop tower. The

superficial velocity of the continuous phase (water) in these experiments varied from 0.142 m/s to about 0.950 m/s. The dispersed phase (air) superficial velocity varied from 0.252 m/s to about 0.690 m/s. High speed cameras were used to obtain images of the flow which were used to determine the existing flow pattern. The second facility consisted of a12.7 mm diameter tube about 1.06 m long. For experiments in this facility reduced gravity was generated using Learjet trajectories. The superficial velocity of the continuous phase (water) in these experiments varied from 0.079 m/s to about 0.940 m/s. The dispersed phase (air) superficial velocity varied from 0.09 m/s to about 25.32 m/s. High speed cameras were used to obtain images of the flow which were used to determine the existing flow pattern. Bubbly flow to annular flow was observed in these facilities. Dukler et al. [16] also attempted to predict the transition from one flow regime to the other. Colin et al. [17] measured void fraction, pressure gradient and flow pattern data for air-water flows at near zero gravity through a 4 cm dia tube about 3 m long. The reduced gravity was created aboard a plane following parabolic trajectories. Bubbly flow to slug flow regimes were observed. High speed cameras were used to obtain images of the flow which were used to determine the existing flow pattern. Colin et al. [17] compared their results to flow pattern transition criteria proposed by Dukler et al. [16] previously. Similar experiments were performed by Zhao and Rezkallah [18], Elkow and Rezkallah [19 and 20] and Lowe and Rezkallah [21]. All the facilities were of 9.53 mm inside diameter and of various lengths. Instruments ranging from high speed cameras to capacitance probes were used in determining the flow patterns. Various models to predict transitions were put forward and checked against the obtained data. NASA's KC-135 and DC-9 microgravity aircrafts were used to generate microgravity conditions. Bousman et al. [22] performed numerous two-phase gas liquid flow experiments on NASA microgravity aircraft to determine the effect of liquid and gas superficial velocities, tube diameter, liquid viscosity and surface tension. Void fraction, liquid film thickness and pressure drop was measured as well as high speed photography was performed. The transition from bubbly to slug flow was found to be affected by tube diameter for air-water flows and by changes in liquid viscosity and surface tension. The transition from

slug to annular flow was not significantly affected by these changes. Void fraction based transition models were developed to predict microgravity flow patterns. Weber number based transition models were also evaluated. Rezkallah [23] proposed Weber number based flow pattern maps for liquid-gas flows at microgravity. Choi et al. [24] obtained data of flow-patterns, void fraction and frictional pressure drop at normal gravity, in microgravity and in hyper-gravity conditions, aboard MU-300 aircraft, capable of parabolic trajectory flying. The gravity dependency of flow patterns was more clearly observed with the decrease in gas and liquid flow rates. The effect of gravity on two-phase flows was found to be insignificant for higher liquid and gas flow rates. Several other similar works have been carried out in the past.

It has been shown that flow regime transition criteria developed for normal-gravity horizontal as well as vertical two-phase flows do not perform well for two-phase flows under reduced gravity conditions [2]. In general, two-phase gas-liquid flow under reduced gravity conditions can be divided into three main flow regimes. These are surface tension controlled, intermediate, and inertial force controlled. The first region is where the forces due to surface tension are significantly higher than those due to inertia ($We<1$), which includes bubbly and slug flows (Fig. 2.1 (a) and (b)). We is given by

$$We = \frac{\rho_c u_r^2 D_b}{\sigma} \tag{2.1}$$

The bubbly to slug flow transition is believed to occur at a critical void fraction which has been shown to vary considerably (Dukler et al. [16], Zhao and Rezkallah [18]) depending on the tube diameter, the length needed to reach fully developed conditions, etc. The second region is where the two forces are comparable ($1<We<20$), which is occupied by transitional flows (frothy slug-annular flow). The third region is where the forces due to inertia are dominant ($We>20$), which is occupied by annular flow. A flow pattern map based on these criteria is shown in Fig. 2.2. The figure also shows data collected by the Microgravity Research Group at the University of Saskatchewan [2] and also air-water data collected by Bousman [22] and Colin et al. [17].

However, above mentioned studies are not enough to understand completely adiabatic two-phase flows under reduced gravity environments. It should be remembered that in reduced gravity environments, especially for low-inertia two-phase flows, the
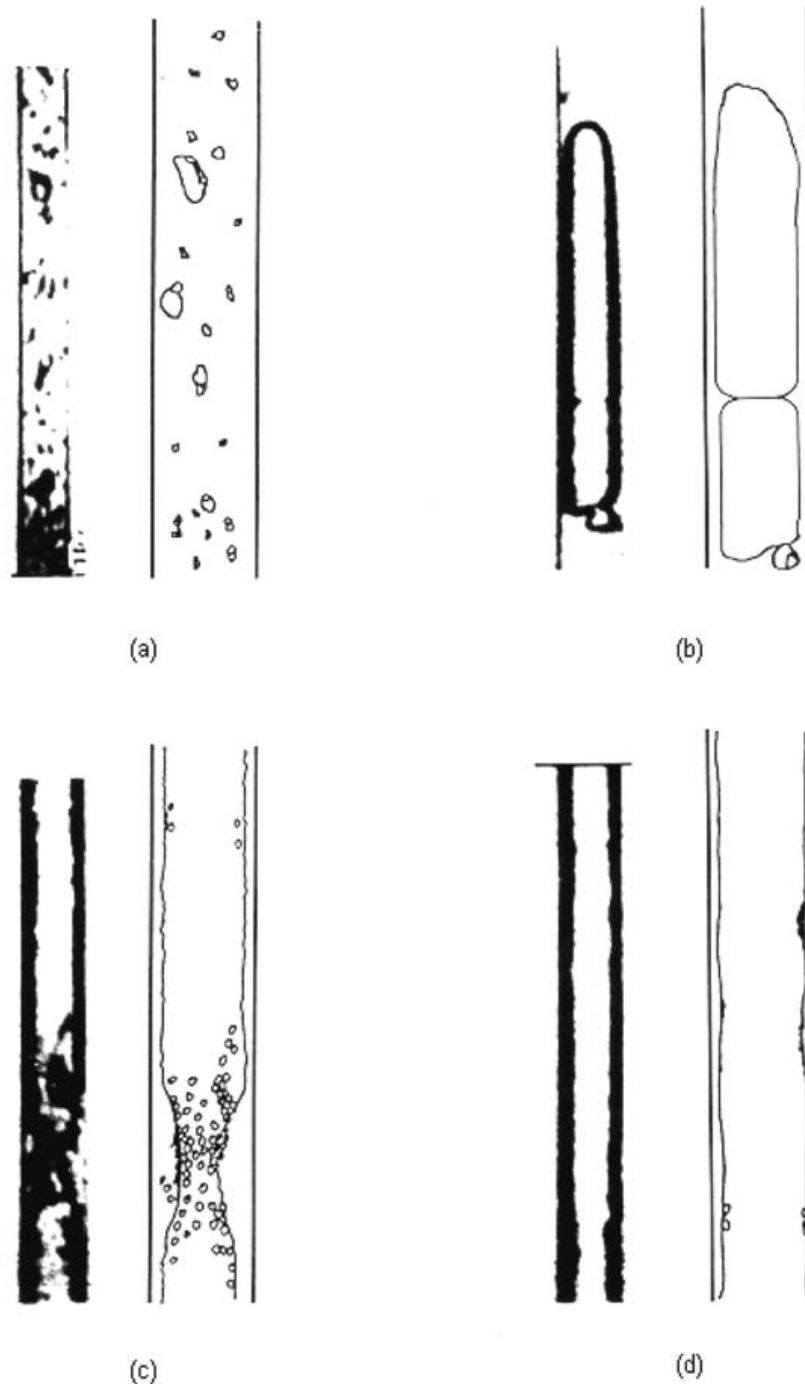
Fig. 2.1: Gas liquid two-phase flow regimes under reduced gravity conditions [2].
(a) Bubbly, (b) Slug, (c) Frothy slug-annular, and (d) Annular.
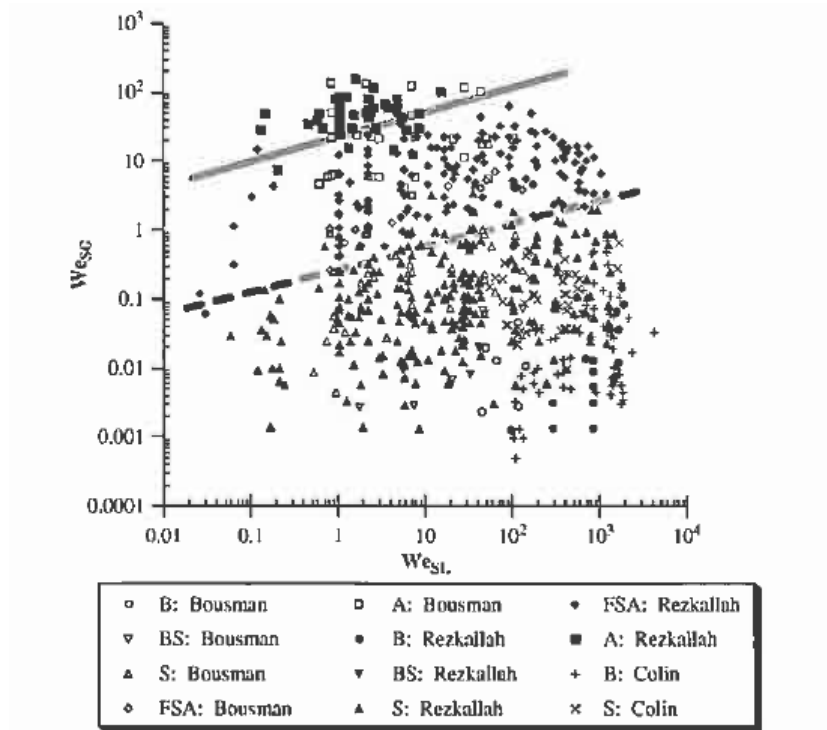
Fig. 2.2: Weber number based flow regime transition criteria [2].

flows will require an extremely large length of flow duct to reach fully developed conditions. This means that above mentioned experimental results have limited applicability in designing two-phase flow systems operating in reduced gravity environments. The reason being that over a large length of the flow duct the two-phase flow will bear a signature of the inlet conditions. As a result the above mentioned experimental results and observations become limited to the injection methods employed in the test facilities. The two-fluid model along with IATE [1] can prove extremely useful for predicting behavior of two-phase flows under reduced gravity environments. That is because this model doesn't make assumptions like fully developed flows, etc. Given the initial conditions this model can predict the subsequent two-phase flow behavior. However, it is extremely essential to first evaluate the predictions of this model against experimental data obtained under reduced gravity environments.

Very few experimental programs have been carried out till date to generate detailed local data against which the two-fluid model along with the IATE can be evaluated. Towards this end Takamasa et al. [25] measured axial developments of one-dimensional void fraction, bubble number density, interfacial area concentration, and Sauter mean diameter of adiabatic nitrogen-water bubbly flows in a 9 mm-diameter pipe under microgravity environments. The flow measurements were performed at four axial locations (L/D_h=7, 30, 45 and 60) under various flow conditions of superficial gas velocity (0.0083-0.022 m/s) and superficial liquid velocity (0.073-0.22 m/s). The interfacial area transport mechanism under microgravity environment was discussed in detail based on the obtained data and visual observation. Marked bubble coalescence was observed due to trailing bubbles near the channel center coalescing with bubbles in the vicinity of the channel wall (velocity profile entrainment). Negligible bubble breakup was observed because of weak turbulence under tested flow conditions. Axial changes of measured interfacial area concentrations were compared with the predictions of IATE (Fig. 2.3). It was found that, for the tested flow conditions, the velocity profile entrainment effect under micro-gravity environment was comparable to the wake entrainment effect under normal gravity environment. This led to insignificant differences between measured interfacial area concentrations and ones predicted by IATE with the wake entrainment model. Vasavada et al. [26] performed extensive experimental studies simulating reduced gravity environments in ground based facilities by using two immiscible liquids of similar densities. Data sets were acquired at a total of eleven flow conditions in bubbly and bubbly to slug flow transition regimes. Flow visualization was performed and a flow regime map developed, which was compared with relevant bubbly to slug flow regime transition criteria. In addition, important two-phase flow local parameters like dispersed phase fraction, interfacial area concentration, droplet number frequency and droplet velocity were acquired at two-axial locations using state-of-the-art multi-sensor conductivity probes. From the acquired data it was shown that coalescence mechanism was enhanced by increasing the flow rate of either phase. Evidence of turbulence induced particle interaction mechanisms was also shown. The data presented

highlighted the differences between flow structures of two-phase flows under normal and reduced gravity environments.

Many works have been done to develop drift-flux model as well as two-fluid model along with IATE which take gravity effects into consideration. Hibiki et al. [27] studied in detail the drift-flux model which takes the gravity effect into account. The constitutive equations of the distribution parameter for bubbly flow, which takes the gravity effect into account, was proposed, and the constitutive equations for slug, churn and annular flows, which are applicable to reduced gravity conditions, were recommended based on existing experimental and analytical studies. The previously derived constitutive equations of the drift velocity in various two-phase flow regimes, which takes the frictional pressure loss into account, were adopted in this study. A
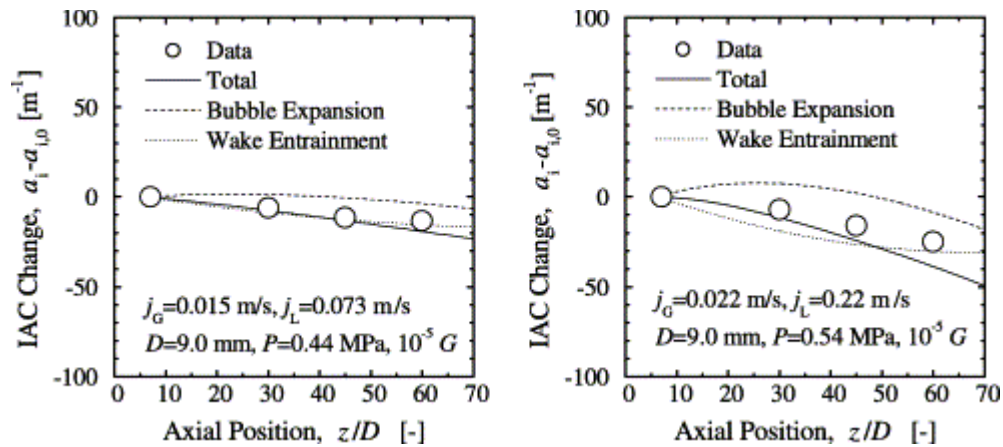
Fig. 2.3: Performance of one dimensional one group IATE under microgravity environments [25].

comparison of the model with experimental data, over various flow regimes and a wide range of flow parameters taken at microgravity conditions, show satisfactory agreement (Fig. 2.4). The drift-flux model was applied to reduced gravity conditions, which correspond to lunar and Martian surface gravities, and the effect of the gravity on the void fraction in two-phase flow systems was discussed. Hibiki et al. [28] studied IATE taking into account the gravity effect. The constitutive equation for the sink term of interfacial area concentration due to wake entrainment was developed by considering

body acceleration due to frictional pressure loss. Comparison of the newly developed interfacial area transport equation with various experimental data taken at microgravity conditions showed satisfactory agreement (Fig. 2.5). It was shown that the effect of gravity on interfacial area transport in a two-phase flow system is more pronounced for low liquid flow and low void fraction conditions, whereas the effect is negligible for high mixture volumetric flux conditions. Vasavada et al. [29] evaluated one dimensional one group IATE against data previously acquired by the author himself. Flow conditions lying in the bubbly and bubbly to slug transition flow regime were used for evaluation purposes. Flow conditions in the bubbly flow regime, where coalescence was expected to dominate, were used to evaluate the available models and relative strength of coalescence due to random collision and wake entrainment mechanisms. These mechanisms were identified as dominant ones. The maximum error between the prediction and experimental data for the area-averaged interfacial area concentration was found to be 22% (Fig. 2.6). From this analysis it was found that wake entrainment had a stronger effect as compared to random collision for flow conditions with low continuous and/or dispersed phase superficial velocity. As the superficial velocities of either phase, and therefore the turbulence in the flow, increased, random collision became more dominant over wake entrainment. The comparisons showed that the modeled interaction mechanisms existing in the one dimensional one group IATE were physically sound. Moreover, they have shown to represent the physics existing in reduced-gravity two-phase flows for the flow conditions considered. The study demonstrated the ability of the IATE to model the evolution of two-phase bubbly flows in reduced-gravity conditions.
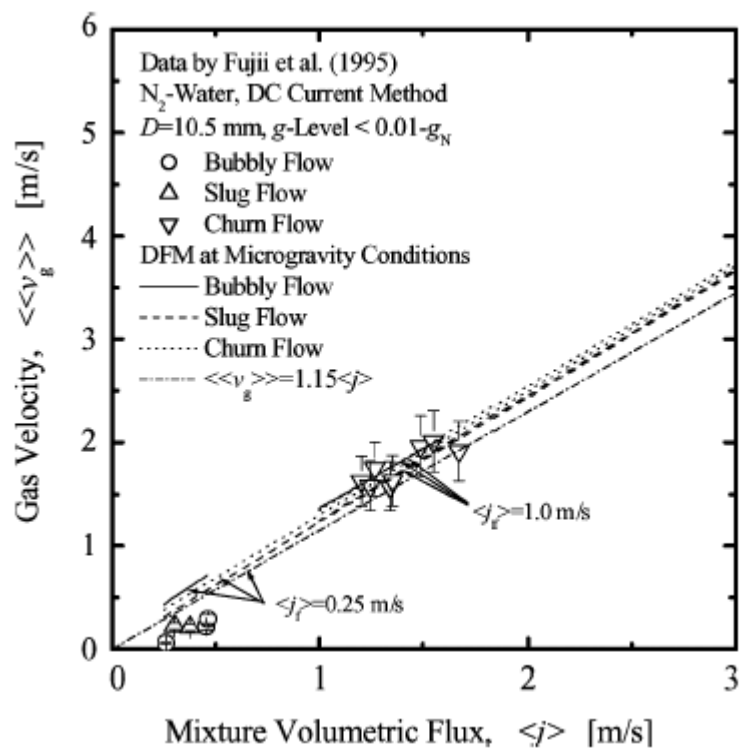
Fig. 2.4: Comparison of drift-flux model at microgravity conditions with data [27].
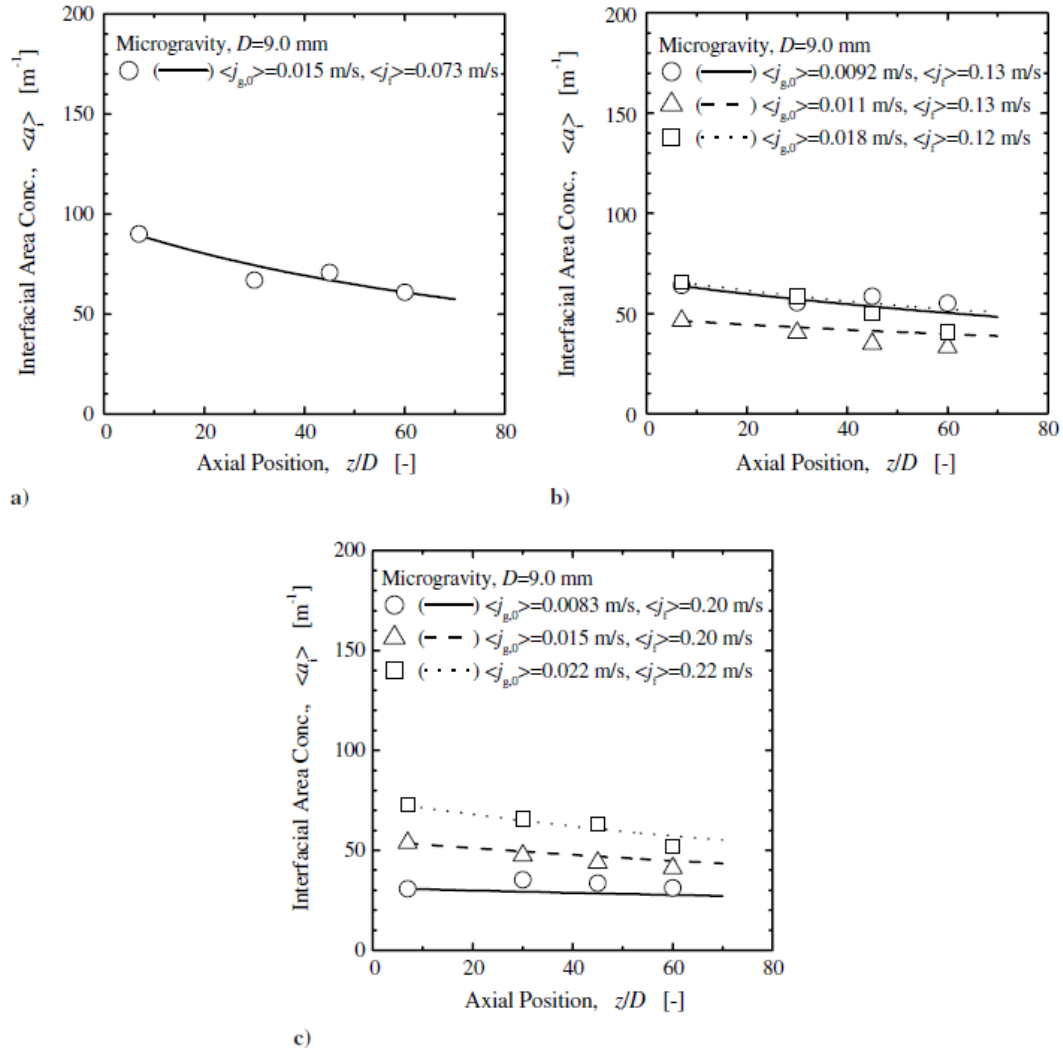
Fig. 2.5: Comparison of IATE with measured interfacial-area concentrations at microgravity conditions [28].
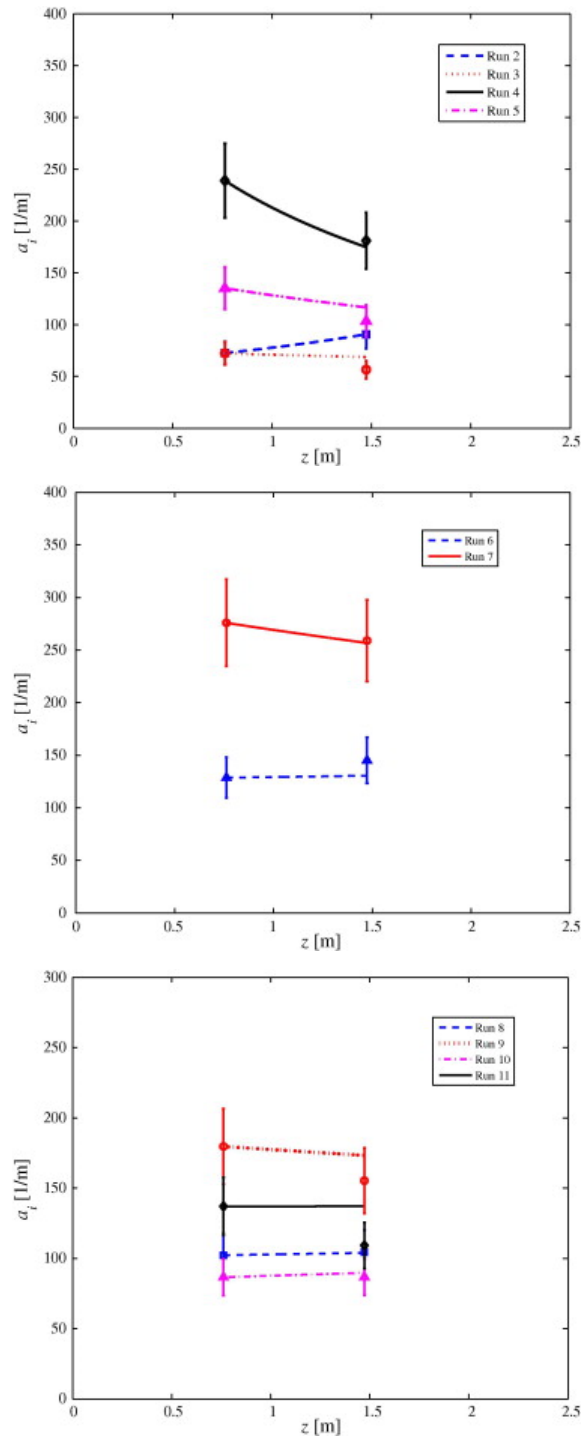
Fig. 2.6: Comparison of predictions of one dimensional one group IATE against experimental data [29].

3. EXPERIMENTAL APPROACH

Most of the investigations in the past two decades in the area of reduced-gravity two-phase flow have focused on flow regime identification along with some studies on the pressure drop and heat transfer characteristics of such flows. However, the mechanisms detailing the effects of reduced-gravity on phase distribution have not been thoroughly revealed. To enhance the understanding of and to be able to accurately predict reduced-gravity two-phase flow behavior, extensive experimental study needs to be performed to examine the local interfacial structures.

3.1 Justification for Current Experimental Approach

The main objective of the current research was to develop a reliable model to dynamically predict two-phase flows in reduced-gravity conditions. For this, an experimental study was used to obtain a reliable database of local two-phase flow parameters and to enhance the understanding of the effects of reduced-gravity on local phase distribution and other parameters such as interfacial area concentration and bubble (drop) size. This required extensive experimentation and parametric study. To meet these objectives, ground-based experiments, wherein a reduced-gravity condition was simulated, were performed. The advantages and disadvantages of various methods of simulating reduced-gravity are summarized in Table. 3.1.

In the current research effort, reduced-gravity condition is simulated by using two immiscible fluids of similar densities in ground-based experimental facilities. Several researchers in the past have used ground-based experiments to study flow structures in reduced-gravity conditions [30, 31 and 32]. Almost always two liquids (single-phase two-component flow) have been used to achieve the desired simulation. Ungar et al. [31],.

Table 3.1: Comparison of means for reduced-gravity experimentation

Method	Value $(\times g_e)$	Duration (s)	Remarks
Aboard Space Stations	10^{-8}-10^{-6}	Indefinite	1. Extremely costly 2. Difficult operation and maintenance 3. Limitations on experimental facility setup 4. Most desirable condition
Parabolic Flights	10^{-3}-10^{-2}	10-20	1. Less expensive as compared to above 2. Longer duration of reduced gravity achievable compared to drop tower 3. Residual acceleration effects
Drop Tower	10^{-4}-10^{-2}	2-5	1. Short duration of reduced gravity environment 2. Limitations on experimental facility setup
Ground-Based Experiments	10^{-2}-10^{-1}	Indefinite	1. Limited range of simulation 2. Flexibility in design and operation of experimental facility 3. Greater parametric variations possible 4. Least expensive of all methods

however, argues that use of two liquids does not capture the difference in inertia between two different phases and have proposed using a single-component two-phase approach for which they have given scaling guidelines. As part of the current research, focus was directed on the regions in which the inertia effect was not dominant. It is expected that these regions will exhibit the most pronounced effect of reduced-gravity on the two-phase flow structure and its development. For the high inertia region, the current simulation may not be completely valid due to the imposed restriction pointed out by Ungar et al. [31]. However, it is expected that the flow structures in such cases will resemble those on earth as inertia will exert maximum influence. This assertion is supported by recent results of Celata [33] where forced convection boiling was investigated aboard parabolic flights. The results show that the heat transfer and hydrodynamical parameters like bubble size and flow pattern are similar between reduced-gravity and normal gravity once the fluid velocity increases beyond a certain critical value. Celata [33] also showed that

similar behavior is obtained if the flow quality increases beyond a threshold at the same velocity.

3.2 Selection of Working Fluids

The selection of the two liquids that will be used for the simulation is a crucial step in the experimental study. Due to the ease of availability and well-known properties, water was chosen as one of the liquids. The selection of the second liquid was carried out based on some important considerations with regard to the simulation as well as the experimentation. The important characteristics identified are as follows:

- Density as close to water as practically possible.
- Relative ease of separation from water using conventional techniques.
- Interfacial tension between the two liquids such that the Bond number has an acceptable value to justify the simulation.
- Compatible with the instrumentation to be used in terms of sensor response and sensor fouling.
- Non-toxic and stable under operating conditions.
- Relatively low cost.

Based on the above requirements a systematic approach in the selection of the appropriate liquid was followed. The preliminary search was conducted on the basis of density difference, form and non-toxicity.

After short listing some potential liquids, samples of these candidates were asked for basic experimentation. However, since many samples could not be obtained, within reasonable time, from their manufacturers, the final selection was made between two synthetic heat transfer fluids, Therminol 59 $^®$ (hereafter referred to as Therminol only), manufactured by Solutia Inc. and Xceltherm XT $^®$ (hereafter referred to as Xceltherm only), manufactured by Radco Industries. Both these liquids are hydrocarbon derivatives and hence organic in composition. A comparative summary of the relevant properties of these liquids is given in Table 3.2.

Table 3.2: Properties of Therminol 59 and Xceltherm XT

Liquid	Composition	Density (kg/m^3)	Density Difference With Water (%)	Dynamic Viscosity $(x10^{-3}$ $kg/m\text{-}s)$	Interfacial Tension With Water $(x10^{-3}$ N/m)
Therminol 59	Alkyl Substituted Aromatic	971.2	2.7	7.0	42.5
Xceltherm XT	Alkyl Substituted Aromatic	996.4	0.18	4.5	Not Measured

Since a centrifugal separator for separation of the liquids was found to be uneconomical, it was decided to use gravity based separation. Therefore, the next test of the liquids involved a simple experiment to determine the ease of gravity based separation. The tests were performed by separately injecting 100 ml of each liquid in the form of drops into 1000 ml of water via an injection syringe and then thoroughly mixing the two fluids using a stirrer. The resulting mixture of each liquid with water was left undisturbed and the progress of the separation process was noted at regular intervals of 6 hours. After 30 hours it was found that Therminol separates completely whereas Xceltherm does not. Another surprising thing was observed in the separation tests. It was found that, sometimes Xceltherm behaved as if it were heavier than water and thereby sank to the bottom of the beaker. The reason for this behavior was identified as the uncertainty in the density of the fluid. Since it contains different hydrocarbon components the exact density varied from sample to sample. The manufacturer specified the possibility of ±10% property variations between separate samples. Since the density of Xceltherm is very close to that of water even a small variation may cause its density to exceed that of water. Due to this behavior Xceltherm was eliminated from consideration. Hence it was decided to test Therminol for compatibility with instrumentation.

State-of-the-art instrumentation to be used in the experimental program included multi-sensor local conductivity probes for measurement of flow parameters. Therminol

was subjected to tests for compatibility with the multi-sensor local conductivity probe since this instrument is intrusive and was to be in contact with Therminol. The response of multi-sensor local conductivity probe depends on the relative difference in the conductivity of the two fluids used. Since the multi-sensor local conductivity probes have been used extensively in air-water flow systems at Purdue University the results of the sensor response when exposed to air and water was used as a reference to compare with the response when exposed to Therminol and water.

Stainless steel acupuncture needles coated with Teflon were used to make the multi-sensor conductivity probes. The needles were coated such that only the tip was exposed. The details about the manufacturing of these probes are given in Kim et al. [34]. One such needle was used in the test to determine the response of a water-Therminol mixture. A beaker containing the separated liquids was used for the purpose of this test. The tip of the needle was first immersed in the layer containing Therminol and then further down in water. The response was acquired for 1 minute at a frequency of 1200 Hz. The signal variation was approximately 0.8 V which is comparable to approximately 1.2 V when the same test was carried using air and water. Hence, the response characteristics were found to be highly acceptable. The fouling of the tip of the needle was also found to be negligible even with repeated immersion.

Since Therminol was found to be compatible with instrumentation, the next step was to determine the interfacial tension of Therminol with air and water. The manufacturers of Therminol provided values of its surface tension with air at three different temperatures. Using a least squares fit, the value of this parameter at 25°C was found to be 37.2×10^{-3} Nm^{-1}. However it was still felt necessary to experimentally measure the interfacial tension of Therminol with both air and water.

The setup which was used to determine the surface tension of Therminol with air is shown in Fig. 3.1. The experimental method was derived from Rashidnia et al. [35]. A Pyrex glass capillary tube of 1.2 mm ID was held using a clamp. The alignment of the clamp in the horizontal direction and the perpendicularity of the tube with the clamp were ensured. An acrylic test cell 31.75 mm×31.75 mm in area and 44.45 mm in height was

filled about halfway with Therminol and placed on a laboratory jack. Prior to the experiments the capillary tube was cleaned using acetone, deionized water and
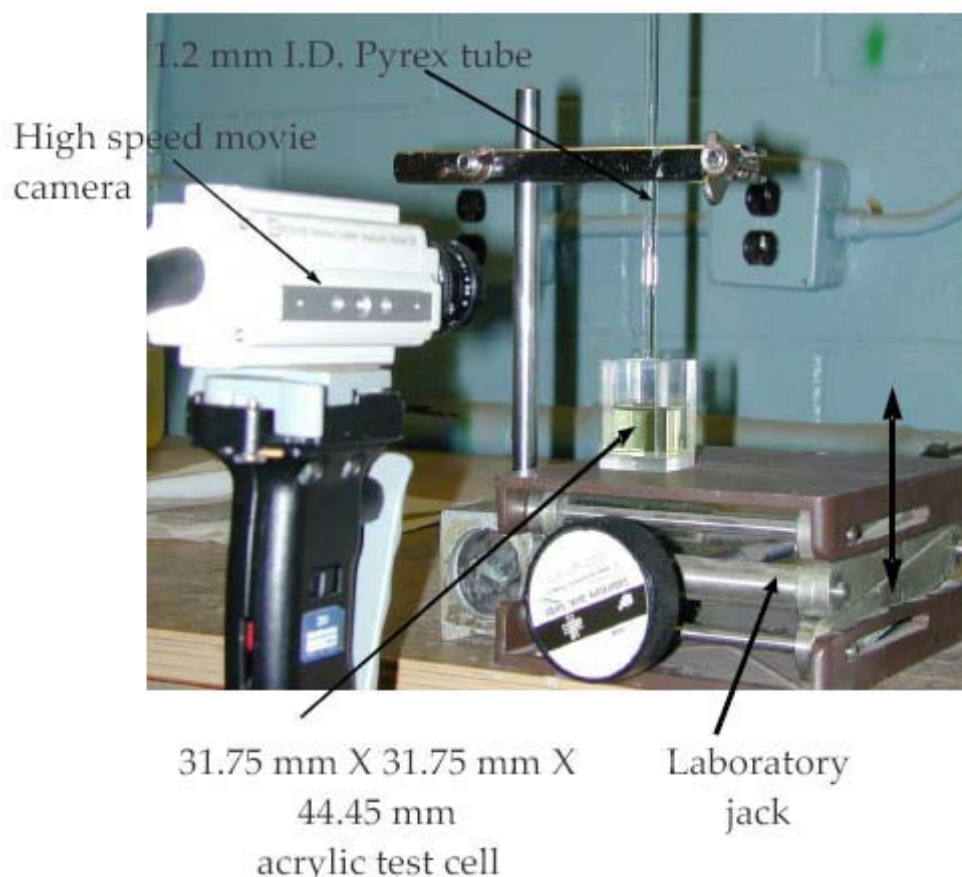
Fig. 3.1: Setup used for experimental determination of interfacial tension between Therminol with both air and water.

compressed air. The tube was then allowed to dry in ambient conditions for at least 15 minutes before being used in the experiment. The experiment involved immersing the tube in Therminol by raising the test cell on the jack. This caused a capillary rise in the tube. A high-speed video camera was used to take pictures of the meniscus once it was stabilized. The prints of the captured pictures were used to determine the height of the meniscus from the free surface and the radius of curvature of the meniscus. The diameter of the tube and height of the test cell were used to determine the magnification of the

camera in the radial and axial directions, respectively. These were used to convert the measured values to actual scale. A commercial drafting program was used to determine the contact angle using the measured values of the radius of curvature and the tube inner diameter. The contact angle and meniscus rise were used in the capillary rise formula to determine the surface tension value. The values obtained fell around a mean of 31.30×10^{-3} Nm^{-1} within an error band of $\pm14\%$. A separate acrylic test cell was also used to determine the surface tension of water with air and hence benchmark the experiments. The value of this parameter was found to be about 10 % less than the ideal value of 72.50×10^{-3} Nm^{-1} at 25°C. The errors encountered in the measurement of surface tension in each case were reasonable considering the lack of rigorous cleaning and of precise apparatus to measure the meniscus details and are within the error range reported in literature. The results gave a surface tension of 32.10×10^{-3} Nm^{-1} which was very close to that measured from the capillary rise method. The value of the interfacial tension between Therminol and water was obtained using the Young-Dupre model and was found to be 42.5×10^{-3} Nm^{-1}. In obtaining this number, the value of the contact angle between Therminol and borosilicate glass was taken as 165° based on the experimental results and the surface tension of water with air was taken as 72.50×10^{-3} Nm^{-1}. The important physical properties of Therminol and water are tabulated in Table 3.3.

Subsequently, a decision was necessary regarding which liquid should constitute the continuous phase. Previous researchers have used the phase with higher viscosity as the continuous phase to maintain the viscosity difference observed between liquid and vapor. However, these researchers have observed inverted flow in which the dispersed phase contacts the wall and the continuous phase becomes dispersed. In the present case water was used as the continuous phase in order to prevent the occurrence of such instability. This choice also preserved the situation in gas-liquid two-phase flows of interest in reduced-gravity environments where the heavier fluid is the continuous phase. Although the dynamic viscosity difference (μ) was not simulated by the current choice of the 'phases', the ratio between the kinematic viscosities (v) of the two 'phases' was similar to that existing in a practical gas-liquid system, where the dispersed phase (gas) has a higher kinematic viscosity as compared to the continuous phase (liquid). In an air-

water system, the ratio of the kinematic viscosity of air to that of water is approximately 15.0 whereas in the present case this ratio was approximately 7.2. It is known that kinematic viscosity is a more important physical parameter as compared to the dynamic viscosity.

Table 3.3: Properties of Therminol and water

Liquid	Composition	Density (kg/m^3)	Dynamic Viscosity $(x10\text{-}3\ kg/m\text{-}s)$	Interfacial Tension $(x10^{-3}\ N/m)$
Therminol	Alkyl Substituted Aromatic	971.2	7.0	42.5
Water	-	998.0	1.0	-

3.3 Experimental Facility

For the current experimental study, a test section consisting of a 304 mm ID round pipe, was used. Since the maximum stable drop diameter is very large for the current experimental study, a large diameter test section enabled the observation of the complete growth of such a drop. In the case of the small diameter test section, drops elongated in lengthwise direction after its size became comparable to channel diameter. Such drops were considered as slug drops.

A schematic diagram showing the general layout of the test facility is shown in Fig. 3.2. The test section is constructed from Pyrex (borosilicate) glass pipes. Pyrex glass was chosen as the material of choice because of its high chemical resistance to attack from alkyl hydrocarbons (such as Therminol). Also, it is comparatively easy to observe fouling of and to clean Pyrex glass. The height of this test section is approximately 4.5 m giving a L/D_h of about 17. The exit of the injector section (see Fig. 3.2) is considered as the origin for measurement in the direction of. As shown in the schematic, water and Therminol are pumped into the test section using centrifugal pumps from their respective

tanks. Therminol is metered using a pair of rotameters. The flow rate of water through the outer and inner annuli is measured using magnetic flowmeters. For the water measurements, the magnetic flowmeters are accurate to within $\pm 1.0\%$. The fluids enter
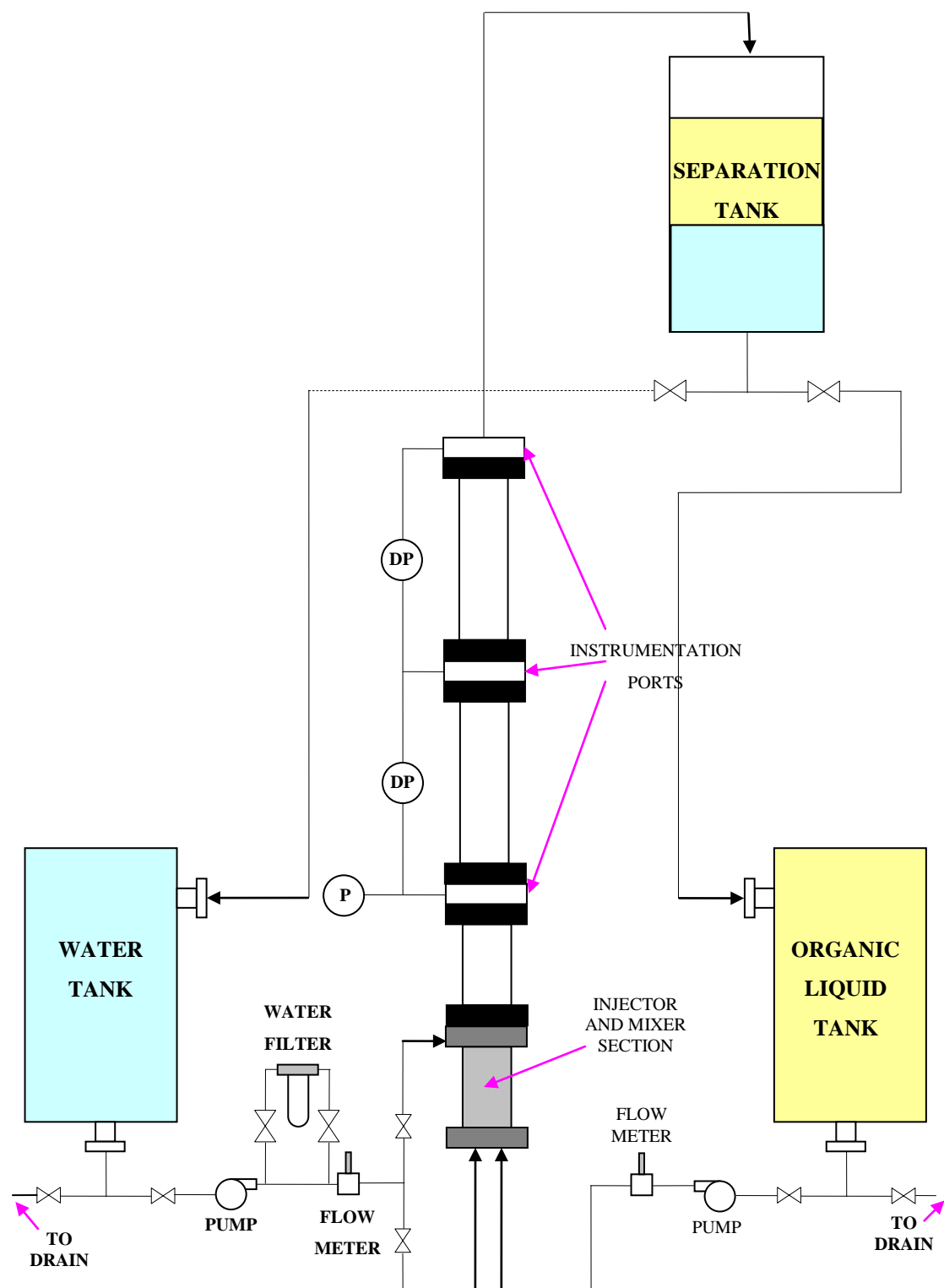
Fig. 3.2: Schematic of experimental facility

the test section through the injector. The mixture then flows through the 304 mm ID test section. Upon exiting the test section, the mixture is injected into a separator tank. The mixture of the two liquids is allowed to separate under effect of gravity in the separator tank. This arrangement requires the experiments to be run as batch processes.

The water pump capacity limits the maximum water flow rate through the test section to about 23 gpm (corresponding to a superficial velocity of about 2.68×10^{-2} m/s). The water tank has a capacity of 250 gallons. This limits the maximum time an experiment can be run, before running out of water, to about 11 minutes. Similarly the organic liquid pump capacity limits the maximum organic liquid flow rate through the test section to about 23 gpm (again corresponding to a superficial velocity of about 2.68×10^{-2} m/s). However, the organic liquid tank only has a capacity of 100 gallons. This limits the maximum time an experiment can be run, before running out of the organic liquid, to about 4 minutes. For most of the experiments performed during this phase of the research the run times varied from 3-5 minutes depending on the flow rate of the organic liquid. Two runs were performed for each flow condition to ensure statistically significant values of local two-phase flow parameters being recorded.

The injector for the 304 mm ID test section is shown in Fig. 3.3. In this case the injector consists of custom-made 'spargers' through which the dispersed phase was discharged into the continuous phase. Each 'sparger' consisted of a 9.5 mm outer diameter (OD) tube into whose wall small holes were drilled. Each 'sparger' was surrounded by a 25 mm outer diameter (OD) stainless steel (S.S.) tube. Water entered the injector section from two locations. A S.S. flange containing eight holes of 25 mm diameter on the injector's sides was used to inject the 'primary' flow of water into the test section. Water also flowed through the annulus formed between each 'sparger' and the 25 mm OD tubes surrounding them. This 'secondary' flow helped to shear off the drops from the 'sparger' holes. The injector also contained a flow straightener to ensure uniformity of the 'primary' flow of water across the flow cross section. This flow straightener consisted of two S.S. meshes with a mesh size of 2 mm which were cut to fit the inner diameter of the pipe enclosing the injector section and were mounted on

supports welded to the inside of this pipe. Delrin balls about 25 mm in diameter were sandwiched between these meshes.
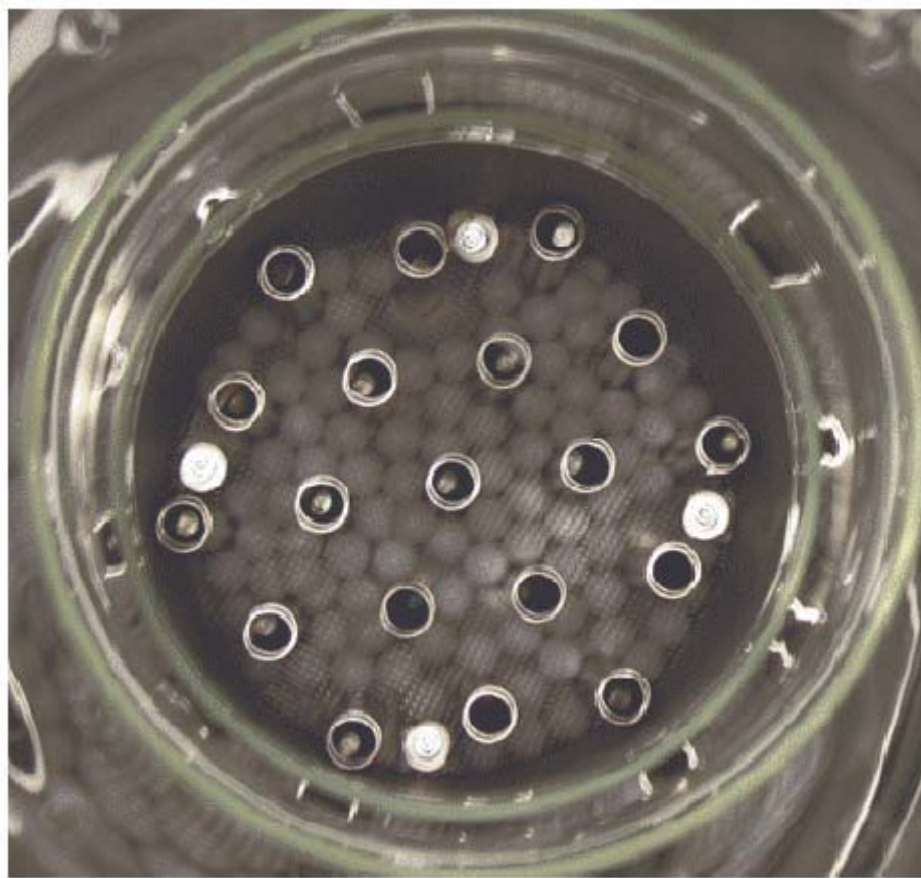
Fig. 3.3: Top view of the injector section for the 304 mm ID
test facility

The time taken for the mixture of water and Therminol to separate under the influence of gravity in the separation tank varied. For low flow rates of both the organic liquid and water good separation was observed within 24-36 hours. However for higher flow rates of either water or Therminol, longer periods of time (of the order of couple of days and sometimes even a week) were needed for good separation. This made these experiments extremely time consuming. Fig. 3.4 shows the experimental facility.

Fig. 3.4: Experimental facility.

3.4 Double Sensor Probe Methodology

The instrumentation port for the 304 mm ID test section had an integrated design consisting of two inserts for local multi-sensor conductivity probes and a multi-sensor impedance voidmeter. The impedance voidmeter was not used during this phase of experiments. The height of each instrumentation port was approximately 68 mm. The instrumentation port for the 304 mm ID test section is shown pictorially in Fig. 3.5.
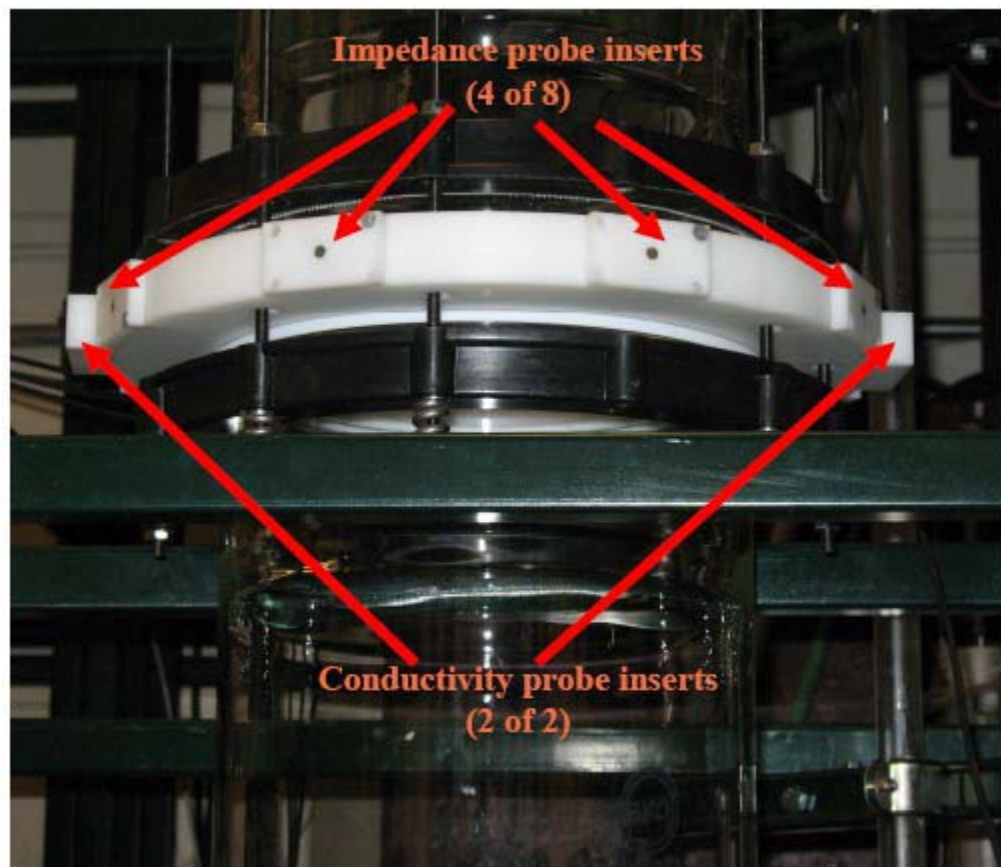
Fig. 3.5: Instrumentation port for the 304 mm ID test facility

The conductivity probe has been one of the most widely used local measurement instruments in two-phase flows. The principle of the probe is based on the intrinsic difference in the electrical conductivity between the dispersed phase and the continuous phase. The characteristic rise/fall of the impedance signals (converted to voltage signals

through an electrical circuit) between the sensors and the common ground can be obtained as the drops pass through the exposed tips of the probe sensors. Therefore, the time-averaged dispersed phase fraction can be obtained by dividing the sum of time occupied by the dispersed phase by the total measurement time. The most important feature of the multi-sensor conductivity probe is its ability to measure the local interfacial velocity of drops and then to determine the local time-averaged interfacial area concentration a_i.

The double-sensor probe is made of two thin electrodes and is shown in Fig. 3.6 (a). The tip of each electrode is exposed to the two-phase mixture and measures the impedance between the probe tip and the common ground. Due to the significant difference in the conductivities of the continuous phase and the dispersed phase, the impedance signal rises sharply when a droplet passes through the probe (Fig. 3.6 (b)). From the front tip signal, the droplet residual time fraction can be obtained. On the other hand, the time delay, Δt, of the two impedance signals (corresponding to responses of the two electrodes) can be utilized to determine the time interval for the droplet surface traveling from the upstream probe sensor to the downstream sensor. Since the separation of the two sensors is known, defined as Δs, a measurable droplet axial velocity, $\Delta s/\Delta t$, is obtained. For the measurement of the local time-averaged interfacial area concentration, the following formula has been suggested after considering the effects of the droplet lateral motion and the probe spacing (from Wu and Ishii [36]):

$$a_i = \left(\frac{2N_b}{\Delta T(N_b - N_{miss})} \right)\left[2 + \left(\frac{V_b{'}}{\overline{V}_b} \right)^{2.25} \right]\sum_j \left(\Delta t_j / \Delta s\right), \quad D = 1.2\Delta s \sim 3\Delta s , \quad (3.1)$$

where, a_i is the interfacial area concentration, the subscript j denotes the jth measured droplet, N_b stands for the number of the droplets that pass the first probe tip in the ΔT time interval used for time-averaging, D refers to the Sauter mean diameter of the droplets, and N_{miss} is the number of the missed droplets. A droplet is defined as missed when the second probe tip either cannot touch the droplet or enters the droplet before the first tip. If the Sauter mean diameter of the measured droplets is in the range of 1.2 to 3

times the probe spacing and the sample size is sufficiently large, the error of this expression is within ±1.5%. The term $\left(V_b'/\overline{V}_b\right)$ in equation (3.1) represents the relative

(a) Schematic of double-sensor probe   (b) Signals form the probe
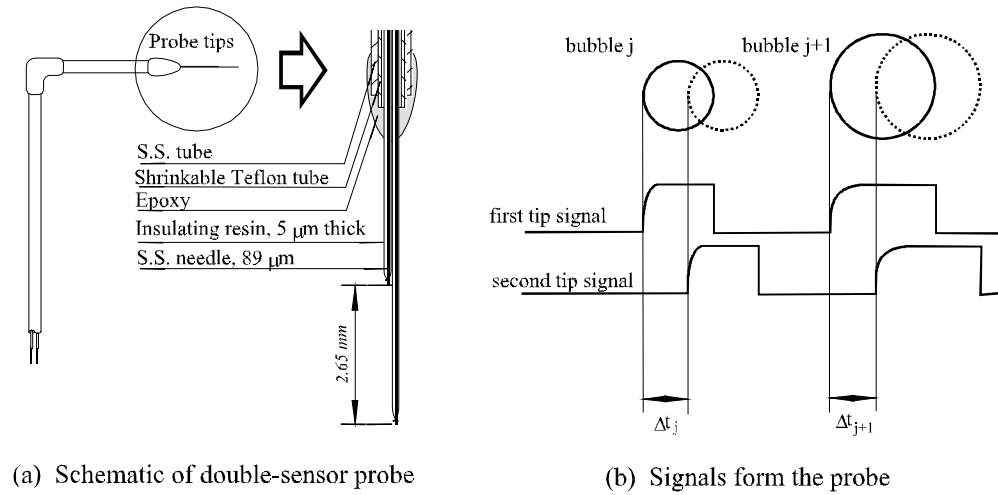
Fig. 3.6: Schematic diagram of double-sensor conductivity probe.

droplet velocity fluctuation, given by:

$$\left(\frac{V_b'}{\overline{V}_b}\right) = 1.2\frac{\sigma_{\Delta t_j}}{\left(\Delta t_j\right)}, \qquad D = 1.2\Delta s \sim 3\Delta s, \tag{3.2}$$

where $\sigma_{\Delta tj}$ is the standard deviation of Δt_j.

The circuit used for each sensor of the double-sensor probe is shown in Fig. 3.7. As mentioned earlier the double-sensor probe is actually a simple instrument which relies on the conductivity of the phase surrounding the exposed tip of the sensor. The circuit shown is used basically to measure the potential difference between the exposed tip and the grounded terminal. A bias resistor, R_B, is used to obtain the maximum voltage difference between each phase of the two-phase mixture. The presence of the bias resistor is necessary due to the various levels of conductivity of the water used. For these experiments, a 100 ml mixture of morpholine and ammonium hydroxide was added to 300 gallons of de-ionized water to add back some ions and increase its electrical conductivity.

The artificial switch in the circuit represents the state of the surrounding medium. When the switch is open, the tip is exposed only to the organic liquid phase. Thus the voltage output is equivalent to the supplied voltage source of 5 volts. When the switch is closed, the tip is exposed the liquid phase and the voltage output is lower than the voltage
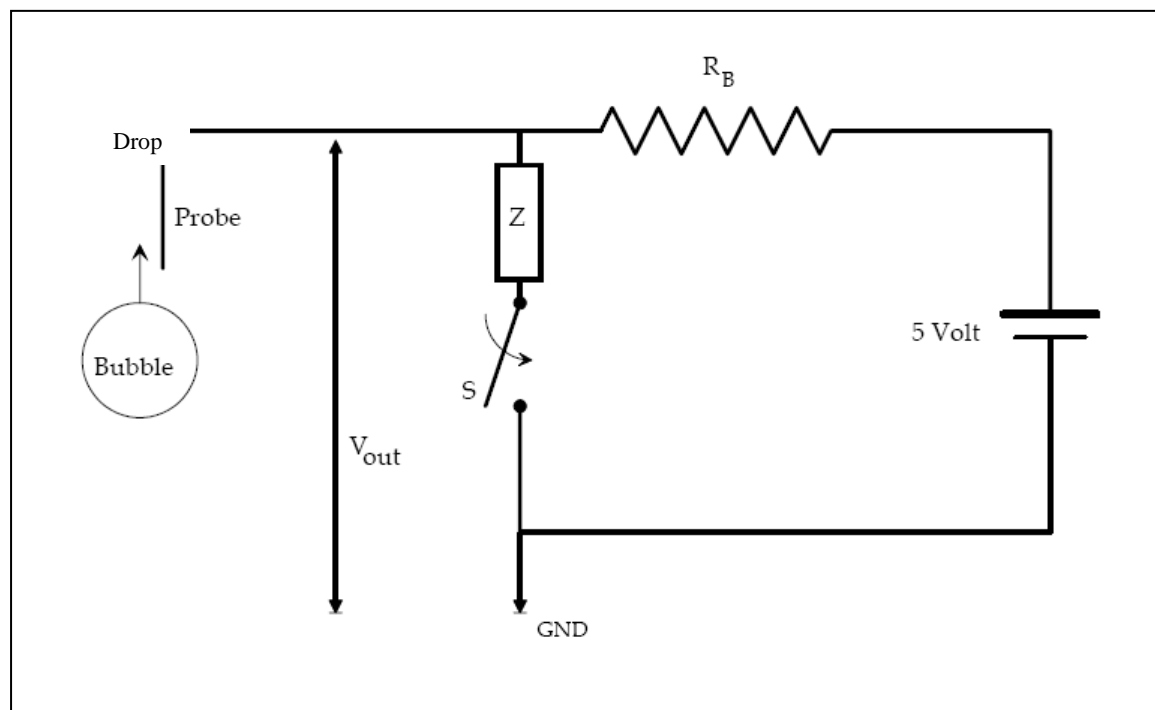
Fig. 3.7: Double-sensor conductivity probe circuit

source. The actual voltage output, in the latter case, depends on the resistance of the bias resistor and on the conductivity of the ionized water.

Fig. 3.8 shows the conventional circuit box used previously with multi sensor conductivity probes. With the large number of double-sensor probes used in experiments usage of a large number of such circuit boxes would have been necessary which would have been unmanageable. So the circuit box was miniaturized (done by Schumaker Technical Assembly, Lafayette, Indiana). The resulting circuit box as shown in Fig. 3.9 can handle ten double-sensor conductivity probes simultaneously.

After the completion of the signal conditioning process, the signals are separated into signals of spherical, distorted, cap, and slug droplets depending on the droplet chord length information. In the present experiments, spherical and distorted droplets are

categorized as group 1, and cap droplets are categorized as group 2. In identifying the group type, the maximum distorted droplet limit was used as the criterion.

Fig. 3.8: Front and back of a conventional multi sensor probe circuit box.

Fig. 3.9: Front and back of the new multi sensor probe circuit box

The maximum distorted droplet limit is given by

$$D_{d\,\max} = 4\sqrt{\frac{\sigma}{g\varDelta\rho}} \quad ; \tag{3.3}$$

Therefore, droplets whose chord lengths are smaller than D_{dmax} are categorized as group 1 droplets and those having chord lengths larger than D_{dmax} are categorized as group 2 droplets. In obtaining the dispersed phase fraction and the droplet chord length, the leading sensor is used. Detailed considerations on missing and non-effective signals are

made in the signal processing scheme (Kim et. al [34]). The local time-averaged two-phase parameters obtained after the completion of the signal processing are: number of droplets, interfacial velocity, void fraction and interfacial area concentration of each group of droplets.

As already mentioned the present experiments were time consuming. So to reduce the numbers of times experiments have to be repeated slightly modified design of double-sensor conductivity probes were used. Ten double-sensor conductivity probes were screwed on to a ¼" OD stainless steel tube as shown in Fig. 3.10. This allowed the measurement of local two-phase flow parameters at ten radial locations simultaneously, thereby, greatly reducing the effort needed to obtain detailed local two-phase flow parameters data. Three such assemblies were used to measure local two-phase flow parameters at three axial locations (L/D_h=1.7, 5.0, 8.3) simultaneously. The total flow area was divided into ten equal segments as shown in Fig. 3.11. The ten double-sensor conductivity probes were then placed at the center of each circle/annulus thus created (again as shown in Fig. 3.11). This would be the most logical way to decide upon the placement of the conductivity probes.
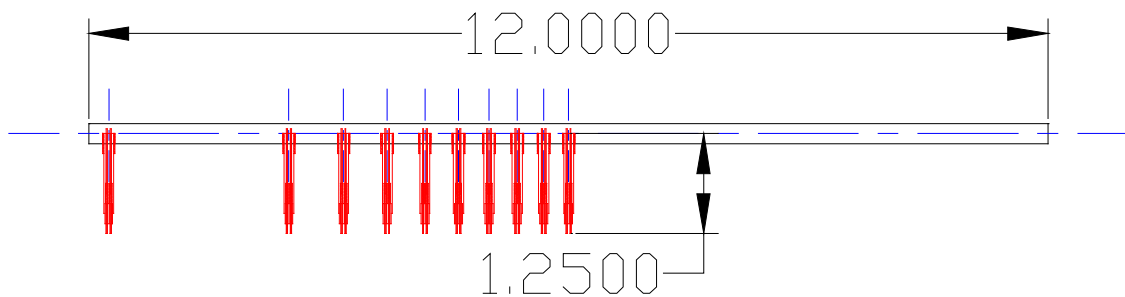
Fig. 3.10: Modified design of double-sensor conductivity probes.
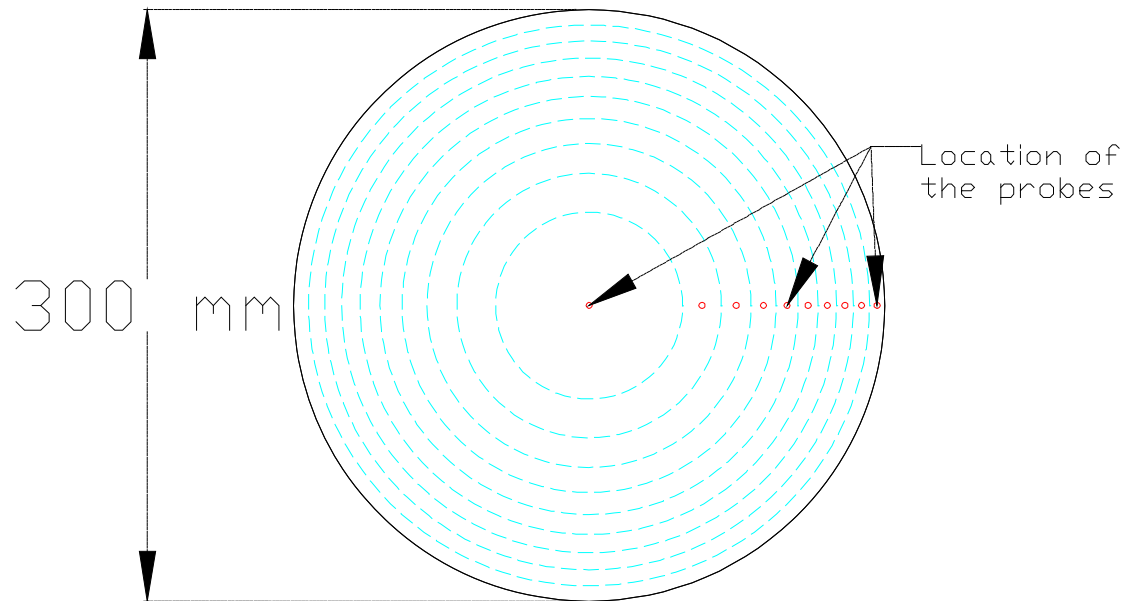
Fig. 3.11: Location of double-sensor conductivity probes along the flow area.

3.5 Data Acquisition

The data acquisition system consisted of two National Instruments (NI) USB 6225 boards (Fig. 3.12) each having capability, among others, to acquire analog signals from 80 channels at the same time. They were connected to two computers (Fig. 3.13) via USB connections. Proper drivers were installed to allow various programs to interact with the boards. NI's LABVIEW SignalExpress software was used to interact with the boards. The entire data acquisition station is shown in Fig. 3.14.
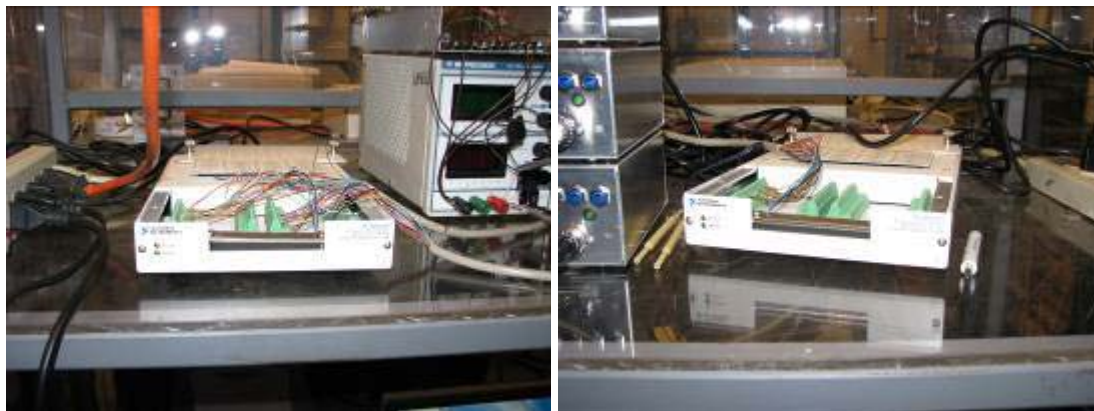
Fig. 3.12: NI USB 6225 data acquisition boards

Fig. 3.13: Data acquisition computers
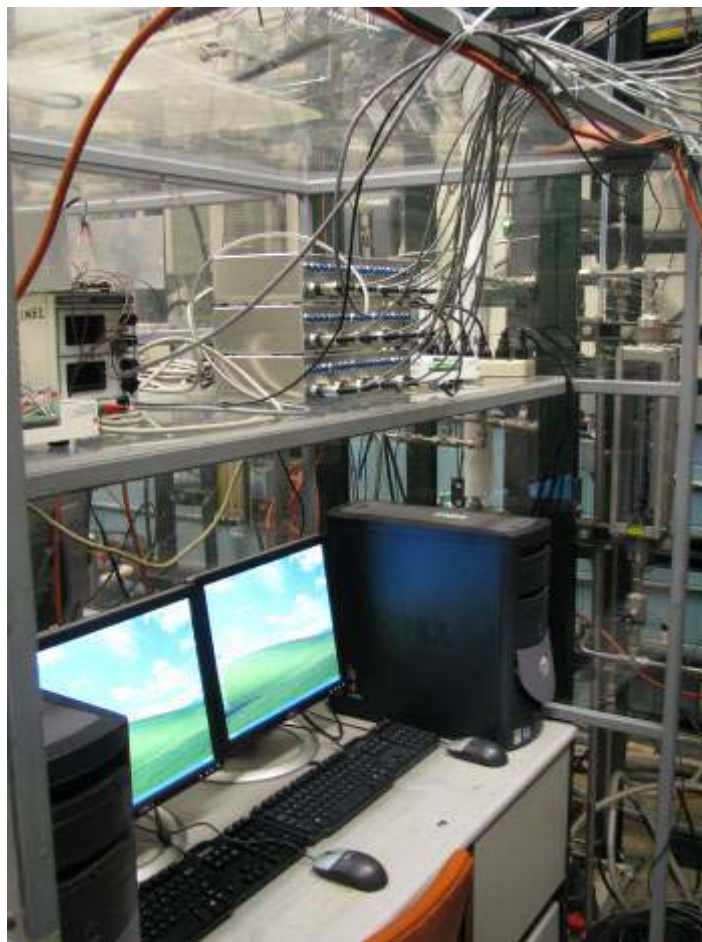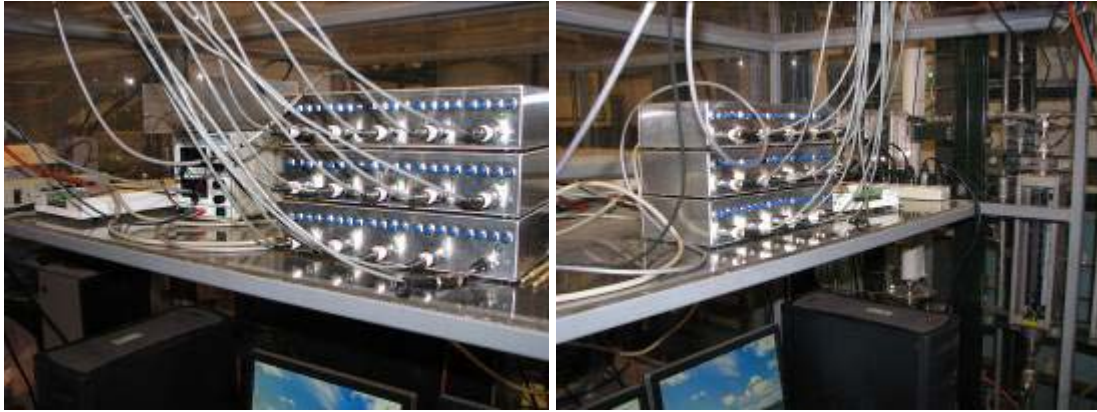
Fig. 3.14: Data acquisition station

One of the factors to decide upon while setting up the data acquisition system was the data acquisition frequency. And it was decided upon by the following way. The

maximum area-averaged mixture velocity $\langle j \rangle$ achievable in the test facility was about 0.06 m/s. The following drift-flux models [1] were used to determine the area-averaged dispersed phase velocities in the various possible flow regimes.

For bubbly flow regime:

$$\langle v_d \rangle = \left(1.2 - 0.2 \sqrt{\frac{\rho_d}{\rho_c}} \right) \langle j \rangle + 1.4 \left(\frac{\sigma g \Delta \rho}{\rho_c^2} \right)^{\frac{1}{4}} \tag{3.4}$$

For cap-bubbly flow regime:

$$\langle v_d \rangle = \left(1.2 - 0.2 \sqrt{\frac{\rho_d}{\rho_c}} \right) \langle j \rangle + 0.54 \sqrt{\left(g D_H \left(\frac{\Delta \rho}{\rho_c} \right) \right)} \tag{3.5}$$

And for slug flow regime:

$$\langle v_d \rangle = \left(1.2 - 0.2 \sqrt{\frac{\rho_d}{\rho_c}} \right) \langle j \rangle + 0.35 \left(\frac{g D \Delta \rho}{\rho_c} \right)^{\frac{1}{2}} \tag{3.6}$$

The area-averaged dispersed phase velocity $\langle v_d \rangle$ comes out to be 0.151 m/s for bubbly flows, 0.222 m/s for cap bubbly flows and 0.169 m/s for slug flows. To be conservative the value of area-averaged dispersed phase velocity $\langle v_d \rangle$ was chosen to be 0.222 m/s. The distance between the two sensor tips of a double sensor probe is about 2 mm/0.002 m. Hence the time taken by a dispersed phase interface to travel from the leading sensor tip to the lagging sensor tip would come to about 9 ms/0.009 s. The errors that would occur in measuring this time if a couple of different data acquisition frequencies were chosen are tabulated in Table 3.4 below.

Table 3.4: Data acquisition frequencies and errors associated with the measurement of traversing times of interfaces

Data Acquisition Frequency (Hz)	Error (%)
5000	2.2
2000	5.6

Another important consideration was to decide on the time for which data needs to be acquired to give statistically significant results. This was decided upon in the following way by performing some computational experiments. A computer program was written which takes a spherical drop of a particular size. It was assumed that the double-sensor conductivity probe has equal probability to hit any point on the cross-section of the drop. Then several drops were allowed to hit the probe and the encountered chord length recorded. Finally the chord length averaged over all previous hits was calculated and plotted. The results are shown for two different drop sizes in Figs. 3.15 and 3.16. Based on these results and considering the time consuming nature of these experiments, it was decided that double-sensor probes hitting about 200-300 drops would be sufficient to give statistically significant results.
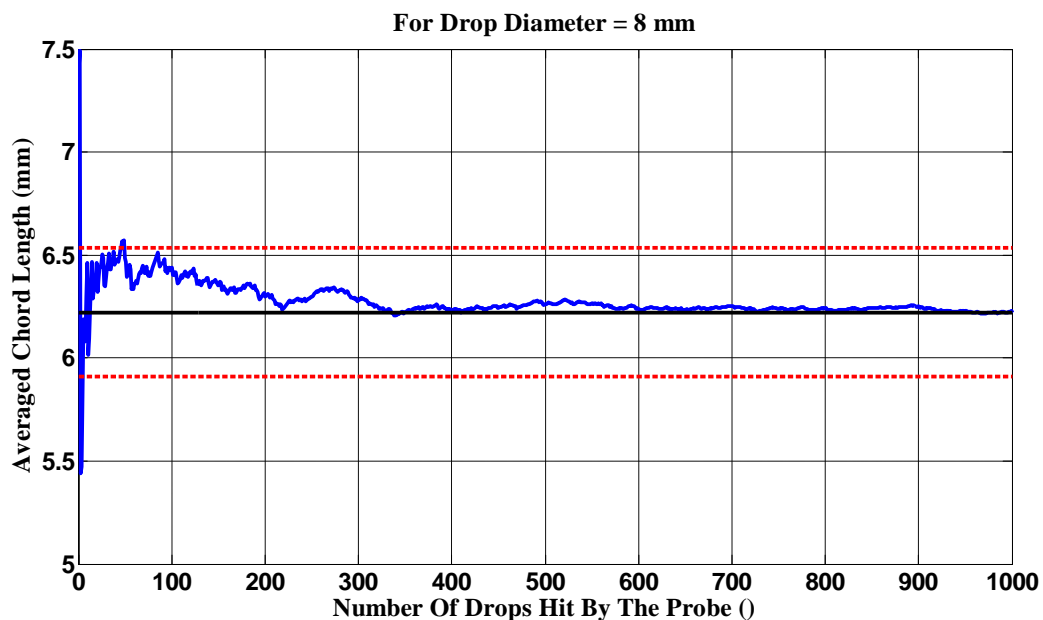
Fig. 3.15: Determination of number of drops to be hit by a double-sensor conductivity probe to give statistically significant measurements (for 8 mm drop size).
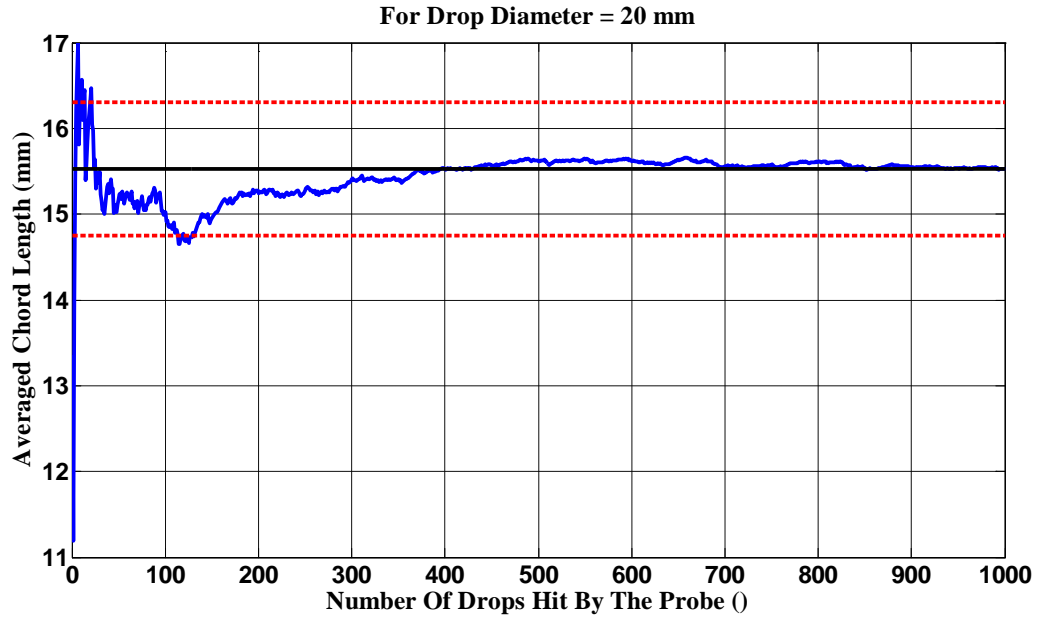
Fig. 3.16: Determination of number of drops to be hit by a double-sensor conductivity
probe to give statistically significant measurements (for 20 mm drop size).

3.6 Scaling

In order to understand the relevance of the experiments performed it is extremely
essential to perform a scaling analysis. For adiabatic two-phase flows under reduced
gravity environments (considering flow through a duct of a particular geometry), the
independent variables are, the hydraulic diameter of the pipe D_h, the densities of the
continuous and the dispersed phases ρ_c and ρ_d, respectively, the dynamic viscosities of the
continuous and the dispersed phases μ_c and μ_d, respectively, the interfacial tension
between the two-phases σ, the superficial velocities of the continuous and the dispersed
phases j_c and j_d, respectively and finally the acceleration due to gravity g. Using
Buckingham's Pi theorem (or from continuity and momentum conservation equations of
both phases) it can be shown that the structure of the two-phase flow will depend on, the
density ratio ρ_c/ρ_d, the continuous phase Reynolds number $Re_c = (\rho_c j_c D_h)/\mu_c$, the
dispersed phase Reynolds number $Re_d = (\rho_d j_d D_h)/\mu_d$, the continuous phase Weber
number $We_c = (\rho_c j_c^2 D_h)/\sigma$, the dispersed phase Weber number $We_d = (\rho_d j_d^2 D_h)/\sigma$ and

the Bond number $Bo = \left((D_h/2)^2\right)/\left(\sigma/\left(g(\rho_c - \rho_d)\right)\right)$. However as mentioned earlier we are more interested in low-inertia two-phase flows since here only the effect of reduced gravity will be pronounced. For such low inertia two-phase flows it can be shown that the most important dimensionless number is the Bond number Bo. It can be shown that Bond number is very similar to the ratio of several internal length scales (of two-phase flows) to the hydraulic diameter of the duct. Thus it becomes clear that several systems, which have similar values for the ratios of critical internal length scales to the hydraulic diameter, will have similar flow structure (provided of course that inertia is not dominant). The several internal length scales of importance are the spherical droplet limit D_{ds}, the distorted droplet limit D_{dmax} and the cap bubble limit D_{cmax}. These are given by the following

where

$$D_{ds} = 4\sqrt{\frac{2\sigma}{g\Delta\rho}} N_{\mu c}^{1/3} \quad with \quad N_{\mu c} = \frac{\mu_c}{\left(\rho_c \sigma \sqrt{\frac{\sigma}{g\Delta\rho}}\right)^{1/2}}$$

and

$$D_{d\max} = 4\sqrt{\frac{\sigma}{g\Delta\rho}}; \quad\quad\quad\quad\quad (3.7)$$

also

$$D_{c\max} = 40\sqrt{\frac{\sigma}{g\Delta\rho}}$$

Table 3.5 compares the physical properties of the Therminol-water system used in the present study with two other systems (one air-water and one steam-water). Table 3.6 compares the Therminol-water system used in the present study with two other systems, one an air-water system at 1 atm and 25 °C with acceleration due to gravity equal to 0.5 m/s^2 and a steam-water system at 1 atm and 100 °C with acceleration due to gravity equal to 0.4 m/s^2. It can be seen that the internal length scales are very similar between these systems. Figs. 3.17 and 3.18 show systems which would have similar flow structure as compared the one used in present studies.

Table 3.5: Physical properties of components of three different systems.

	System 1		System 2		System 3	
	Therminol 59 (1 atm, 25 ° C)	*Water (1 atm, 25 ° C)*	*Air (1 atm, 25 ° C)*	*Water (1 atm, 25 ° C)*	*Steam (1 atm, 100 ° C)*	*Water (1 atm, 100 ° C)*
Density (kg/m^3)	$9.71 \times 10^{+02}$	$9.98 \times 10^{+02}$	$1.18 \times 10^{+00}$	$9.98 \times 10^{+02}$	5.90×10^{-01}	$9.59 \times 10^{+02}$
Dynamic Viscosity (kg/m-s)	7.00×10^{-03}	1.00×10^{-03}	1.78×10^{-05}	1.00×10^{-03}	1.23×10^{-05}	2.83×10^{-04}
Interfacial Tension (N/m)	4.25×10^{-02}		7.20×10^{-02}		5.90×10^{-02}	

Table 3.6: Internal length scales of three different systems.

	Therminol 59 - Water (1 atm, 25 ° C)	*Air-Water (1 atm, 25 ° C)*	*Steam-Water (1 atm, 100 ° C)*
	g= 9.81 m/s2	*g= 0.50 m/s2*	*g= 0.40 m/s2*
D_{ds} (mm)	8	7	5
D_{dmax} (mm)	51	48	50
D_{cmax} (mm)	509	481	496
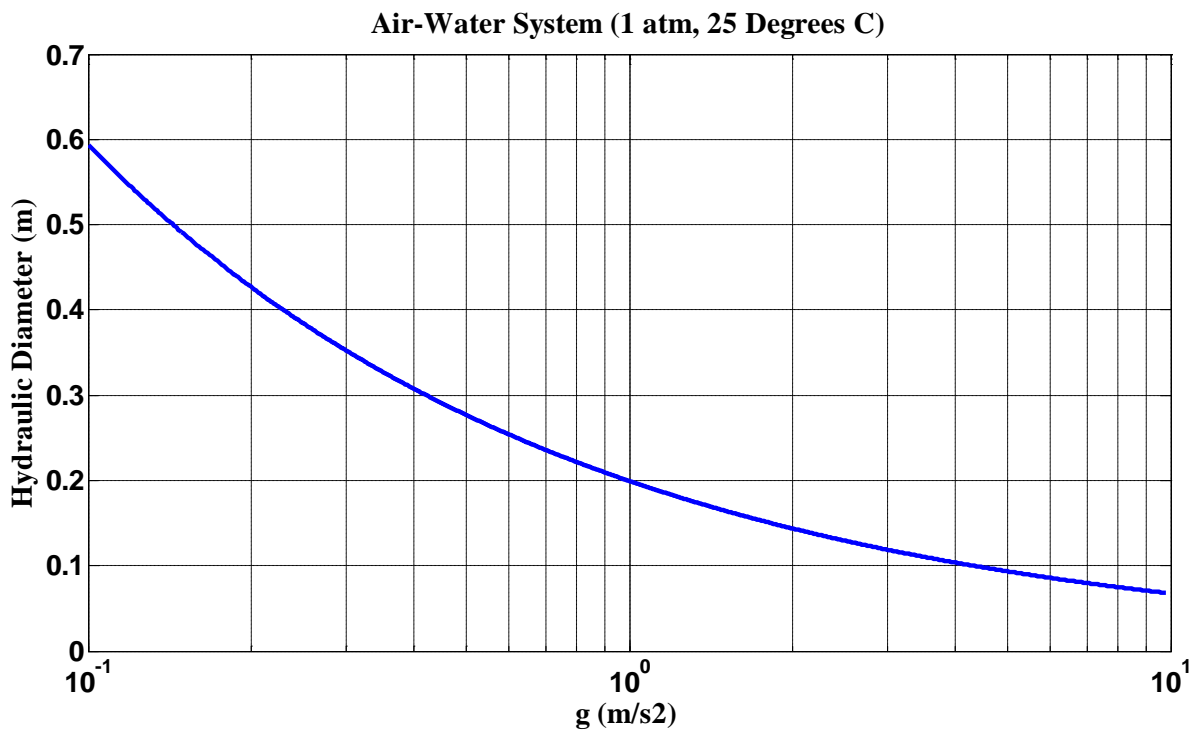
Fig. 3.17: Similarity between Therminol-water (1 atm, 25 °C) test facility and air-water

systems
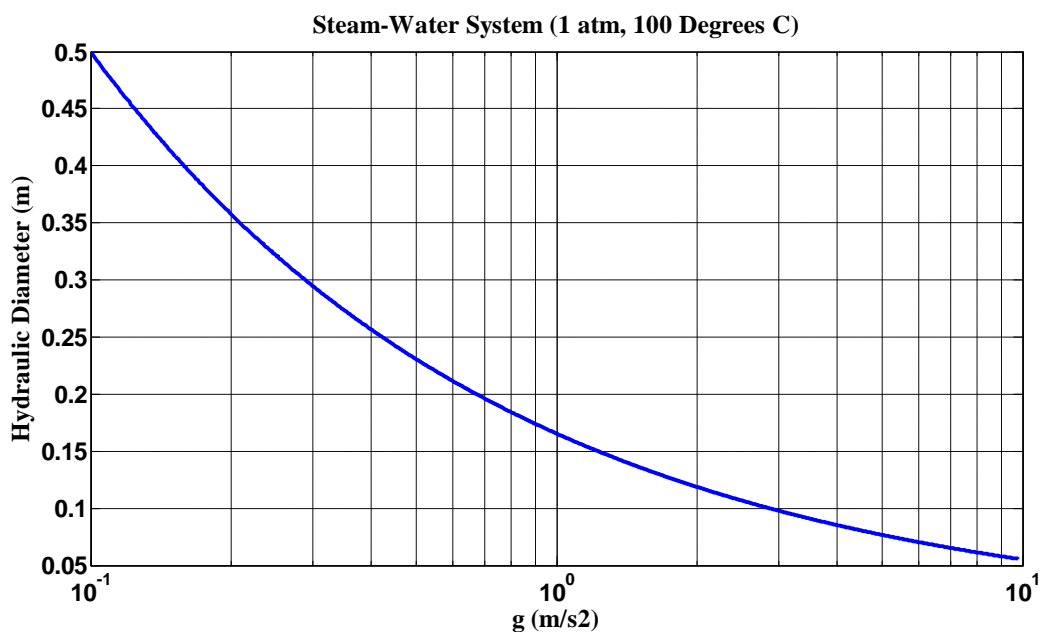
Fig. 3.18: Similarity between Therminol-water (1 atm, 25 °C) test facility and steam-

water systems

4. EXPERIMENTAL RESULTS AND DISCUSSION

Based on the limitations of the test facility, local two-phase flow data were obtained for 12 flow conditions which are tabulated in Table 4.1 and are plotted in Fig. 4.1. Four different continuous phase (water) superficial velocities were chosen for each of three different dispersed phase (organic liquid – Therminol) superficial velocities. The bold lines on the plot in Fig. 4.1 represent flow regime transition boundaries as predicted by the Mishima-Ishii [37] correlation. The flow conditions were chosen around the predicted bubbly to slug flow transition boundary. This was to generate a more meaningful local two-phase flow parameter database against which the evaluation of the IATE can be performed. The experimental results are tabulated in detail in Appendix A while the same are plotted in Appendix B.

As can be observed in the results plotted in Appendix B, Group-2 drops exist in almost all flow conditions. Apparently this is not to be expected according to the Mishima-Ishii correlation. However, it is to be kept in mind that Mishima-Ishii correlation is applicable to fully developed two-phase flows. And in low inertia two-phase flows under reduced gravity environments as is simulated by current experiments, it is not easy to attain fully developed two-phase flows. That implies that inlet conditions would tend to affect the subsequent flow structure. In the current experiments the size of the droplets at the inlet were found to be relatively big which corroborates well with the measurements. Lots of inter- and intra-group droplet interaction mechanisms could be seen at play, especially at high flow rates of either phases. Due to low inertia of the flows turbulent disintegration and random collision mechanisms of interfacial area creation/destruction can be expected to be less dominant. On the other hand, other mechanisms such as wake entrainment, shearing-off and surface instability can be

Table 4.1: Test Matrix

(a)

Run #	$\langle j_c \rangle$ [m/s]	$\langle j_d \rangle$ [m/s]	Port 1 ($z/D_h=1.7$)				Port 2 ($z/D_h=5.0$)				Port 3 ($z/D_h=8.3$)			
			$\langle v_1 \rangle$ [m/s]	$\langle v_2 \rangle$ [m/s]	$\langle D_{sm1} \rangle$ [m]	$\langle D_{sm2} \rangle$ [m]	$\langle v_1 \rangle$ [m/s]	$\langle v_2 \rangle$ [m/s]	$\langle D_{sm1} \rangle$ [m]	$\langle D_{sm2} \rangle$ [m]	$\langle v_1 \rangle$ [m/s]	$\langle v_2 \rangle$ [m/s]	$\langle D_{sm1} \rangle$ [m]	$\langle D_{sm2} \rangle$ [m]
1	0.00E+00	8.93E-03	8.35E-02	7.22E-02	7.11E-03	2.94E-02	8.48E-02	7.30E-02	6.09E-03	2.29E-02	1.02E-01	8.92E-02	7.28E-03	2.34E-02
2	8.93E-03	8.93E-03	9.70E-02	8.09E-02	6.73E-03	2.96E-02	1.04E-01	8.76E-02	5.63E-03	2.41E-02	1.06E-01	8.70E-02	5.52E-03	2.08E-02
3	1.79E-02	8.93E-03	9.79E-02	8.59E-02	6.59E-03	2.82E-02	1.08E-01	9.44E-02	6.58E-03	2.35E-02	1.07E-01	9.17E-02	5.22E-03	2.18E-02
4	2.68E-02	8.93E-03	9.76E-02	7.93E-02	5.41E-03	2.75E-02	1.15E-01	1.01E-01	4.72E-03	2.72E-02	1.21E-01	1.02E-01	4.81E-03	4.86E-02
5	0.00E+00	1.79E-02	9.66E-02	8.19E-02	6.66E-03	2.85E-02	1.00E-01	8.09E-02	4.95E-03	2.78E-02	9.58E-02	6.67E-02	4.54E-03	2.05E-02
6	8.93E-03	1.79E-02	1.03E-01	9.27E-02	5.93E-03	2.86E-02	1.06E-01	7.14E-02	4.22E-03	7.29E-02	1.05E-01	7.95E-02	4.49E-03	2.11E-02
7	1.79E-02	1.79E-02	1.09E-01	7.74E-02	5.85E-03	3.20E-02	1.19E-01	9.10E-02	5.48E-03	2.86E-02	1.19E-01	8.78E-02	6.04E-03	2.25E-02
8	2.68E-02	1.79E-02	1.05E-01	8.66E-02	5.19E-03	2.68E-02	1.22E-01	8.39E-02	4.30E-03	2.68E-02	1.20E-01	8.78E-02	4.89E-03	1.87E-02
9	0.00E+00	2.68E-02	8.55E-02	6.76E-02	7.00E-03	3.02E-02	9.71E-02	7.94E-02	7.12E-03	2.27E-02	1.11E-01	8.33E-02	6.97E-03	2.28E-02
10	8.93E-03	2.68E-02	1.10E-01	8.39E-02	6.67E-03	2.96E-02	1.03E-01	7.59E-02	4.84E-03	2.55E-02	1.10E-01	8.29E-02	5.12E-03	2.25E-02
11	1.79E-02	2.68E-02	1.04E-01	8.50E-02	6.62E-03	2.51E-02	1.19E-01	8.79E-02	6.22E-03	2.65E-02	1.20E-01	8.19E-02	5.13E-03	2.29E-02
12	2.68E-02	2.68E-02	1.11E-01	8.00E-02	2.98E-03	2.54E-02	1.38E-01	9.10E-02	2.99E-03	2.01E-02	1.36E-01	9.75E-02	2.44E-03	1.70E-02

(b)

Run #	$\langle j_c \rangle$ [m/s]	$\langle j_d \rangle$ [m/s]	Port 1 ($z/D_h=1.7$)				Port 2 ($z/D_h=5.0$)				Port 3 ($z/D_h=8.3$)			
			$\langle v_1 \rangle$ [m/s]	$\langle v_2 \rangle$ [m/s]	$\langle D_{sm1} \rangle$ [m]	$\langle D_{sm2} \rangle$ [m]	$\langle v_1 \rangle$ [m/s]	$\langle v_2 \rangle$ [m/s]	$\langle D_{sm1} \rangle$ [m]	$\langle D_{sm2} \rangle$ [m]	$\langle v_1 \rangle$ [m/s]	$\langle v_2 \rangle$ [m/s]	$\langle D_{sm1} \rangle$ [m]	$\langle D_{sm2} \rangle$ [m]
1	0.00E+00	8.93E-03	8.35E-02	7.22E-02	7.11E-03	2.94E-02	8.48E-02	7.30E-02	6.09E-03	2.29E-02	1.02E-01	8.92E-02	7.28E-03	2.34E-02
2	8.93E-03	8.93E-03	9.70E-02	8.09E-02	6.73E-03	2.96E-02	1.04E-01	8.76E-02	5.63E-03	2.41E-02	1.06E-01	8.70E-02	5.52E-03	2.08E-02
3	1.79E-02	8.93E-03	9.79E-02	8.59E-02	6.59E-03	2.82E-02	1.08E-01	9.44E-02	6.58E-03	2.35E-02	1.07E-01	9.17E-02	5.22E-03	2.18E-02
4	2.68E-02	8.93E-03	9.76E-02	7.93E-02	5.41E-03	2.75E-02	1.15E-01	1.01E-01	4.72E-03	2.72E-02	1.21E-01	1.02E-01	4.81E-03	4.86E-02
5	0.00E+00	1.79E-02	9.66E-02	8.19E-02	6.66E-03	2.85E-02	1.00E-01	8.09E-02	4.95E-03	2.78E-02	9.58E-02	6.67E-02	4.54E-03	2.05E-02
6	8.93E-03	1.79E-02	1.03E-01	9.27E-02	5.93E-03	2.86E-02	1.06E-01	7.14E-02	4.22E-03	7.29E-02	1.05E-01	7.95E-02	4.49E-03	2.11E-02
7	1.79E-02	1.79E-02	1.09E-01	7.74E-02	5.85E-03	3.20E-02	1.19E-01	9.10E-02	5.48E-03	2.86E-02	1.19E-01	8.78E-02	6.04E-03	2.25E-02
8	2.68E-02	1.79E-02	1.05E-01	8.66E-02	5.19E-03	2.68E-02	1.22E-01	8.39E-02	4.30E-03	2.68E-02	1.20E-01	8.78E-02	4.89E-03	1.87E-02
9	0.00E+00	2.68E-02	8.55E-02	6.76E-02	7.00E-03	3.02E-02	9.71E-02	7.94E-02	7.12E-03	2.27E-02	1.11E-01	8.33E-02	6.97E-03	2.28E-02
10	8.93E-03	2.68E-02	1.10E-01	8.39E-02	6.67E-03	2.96E-02	1.03E-01	7.59E-02	4.84E-03	2.55E-02	1.10E-01	8.29E-02	5.12E-03	2.25E-02
11	1.79E-02	2.68E-02	1.04E-01	8.50E-02	6.62E-03	2.51E-02	1.19E-01	8.79E-02	6.22E-03	2.65E-02	1.20E-01	8.19E-02	5.13E-03	2.29E-02
12	2.68E-02	2.68E-02	1.11E-01	8.00E-02	2.98E-03	2.54E-02	1.38E-01	9.10E-02	2.99E-03	2.01E-02	1.36E-01	9.75E-02	2.44E-03	1.70E-02

Fig. 4.1: Test matrix and Mishima-Ishii flow regime transition boundaries.

expected to be dominant. However conclusive remarks about these mechanisms can only be made only after IATE has been evaluated against the obtained data.

The axial development of area-averaged interfacial velocity of Group1 drops and Group 2 drops are plotted in Figs. 4.2 and 4.3, respectively. It can be seen that for both Group1 and Group 2 drops, increase in flow-rate of the continuous phase for a particular flow-rate of the dispersed phase results in an increase of area-averaged interfacial velocity of the dispersed phase. Also if looked at carefully it can be seen that for a particular flow-rate of the continuous phase if the dispersed phase flow rate is increased that also results in an increase of area-averaged interfacial velocity of the dispersed phase. Over the axial length of the test section the area-averaged interfacial velocity of both Group 1 and Group 2 drops has a tendency to either increase slightly or stay unchanged. On a very few occasions however, it can be seen to have actually decreased.

The axial development of area-averaged dispersed phase fraction of Group1 drops and Group 2 drops are plotted in Figs. 4.4 and 4.5, respectively. It can be seen that for both Group1 and Group 2 drops, increase in flow-rate of the continuous phase for a particular flow-rate of the dispersed phase results in a decrease of area-averaged dispersed phase fraction. This corresponds well with the increase in interfacial velocity of dispersed phase noted in the previous paragraph. However it can be seen that for a particular flow-rate of the continuous phase if the dispersed phase flow rate is increased it results in an increase of area-averaged dispersed phase fraction. Over the axial length of the test section the area-averaged dispersed phase fraction of both Group 1 and Group 2 drops has a tendency to either increase slightly for some cases, stay unchanged for some cases and even decrease for the remaining. The changes in area-averaged dispersed phase fractions and area-averaged interfacial velocities (for a particular dispersed phase flow rate) are related in such a way that the sum of the products of the area-averaged dispersed phase fraction of a particular group of drops and area-averaged interfacial velocity for the same group remains unchanged. This is due to the law of conservation of mass and noting that the dispersed phase is incompressible.
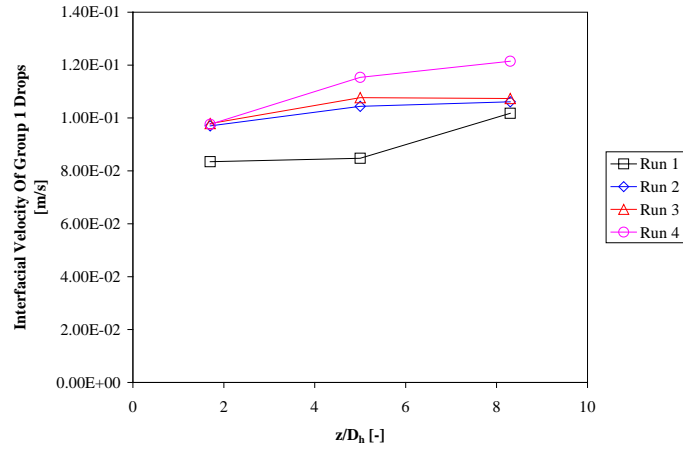
(a)
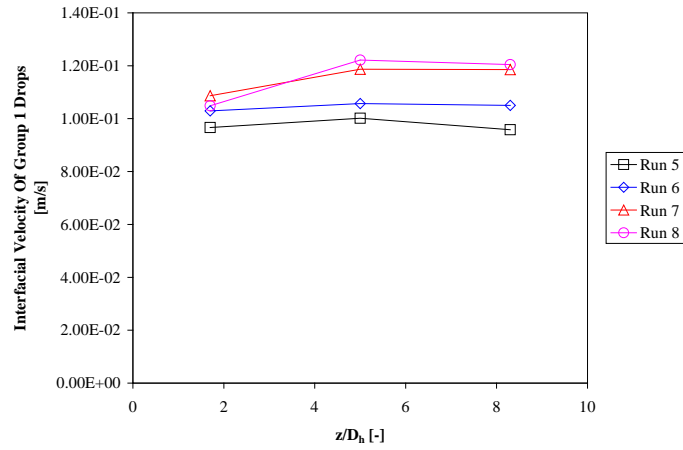
(b)
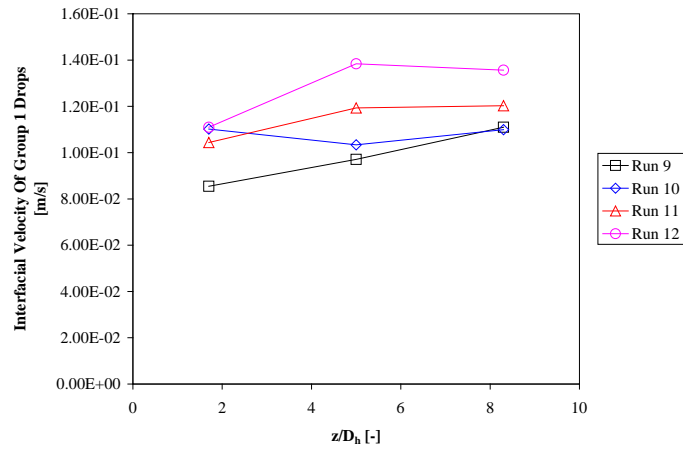
(c)

Fig. 4.2: Area averaged interfacial velocity of Group 1 drops for (a) $\langle j_d \rangle$=0.0089 m/s,

(b) $\langle j_d \rangle$=0.0179 m/s and (c) $\langle j_d \rangle$=0.0268 m/s.

(a)

(b)

(c)

Fig. 4.3: Area averaged interfacial velocity of Group 2 drops for (a) $\langle j_d \rangle$=0.0089 m/s,

(b) $\langle j_d \rangle$=0.0179 m/s and (c) $\langle j_d \rangle$=0.0268 m/s.
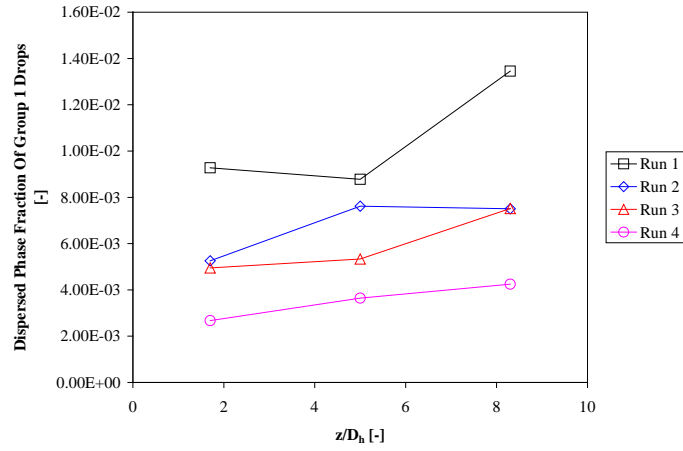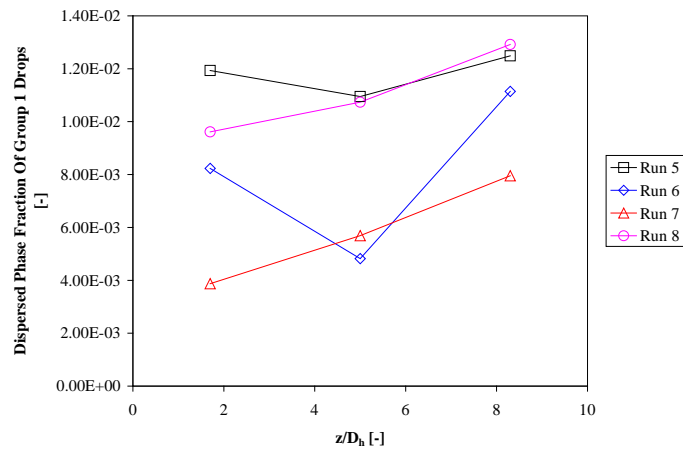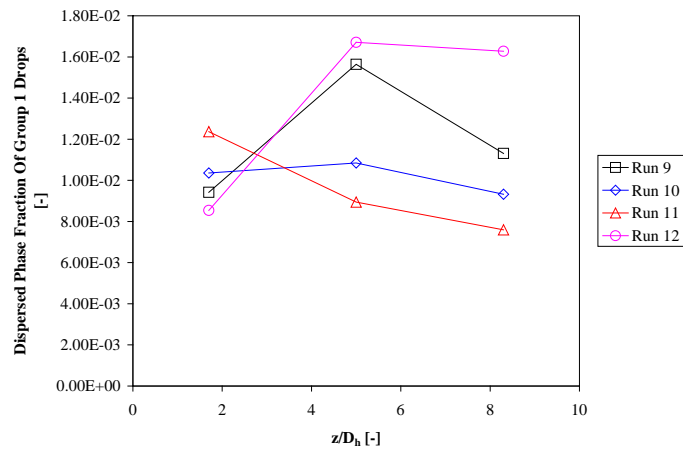
Fig. 4.4: Area averaged dispersed phase fraction of Group 1 drops for (a) $\langle j_d \rangle$=0.0089 m/s, (b) $\langle j_d \rangle$=0.0179 m/s and (c) $\langle j_d \rangle$=0.0268 m/s.
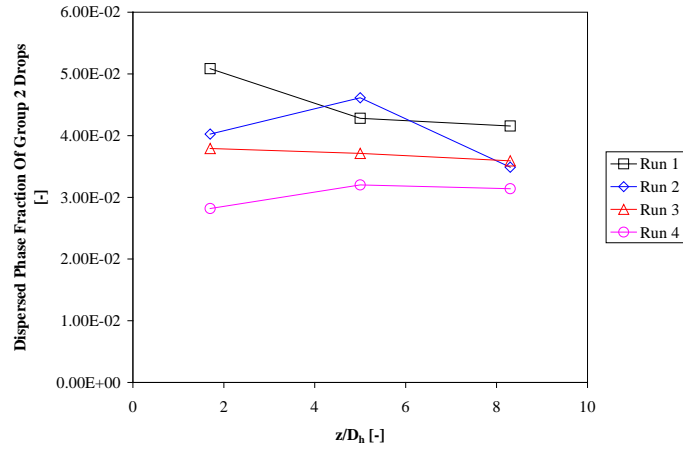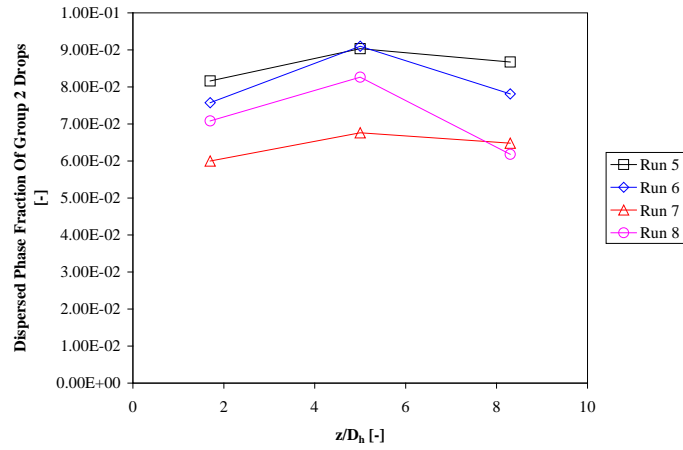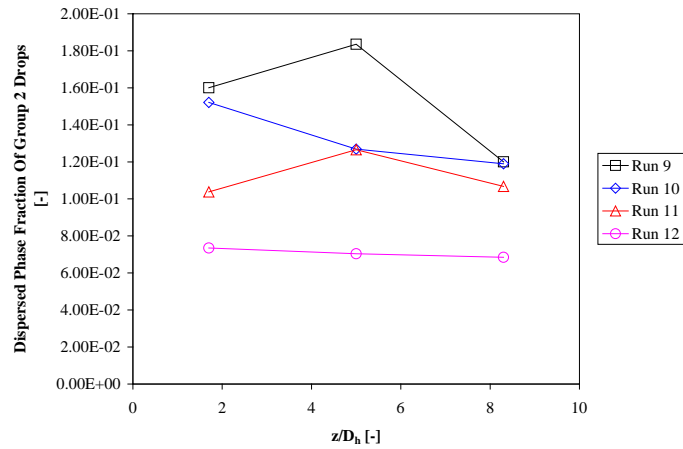
Fig. 4.5: Area averaged dispersed phase fraction of Group 2 drops for
(a) $\langle j_d \rangle$ =0.0089 m/s, (b) $\langle j_d \rangle$ =0.0179 m/s and (c) $\langle j_d \rangle$ =0.0268 m/s.

The axial development of area-averaged interfacial area concentration of Group1 drops and Group 2 drops are plotted in Figs. 4.6 and 4.7, respectively. For Group 1 drops it can be seen that as the continuous phase flow-rate increases for a particular dispersed phase velocity the interfacial area concentration decreases. This may be because of the dominance of random collision mechanism which acts as a sink for interfacial area. Sometimes however (like for Runs 8 and 12) as the continuous phase flow-rate increases for a particular dispersed phase velocity the interfacial area concentration increases. This may be due to dominance of turbulence impact mechanism over other mechanisms. Turbulence impact mechanism acts as a source of interfacial area. Similar observations can be made for Group 2 drops. The interfacial area concentration of Group 1 drops can be seen to increase along the flow direction, generally. This may be because of breakage of Group 1 drops due to turbulence of the continuous phase, which creates more interfacial area, as also generation of Group 1 drops from Group 2 drops by shearing off and other mechanisms. The interfacial area concentration of Group 2 drops can be seen to have a general trend of increasing at first along the flow direction and then either staying unchanged or decreasing a little bit. However, in some cases it can be seen to be increasing monotonically.

The axial development of area-averaged Sauter mean diameter of Group1 drops and Group 2 drops are plotted in Figs. 4.8 and 4.9, respectively. For Group 1 drops it can be seen that as the continuous phase flow-rate increases for a particular dispersed phase velocity the Sauter mean diameter decreases. Similar statement can be made for the Sauter mean diameter of Group 2 drops. However, along the flow direction the Sauter mean diameter has a tendency to decrease for both Group 1 and Group 2 drops.

For a particular continuous phase flow rate, increase in dispersed phase flow rate is accompanied by an increase in the area averaged dispersed phase fraction of both Group 1 and Group 2 drops as can be seen in Fig. 4.10. Similar statements can be made about the area averaged interfacial area concentration (Fig. 4.11) and Group 1 drops interfacial velocity (Fig. 4.12 (a)). The behavior of Group 2 drops interfacial velocity (Fig. 4.12 (b)) is just the opposite. The area averaged Sauter mean diameter of Group 1 drops first decreases and then increases with increase in dispersed phase flow rate at a
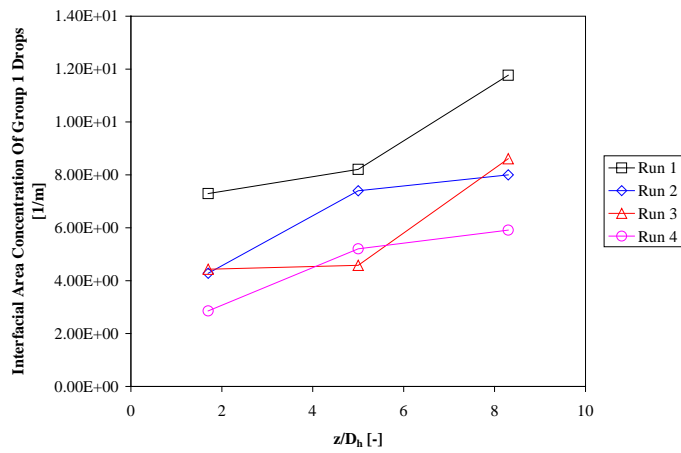
(a)
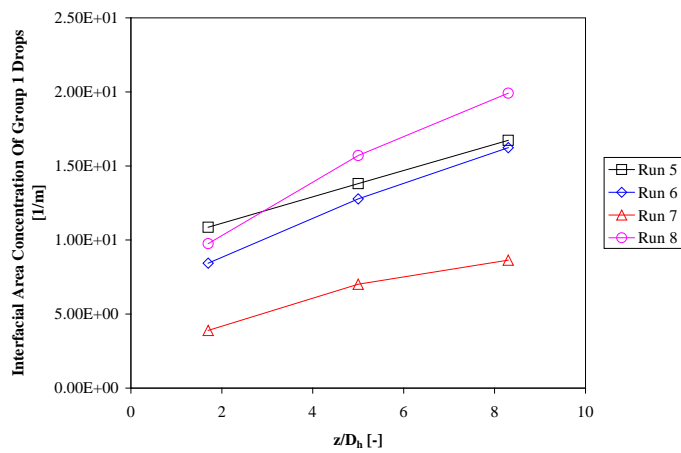
(b)
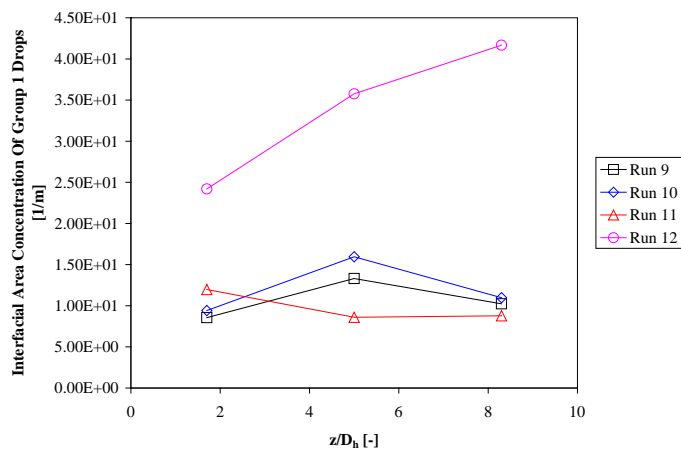
(c)

Fig. 4.6: Area averaged interfacial area concentration of Group 1 drops for

(a) $\langle j_d \rangle$=0.0089 m/s, (b) $\langle j_d \rangle$=0.0179 m/s and (c) $\langle j_d \rangle$=0.0268 m/s.
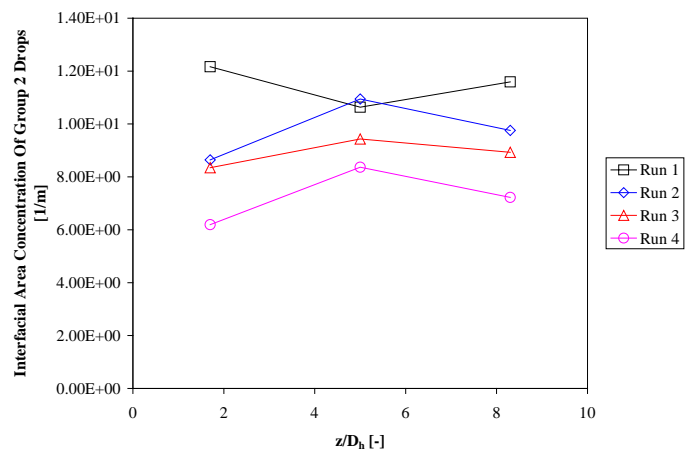
(a)
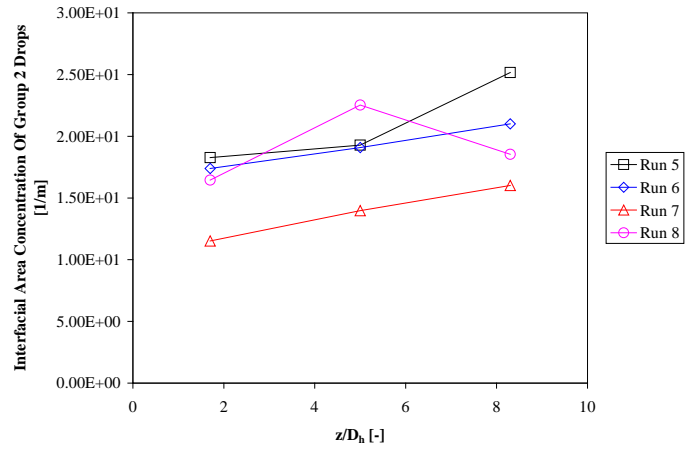
(b)
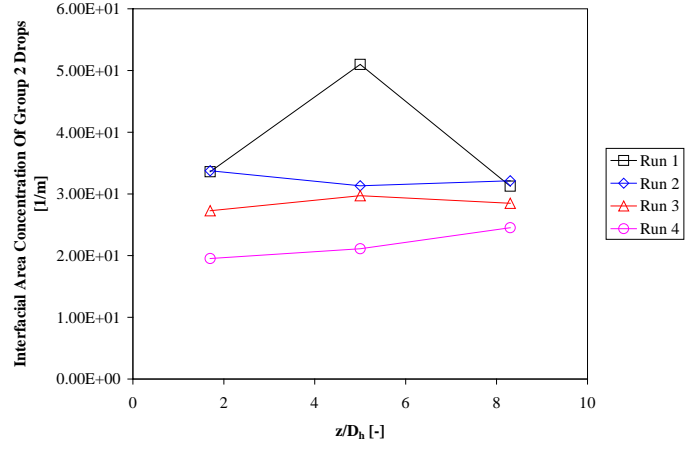
(c)

Fig. 4.7: Area averaged interfacial area concentration of Group 2 drops for

(a) $\langle j_d \rangle$=0.0089 m/s, (b) $\langle j_d \rangle$=0.0179 m/s and (c) $\langle j_d \rangle$=0.0268 m/s.
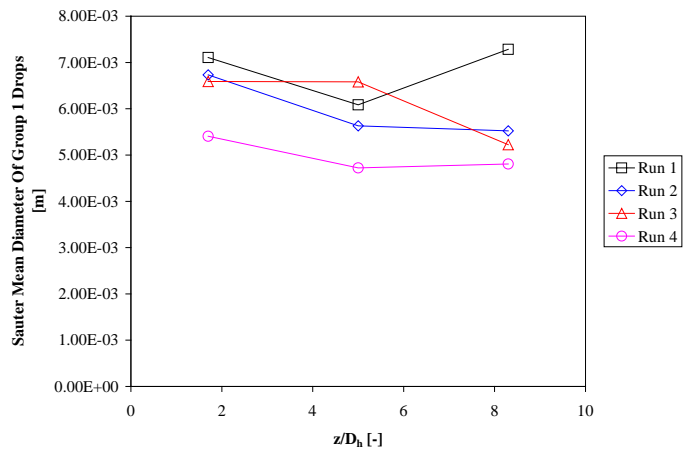
(a)
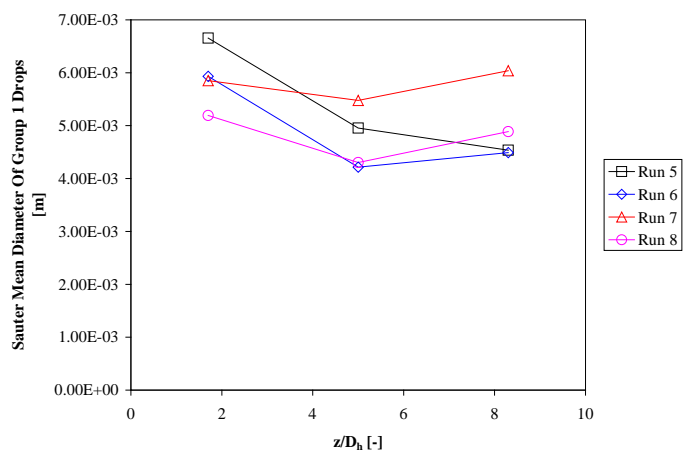
(b)
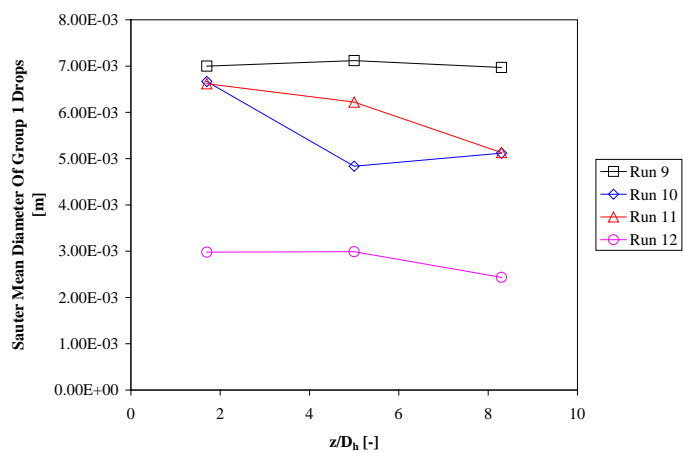
(c)

Fig. 4.8: Area averaged Sauter mean diameter of Group 1 drops for (a) $\langle j_d \rangle$ =0.0089 m/s,

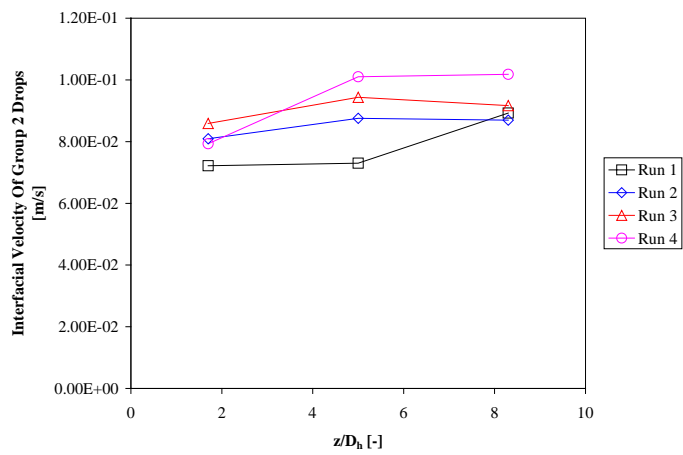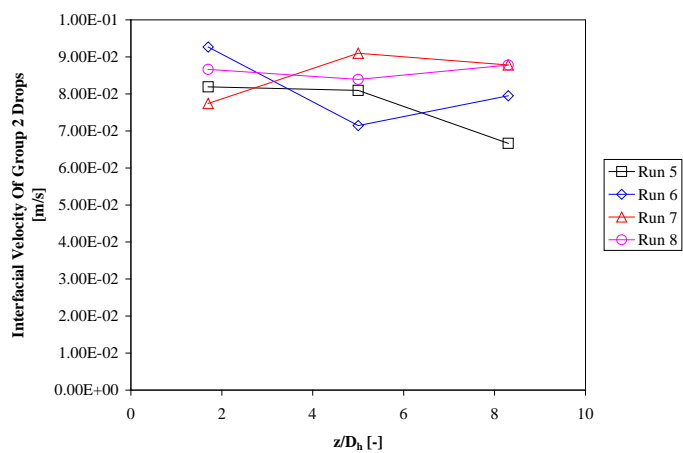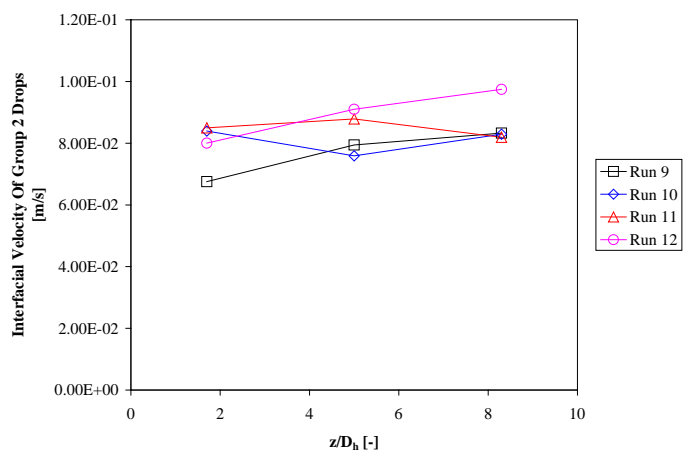(b) $\langle j_d \rangle$ =0.0179 m/s and (c) $\langle j_d \rangle$ =0.0268 m/s.
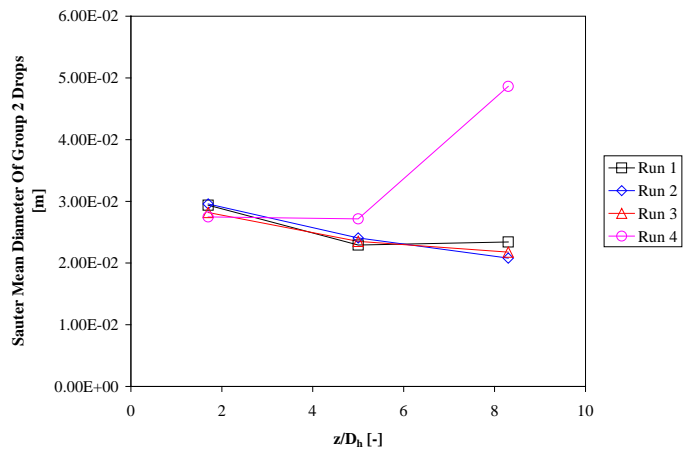
(a)
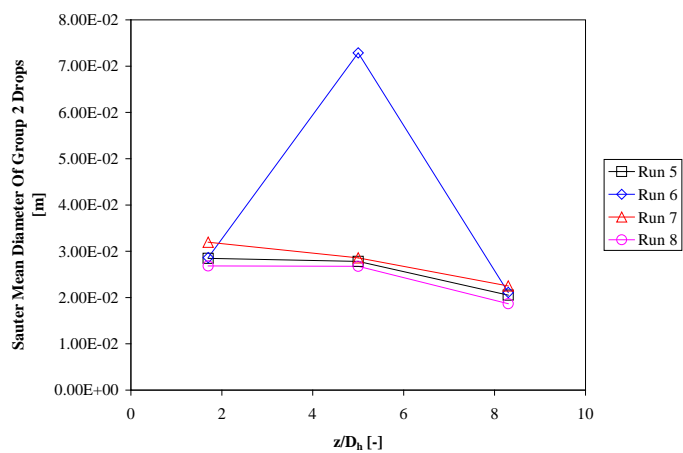
(b)
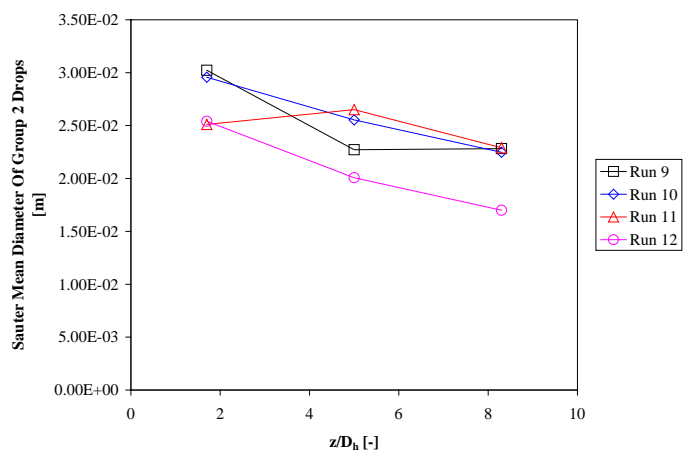
(c)

Fig. 4.9: Area averaged Sauter mean diameter of Group 2 drops for (a) $\langle j_d \rangle$=0.0089 m/s,

(b) $\langle j_d \rangle$=0.0179 m/s and (c) $\langle j_d \rangle$=0.0268 m/s.
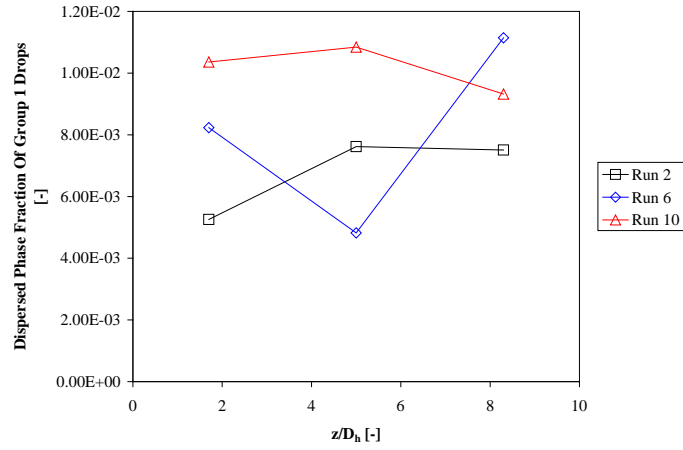
(a)
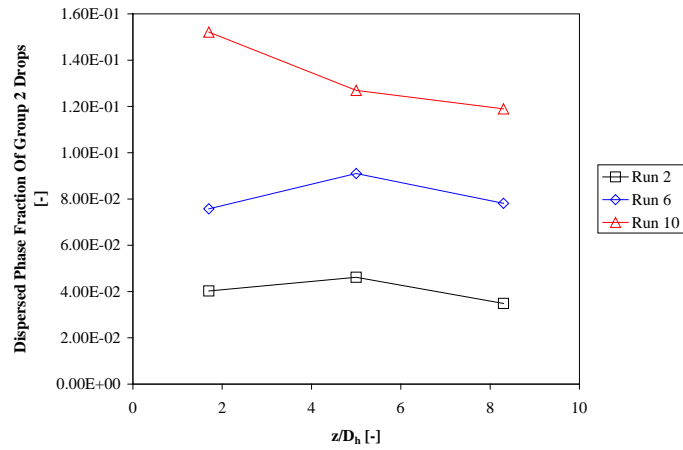
(b)

Fig. 4.10: Area averaged dispersed phase fraction of (a) Group 1 drops and (b) Group 2 drops for $\langle j_c \rangle$ =0.0089 m/s.
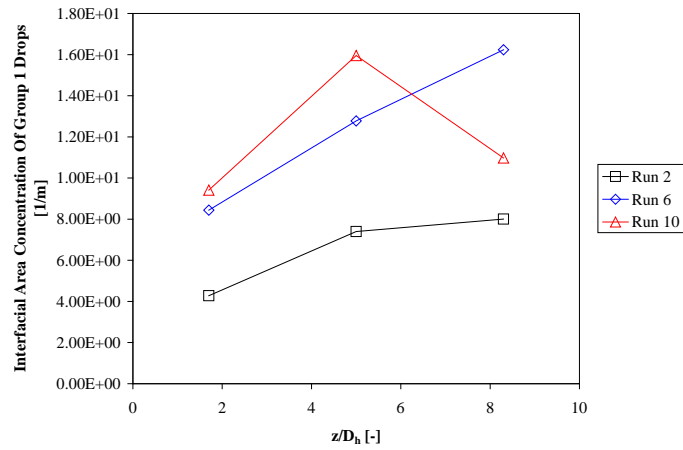
(a)
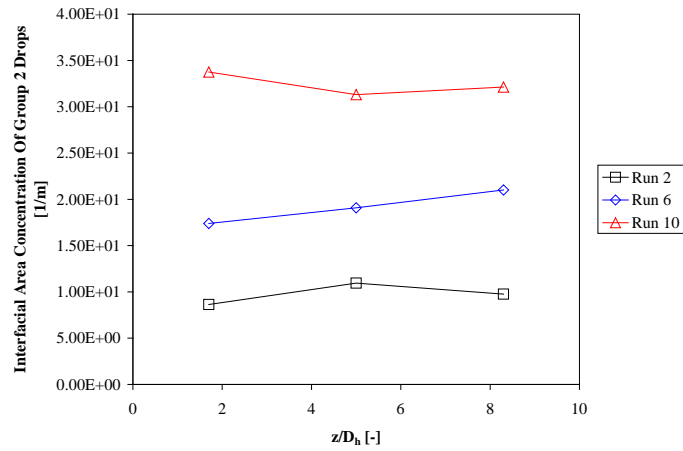
(b)

Fig. 4.11: Area averaged interfacial area concentration of (a) Group 1 drops and (b) Group 2 drops for $\langle j_c \rangle$=0.0089 m/s.
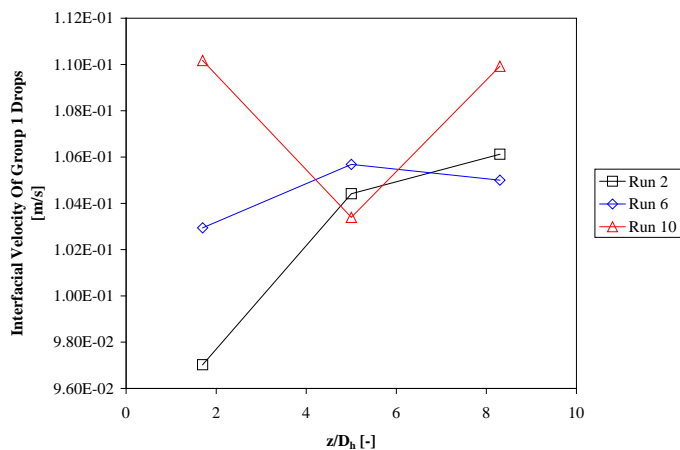
(a)
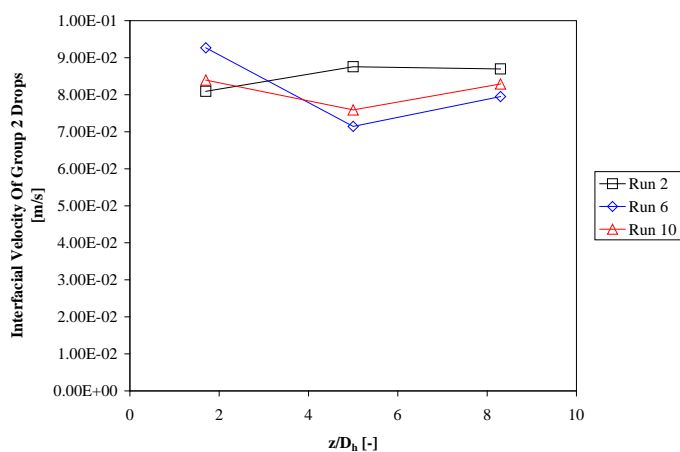
(b)

Fig. 4.12: Area averaged interfacial velocity of (a) Group 1 drops and (b) Group 2 drops for $\langle j_c \rangle$ =0.0089 m/s.

particular continuous phase flow rate, while for Group 2 it practically remains unchanged.

5. EVALUATION OF INTERFACIAL AREA TRANSPORT EQUATION UNDER REDUCED GRAVITY ENVIRONMENTS

5.1 Two-Fluid Model and Interfacial Area Concentration

As mentioned in Chapter 1 there are two fundamental approaches in describing two-phase flow systems depending on the mathematical treatment of the two phases. In one the two phases are treated as a mixture. In the other each phase is treated separately. A general two-phase flow problem can be described by either model depending on the degree of dynamic coupling between the two phases.

The mixture formulation has been used extensively due to its simplicity in both field equations and the necessary constitutive relations. Advanced mixture model such as the drift flux model [1, 38 and 39-42] is considered a reliable tool to predict behavior of two-phase flows presently. In the drift flux model, the mathematical formulation is based on the mixture properties, void fraction and the drift velocity, $\bar{V}_{gj}$. The drift flux model is expressed in terms of four field equations, namely, the mixture continuity, mixture momentum, mixture energy equation and the diffusion equation. Due to its simplicity and its applicability to a wide range of two-phase flow problems of practical interest, the drift flux model is of considerable importance. Analysis based on the drift flux model is quite accurate when the two phases are strongly coupled. However, application of the drift flux model to more complicated two-phase systems is questionable. The drift flux model assumes that the dynamics of two phases is expressed by the mixture-momentum equation with the kinematic constitutive equation specifying the relative motion between the two phases. Therefore, for two-phase flow problems where the inertia terms of each phase should be treated separately, analysis based on the drift flux model becomes doubtful.

On the other hand, the two-fluid model is expressed in terms of two sets of conservation equations which govern the balance of mass, momentum and energy with proper averaging method [1 and 38]. A full 3-D model is obtained from time averaging, whereas a 1-D model can be formulated through area averaging. The 3-D two-fluid model after the averaging processes has phase interaction terms in the conservation equations which account for the transport of mass, momentum and energy across the interface, because the averaged macroscopic fields of each phase are not independent of each other. A simplified version of the 3-D two-fluid model, suitable for most practical applications, can be expressed as follows [1 and 38].

Continuity equation:

$$\frac{\partial \alpha_k \rho_k}{\partial t} + \nabla \cdot (\alpha_k \rho_k \vec{v_k}) = \Gamma_k \tag{5.1}$$

Momentum equation:

$$\frac{\partial \alpha_k \rho_k \vec{v_k}}{\partial t} + \nabla \cdot (\alpha_k \rho_k \vec{v_k} \vec{v_k})$$
$$= -\alpha_k \nabla p_k + \overline{M}_{ik} + \nabla \alpha_k (\overline{\overline{\tau}} + \tau_k^t) + \alpha_k \rho_k \vec{g} + v_{ki} \Gamma_k + \overline{M}_{ik} - \nabla \alpha_k \cdot \overline{\overline{\tau}}_{ki} \tag{5.2}$$

Energy equation:

$$\frac{\partial \alpha_k \rho_k i_k}{\partial t} + \nabla \cdot (\alpha_k \rho_k i_k v_k)$$
$$= -\nabla \cdot \alpha_k (\overline{\overline{q}}_k + q_k^t) + \alpha_k \frac{D_k p_k}{Dt} + i_{ki} \Gamma_k + \Gamma_i q_{ki}^{"} + \phi_k \tag{5.3}$$

where the subscript i stands for the values at the interface, and Γ_k, $\overline{M}_{ik}$, $\overline{\overline{\tau}}_{ki}$, $q_{ki}^{"}$ and ϕ_k are the mass generation, generalized interfacial drag, interfacial shear stress, interfacial heat flux and dissipation, respectively. The interfacial area concentration, a_i, is defined as

$$a_i = \frac{1}{L_s} = \frac{\text{total interfacial area}}{\text{mixture volume}} \tag{5.4}$$

where L_s represents the length scale at the interface. Thus, the physical meaning of the interfacial area concentration, a_i, is the interfacial area per unit mixture volume [1 and 38].

It can be found that several interfacial transfer terms arise on the right hand side of the mass, momentum and energy equations. Since the interfacial transfer terms should obey the balance laws at the interface, the interfacial transfer conditions are obtained from an average of the local jump conditions which are as follows [1 and 38]:

$$\sum_k \Gamma_k = 0 \tag{5.5}$$

$$\sum_k \overline{M}_{ik} = 0 \tag{5.6}$$

$$\sum_k (\Gamma_k i_{ki} + q_{ki}^{"} a_i) = 0 \tag{5.7}$$

Hence, the two-fluid model is based on the governing equations given by Equations 5.1, 5.2 and 5.3 and three interfacial jump conditions given by Equations 5.5, 5.6 and 5.7. Therefore, in order to solve the two-fluid model, constitutive relations for the interfacial transfer terms should be specified.

It is clear that constitutive relations for generalized interfacial drag, interfacial mass transfer and interfacial energy transfer terms should be established. These can be expressed in terms of interfacial area concentration and corresponding driving forces [1, 38 and 43] as

$$\text{(Interfacial transfer term)} = a_i \times \text{(Driving force)} \tag{5.8}$$

Equation 5.8 clearly shows the significance and importance of the accurate prediction of the interfacial area concentration in regards to using the two-fluid model. Thus, constitutive relation to close interfacial area concentration is required. Great efforts were devoted to develop flow regime dependent experimental correlations for the interfacial area concentrations as well as to establish the flow regime transition criteria [1, 37, 38 and 43-46]. The flow regime based approach was also used successfully in the system codes for nuclear reactor safety analysis such as RELAP5, TRAC-G and CATHARE. However, these system codes have shown to exhibit numerical bifurcation for conditions that are at the flow regime transition boundary. The two-step approach based on the flow regime dependent experimental correlations and the flow regime transition criteria neither dynamically represent the changes in the interfacial structure, nor does it correctly reflect the boundary conditions and the entrance effects. Furthermore, the prediction of two-phase flow regime itself in many practical applications may be much more difficult, as pointed

out by Ishii [47]. Based on the above discussions, a better approach to compute the interfacial area concentration should be developed to improve the accuracy and feasibility of the two-fluid model. In view of this, a new approach, namely, the IATE was proposed by Kocamustafaogullari and Ishii [48]. The IATE is discussed in the following section.

5.2 Interfacial Area Transport Equation

The significance of the interfacial area concentration for the two-fluid model and the shortcomings of the flow regime based approach for its determination were discussed in the previous section. Kocamustafaogullari and Ishii [48] proposed the IATE by employing the particle population balance approach suggested by Reyes [49]. The particle number density is considered to be a key parameter in determining the interfacial area concentration. The number density transport equation of fluid particles of volume V was formulated by accounting for the fluid particles entering and leaving a control volume such that [48, 49 and 50]

$$\frac{\partial f(\bar{x},V,t)}{\partial t} + \nabla \cdot \left(f(\bar{x},V,t)\bar{v}_P(\bar{x},V,t) \right) = \sum_j S_j(\bar{x},V,t) + S_{ph}(\bar{x},V,t) \tag{5.9}$$

where $f(\bar{x},V,t)$ is the particle density distribution function, which specifies the probable number density of fluid particles at a given time t, in the spatial range $d\bar{x}$ about a position $\bar{x}$, with particle volumes between V and $V+dV$. $\bar{v}_P(\bar{x},V,t)$ is the local velocity of fluid particles of volume between V and $V+dV$ at time t. In the right hand side (RHS) of the equation, $\sum_j S_j(\bar{x},V,t)$ represents the net rate of change in $f(\bar{x},V,t)$ due to fluid particle interactions such as coalescence and disintegration, while $S_{ph}(\bar{x},V,t)$ is the fluid particle source and sink rates due to phase change.

Equation (1-9) is too complicated and not practical for most two-phase flow applications where the primary focus is on the average behavior of fluid particles. Therefore, Kocamustafaogullari and Ishii [48] integrated this equation over fluid particle volumes of all sizes to obtain the averaged particle number density transport equation as

$$\frac{\partial n}{\partial t} + \nabla \cdot \left(n\vec{v}_{pm} \right) = \sum_j R_j + R_{ph} \tag{5.10}$$

where, $n(\vec{x},t)$ is the total number of fluid particles of all sizes per unit mixture volume and defined by

$$n(\vec{x},t) \equiv \int_{V_{min}}^{V_{max}} f(\vec{x},V,t)dV \tag{5.11}$$

and $\vec{v}_{pm}$ in Equation (5.10) is the local average particle velocity weighted by particle number density defined as

$$\vec{v}_{pm}(\vec{x},t) \equiv \frac{\int_{V_{min}}^{V_{max}} f(\vec{x},V,t)\vec{v}_p(\vec{x},V,t)dV}{\int_{V_{min}}^{V_{max}} f(\vec{x},V,t)dV} = \frac{\int_{V_{min}}^{V_{max}} f(\vec{x},V,t)\vec{v}_p(\vec{x},V,t)dV}{n(\vec{x},t)} \tag{5.12}$$

The source and sink terms for fluid particle number density due to particle interactions and phase change, R_j and R_{ph}, are defined as

$$R_j \equiv \int_{V_{min}}^{V_{max}} S_j dV \text{ and } R_{ph} \equiv \int_{V_{min}}^{V_{max}} S_{ph} dV \tag{5.13}$$

By multiplying Equation (5.9) by the average surface area of fluid particles of volume V, $A_i(V)$, and integrating it over the bubble volume, Hibiki and Ishii [1] derived the IATE as

$$\frac{\partial a_i}{\partial t} + \nabla \cdot \left(a_i \vec{v}_i \right) - \frac{2}{3}\left(\frac{a_i}{\alpha_g} \right)\left(\frac{\partial \alpha_g}{\partial t} + \nabla \cdot \left(\alpha_g \vec{v}_g \right) - \eta_{ph} \right) = \sum_j \phi_j + \phi_{ph} \tag{5.14}$$

where $a_i(\vec{x},t)$ is the average interfacial area concentration of all-sized particles at location $\vec{x}$ and $\vec{v}_i(\vec{x},t)$ is the interfacial velocity. They are defined by

$$a_i(\vec{x},t) \equiv \int_{V_{min}}^{V_{max}} f(\vec{x},V,t)A_i(V)dV \tag{5.15}$$

and

$$\vec{v}_i(\vec{x},t) \equiv \frac{\int\limits_{V_{\min}}^{V_{\max}} f(\vec{x},V,t)A_i(V)\vec{v}_p(\vec{x},V,t)dV}{\int\limits_{V_{\min}}^{V_{\max}} f(\vec{x},V,t)A_i(V)dV} = \frac{\int\limits_{V_{\min}}^{V_{\max}} f(\vec{x},V,t)A_i(V)\vec{v}_p(\vec{x},V,t)dV}{a_i(\vec{x},t)} \qquad (5.16)$$

respectively. The ϕ_j and ϕ_{ph} in the RHS of Equation (5.14) represent the rate of change in the interfacial area concentration due to fluid particle interactions, such as breakup and coalescence, and due to evaporation or condensation processes, respectively. They are defined by

$$\phi_j \equiv \int\limits_{V_{\min}}^{V_{\max}} S_j(\vec{x},V,t)A_i(V)dV \qquad (5.17)$$

and

$$\phi_{ph} \equiv \int\limits_{V_{\min}}^{V_{\max}} S_{ph}(\vec{x},V,t)A_i(V)dV \qquad (5.18)$$

From the above basis, the theoretical models of fluid particle interaction mechanisms are required for the source and sink terms in order to close the IATE. Therefore, Kocamustafaogullari and Ishii [48] suggested some major fluid particle coalescence and breakup mechanisms. The mechanism of particle breakup may be related to the local turbulence structure in turbulent flows, viscous shear in laminar flows, and interfacial instability (Rayleigh-Taylor and Kelvin-Helmholtz instabilities). On the other hand, the coalescence mechanism may be caused by the turbulent fluctuation, size dependent rise velocity differences, wake entrainment, and shear layer induced velocity difference.

In order to formulate the IATE describing the transport phenomena of fluid particles in a wide range of flow regimes, it should be noted that there exist various types of bubbles with different size depending on the flow conditions, and the geometry and dimensions of the flow channel. In a general two-phase flow, these may consist of spherical, distorted, cap, slug, and/or churn-turbulent bubbles. The differences in shape and size of these bubbles lead to considerable differences in their transport mechanisms due to the differences in interfacial forces. Therefore, in view of the transport characteristics, the bubbles may be simply categorized into two groups, namely, the Group-1 for the spherical

and distorted bubbles and the Group-2 for the cap, slug and churn-turbulent bubbles. Thus, two sets of IATE should be formulated in order to describe the general two-phase transport phenomena [51]. However, in the bubbly flow regime, where the void fraction is not very high, it is reasonable to apply the one-group IATE and to assume the bubbles are nearly spherical in shape. Wu et al. [52] and Kim [53] formulated the one-group IATE, which is applicable to bubbly flow. In this equation, three bubble interaction mechanisms were mechanistically modeled. These three bubble interaction mechanisms are as follows: bubble disintegration due to turbulent impact (TI), bubble coalescence through random collision driven by the surrounding liquid turbulent eddies (RC), and bubble coalescence due to the wake entrainment of the following bubbles by a preceding bubble (WE).

In the development of the one-group IATE, bubbles are assumed close to spherical in shape and with similar size [52 and 53]. However, in developing the transport equation applicable to wide range of two-phase flows, the differences in the shape and size of bubbles and in the characteristic transport phenomena should be accounted for. In view of this, the two-group IATE was proposed by Wu et al. [54], and preliminary work was performed by Hibiki and Ishii [55] for the interfacial area transport at the transition from bubbly to slug flow. Ishii et al. [56] also developed the framework for the two-group IATE. To solve the two-group IATE, the bubble interaction mechanisms such as coalescence and disintegration, should be modeled to serve as the two-group source and sink terms. Both the interactions within same group (intra-group) and those between different groups (inter-group) should be considered in the modeling process. For general gas-liquid two-phase flow, five major bubble interaction mechanisms may be considered [56 and 57]. They are summarized as: (1) random collision (RC) as bubble coalescence due to turbulent eddies; (2) wake entrainment (WE) as bubble coalescence due to acceleration of the following bubbles in the wake of a preceding bubble; (3) turbulent impact (TI) as bubble disintegration due to impact of turbulent eddies; (4) shearing off (SO) as small bubbles shearing off around the base rim of a large bubble; and (5) surface instability (SI) as breakup of a large bubble due to surface instability at the interface.

As mentioned earlier there are very few experimental databases of detailed local two-phase flow parameters obtained under reduced gravity environments. These are needed

to evaluate the IATE. Hence the best course of action would seem to be to evaluate the simplest versions of IATE first and then go towards more complex ones. In the following only the steady state and one dimensional version of IATE will be evaluated. First one group, steady state, one dimensional IATE will be evaluated against data acquired by various researchers. Then two group, steady state, one dimensional IATE will be evaluated against data acquired by various researchers.

5.3 Evaluation of One Group, Steady State, One Dimensional IATE under Reduced Gravity

The one group, steady state, one dimensional IATE is given by the following [58]:

$$\frac{d}{dz}\left(\langle a_i \rangle \langle\langle v_{dz} \rangle\rangle\right) = \langle S_{a,RC} \rangle + \langle S_{a,WE} \rangle + \langle S_{a,TI} \rangle \tag{5.19}$$

where, a_i is the interfacial area concentration, v_{dz} is the axial velocity of the dispersed phase and $S_{a,RC}$, $S_{a,WE}$ and $S_{a,TI}$ are interfacial area source and sink terms due to random collision (RC), wake entrainment (WE) and turbulent impact (TI), respectively. Furthermore, the symbols $\langle \ \rangle$ and $\langle\langle \ \rangle\rangle$ represent area-averaging and void weighted area-averaging, respectively; and z is the co-ordinate along the flow direction. The interfacial area source and sink terms are given by the following:

$$\langle S_{a,RC} \rangle = -\frac{1}{3\pi}C_{RC}\left(u_t \langle a_i \rangle^2\right)\left[\frac{1}{\langle \alpha_{\max} \rangle^{1/3}\left(\langle \alpha_{\max} \rangle^{1/3} - \langle \alpha \rangle^{1/3}\right)}\right] \times \left[1 - \exp\left(-C\frac{\langle \alpha_{\max} \rangle^{1/3}\langle \alpha \rangle^{1/3}}{\langle \alpha_{\max} \rangle^{1/3} - \langle \alpha \rangle^{1/3}}\right)\right]$$

$$\tag{5.20}$$

$$\langle S_{a,WE} \rangle = -\frac{1}{3\pi}C_{WE}u_t \langle a_i \rangle^2 \tag{5.21}$$

$$\langle S_{a,TI} \rangle = \frac{1}{18}C_{TI}u_t\left(\frac{\langle a_i \rangle^2}{\langle \alpha \rangle}\right)\left(1 - \frac{We_{cr}}{We}\right) \times \exp\left(-\frac{We_{cr}}{We}\right), \quad We > We_{cr} \tag{5.22}$$

where, C_{RC} , C, C_{WE} and C_{TI} are coefficients in the models and have been determined previously experimentally. u_t is the average turbulent fluctuating velocity, α is the dispersed phase fraction, α_{max} is the dispersed phase fraction at maximum packing limit for distorted bubbles/drops and We is the Weber number defined as:

$$We = \frac{\rho_c u_r^2 D_b}{\sigma} \tag{5.23}$$

where, ρ_c is the density of the continuous phase, u_r is the relative velocity between the two-phases, D_b is the average bubble diameter and σ is the interfacial tension between the phases. We_{crit} is the critical Weber number and bubble disintegration due to turbulent impact can only occur if $We>We_{crit}$.

The values of the adjustable coefficients were taken as the following [58]:

$$C_{RC} = 0.0021, C = 3.0, C_{WE} = 0.151, C_{TI} = 0.18, \alpha_{max} = 0.52 \, and \, We_{cr} = 2.0 \tag{5.24}$$

All the values were same as ones used for normal gravity conditions except for α_{max} which was changed to account for the presence of large sizes of bubbles under reduced gravity conditions [29].

A MATLAB$^®$ script was written to solve Equation (5.19) numerically. As can be seen from Equations 5.19 – 5.22, values of $\left\langle\left\langle v_{dz} \right\rangle\right\rangle$ and α are needed at various z values (depending on the discretization of z-axis) in order to be able to solve Equation 5.19. In order to simplify the evaluation, in the current study, values of $\left\langle\left\langle v_{dz} \right\rangle\right\rangle$ and α at a given z-location were estimated by interpolating the measured values of these parameters at different axial locations.

The average turbulent fluctuating velocity, u_t was estimated using the following [29]:

$$u_t = 1.4(\varepsilon D_b)^{\frac{1}{3}} \tag{5.25}$$

where, ε is the turbulent kinetic energy dissipation rate per unit mixture mass of two-phase flow and D_b is the average bubble diameter. ε was determined using the following equation

$$\varepsilon = f_{TW} \frac{\left\langle v_m \right\rangle^3}{2D_h} \tag{5.26}$$

where, f_{TW} is the two-phase friction factor, $\langle v_m \rangle$ is the mixture velocity and D_h is the hydraulic diameter of the test section. f_{TW} in the present case was determined experimentally.

Two databases were used to evaluate the one group, steady state, one dimensional IATE against. The first one was acquired by Vasavada et al. [26]. Vasavada et al. [26] performed extensive experimental studies simulating reduced gravity environments in a ground based facility by using two immiscible liquids of similar densities. The test section was of 25.4 mm ID and 2.8 m height. Data sets were acquired at a total of eleven flow conditions in bubbly and bubbly to slug flow transition regimes. Important two-phase flow local parameters like dispersed phase fraction, interfacial area concentration, droplet number frequency and droplet velocity were acquired at two-axial locations (z/D_h =30, 58) using state-of-the-art multi-sensor conductivity probes. More details of the experimental facility, instrumentation, etc. can be found in Vasavada et al. [26]. The flow conditions are listed in Table 5.1 and also plotted on a flow regime map in Fig. 5.1.

The results of the evaluation are shown in Figs. 5.2 – 5.5. The magnitudes of various terms that contribute to interfacial area creation and destruction are plotted in Figs. 5.6 – 5.9.

Table 5.1: Flow conditions for data acquired by Vasavada et al. [26].

Run	j_{c1} (m/s)	j_{c2} (m/s)	j_c (m/s)	j_d (m/s)	Re_c (−)	Re_d (−)	Re_d/Re_c (−)	$\Delta P_f/\Delta P_g$ (−)
2	0.121	0.094	0.215	0.012	5460	44	0.008	0.005
3	0.262	0.094	0.356	0.012	9011	44	0.005	0.010
4	0.115	0.094	0.209	0.050	5302	176	0.033	0.005
5	0.249	0.094	0.343	0.050	8696	176	0.020	0.014
6	0.124	0.094	0.218	0.112	5531	395	0.071	0.007
7	0.211	0.094	0.305	0.112	7733	395	0.051	0.020
8	0.402	0.093	0.496	0.056	12563	198	0.016	0.040
9	0.402	0.093	0.496	0.112	12563	395	0.031	0.040
10	0.651	0.093	0.745	0.056	18877	198	0.010	0.080
11	0.649	0.093	0.742	0.112	18814	395	0.021	0.070
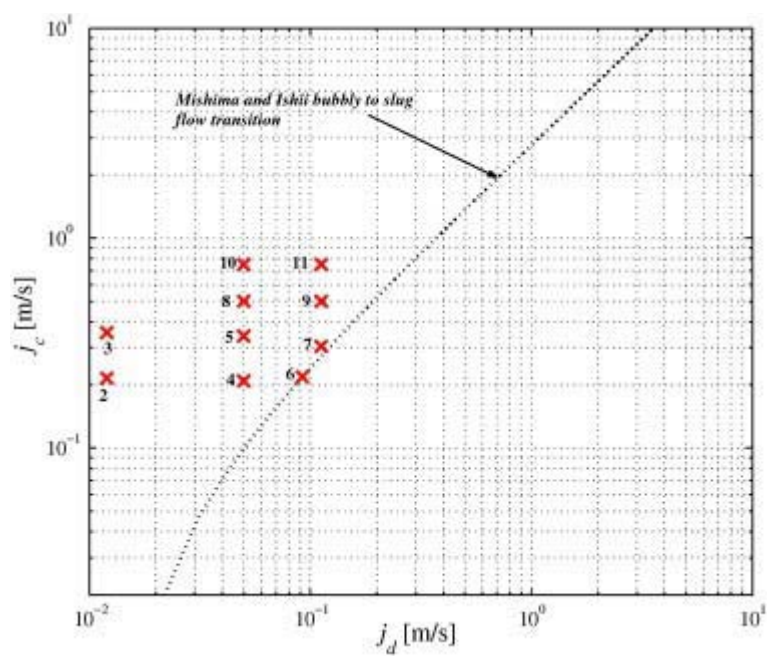
Fig. 5.1: Flow conditions in Table 5.1 on a flow pattern map.
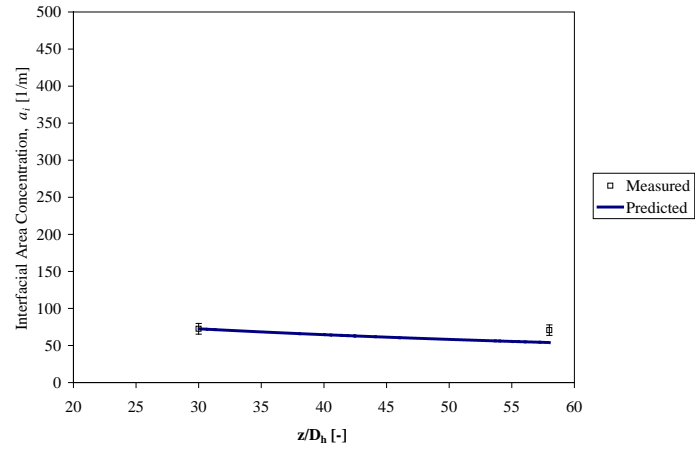
(a)
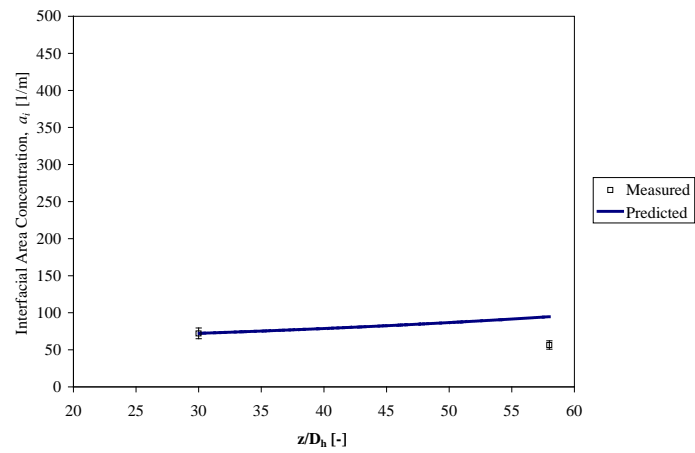
(b)
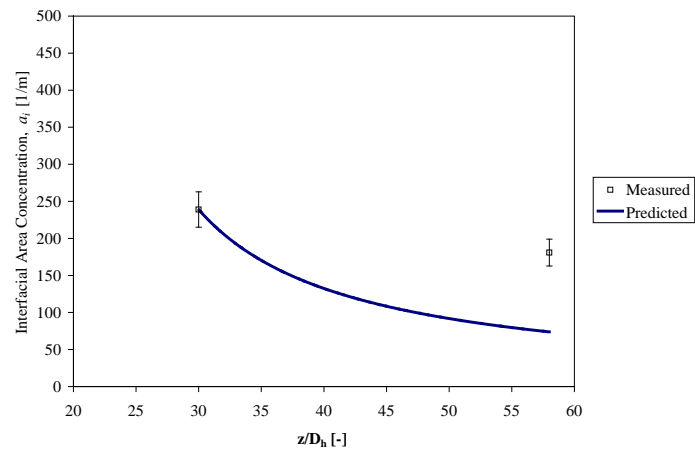
(c)

Fig. 5.2: Comparison of prediction of one group, steady state, one dimensional IATE with experimental results of Vasavada et al. [26] for (a) Run 2, (b) Run 3 and (c) Run 4.
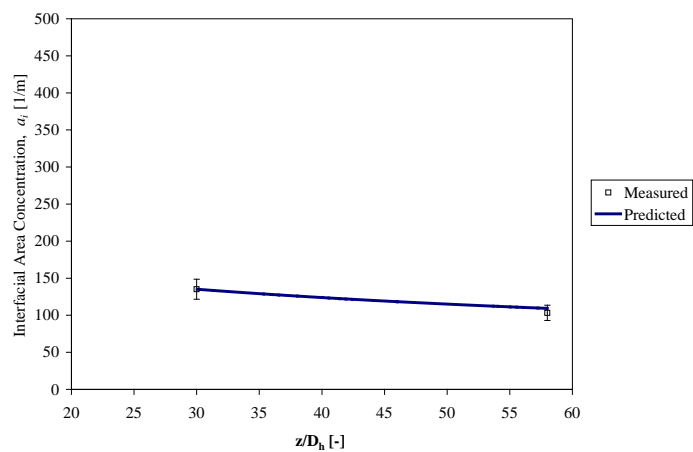
(a)
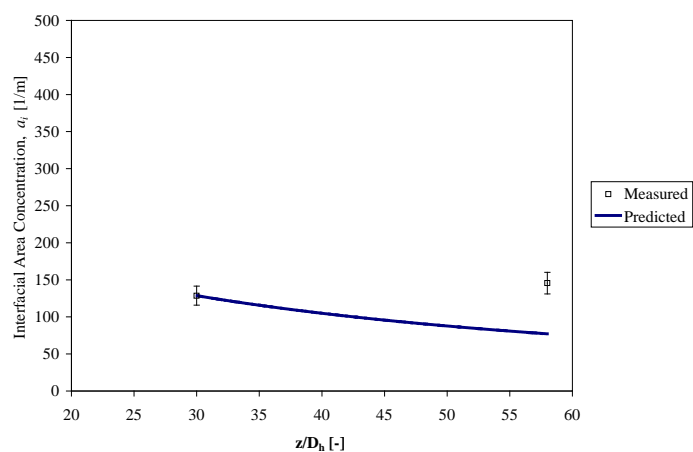
(b)

(c)

Fig. 5.3: Comparison of prediction of one group, steady state, one dimensional IATE with experimental results of Vasavada et al. [26] for (a) Run 5, (b) Run 6 and (c) Run 7.

(a)

(b)
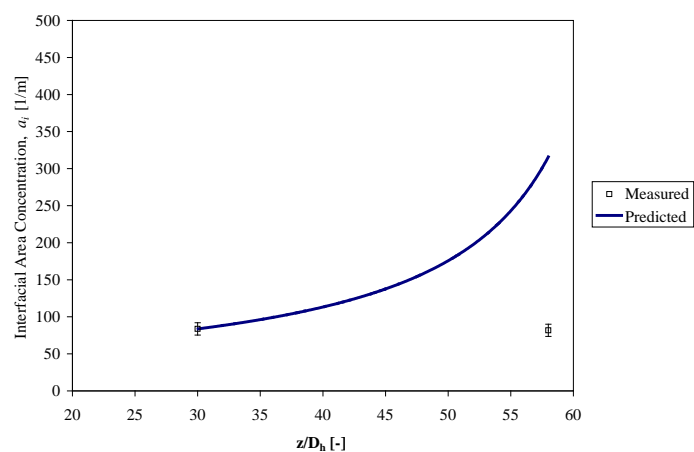
(c)

Fig. 5.4: Comparison of prediction of one group, steady state, one dimensional IATE with experimental results of Vasavada et al. [26] for (a) Run 8, (b) Run 9 and (c) Run 10.
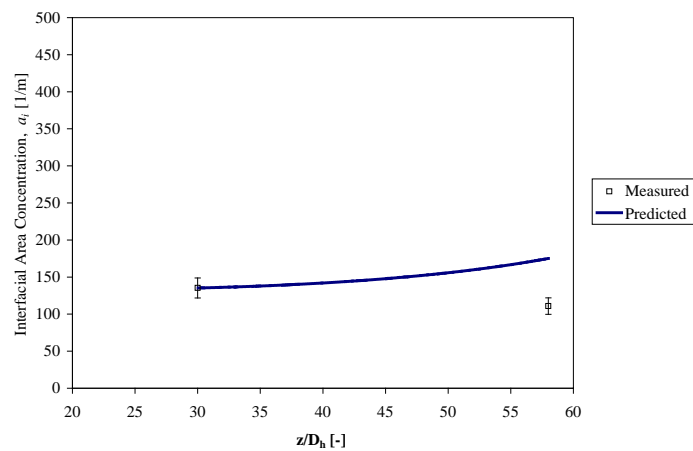
Fig. 5.5: Comparison of prediction of one group, steady state, one dimensional IATE with experimental results of Vasavada et al. [26] for Run 11.
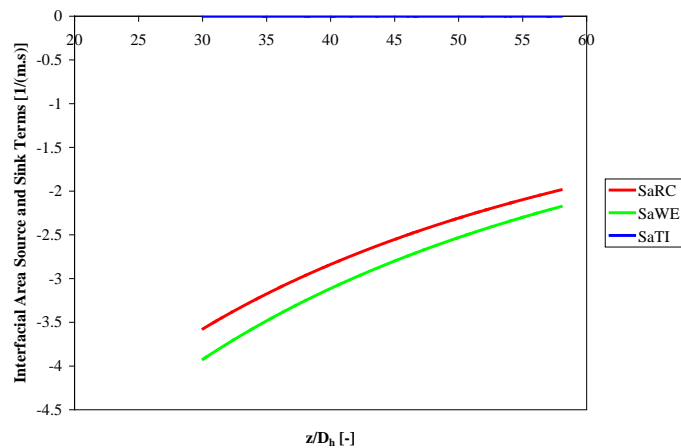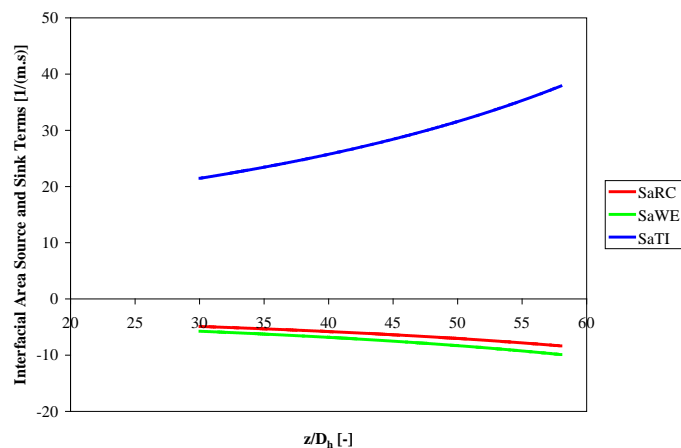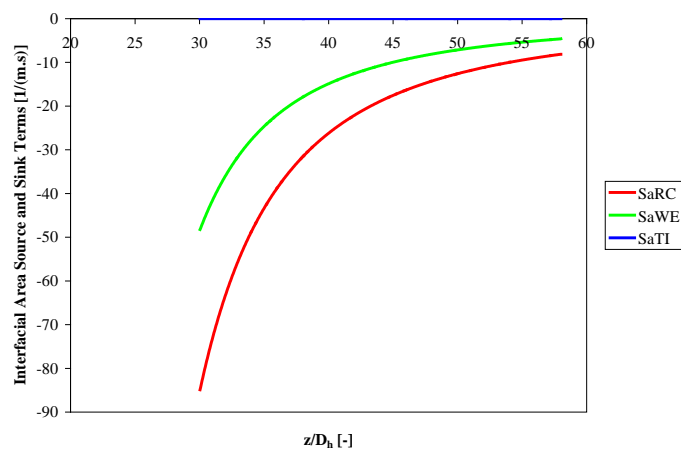
Fig. 5.6: Interfacial area source and sink terms for test conditions of Vasavada et al. [26] for (a) Run 2, (b) Run 3 and (c) Run 4.
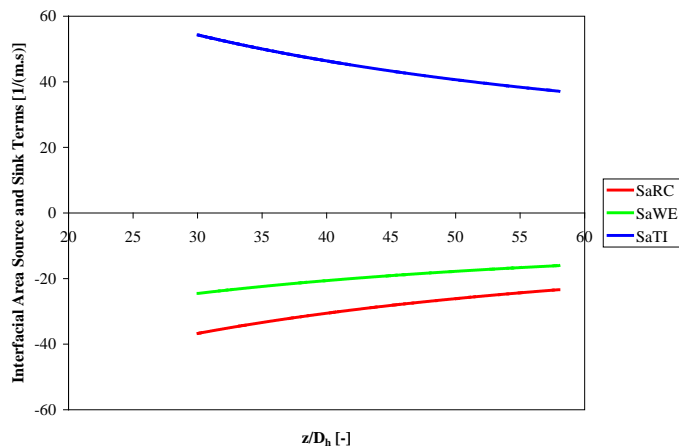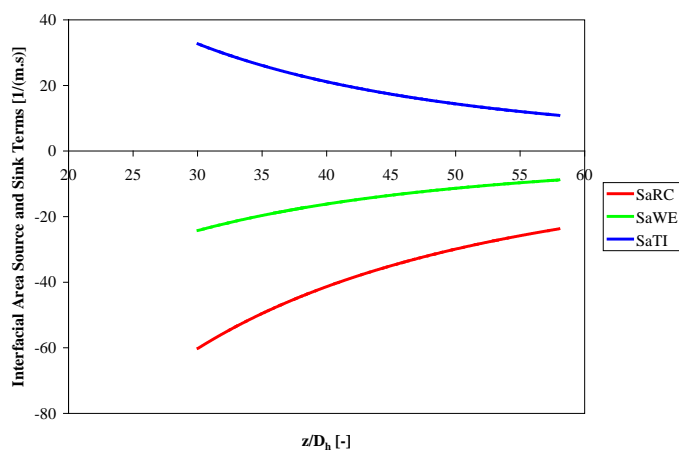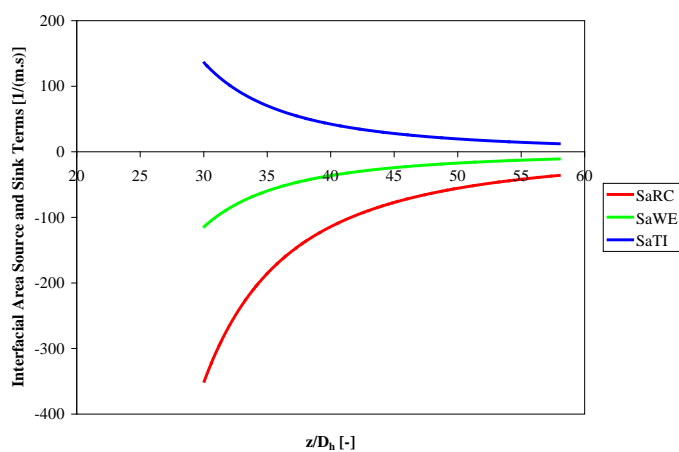
Fig. 5.7: Interfacial area source and sink terms for test conditions of Vasavada et al. [26] for (a) Run 5, (b) Run 6 and (c) Run 7.
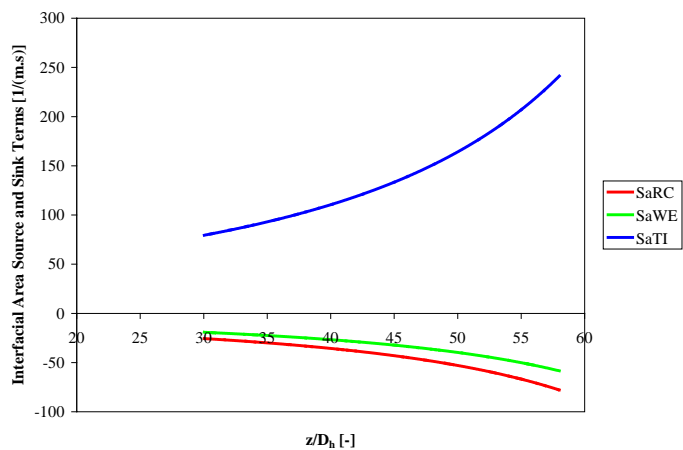
(a)
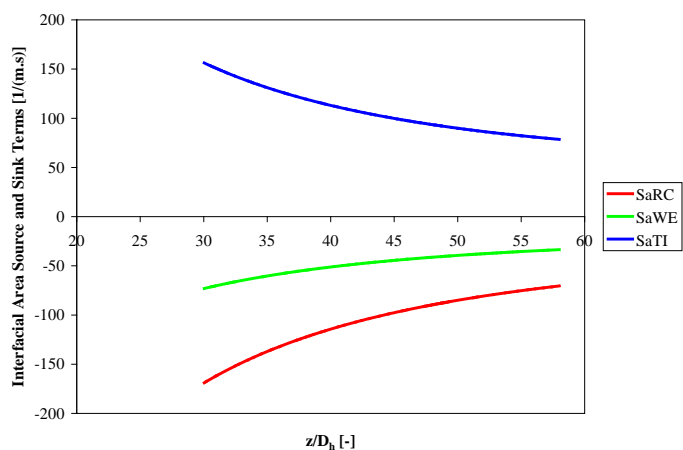
(b)
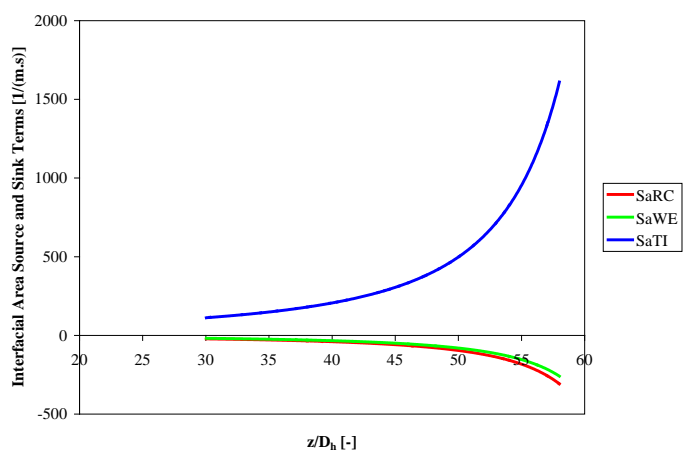
(c)

Fig. 5.8: Interfacial area source and sink terms for test conditions of Vasavada et al. [26] for

(a) Run 8, (b) Run 9 and (c) Run 10.
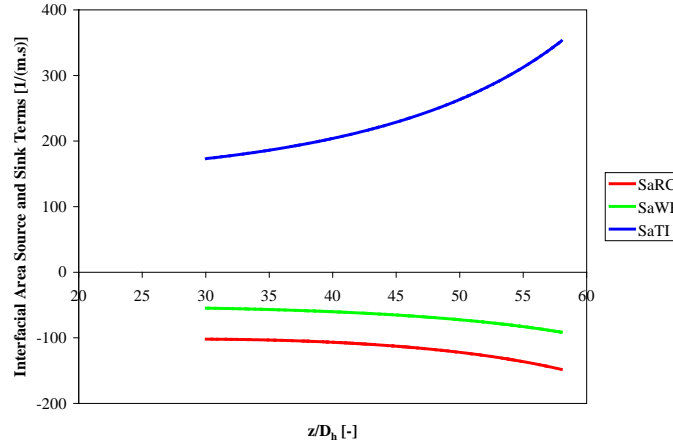
Fig. 5.9: Interfacial area source and sink terms for test conditions of Vasavada et al. [26] for Run 11.

The following observations can be made after looking at the Figs. 5.2 – 5.9. At relatively high values of the continuous phase velocity (Runs 10 and 11) the interfacial area source term due to turbulent impact has a tendency to blow up (Figs. 5.8 (c) and 5.9). This results in over-prediction of interfacial area concentration as shown in Figs. 5.4 (c) and 5.5. This is probably due to the fact that the critical Weber number, We_{cr}, under experimental conditions may be higher than 2.0. If that is the case, the problem can easily be mitigated by using a suitable higher value of the critical Weber number, We_{cr}. Also at very low flow rates of the continuous phase (Runs 2, 4 and 6) there appears to be an over existence of random collision induced destruction of interfacial area (Figs. 5.6 (a), (c) and 5.7 (b)). This leads to an under-prediction of interfacial area concentration as shown in Figs. 5.2 (a), (c) and 5.3 (b). At intermediate flow rates of either phases the prediction appears to be reasonable (Runs 3, 5 and 9).

The second database against which the one group, steady state, one dimensional IATE was evaluated was acquired by Takamasa et al. [25]. Takamasa et al. [25] measured axial developments of one-dimensional void fraction, bubble number density, interfacial area concentration, and Sauter mean diameter of adiabatic nitrogen-water bubbly flows in a 9 mm-diameter pipe under microgravity environments. The measurements were performed

using an image processing method. The measurements were performed at four axial locations (L/D_h=7, 30, 45 and 60) under various flow conditions of superficial gas velocity (0.0083-0.022 m/s) and superficial liquid velocity (0.073-0.22 m/s). More details of the experimental facility, instrumentation, etc. can be found in Takamasa et al. [25]. The flow conditions are listed in Table 5.2. The results of the evaluation are shown in Figs. 5.10 – 5.12. Since only bubble coalescence due to a mechanism very similar to wake entrainment was observed only the term representing interfacial area destruction by wake entrainment was kept on the RHS of Equation 5.19. The magnitude of this term is plotted in Figs. 5.13 – 5.15. The following observations can be made from the evaluation results. The predictions are reasonably well. The wake entrainment model in the one-group, steady state, one-dimensional IATE captures the physics involved in the flow development process. However, the predictions over-estimate the interfacial area concentration generally. The co-efficient C_{WE} may need to be adjusted slightly to get better prediction results.

Table 5.2: Flow conditions for data acquired by Takamasa et al. [25].

| Run #	P (MPa)	$\langle j_g \rangle$ (m/s)	$\langle j_f \rangle$ (m/s)	Re_g (-)	Re_f (-)
1	0.46	0.00906	0.156	24.1	1400
2	0.46	0.00871	0.222	23.2	1990
3	0.46	0.00972	0.280	25.9	2510
4	0.47	0.00963	0.440	26.2	3940
5	0.47	0.00895	0.529	24.3	4750
6	0.46	0.00910	0.174	24.2	1560
7	0.43	0.0103	0.330	25.5	2960
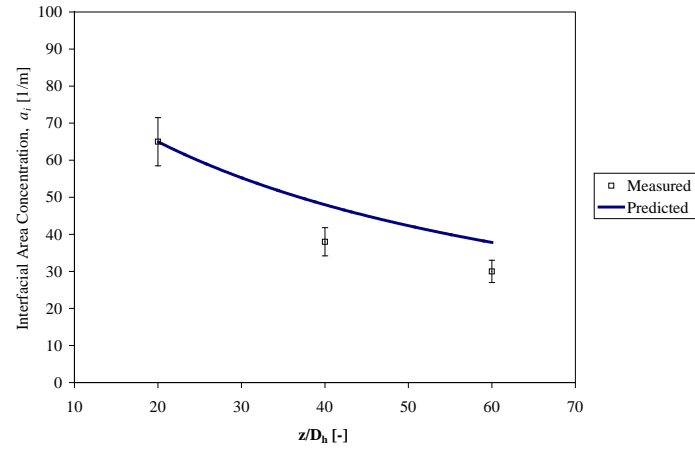
(a)
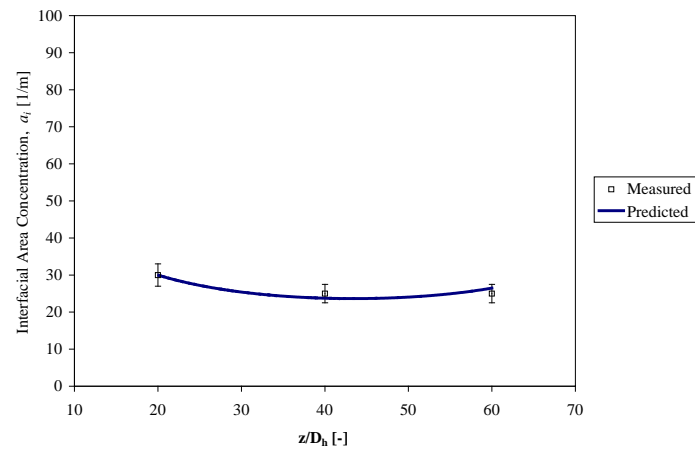
(b)
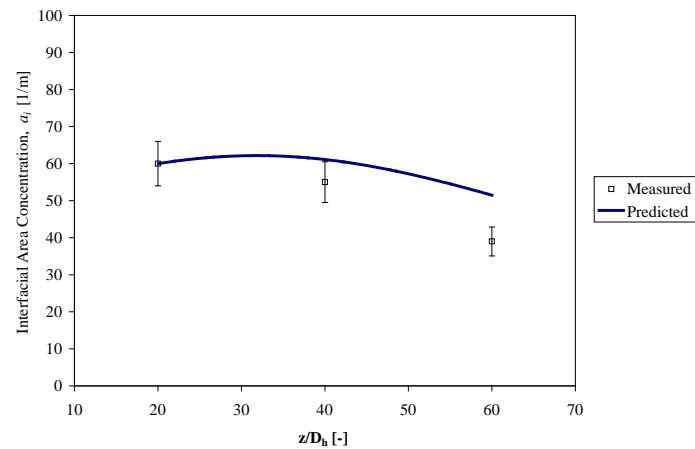
(c)

Fig. 5.10: Comparison of prediction of one group, steady state, one dimensional IATE with experimental results of Takamasa et al. [25] for (a) Run 1, (b) Run 2 and (c) Run 3.
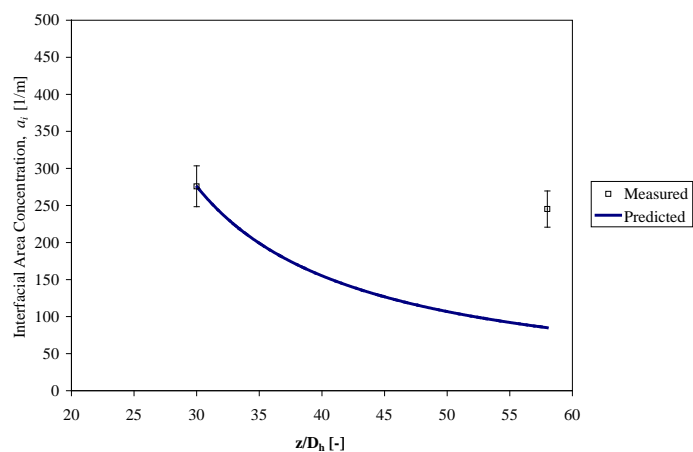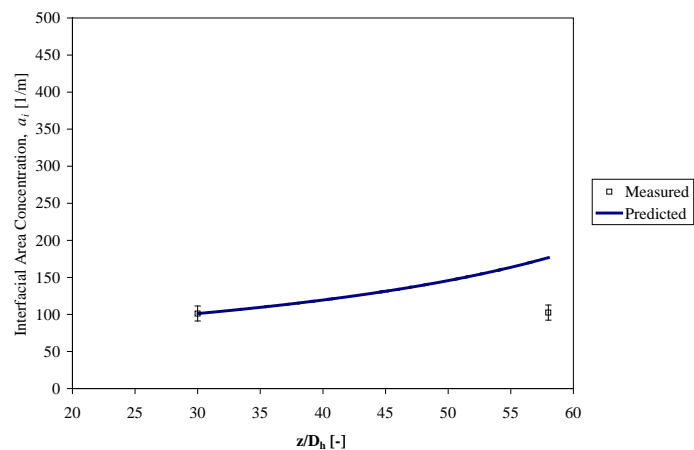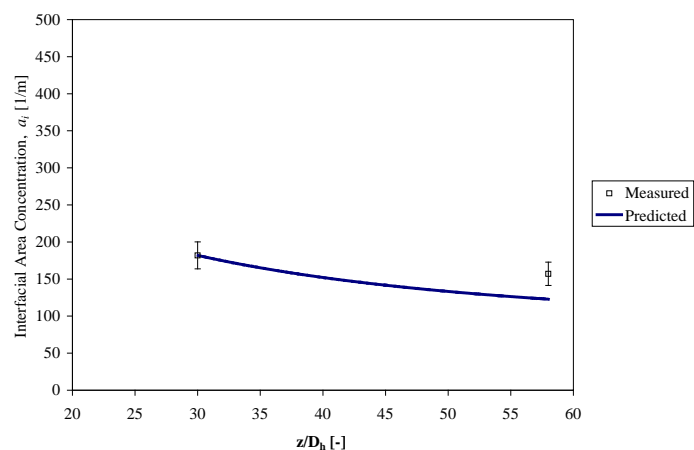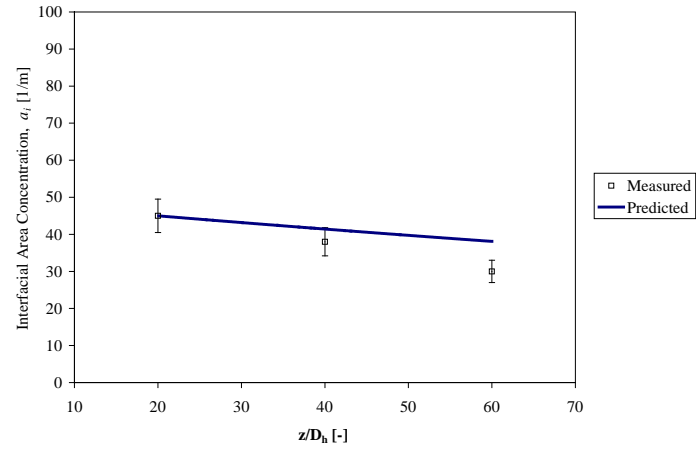
(a)
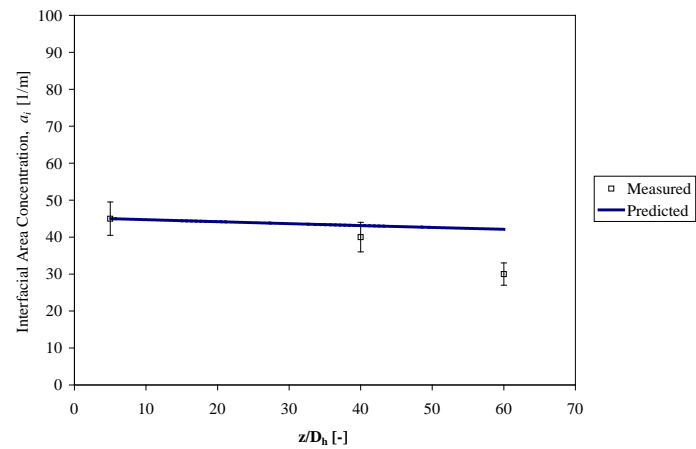
(b)
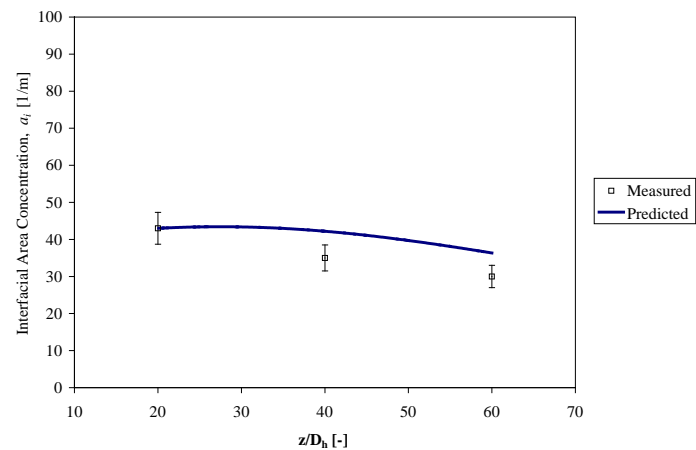
(c)

Fig. 5.11: Comparison of prediction of one group, steady state, one dimensional IATE with experimental results of Takamasa et al. [25] for (a) Run 4, (b) Run 5 and (c) Run 6.
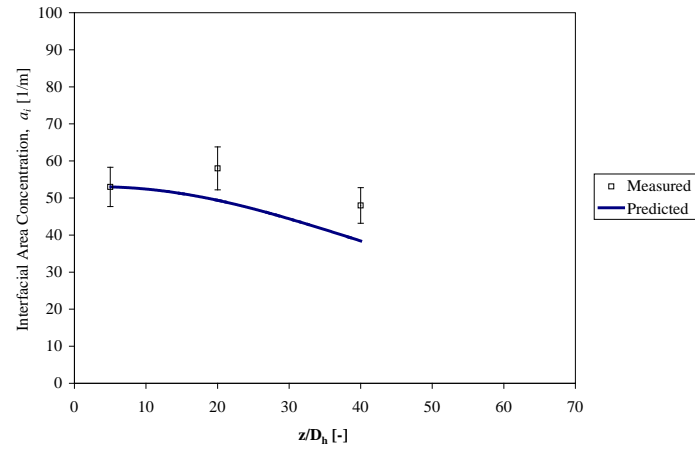
Fig. 5.12: Comparison of prediction of one group, steady state, one dimensional IATE with experimental results of Takamasa et al. [25] for Run 7.
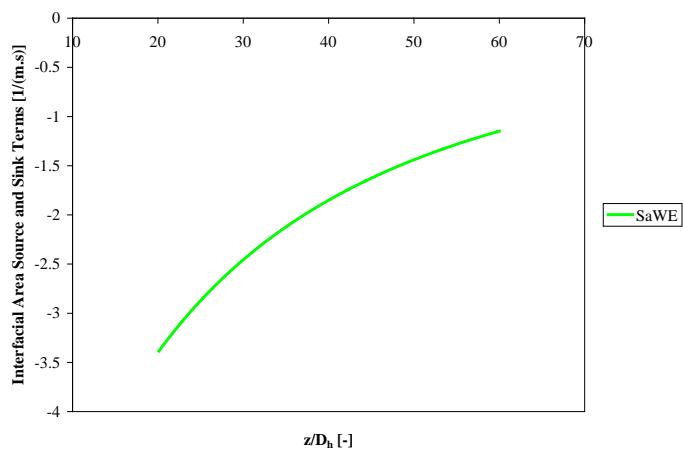
(a)
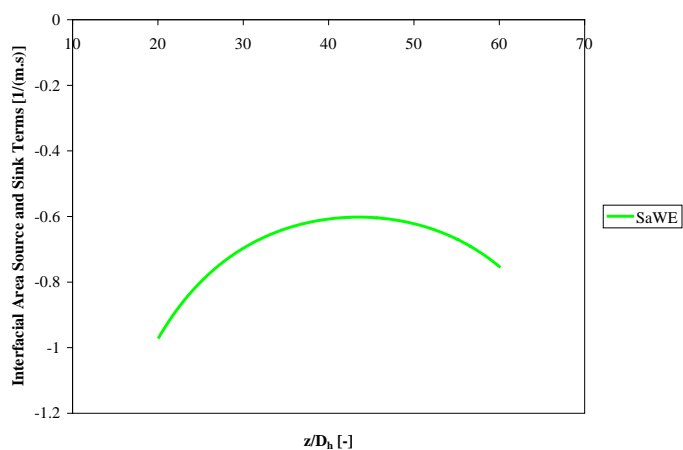
(b)
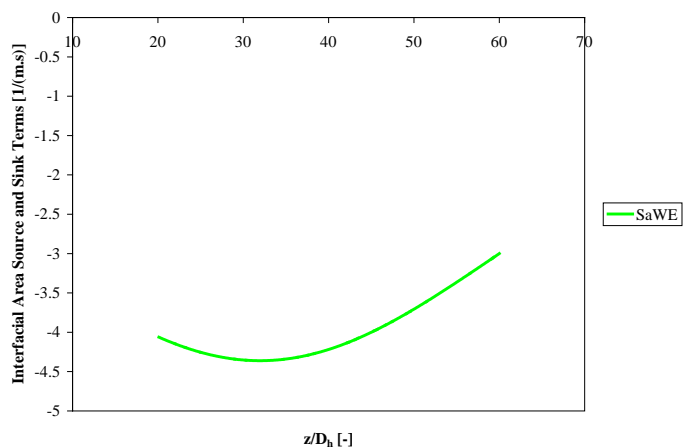
(c)

Fig. 5.13: Interfacial area source and sink terms for test conditions of Takamasa et al. [25] for (a) Run 1, (b) Run 2 and (c) Run 3.
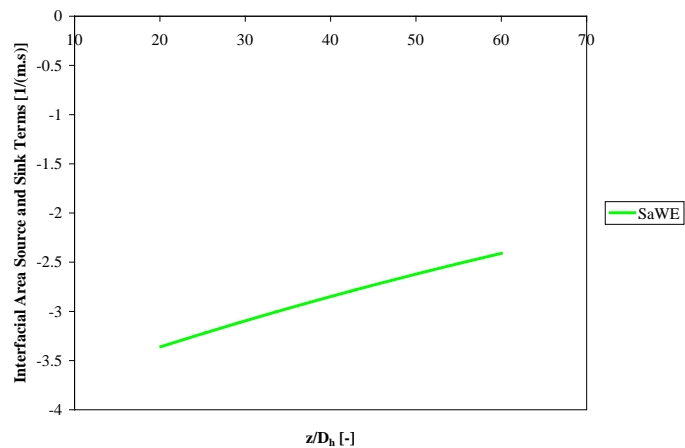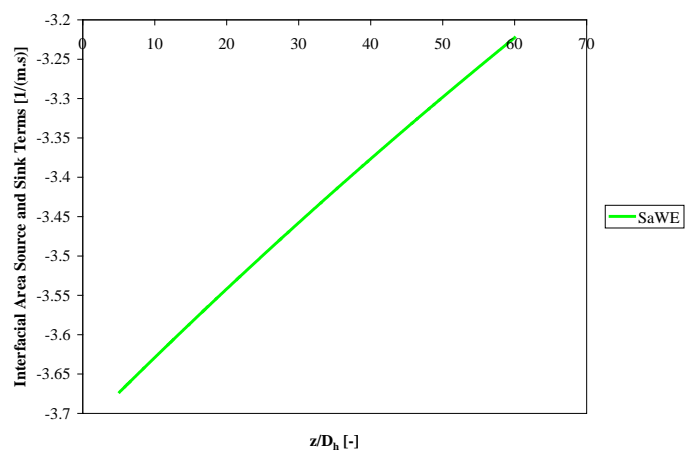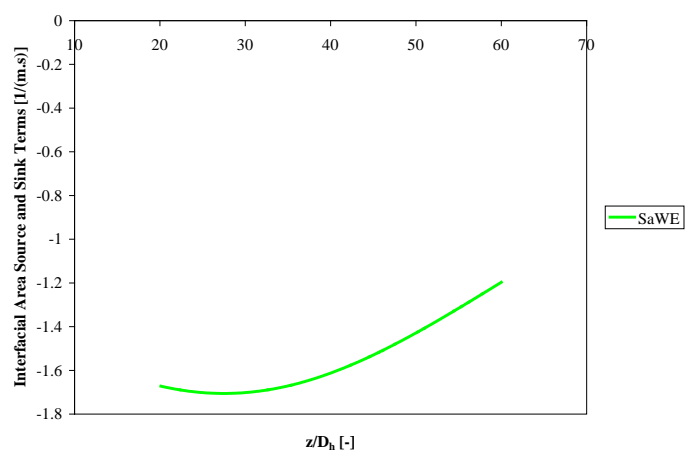
Fig. 5.14: Interfacial area source and sink terms for test conditions of Takamasa et al. [25]

for (a) Run 4, (b) Run 5 and (c) Run 6.
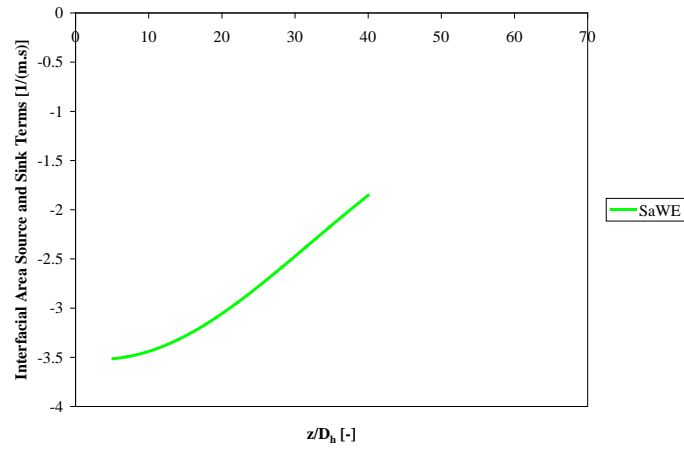
Fig. 5.15: Interfacial area source and sink terms for test conditions of Takamasa et al. [25]

for Run 7.

5.4 Evaluation of Two Group, Steady State, One Dimensional IATE under Reduced Gravity

In addition to the development of the one-group IATE which is applicable to bubbly flows, the two-group IATE was proposed by Wu et al. [54]. The preliminary work was performed by Hibiki and Ishii [55] for the interfacial area transport at the transition from bubbly to slug flow. Ishii et al. [56] also developed the framework for the two-group IATE.

In generalized gas-liquid two-phase flows, various types of the bubbles may exist depending on the flow conditions, the geometry and dimension of the flow channel. Most two-phase flow conditions include the spherical, distorted, cap, slug and churn-turbulent bubbles [59]. Such differences of bubbles in size and shape cause substantial differences in their transport phenomena. In view of their transport characteristics, the bubbles can be classified into two major groups. The spherical and distorted bubbles are considered as the Group-1 bubbles, while the Group-2 bubbles include the cap, slug and churn-turbulent bubbles [1].

In one-group transport equation, the shape of the particles and their transport phenomena are assumed to be similar over a range of particle volumes, and the transport equation is averaged by integrating it over volumes of particles of all sizes. In the two-group formulation, however, the integration limit for each group transport equation should be bounded by a certain fluid particle volume. Thus, a critical particle volume, V_c, should be defined to separate the bubble groups. For gas-liquid two-phase flows, V_c is the bubble volume corresponding to the maximum distorted bubble limit, $D_{d,\max}$, given by [60]

$$D_{d,\max} = 4\sqrt{\frac{\sigma}{g\Delta\rho}} \tag{5.27}$$

The bubble number density distribution function strongly depends on the flow conditions. However, in order to obtain analytical forms for the bubble interaction mechanisms, it is necessary to make some simplifications. Sun [59] assumed that the

bubble number density distribution functions f_1 and f_2 are uniform over the Group-1 bubble region and over the Group-2 bubble region, respectively, as shown schematically in Fig. 5.16. $V_{\min}$ is the volume for the minimum bubble in the system, and $V_{c,\max}$ is the volume of the maximum stable bubble given by [50]

$$D_{c,\max} = 40\sqrt{\frac{\sigma}{g\Delta\rho}} \tag{5.28}$$

Here, $D_{c,\max}$ provides an upper limit for the maximum bubble size, beyond which the bubbles disintegrate instantaneously. V_{m1} and V_{m2} are the maximum bubble volumes for the Group-1 and Group-2 bubbles, respectively, for a given flow condition, by assuming the uniform bubble number density distribution. V_c is the critical bubble volume which gives the boundary for the Group 1 and Group 2 bubbles, which is corresponding to $D_{d,\max}$, given by Equation 5.27.

By considering relevant inter- and intra-group interactions, Ishii and Kim [51] derived the following two-group IATE for adiabatic air-water system.

$$\frac{\partial a_{i1}}{\partial t} + \nabla \cdot (a_{i1}\vec{v}_{i1}) = \left(\frac{2}{3} - \chi D_{c1}^{*\,2}\right)\left(\frac{a_{i1}}{\alpha_{g1}}\right)\left(\frac{\partial \alpha_{g1}}{\partial t} + \nabla \cdot \alpha_{g1}\vec{v}_{g1} - \eta_{ph}\right) + \sum_j \phi_{j,1} \tag{5.28}$$

for Group-1 bubbles where χ is a coefficient accounting for the inter-group void transport at the group boundary due to expansion, compression and phase change, and should be bounded by 0 and 2 for various particle distributions [51], and

$$\begin{aligned}
\frac{\partial a_{i2}}{\partial t} + \nabla \cdot (a_{i2}\vec{v}_{i2}) &= \frac{2}{3}\left(\frac{a_{i2}}{\alpha_{g2}}\right)\left(\frac{\partial \alpha_{g2}}{\partial t} + \nabla \cdot \alpha_{g2}\vec{v}_{g2}\right) \\
&\quad + \chi D_{c1}^{*\,2}\left(\frac{a_{i1}}{\alpha_{g1}}\right)\left(\frac{\partial \alpha_{g1}}{\partial t} + \nabla \cdot \alpha_{g1}\vec{v}_{g1} - \eta_{ph}\right) + \sum_j \phi_{j,2}
\end{aligned} \tag{5.29}$$

for Group 2 bubbles, where D_{c1}^{*} is defined as follows,

$$\frac{D_{c1}}{D_{s1}} \approx \frac{D_{c1}}{D_{sm1}} = D_{c1}^{*} \tag{5.30}$$

where D_{c1} is defined as volume equivalent diameter of volume V_c. However, the surface area-equivalent and volume-equivalent diameters are the same. ϕ_j is the interfacial area
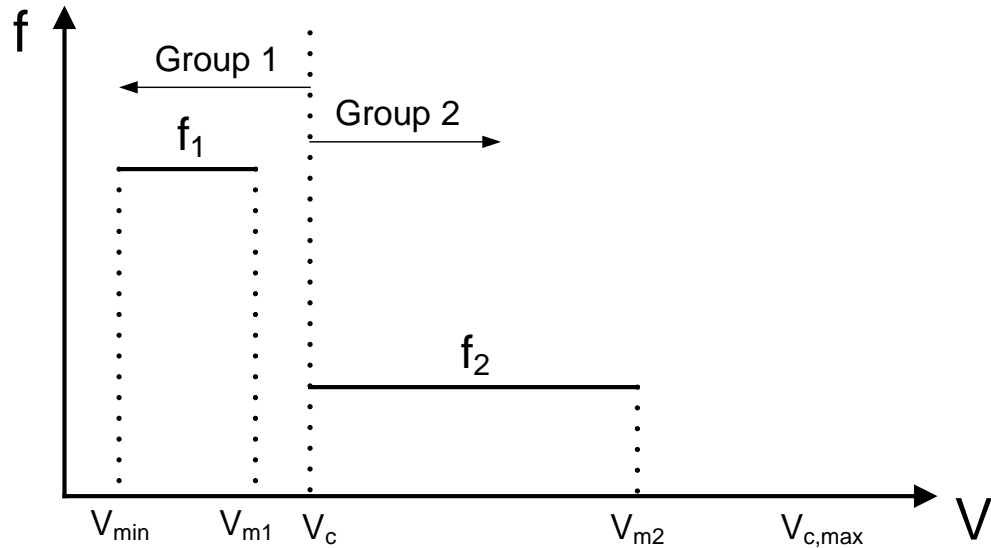
Fig. 5.16: Schematic of simplified bubble number density distribution function [59].

concentration source/sink due to bubble interactions. The subscripts of 1 and 2 denote the contribution to Group 1 and Group 2 bubbles, respectively.

In order to solve the IATE, the source/sink terms should be established through the theoretical modeling of particle interaction mechanisms. Sun [59] summarized the major bubble interaction mechanisms such as the turbulent impact, random collision, wake entrainment, shearing-off, and surface instability. Table 5.3 summarizes the inter- and intra-group bubble interaction mechanisms for the two-group IATE. Fig. 5.17 shows the schematic view of the bubble interaction mechanisms for the two-group IATE.

Table 5.3: Summary of Inter- and Intra-Group Bubble Interaction Mechanisms [59]

Notation	Mechanisms	Contribution	Remarks
$R_{TI}^{(1)}$	Turbulent impact	$(1) \rightarrow (1) + (1)$	Source in 1
$R_{TI}^{(2,11)}$	Turbulent impact	$(2) \rightarrow (1) + (1)$	Source in 1 Sink in 2
$R_{TI}^{(2,12)}$	Turbulent impact	$(2) \rightarrow (1) + (2)$	Source in 1 Sink in 2 (no number change)
$R_{TI}^{(2)}$	Turbulent impact	$(2) \rightarrow (2) + (2)$	Source in 2
$R_{RC}^{(1)}$	Random collision	$(1) + (1) \rightarrow (1)$	Sink in 1
$R_{RC}^{(11,2)}$	Random collision	$(1) + (1) \rightarrow (2)$	Sink in 1 Source in 2
$R_{RC}^{(12,2)}$	Random collision	$(1) + (2) \rightarrow (2)$	Sink in 1 Source in 2 (no number change)
$R_{RC}^{(2)}$	Random collision	$(2) + (2) \rightarrow (2)$	Sink in 2
$R_{WE}^{(1)}$	Wake entrainment	$(1) + (1) \rightarrow (1)$	Sink in 1
$R_{WE}^{(11,2)}$	Wake entrainment	$(1) + (1) \rightarrow (2)$	Sink in 1 Source in 2
$R_{RC}^{(12,2)}$	Wake entrainment	$(1) + (2) \rightarrow (2)$	Sink in 1 Source in 2 (no number change)
$R_{WE}^{(2)}$	Wake entrainment	$(2) + (2) \rightarrow (2)$	Sink in 2
$R_{SO}^{(2,12)}$	Shearing-off	$(2) \rightarrow (2) + N(1)$	Source in 1 (multiple number) Sink in 2 (no number change)
$R_{SI}^{(2)}$	Surface instability	$(2) + (2) \rightarrow (2)$	Source in 2
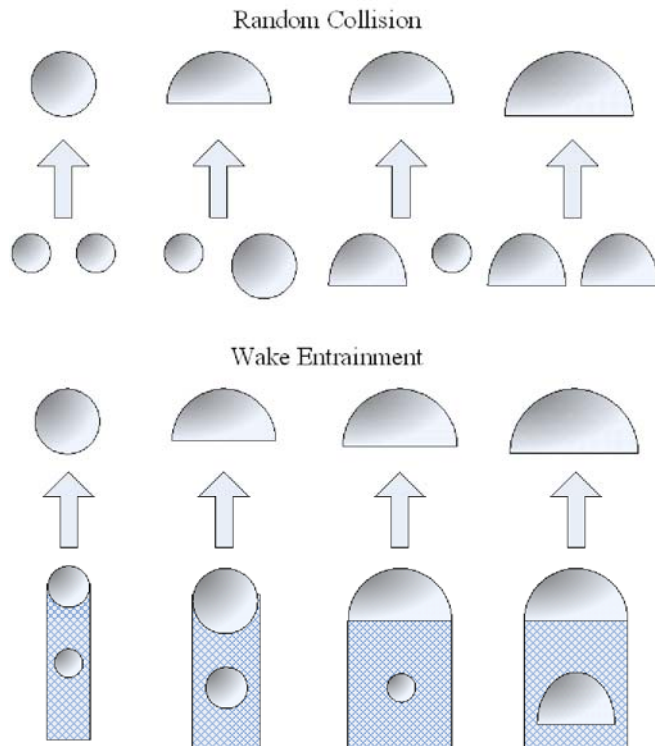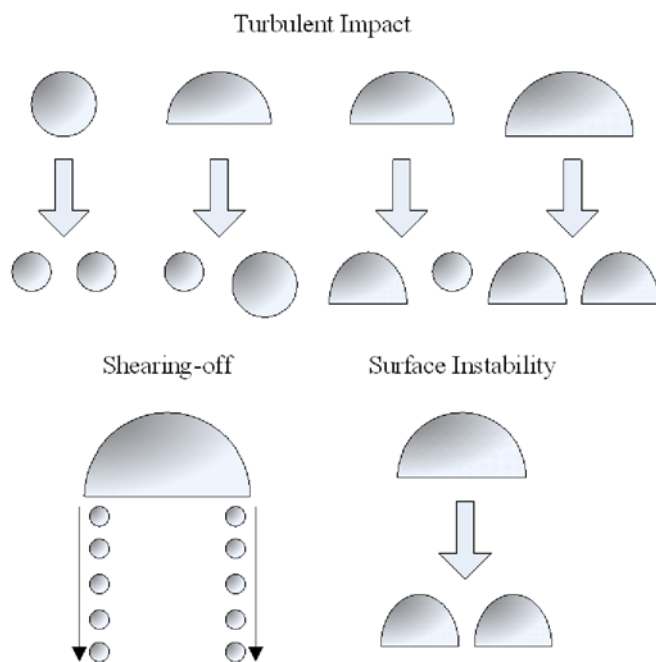
Fig. 5.17: Schematic of two-group bubble interaction [56]

When developing the two-group IATE, Sun [59] considered following mechanisms as source/sink terms for the individual groups.

(1) Random collision: the coalescence due to random collision driven by turbulence

(2) Wake entrainment: the coalescence due to wake entrainment

(3) Turbulent impact: the breakup due to the impact of turbulent eddies

(4) Shearing-off: the breakup due to the shearing-off from a large bubble

(5) Surface instability: the breakup of a large cap bubble due to the flow instability on the bubble surface

The interfacial area source/sink terms for the Group-1 bubbles are summarized in the following. The expansion source/sink term for the Group-1 bubbles is given by the following form

$$\phi_{EXP,1} = -\left(\frac{2}{3} - \chi D_{c1}^{*2}\right)\left(\frac{a_{i1}}{\alpha_{g1}}\right)\left(\frac{\Delta \dot{m}_{12}}{\rho_g} + \frac{\alpha_{g1}\bar{v}_{g1}}{p}\cdot\nabla p\right) \tag{5.31}$$

The coefficient χ accounts for the effect of the inter-group transport at the group boundary. The random collision source/sink terms for the Group-1 bubbles are given by

$$\phi_{RC}^{(1)} = -0.17 C_{RC}^{(1)} \frac{\varepsilon^{1/3} \alpha_{g1}^{1/3} a_{i1}^{5/3}}{\alpha_{g1,\max}^{1/3}(\alpha_{g1,\max}^{1/3} - \alpha_{g1}^{1/3})}\left[1 - \exp\left(-C_{RC1}\frac{\alpha_{g1,\max}^{1/3}\alpha_{g1}^{1/3}}{\alpha_{g1,\max}^{1/3} - \alpha_{g1}^{1/3}}\right)\right] \tag{5.32}$$

$$\phi_{RC,1}^{(12,2)} = -4.85 C_{RC}^{(12,2)} \varepsilon^{1/3} \frac{a_{i1}\alpha_{g1}^{2/3}\alpha_{g2}^2}{R_{2,\max}^{2/3}}\left[1 - \exp\left(-C_{RC1}\frac{\alpha_{g1,\max}^{1/3}\alpha_{g1}^{1/3}}{\alpha_{g1,\max}^{1/3} - \alpha_{g1}^{1/3}}\right)\right] \tag{5.33}$$

where $R_{2,\max}$ is the radius of curvature of the maximum bubble in the system. The wake entrainment source/sink terms for the Group-1 bubbles are given by

$$\phi_{WE}^{(1)} = -0.27 C_{WE}^{(1)} \bar{v}_{r1} C_{D1}^{1/3} a_{i1}^2 \tag{5.34}$$

$$\phi_{WE,1}^{(12,2)} = -4.35 C_{WE}^{(12,2)} \sqrt{g C_{D2} G} \frac{a_{i1}\alpha_{g2}}{R_{2,\max}} \tag{5.35}$$

where C_{D1} and C_{D2} are the drag force coefficient for Group-1 and the Group-2 bubbles, respectively, which were obtained by Ishii and Chawla [61] and Ishii and Zuber [62], and u_r is the relative velocity between liquid and gas phase.

The turbulent impact source/sink terms for the Group-1 bubbles are given by

$$\phi_{TI}^{(1)} = \begin{cases} 0.12C_{TI}^{(1)}\varepsilon^{1/3}\left(1-\alpha_g\right)\dfrac{a_{i1}^{5/3}}{\alpha_{g1}^{2/3}}\exp\left(-\dfrac{We_{c,TI1}}{We_1}\right)\sqrt{1-\dfrac{We_{c,TI1}}{We_1}}\ , \ We_1 > We_{c,TI1} \\ 0\ , \ We_1 < We_{c,TI1} \end{cases} \tag{5.36}$$

$$\phi_{TI,1}^{(2,1)} = 2.71C_{TI}^{(2)}\alpha_{g2}\left(1-\alpha_g\right)\dfrac{\varepsilon^{1/3}G^{2/3}R_c^{*5/3}\left(1-R_c^{*5/3}\right)}{R_{2,\max}^{7/3}}\exp\left(-\dfrac{We_{c,TI2}}{We_2}\right)\sqrt{1-\dfrac{We_{c,TI2}}{We_2}} \tag{5.37}$$

where R_c^* is the critical dimensionless radius given by

$$R_c^* = \dfrac{R_{c1}}{R_{2,\max}} \tag{5.38}$$

The shearing-off source term for the Group-1 bubbles are given by

$$\phi_{SO,1}^{(2,12)} = 64.51C_{SO}C_d^2\dfrac{\alpha_{g2}\bar{v}_{rb}}{GR_{2,\max}}\left[1-\left(-\dfrac{We_{c,SO}}{We_{2,\max}}\right)^3\right] \tag{5.39}$$

where $\bar{v}_{rb}$ is the relative velocity of the large bubble with respect to the liquid film near the cap bubble base, and $We_{2,\max}$ is defined by

$$We_{2,\max} \equiv \dfrac{2\rho_f\bar{v}_{rb}^2R_{2,\max}}{\sigma} \tag{5.40}$$

The interfacial area source/sink terms for the Group-2 bubbles are summarized in the followings. The expansion source/sink term for the Group-2 bubbles is given by the following form

$$\phi_{EXP,2} = \dfrac{2}{3}\left(\dfrac{a_{i2}}{\alpha_{g2}}\right)\left(\dfrac{\Delta\dot{m}_{12}}{\rho_g}-\dfrac{\alpha_{g2}\bar{v}_{g2}}{p}\cdot\nabla p\right) - \chi D_{c1}^{*2}\left(\dfrac{a_{i1}}{\alpha_{g1}}\right)\left(\dfrac{\Delta\dot{m}_{12}}{\rho_g}+\dfrac{\alpha_{g1}\bar{v}_{g1}}{p}\cdot\nabla p\right) \tag{5.41}$$

The random collision source/sink terms for the Group-2 bubbles are given by

$$\phi_{RC,2}^{(11,2)} = 0.68 C_{RC}^{(1)} \varepsilon^{1/3} \frac{\alpha_{g1}^2 a_{i1}^{2/3}}{\alpha_{g1,max}^{2/3} G} \left[1 - \exp\left(-C_{RC1} \frac{\alpha_{g1,max}^{1/3} \alpha_{g1}^{1/3}}{\alpha_{g1,max}^{1/3} - \alpha_{g1}^{1/3}} \right) \right]$$
$$\times \left[1 + 0.7 G^{7/6} \sqrt{\frac{a_{i1}}{\alpha_{g1}}} \left(\frac{\sigma}{g\Delta\rho} \right)^{-1/3} \right] \left(1 - \frac{2}{3} D_{c1}^* \right) \text{ for } D_{c1}^* < 1.5 \tag{5.42}$$

$$\phi_{RC,2}^{(12,2)} = 13.6 C_{RC}^{(12,2)} \varepsilon^{1/3} \frac{a_{i1}\alpha_{g1}^{5/3}\alpha_{g2}^2}{R_{2,max}^{2/3} G} \left(1 + \frac{10.3G}{R_{2,max}} \right) \left[1 - \exp\left(-C_{RC1} \frac{\alpha_{g1,max}^{1/3} \alpha_{g1}^{1/3}}{\alpha_{g1,max}^{1/3} - \alpha_{g1}^{1/3}} \right) \right] \tag{5.43}$$

$$\phi_{RC}^{(2)} = -13.6 C_{RC}^{(2)} \frac{\alpha_{g2}^2 \varepsilon^{1/3}}{W^2 G} R_{2,max}^{4/3} \left(1 - 2.0 R_c^{*2} + \frac{9.0G}{R_{2,max}} \right) \left[1 - \exp\left(-C_{RC2} \alpha_{g2}^{1/2} \right) \right] \tag{5.44}$$

The wake entrainment source/sink terms for the Group-2 bubbles are given by

$$\phi_{WE,2}^{(11,2)} = 1.08 C_{WE}^{(11,2)} \vec{v}_{r1} C_{D1}^{1/3} \frac{\alpha_{g1} a_{i1}}{G} \left(1 - \frac{2}{3} D_{c1}^* \right)$$
$$\times \left[1 + 0.7 G^{7/6} \left(\frac{a_{i1}}{\alpha_{g1}} \right)^{1/2} \left(\frac{\sigma}{g\Delta\rho} \right)^{-1/3} \right] \text{ for } D_{c1}^* < 1.5 \tag{5.45}$$

$$\phi_{WE,2}^{(12,2)} = 26.1 C_{WE}^{(12,2)} \alpha_{g1}\alpha_{g2} \sqrt{\frac{gC_{D2}}{G}} \frac{1}{R_{2,max}} \left(1 + 4.31 \frac{G}{R_{2,max}} \right) \tag{5.46}$$

$$\phi_{WE}^{(2)} = -15.9 C_{WE}^{(2)} \frac{\alpha_{g2}^2}{R_{2,max}^2} \sqrt{gC_{D2}G} \left(1 + 0.51 R_c^* \right) \tag{5.47}$$

The turbulent impact source term for the Group-2 bubbles is given by

$$\phi_{TI,2}^{(2)} = 1.4 C_{TI}^{(2)} \alpha_{g2} \frac{\varepsilon^{1/3} G}{R_{2,max}^{8/3}} \left(1 - \alpha_g \right) \left(1 - 2R_c^* \right) \exp\left(-\frac{We_{c,TI2}}{We_2} \right) \sqrt{1 - \frac{We_{c,TI2}}{We_2}} \tag{5.48}$$

The shearing-off sink term for the Group-2 bubbles is given by

$$\phi_{SO,2}^{(2,12)} = -21.50 C_{SO} C_d^3 \left(\frac{\sigma}{\rho_f} \right)^{3/5} \frac{\alpha_{g2}}{\vec{v}_{rb}^{1/5} G^{8/5} R_{2,max}}$$
$$\times \left[1 - \left(-\frac{We_{c,SO}}{We_{2,max}} \right)^3 + \frac{3.24G}{R_{2,max}} \left\{ 1 - \left(\frac{We_{c,SO}}{We_{2,max}} \right)^3 \right\} \right] \tag{5.49}$$

And the surface instability source term for the Group-2 bubbles is given by

$$\phi_{SI}^{(2)} = 1.25\alpha_{g2}\left(\frac{\sigma}{g\Delta\rho}\right)^{-1}\left[C_{RC}^{(2)}\frac{\varepsilon^{1/3}}{W^2}\left(\frac{\sigma}{g\Delta\rho}\right)^{7/6}\right.$$
$$\left.\times\left\{1-\exp\left(-C_{RC2}\alpha_{g2}^{1/2}\right)\right\}+2.3\times10^{-4}C_{WE}^{(2)}\sqrt{C_{D2}gG}\right]$$
(5.50)

The inter-group void fraction transport from Group-1 to the Group-2 bubbles, $\eta_{j,2}$, for specifying the mass transfer rate should be established as well. The random collision void source terms for the Group-2 bubbles are given by

$$\eta_{RC,2}^{(11,2)} = 3.4C_{RC}^{(1)}\frac{\varepsilon^{1/3}\alpha_{g1}^2 a_{i1}^{2/3}}{\alpha_{g1,\max}^{2/3}}\left[1-\exp\left(-C_{RC1}\frac{\alpha_{g1,\max}^{1/3}\alpha_{g1}^{1/3}}{\alpha_{g1,\max}^{1/3}-\alpha_{g1}^{1/3}}\right)\right]\left(1-\frac{2}{3}D_{c1}^*\right)$$
(5.51)

for $D_{c1}^* < 1.5$

$$\eta_{RC,2}^{(12,2)} = 4.85C_{RC}^{(12,2)}\varepsilon^{1/3}\frac{\alpha_{g1}^{5/3}\alpha_{g2}^2}{R_{2,\max}^{2/3}}\left[1-\exp\left(-C_{RC1}\frac{\alpha_{g1,\max}^{1/3}\alpha_{g1}^{1/3}}{\alpha_{g1,\max}^{1/3}-\alpha_{g1}^{1/3}}\right)\right]$$
(5.52)

The wake entrainment void source terms for the Group-2 bubbles are given by

$$\eta_{WE,2}^{(11,2)} = 5.40C_{WE}^{(11,2)}\vec{v}_{r1}C_{D1}^{1/3}\alpha_{g1}a_{i1}\left(1-\frac{2}{3}D_{c1}^*\right)\text{ for }D_{c1}^* < 1.5$$
(5.53)

$$\eta_{WE,2}^{(12,2)} = 4.35C_{WE}^{(12,2)}\sqrt{gC_{D2}G}\frac{\alpha_{g1}\alpha_{g2}}{R_{2,\max}}$$
(5.54)

The turbulent impact void source term for the Group-2 bubbles is given by

$$\eta_{TI,2}^{(2,1)} = -0.34C_{TI}^{(2)}\alpha_{g2}\left(1-\alpha_g\right)\frac{G\varepsilon^{1/3}R_c^{*7/3}\left(1-2R_c^{*5/3}\right)}{R_{2,\max}^{5/3}}\exp\left(-\frac{We_{c,TI2}}{We_2}\right)\sqrt{1-\frac{We_{c,TI2}}{We_2}}$$
(5.55)

And the shearing-off void source term for the Group-2 bubbles is given by

$$\eta_{SO,2}^{(2,12)} = -10.75C_{SO}C_d^3\left(\frac{\sigma}{\rho_f G}\right)^{3/5}\frac{\alpha_{g2}}{\vec{v}_{rb}^{1/5}R_{2,\max}}\left[1-\left(-\frac{We_{c,SO}}{We_{2,\max}}\right)^3\right]$$
(5.56)

In addition to Equation 5.51 through 5.56, the expansion void source from Group-1 bubbles to Group-2 bubbles to determine the mass transfer term is given as

$$\eta_{EXP} = -\chi\left(D_{c1}^*\right)^3\frac{\alpha_{g1}\vec{v}_{g1}}{p}\cdot\nabla p$$
(5.57)

As can be seen in Equation 5.31 through 5.57, there are several model coefficients in the source and sink terms of the two-group IATE which should be determined based on the experiment. These model coefficients and constants are summarized in Table 5.4. All model coefficients and constants are kept the same as those given by Sun [59]. The volume sources for the Group-2 bubbles due to the intra-group transfer and their coefficients are summarized in Table 5.5 as well.

The evaluation of two-group, steady state, one-dimensional IATE under reduced gravity conditions is ongoing.

Table 5.4: Summary of Coefficients and Constants for Source and Sink Terms of IATE [59].

Mechanisms	Source & Sink Terms		Coefficients/Constants
Expansion	Group-1	$\phi_{EXP,1}$	
	Group-2	$\phi_{EXP,2}$	
Random Collision	Group-1	$\phi_{RC}^{(1)}$	$C_{RC}^{(1)} = 0.005$, $C_{RC1} = 3.0$, $\alpha_{g1,\max} = 0.62$
		$\phi_{RC,1}^{(12,2)}$	$C_{RC}^{(12,2)} = 0.005$, $C_{RC1} = 3.0$, $\alpha_{g1,\max} = 0.62$
	Group-2	$\phi_{RC,2}^{(11,2)}$	$C_{RC}^{(1)} = 0.005$, $C_{RC1} = 3.0$, $\alpha_{g1,\max} = 0.62$
		$\phi_{RC,2}^{(12,2)}$	$C_{RC}^{(12,2)} = 0.005$, $C_{RC1} = 3.0$, $\alpha_{g1,\max} = 0.62$
		$\phi_{RC}^{(2)}$	$C_{RC}^{(2)} = 0.005$, $C_{RC2} = 3.0$
Wake Entrainment	Group-1	$\phi_{WE}^{(1)}$	$C_{WE}^{(1)} = 0.002$
		$\phi_{WE,1}^{(12,2)}$	$C_{WE}^{(12,2)} = 0.002$
	Group-2	$\phi_{WE,2}^{(11,2)}$	$C_{WE}^{(11,2)} = 0.002$
		$\phi_{WE,2}^{(12,2)}$	$C_{WE}^{(12,2)} = 0.002$
		$\phi_{WE}^{(2)}$	$C_{WE}^{(2)} = 0.005$
Turbulent Impact	Group-1	$\phi_{TI}^{(1)}$	$C_{TI}^{(1)} = 0.1$, $We_{c,TI1} = 6.5$
		$\phi_{TI,1}^{(2,1)}$	$C_{TI}^{(2)} = 0.02$, $We_{c,TI2} = 7.0$
	Group-2	$\phi_{TI,2}^{(2)}$	$C_{TI}^{(2)} = 0.02$, $We_{c,TI2} = 7.0$
Shearing-Off	Group-1	$\phi_{SO,1}^{(2,12)}$	$C_{SO} = 3.8 \times 10^{-5}$, $C_d = 4.8$, $We_{c,SO} = 4500$
	Group-2	$\phi_{SO,2}^{(2,12)}$	$C_{SO} = 3.8 \times 10^{-5}$, $C_d = 4.8$, $We_{c,SO} = 4500$
Surface Instability	Group-2	$\phi_{SI}^{(2)}$	$C_{RC}^{(2)} = 0.005$, $C_{WE}^{(2)} = 0.005$

Table 5.5: Summary of Coefficients and Constants for Source and Sink Terms of Void
Source due to Intra-Group Transfer [59].

Mechanisms	Source & Sink Terms	Coefficients/Constants
Expansion	η_{EXP}	
Random Collision	$\eta_{RC,2}^{(11,2)}$	$C_{RC}^{(1)} = 0.005$, $C_{RC1} = 3.0$, $\alpha_{g1,\max} = 0.62$
	$\eta_{RC,2}^{(12,2)}$	$C_{RC}^{(12,2)} = 0.005$, $C_{RC1} = 3.0$, $\alpha_{g1,\max} = 0.62$
Wake Entrainment	$\eta_{WE,2}^{(11,2)}$	$C_{WE}^{(11,2)} = 0.002$
	$\eta_{WE,2}^{(12,2)}$	$C_{WE}^{(12,2)} = 0.002$
Turbulent Impact	$\eta_{TI,2}^{(2,1)}$	$C_{TI}^{(2)} = 0.02$, $We_{c,TI2} = 7.0$
Shearing-Off	$\eta_{SO,2}^{(2,12)}$	$C_{SO} = 3.8 \times 10^{-5}$, $C_d = 4.8$, $We_{c,SO} = 4500$

6. SUMMARY, CONCLUSIONS AND FUTURE WORK

Study of gas-liquid two-phase flows under reduced gravity conditions is extremely important. One of the major applications of gas-liquid two-phase flows under reduced gravity conditions is in the design of active thermal control systems for future space applications. Previous space crafts were characterized by low heat generation within the spacecraft which needed to be redistributed within the craft or rejected to space. This task could easily have been accomplished by pumped single-phase loops or passive systems such as heat pipes and so on. However with increase in heat generation within the space craft as predicted for future missions, pumped boiling two-phase flows are being considered. This is because of higher heat transfer co-efficients associated with boiling heat transfer among other advantages. Two-phase flows under reduced gravity conditions also find important applications in space propulsion as in space nuclear power reactors as well as in many other life support systems of space crafts.

Two-fluid model along with Interfacial Area Transport Equation (IATE) is a useful tool available to predict the behavior of gas-liquid two-phase flows under reduced gravity conditions. It should be noted that considerable differences exist between two-phase flows under reduced and normal gravity conditions especially for low inertia flows. This is because due to suppression of the gravity field the gas-liquid two-phase flows take a considerable time to develop under reduced gravity conditions as compared to normal gravity conditions. Hence other common methods of analysis applicable for fully developed gas-liquid two-phase flows under normal gravity conditions, like flow regimes and flow regime transition criteria, will not be applicable to gas-liquid two-phase flows under reduced gravity conditions.

However the two-fluid model and the IATE need to be evaluated first against detailed experimental data obtained under reduced gravity conditions. Although lot of studies have been done in the past to understand the global structure of gas-liquid two-phase flows under reduced gravity conditions, using experimental setups aboard drop towers or aircrafts flying parabolic flights, detailed data on local structure of such two-phase flows are extremely rare.

Hence experiments were carried out in a 304 mm inner diameter (ID) test facility on earth. Keeping in mind the detailed experimental data base that needs to be generated to evaluate two-fluid model along with IATE, ground based simulations provide the only economic path. Here the reduced gravity condition is simulated using two-liquids of similar densities (water and Therminol 59 ® in the present case). Only adiabatic two-phase flows were concentrated on at this initial stage. Such a large diameter test section was chosen to study the development of drops to their full extent (it is to be noted that under reduced gravity conditions the stable bubble size in gas-liquid two-phase flows is much larger than that at normal gravity conditions). Twelve flow conditions were chosen around predicted bubbly flow to cap-bubbly flow transition region. Detailed local data was obtained at ten radial locations for each of three axial locations using state-of-the art multi-sensor conductivity probes. The results are presented and discussed. Also one-group as well as two-group, steady state, one-dimensional IATE was evaluated against data obtained here and by other researchers, and the results presented and discussed.

Some of the differences between normal gravity and reduced gravity two-phase flows were highlighted from the experimental results. Like although widely accepted flow regime transition criteria do not predict the existence of Group 2 drops a large number of them were found. This is because of the fact that low inertia gas-liquid two-phase flows do not develop so quickly under reduced gravity environments. This means that the entrance effects persist for a long flow length. And a lot of big droplets were observed at the inlet of the current test facility for almost all flow conditions.

Now an extensive database of global and local two-phase flow parameters has been generated in test sections of two different inner diameters: 25.4 mm and 304 mm. This is extremely useful for evaluating two-fluid model along with IATE. One-group and

two-group, steady state, one-dimensional IATE evaluation has already been started as presented and discussed in an earlier chapter. Models for mechanisms of interfacial area generation or destruction should be reevaluated, in the light of the results presented, to lessen the little discrepancies that presently exist between the predicted and measured values of interfacial area concentration. One can then take up the task to evaluate three-dimensional two-fluid model along with one- or two-group IATE using a commercially available CFD code and compare the results with the detailed local data already obtained experimentally. This is currently being done for normal gravity gas-liquid two-phase flows.

BIBLIOGRAPHY

BIBLIOGRAPHY

1. M. Ishii and T. Hibiki, *Thermo-fluid dynamic theory of two-phase flow*. Springer, New York, 2006.

2. K. S. Gabriel, *Microgravity two-phase flow and heat transfer.* Springer, A A Dordrecht, 2007.

3. D. G. Gilmore, *Spacecraft thermal control handbook Volume I: Fundamental technologies.* The Aerospace Press, El Segundo, 2002.

4. Space Studies Board, National Research Council. *Microgravity research in support of technologies for the human exploration and development of space and planetary bodies.* National Academy Press, Washington, D.C., 2000.

5. K. S. Rezkallah, Two-phase flow and heat transfer at reduced gravity: a literature survey, *ANS Proceedings of 1988 National Heat Transfer Conference* (1988).

6. I. Y. Chen, E. K. Ungar, D. Y. Lee and P. S. Beckstrom, Prototype test article verification of the Space Station Freedom active thermal control system microgravity performance, *AIAA Proceedings of the 28th Thermophysics Conference* (1993).

7. I. Y. Chen, R. Duffy, S. Paramanathan, J. Goepp and J. Cornwell, Space Station Freedom two-phase integrated thermal system flight test article design and analysis, *AIAA Proceedings of the 32nd Aerospace Sciences Meeting and Exhibit* (1994).

8. T. R. Reinarts, E. K. Ungar and T. D. Mai, Gravity independent two-phase flow quality transients: experiments and modeling, *AIAA Proceedings of the 33rd Aerospace Sciences Meeting and Exhibit* (1995).

9. E. K. Ungar, Single phase vs. two-phase active thermal control systems for space applications: a trade study, *AIAA Proceedings of the 33rd Aerospace Sciences Meeting and Exhibit* (1995).

10. S. Vasavada, X. Sun, and M. Ishii. Technical progress report on study of two-fluid model and interfacial area transport in microgravity condition. Technical Report PU/NE 04-11, Purdue University, 2004.

11. S. Vasavada, X. Sun, and M. Ishii. Technical progress report on study of two-fluid model and interfacial area transport in microgravity condition. Technical Report PU/NE 05-06, Purdue University, 2005.

12. S. Vasavada, X. Sun, and M. Ishii. Technical progress report on study of two-fluid model and interfacial area transport in microgravity condition. Technical Report PU/NE 07-12, Purdue University, 2007.

13. S. Vasavada, X. Sun, and M. Ishii. Technical progress report on study of two-fluid model and interfacial area transport in microgravity condition. Technical Report PU/NE 08-07, Purdue University, 2008.

14. M. Ishii, X. Sun, S. Vasavada and T. Roy. Technical progress report on study of two-fluid model and interfacial area transport in microgravity condition. Technical Report PU/NE-10-03, Purdue University, 2010.

15. D. B. Hepner, C. D. King and J. W. Littles, Zero-G experiments in two-phase fluid flow regimes, *ASME Paper 75-ENAs-24* (1975).

16. A. E. Dukler, J. A. Fabre, J. B. McQuillen and R. Vernon, Gas-liquid flow at microgravity conditions: flow patterns and their transitions, *International Journal of Multiphase Flow*, Vol. 14, No. 4, pp. 389-400, 1988.

17. C. Colin, J. Fabre and A. E. Dukler, Gas-liquid flow at microgravity conditions – I, *International Journal of Multiphase Flow*, Vol. 17, No. 4, pp. 533-544, 1991.

18. L. Zhao and K. S. Rezkallah, Gas-liquid flow patterns at microgravity conditions, *International Journal of Multiphase Flow*, Vol. 19, No. 5, pp. 751-763, 1993.

19. K. J. Elkow and K. S. Rezkallah, Void fraction measurements in gas-liquid flows under 1-g and μ-g conditions using capacitance sensors, *International Journal of Multiphase Flow*, Vol. 23, No. 5, pp. 815-829, 1997.

20. K. J. Elkow and K. S. Rezkallah, Statistical analysis of void fluctuations in gas-liquid flows under 1-*g* and *μ-g* conditions using a capacitance sensor, *International Journal of Multiphase Flow*, Vol. 23, No. 5, pp. 831-844, 1997.

21. D. C. Lowe and K. S. Rezkallah, Flow regime identification in microgravity two-phase flows using void fraction signals, *International Journal of Multiphase Flow*, Vol. 25, pp. 433-457, 1999.

22. W. S. Bousman, J. B. McQuillen and L.C. Witte, Gas-liquid flow patterns in microgravity: effects of tube diameter, liquid viscosity and surface tension, *International Journal of Multiphase Flow*, Vol. 22, No. 6, pp. 1035-1053, 1996.

23. K. S. Rezkallah, Weber number based flow-pattern maps for liquid-gas flows at microgravity, *International Journal of Multiphase Flow*, Vol. 22, No. 6, pp. 1265-1270, 1996.

24. B. Choi, T. Fujii, H. Asano and K. Sugimoto, A study of flow characteristics in air-water two-phase flow under microgravity (Results of flight experiments), *JSME International Journal: Series B,* Vol. 46, No. 2, pp. 262-269, 2003.

25. T. Takamasa, T. Iguchi, T. Hazuku, T. Hibiki and M. Ishii, Interfacial area transport of bubbly flow under microgravity environment, *International Journal of Multiphase Flow*, Vol. 29, pp. 291-304, 2003.

26. S. Vasavada, X. Sun, M. Ishii and W. Duval, Study of two-phase flows in reduced gravity using ground based experiments, *Experiments in Fluids,* Vol. 43, pp. 53-75, 2007.

27. T. Hibiki, T. Takamasa, M. Ishii and K. S. Gabriel, One-dimensional drift flux model at reduced gravity conditions, *AIAA Journal,* Vol. 44, No. 7, pp. 1635-1642, 2006.

28. T. Hibiki, T. Hazuku, T. Takamasa and M. Ishii, Interfacial-area transport equation at reduced-gravity conditions, *AIAA Journal,* Vol. 47, No. 5, pp. 1123-1131, 2009.

29. S. Vasavada, X. Sun, M. Ishii and W. Duval, Benchmarking of the one-dimensional one-group interfacial area transport equation for reduced gravity bubbly flows, *International Journal of Multiphase Flow*, Vol. 35, pp. 323-334, 2009.

30. T.K. Lovell. Liquid-vapor flow regime transition for use in the design of heat transfer loops in spacecraft: An investigation of two phase flow in zero gravity conditions. Technical Report TR-85-3021, AFWAL (Air Force Wright Aeronautical Labs), 1985.

31. E.K. Ungar, I.Y. Chen, and S.H. Chan. Selection of a gravity insensitive ground test fluid and test configuration to allow simulation of two-phase flow in microgravity. In *Proceedings of 7th AIAA/ASME Joint Thermophysics and Heat Transfer Conference*, number 3, 1996.

32. T.R. Nigmatulin, F.J. Bonetto, A.E. Larreteguy, R.T. Lahey Jr., and J.B. Mc-Quillen, An experimental study of dispersed liquid/liquid two-phase upflow in a pipe, *Chemical Engineering Communications*, Vol. 182, pp. 121–162, 2000.

33. G.P. Celata. Flow boiling heat transfer in microgravity. In T. Kunugi and Z. Kawara, editors, *Proceedings of International Seminar on Multiphase Flow Phenomena*, pages 1–17, Kyoto, Japan, September 2006.

34. S. Kim, X. Y. Fu, X. Wang, and M. Ishii. Development of the miniaturized four-sensor conductivity probe and the signal processing scheme. *International Journal of Heat and Mass Transfer*, 43:4101–4118, 2000.

35. N. Rashidnia, R. Balasubramaniam, and D. Del Signore. Interfacial tension measurement of immiscible liquids using a capillary tube. *AIChe Journal*, 38, 1992.

36. Wu, Q. and Ishii, M., 1999, Sensitivity study on double-sensor conductivity probe for the measurement of interfacial area concentration in bubbly flow, *International Journal of Multiphase Flow*, Vol. 25, No. 1, pp. 155-173.

37. K. Mishima and M. Ishii, Flow regime transition criteria for upward two-phase flow in vertical tubes, *International Journal of Heat and Mass Transfer*, 27, pp. 723-737, 1984.

38. M. Ishii, Thermo-fluid dynamic theory of two-phase flow, Eyrolles, Paris, 1975.

39. N. Zuber and J. A. Findlay, Average volumetric concentration in two-phase flow systems, *Journal of Heat Transfer*, 87, pp. 453, 1965.

40. M. Ishii, One-dimensional drift-flux model and constitutive relations for relative motion between phases in various two-phase flow regimes, ANL-77-47, 1977.

41. T. C. Chawla and M. Ishii, Equations of motion for two-phase flow in a pin bundle of a nuclear reactor, *International Journal of Heat and Mass Transfer*, 21, pp. 1057, 1978.

42. M. Ishii and N. Zuber, Drag coefficient and relative velocity in bubbly, droplet or particulate flows, *AIChE Journal*, 25, pp. 843, 1979.

43. M. Ishii and K. Mishima, Two-fluid model and hydrodynamic constitutive relations, *Nuclear Engineering and Design*, 82, pp. 107-126, 1984.

44. N. Zuber, On the dispersed two-phase flow on the laminar flow regime, *Chemical Engineering Science*, 19, pp. 897, 1964.

45. G. Kasturi and J. B. Stepanek, Two-phase flow-III. Interfacial area in cocurrent gas-liquid flow, *Chemical Engineering Science*, 29, pp. 713-719, 1974.

46. M. Ishii, K. Mishima, I. Kataoka, and G. Kocamustafogullari, Two-fluid model and importance of the interfacial area in two-phase flow analysis, Proc. 9th U.S. National Congress of Applied Mechanics, Ithaca, New York, June 21-25, 1982, pp. 73-80, 1982.

47. M. Ishii, Interfacial area in two-phase flow, ASME HTD-197, Two-phase and flow heat transfer, Book No. H00755-1992, pp. 1-5, 1992.

48. G. Kocamustafaogullari and M. Ishii, Foundations of the interfacial area transport equation and its closure relations, *International Journal of Heat and Mass Transfer*, 38, pp. 481-493, 1995.

49. J. N. Reyes, Statistically derived conservation equations for fluid particle flows, Proceedings of ANS-THD, 5, ANS Winter Meeting, San Francisco, pp. 12-19, 1989.

50. M. Ishii and G. Kojasoy, Interfacial area transport equation and preliminary considerations on closure relations, PU/NE-93-6, Report of School of Nuclear Engineering, Purdue University, West Lafayette, IN, USA, 1993.

51. M. Ishii and S. Kim, Interfacial area transport equation: two-group formulation, PU/NE-00-04, Report of School of Nuclear Engineering, Purdue University, West Lafayette, IN, USA, 2000.

52. Q. Wu, M. Ishii, and J. Uhle, Framework of two-group model for interfacial area transport equation in vertical two-phase flows, *Transactions of the American Nuclear Society*, 79, pp. 351-352, 1998.

53. S. Kim, Interfacial area transport equation and measurement of local interfacial characteristics, Ph.D. Thesis, Purdue University, West Lafayette, IN, USA, 1999.

54. Q. Wu, M. Ishii, and J. Uhle, Framework of two-group model for interfacial area transport equation in vertical two-phase flows, Trans. ANS, 79, pp. 351-352, 1998.

55. T. Hibiki and M. Ishii, Two-group interfacial area transport equations at bubbly-to-slug flow transition, *Nuclear Engineering and Design*, 202, pp. 39-76, 2000b.

56. M. Ishii, S. Kim, and J. Uhle, Interfacial area transport equation: model development and benchmark experiments, *International Journal of Heat and Mass Transfer*, 45, pp. 3111-3123, 2002.

57. M. Ishii, X. Sun, and S. Kim, Modeling strategy of the source and sink terms in the two-group interfacial area transport equation, *Annals of Nuclear Energy*, 30, pp. 1309-1331, 2003.

58. Q. Wu, S. Kim, M. Ishii, and S. G. Beus, One group interfacial area transport in vertical bubbly flow, *International Journal of Heat and Mass Transfer*, 41, pp. 1103-1112, 1998.

59. X. Sun, Two-Group Interfacial area transport equation for a confined test section, Ph.D. Thesis, Purdue University, West Lafayette, IN, USA, 2001.

60. G. Kocamustafaogullari, W. D. Huang, and J. Razi, Measurement and modeling of average void fraction, bubble size and interfacial area, *Nuclear Engineering and Design*, 148 (2/3), pp. 437-453, 1994.

61. M. Ishii and T. C. Chawla, Local drag laws in dispersed two-phase flow, Argonne National Laboratory Report, ANL-79-105, NUREG/GR-1230, 1979.

62. M. Ishii and N. Zuber, Drag coefficient and relative velocity in bubbly, droplet or particulate flows, *AIChE Journal*, 25, pp. 843, 1979.

APPENDICES

Appendix A: Local Data Tables

Table A.1: Values of local two-phase flow parameters at (a) z/D=1.7, (b) z/D=5.0 & (c) z/D=8.3; Run # 1

(a)

Radial Location	Number Of Drops		Dispersed Phase Fraction		Interfacial Area Concentration		Interface Velocity		Sauter Mean Diameter	
r/R	N_1	N_2	α_1	α_2	a_1	a_2	v_1	v_2	D_{sm1}	D_{sm2}
[-]	[-]	[-]	[-]	[-]	[1/m]	[1/m]	[m/s]	[m/s]	[m]	[m]
0.96	0	0	0.00E+00	0.00E+00	0.00E+00	0.00E+00	0.00E+00	0.00E+00	-	-
0.91	7	18	4.43E-04	2.68E-02	4.56E-01	3.67E+00	1.02E-01	7.74E-02	5.83E-03	4.38E-02
0.85	13	34	1.33E-03	6.07E-02	1.09E+00	9.04E+00	7.47E-02	7.43E-02	7.31E-03	4.03E-02
0.80	34	34	5.96E-03	5.43E-02	6.12E+00	1.12E+01	7.91E-02	7.50E-02	5.84E-03	2.90E-02
0.73	55	34	1.06E-02	4.80E-02	1.12E+01	1.34E+01	8.35E-02	7.57E-02	5.70E-03	2.15E-02
0.66	57	49	1.05E-02	7.36E-02	8.66E+00	2.28E+01	9.34E-02	6.95E-02	7.31E-03	1.93E-02
0.58	51	43	8.01E-03	5.67E-02	7.30E+00	1.32E+01	9.59E-02	8.41E-02	6.59E-03	2.58E-02
0.49	85	39	2.01E-02	5.31E-02	1.49E+01	1.36E+01	9.51E-02	8.65E-02	8.09E-03	2.34E-02
0.38	72	43	1.62E-02	5.54E-02	1.00E+01	1.42E+01	1.08E-01	8.77E-02	9.69E-03	2.34E-02
0.00	92	65	1.96E-02	8.00E-02	1.32E+01	2.04E+01	1.03E-01	9.15E-02	8.89E-03	2.35E-02

(b)

Radial Location	Number Of Drops		Dispersed Phase Fraction		Interfacial Area Concentration		Interface Velocity		Sauter Mean Diameter	
r/R	N_1	N_2	α_1	α_2	a_1	a_2	v_1	v_2	D_{sm1}	D_{sm2}
[-]	[-]	[-]	[-]	[-]	[1/m]	[1/m]	[m/s]	[m/s]	[m]	[m]
0.96	10	5	1.33E-03	7.15E-03	2.58E+00	2.65E+00	6.44E-02	5.52E-02	3.10E-03	1.62E-02
0.91	30	10	5.31E-03	1.28E-02	7.93E+00	4.15E+00	8.10E-02	8.58E-02	4.02E-03	1.85E-02
0.85	40	17	7.15E-03	2.76E-02	9.04E+00	7.70E+00	8.38E-02	6.05E-02	4.74E-03	2.15E-02
0.80	38	24	6.62E-03	3.72E-02	4.93E+00	1.08E+01	7.35E-02	5.24E-02	8.06E-03	2.06E-02
0.73	35	31	6.10E-03	4.67E-02	8.17E+00	1.08E+01	6.33E-02	4.43E-02	4.48E-03	2.59E-02
0.66	38	37	5.93E-03	5.22E-02	5.88E+00	1.40E+01	7.91E-02	7.23E-02	6.04E-03	2.24E-02
0.58	71	43	1.26E-02	5.73E-02	1.24E+01	1.48E+01	8.80E-02	7.83E-02	6.11E-03	2.32E-02
0.49	68	46	1.23E-02	5.80E-02	8.93E+00	1.37E+01	1.04E-01	8.19E-02	8.27E-03	2.54E-02
0.38	57	65	8.19E-03	7.69E-02	6.51E+00	1.60E+01	1.04E-01	9.89E-02	7.56E-03	2.88E-02
0.00	102	41	2.22E-02	5.21E-02	1.57E+01	1.17E+01	1.07E-01	1.00E-01	8.49E-03	2.68E-02

(c)

Radial Location	Number Of Drops		Dispersed Phase Fraction		Interfacial Area Concentration		Interface Velocity		Sauter Mean Diameter	
r/R	N_1	N_2	α_1	α_2	a_1	a_2	v_1	v_2	D_{sm1}	D_{sm2}
[-]	[-]	[-]	[-]	[-]	[1/m]	[1/m]	[m/s]	[m/s]	[m]	[m]
0.96	17	3	4.51E-03	4.07E-03	3.55E+00	9.88E-01	1.07E-01	9.69E-02	7.63E-03	2.47E-02
0.91	18	8	4.40E-03	1.38E-02	2.16E+00	2.30E+00	1.15E-01	7.81E-02	1.23E-02	3.58E-02
0.85	42	14	7.69E-03	1.99E-02	8.90E+00	5.06E+00	9.19E-02	8.87E-02	5.18E-03	2.35E-02
0.80	62	28	8.70E-03	3.45E-02	1.11E+01	8.55E+00	9.92E-02	8.94E-02	4.69E-03	2.42E-02
0.73	88	37	1.44E-02	4.74E-02	1.74E+01	1.50E+01	9.52E-02	8.32E-02	4.97E-03	1.90E-02
0.66	96	40	2.02E-02	5.45E-02	1.71E+01	1.69E+01	9.54E-02	8.56E-02	7.08E-03	1.93E-02
0.58	85	52	1.53E-02	6.50E-02	1.24E+01	2.17E+01	1.05E-01	8.30E-02	7.40E-03	1.80E-02
0.49	102	42	2.13E-02	5.02E-02	1.61E+01	1.36E+01	1.10E-01	9.55E-02	7.91E-03	2.21E-02
0.38	86	60	1.56E-02	7.08E-02	1.24E+01	1.75E+01	1.07E-01	1.03E-01	7.56E-03	2.42E-02
0.00	99	44	2.25E-02	5.54E-02	1.65E+01	1.43E+01	9.32E-02	8.95E-02	8.16E-03	2.32E-02

Table A.2: Values of local two-phase flow parameters at (a) z/D=1.7, (b) z/D=5.0 & (c) z/D=8.3; Run # 2

(a)

Radial Location	Number Of Drops		Dispersed Phase Fraction		Interfacial Area Concentration		Interface Velocity		Sauter Mean Diameter	
r/R	N_1	N_2	α_1	α_2	a_1	a_2	v_1	v_2	D_{sm1}	D_{sm2}
[-]	[-]	[-]	[-]	[-]	[1/m]	[1/m]	[m/s]	[m/s]	[m]	[m]
0.96	0	0	0.00E+00	0.00E+00	0.00E+00	0.00E+00	0.00E+00	0.00E+00	-	-
0.91	14	9	1.45E-03	1.01E-02	1.77E+00	2.20E+00	9.32E-02	7.97E-02	4.92E-03	2.76E-02
0.85	18	19	1.19E-03	2.07E-02	1.60E+00	4.42E+00	9.55E-02	6.49E-02	4.46E-03	2.80E-02
0.80	27	29	2.24E-03	3.04E-02	2.21E+00	6.19E+00	1.03E-01	7.70E-02	6.06E-03	2.94E-02
0.73	36	39	3.28E-03	4.01E-02	2.82E+00	7.96E+00	1.10E-01	8.90E-02	6.97E-03	3.02E-02
0.66	74	44	7.85E-03	4.01E-02	8.42E+00	1.15E+01	9.30E-02	8.02E-02	5.60E-03	2.09E-02
0.58	58	63	5.18E-03	5.19E-02	4.66E+00	1.08E+01	1.12E-01	9.18E-02	6.66E-03	2.89E-02
0.49	91	76	9.90E-03	6.15E-02	8.10E+00	1.31E+01	1.16E-01	1.04E-01	7.34E-03	2.82E-02
0.38	77	95	7.55E-03	7.45E-02	4.71E+00	1.45E+01	1.24E-01	1.08E-01	9.62E-03	3.09E-02
0.00	118	96	1.39E-02	7.32E-02	8.49E+00	1.58E+01	1.23E-01	1.14E-01	9.85E-03	2.78E-02

(b)

Radial Location	Number Of Drops		Dispersed Phase Fraction		Interfacial Area Concentration		Interface Velocity		Sauter Mean Diameter	
r/R	N_1	N_2	α_1	α_2	a_1	a_2	v_1	v_2	D_{sm1}	D_{sm2}
[-]	[-]	[-]	[-]	[-]	[1/m]	[1/m]	[m/s]	[m/s]	[m]	[m]
0.96	14	7	9.89E-04	5.89E-03	2.09E+00	3.01E+00	9.99E-02	4.64E-02	2.84E-03	1.17E-02
0.91	28	10	3.10E-03	8.84E-03	4.21E+00	2.79E+00	1.00E-01	8.89E-02	4.42E-03	1.90E-02
0.85	43	38	3.23E-03	3.44E-02	5.20E+00	9.78E+00	8.76E-02	9.39E-02	3.73E-03	2.11E-02
0.80	48	50	3.68E-03	4.19E-02	5.52E+00	1.17E+01	8.90E-02	7.84E-02	4.00E-03	2.15E-02
0.73	52	61	4.12E-03	4.95E-02	5.52E+00	1.17E+01	9.04E-02	6.29E-02	4.48E-03	2.54E-02
0.66	70	67	6.48E-03	5.71E-02	5.84E+00	1.36E+01	1.01E-01	8.48E-02	6.66E-03	2.52E-02
0.58	123	41	1.01E-02	6.11E-02	1.50E+01	9.13E+00	1.14E-01	1.01E-01	4.04E-03	4.02E-02
0.49	115	85	1.37E-02	6.51E-02	9.81E+00	1.47E+01	1.15E-01	1.01E-01	8.39E-03	2.65E-02
0.38	115	85	1.42E-02	6.88E-02	9.50E+00	1.63E+01	1.20E-01	1.04E-01	8.98E-03	2.54E-02
0.00	136	92	1.66E-02	6.88E-02	1.13E+01	1.68E+01	1.28E-01	1.14E-01	8.79E-03	2.46E-02

(c)

Radial Location	Number Of Drops		Dispersed Phase Fraction		Interfacial Area Concentration		Interface Velocity		Sauter Mean Diameter	
r/R	N_1	N_2	α_1	α_2	a_1	a_2	v_1	v_2	D_{sm1}	D_{sm2}
[-]	[-]	[-]	[-]	[-]	[1/m]	[1/m]	[m/s]	[m/s]	[m]	[m]
0.96	25	3	2.30E-03	2.89E-03	4.65E+00	1.47E+00	8.06E-02	4.57E-02	2.96E-03	1.18E-02
0.91	41	10	3.04E-03	8.36E-03	5.91E+00	2.50E+00	1.06E-01	9.59E-02	3.09E-03	2.00E-02
0.85	50	24	3.24E-03	2.21E-02	5.55E+00	6.98E+00	1.15E-01	6.34E-02	3.51E-03	1.90E-02
0.80	62	28	5.77E-03	2.54E-02	7.81E+00	6.30E+00	1.11E-01	9.72E-02	4.43E-03	2.42E-02
0.73	41	55	3.27E-03	4.74E-02	2.61E+00	1.02E+01	1.21E-01	8.54E-02	7.51E-03	2.80E-02
0.66	108	38	1.29E-02	3.26E-02	1.56E+01	1.03E+01	9.31E-02	9.14E-02	4.94E-03	1.89E-02
0.58	78	71	1.27E-02	4.18E-02	8.08E+00	1.80E+01	1.03E-01	8.50E-02	9.45E-03	1.40E-02
0.49	107	62	1.26E-02	5.11E-02	1.17E+01	1.30E+01	1.07E-01	1.04E-01	6.48E-03	2.36E-02
0.38	98	68	9.41E-03	5.24E-02	9.74E+00	1.35E+01	1.13E-01	1.00E-01	5.79E-03	2.34E-02
0.00	94	83	9.87E-03	6.47E-02	8.38E+00	1.54E+01	1.13E-01	1.01E-01	7.07E-03	2.52E-02

Table A.3: Values of local two-phase flow parameters at (a) z/D=1.7, (b) z/D=5.0 & (c) z/D=8.3; Run # 3

(a)

Radial Location	Number Of Drops		Dispersed Phase Fraction		Interfacial Area Concentration		Interface Velocity		Sauter Mean Diameter	
r/R	N_1	N_2	α_1	α_2	a_1	a_2	v_1	v_2	D_{sm1}	D_{sm2}
[-]	[-]	[-]	[-]	[-]	[1/m]	[1/m]	[m/s]	[m/s]	[m]	[m]
0.96	0	0	0.00E+00	0.00E+00	0.00E+00	0.00E+00	0.00E+00	0.00E+00	-	-
0.91	32	7	3.77E-03	6.79E-03	5.13E+00	2.21E+00	9.71E-02	8.65E-02	4.41E-03	1.84E-02
0.85	42	22	5.13E-03	2.05E-02	4.78E+00	4.73E+00	9.69E-02	8.33E-02	6.44E-03	2.60E-02
0.80	40	37	4.19E-03	3.18E-02	3.80E+00	6.97E+00	1.03E-01	8.80E-02	6.62E-03	2.74E-02
0.73	38	51	3.25E-03	4.31E-02	2.81E+00	9.21E+00	1.10E-01	9.28E-02	6.93E-03	2.81E-02
0.66	56	56	4.98E-03	4.60E-02	5.48E+00	1.24E+01	9.58E-02	8.68E-02	5.44E-03	2.23E-02
0.58	65	63	6.32E-03	5.42E-02	6.00E+00	1.25E+01	1.02E-01	9.78E-02	6.32E-03	2.60E-02
0.49	58	62	5.46E-03	5.26E-02	4.35E+00	1.04E+01	1.22E-01	1.02E-01	7.54E-03	3.02E-02
0.38	70	60	7.02E-03	5.13E-02	5.69E+00	1.03E+01	1.19E-01	1.03E-01	7.40E-03	2.99E-02
0.00	96	101	9.40E-03	7.29E-02	6.29E+00	1.47E+01	1.33E-01	1.19E-01	8.96E-03	2.97E-02

(b)

Radial Location	Number Of Drops		Dispersed Phase Fraction		Interfacial Area Concentration		Interface Velocity		Sauter Mean Diameter	
r/R	N_1	N_2	α_1	α_2	a_1	a_2	v_1	v_2	D_{sm1}	D_{sm2}
[-]	[-]	[-]	[-]	[-]	[1/m]	[1/m]	[m/s]	[m/s]	[m]	[m]
0.96	20	16	1.09E-03	1.37E-02	2.38E+00	3.97E+00	9.04E-02	6.81E-02	2.75E-03	2.07E-02
0.91	35	23	2.96E-03	1.84E-02	3.88E+00	5.08E+00	1.01E-01	9.88E-02	4.58E-03	2.18E-02
0.85	35	36	2.45E-03	3.21E-02	3.15E+00	7.01E+00	1.12E-01	9.64E-02	4.66E-03	2.75E-02
0.80	42	37	4.35E-03	3.21E-02	4.33E+00	1.05E+01	1.01E-01	8.77E-02	6.02E-03	1.83E-02
0.73	48	38	6.25E-03	3.21E-02	5.52E+00	1.40E+01	8.92E-02	7.90E-02	6.79E-03	1.37E-02
0.66	46	44	4.00E-03	3.46E-02	4.01E+00	9.88E+00	1.10E-01	8.96E-02	5.98E-03	2.10E-02
0.58	63	37	7.24E-03	2.95E-02	7.14E+00	7.97E+00	1.06E-01	9.97E-02	6.09E-03	2.22E-02
0.49	65	64	7.52E-03	5.21E-02	4.90E+00	1.08E+01	1.18E-01	9.87E-02	9.21E-03	2.90E-02
0.38	62	79	5.92E-03	6.14E-02	3.76E+00	1.13E+01	1.25E-01	1.08E-01	9.43E-03	3.27E-02
0.00	96	86	1.16E-02	6.52E-02	6.74E+00	1.39E+01	1.23E-01	1.18E-01	1.03E-02	2.81E-02

(c)

Radial Location	Number Of Drops		Dispersed Phase Fraction		Interfacial Area Concentration		Interface Velocity		Sauter Mean Diameter	
r/R	N_1	N_2	α_1	α_2	a_1	a_2	v_1	v_2	D_{sm1}	D_{sm2}
[-]	[-]	[-]	[-]	[-]	[1/m]	[1/m]	[m/s]	[m/s]	[m]	[m]
0.96	26	0	3.18E-03	0.00E+00	5.69E+00	0.00E+00	8.82E-02	0.00E+00	3.35E-03	#DIV/0!
0.91	25	7	2.80E-03	4.50E-03	3.74E+00	1.85E+00	1.07E-01	1.12E-01	4.49E-03	1.45E-02
0.85	63	7	6.59E-03	4.48E-03	1.04E+01	2.78E+00	1.08E-01	1.12E-01	3.80E-03	9.66E-03
0.80	67	16	7.13E-03	1.48E-02	1.16E+01	4.21E+00	8.94E-02	1.12E-01	3.70E-03	2.11E-02
0.73	34	51	2.85E-03	4.18E-02	1.00E+01	7.13E+00	1.05E-01	8.85E-02	1.71E-03	3.52E-02
0.66	69	38	5.54E-03	4.91E-02	8.44E+00	1.00E+01	1.01E-01	7.94E-02	3.93E-03	2.93E-02
0.58	84	74	8.22E-03	5.64E-02	8.29E+00	1.68E+01	1.12E-01	8.72E-02	5.95E-03	2.01E-02
0.49	113	79	1.16E-02	5.90E-02	1.06E+01	1.51E+01	1.18E-01	1.01E-01	6.57E-03	2.35E-02
0.38	115	84	1.52E-02	6.33E-02	9.11E+00	1.42E+01	1.22E-01	1.18E-01	1.00E-02	2.68E-02
0.00	104	87	1.20E-02	6.57E-02	8.27E+00	1.72E+01	1.23E-01	1.07E-01	8.70E-03	2.29E-02

Table A.4: Values of local two-phase flow parameters at (a) z/D=1.7, (b) z/D=5.0 & (c) z/D=8.3; Run # 4

(a)

Radial Location	Number Of Drops		Dispersed Phase Fraction		Interfacial Area Concentration		Interface Velocity		Sauter Mean Diameter	
r/R	N_1	N_2	α_1	α_2	a_1	a_2	v_1	v_2	D_{sm1}	D_{sm2}
[-]	[-]	[-]	[-]	[-]	[1/m]	[1/m]	[m/s]	[m/s]	[m]	[m]
0.96	0	0	0.00E+00	0.00E+00	0.00E+00	0.00E+00	0.00E+00	0.00E+00	-	-
0.91	9	1	1.49E-03	7.11E-04	1.67E+00	1.85E-01	9.02E-02	0.00E+00	5.35E-03	2.30E-02
0.85	21	11	1.71E-03	9.99E-03	2.37E+00	2.95E+00	9.52E-02	7.53E-02	4.33E-03	2.03E-02
0.80	29	20	2.26E-03	1.74E-02	3.31E+00	4.67E+00	9.58E-02	9.17E-02	4.10E-03	2.24E-02
0.73	37	29	2.81E-03	2.49E-02	4.24E+00	6.39E+00	9.64E-02	1.08E-01	3.97E-03	2.33E-02
0.66	47	27	4.45E-03	2.24E-02	5.25E+00	6.61E+00	1.02E-01	8.59E-02	5.09E-03	2.03E-02
0.58	24	51	9.50E-04	4.24E-02	1.11E+00	7.28E+00	1.24E-01	9.13E-02	5.14E-03	3.49E-02
0.49	39	50	2.73E-03	3.66E-02	2.94E+00	8.27E+00	1.13E-01	1.02E-01	5.57E-03	2.66E-02
0.38	44	82	2.19E-03	6.03E-02	2.57E+00	1.17E+01	1.20E-01	1.09E-01	5.13E-03	3.11E-02
0.00	93	104	8.13E-03	6.72E-02	5.10E+00	1.39E+01	1.39E-01	1.30E-01	9.56E-03	2.89E-02

(b)

Radial Location	Number Of Drops		Dispersed Phase Fraction		Interfacial Area Concentration		Interface Velocity		Sauter Mean Diameter	
r/R	N_1	N_2	α_1	α_2	a_1	a_2	v_1	v_2	D_{sm1}	D_{sm2}
[-]	[-]	[-]	[-]	[-]	[1/m]	[1/m]	[m/s]	[m/s]	[m]	[m]
0.96	9	11	4.69E-04	7.44E-03	6.10E-01	2.19E+00	1.05E-01	7.32E-02	4.61E-03	2.04E-02
0.91	20	17	1.37E-03	1.30E-02	2.19E+00	3.64E+00	9.32E-02	1.04E-01	3.76E-03	2.14E-02
0.85	20	39	8.40E-04	2.49E-02	9.91E-01	5.21E+00	1.21E-01	1.08E-01	5.08E-03	2.86E-02
0.80	32	44	1.82E-03	3.05E-02	2.38E+00	1.17E+01	1.17E-01	9.51E-02	4.59E-03	1.56E-02
0.73	43	48	2.80E-03	3.61E-02	3.77E+00	1.82E+01	1.14E-01	8.19E-02	4.46E-03	1.19E-02
0.66	97	14	4.95E-03	3.72E-02	1.48E+01	3.65E+00	1.07E-01	8.58E-02	2.01E-03	6.11E-02
0.58	77	26	4.95E-03	3.72E-02	9.16E+00	5.52E+00	1.20E-01	1.09E-01	3.24E-03	4.04E-02
0.49	82	56	7.09E-03	3.83E-02	7.59E+00	1.04E+01	1.14E-01	9.97E-02	5.61E-03	2.21E-02
0.38	77	70	5.48E-03	4.48E-02	5.43E+00	1.24E+01	1.21E-01	1.24E-01	6.06E-03	2.16E-02
0.00	84	81	6.70E-03	5.08E-02	5.16E+00	1.07E+01	1.41E-01	1.28E-01	7.79E-03	2.84E-02

(c)

Radial Location	Number Of Drops		Dispersed Phase Fraction		Interfacial Area Concentration		Interface Velocity		Sauter Mean Diameter	
r/R	N_1	N_2	α_1	α_2	a_1	a_2	v_1	v_2	D_{sm1}	D_{sm2}
[-]	[-]	[-]	[-]	[-]	[1/m]	[1/m]	[m/s]	[m/s]	[m]	[m]
0.96	19	10	1.55E-03	7.62E-03	1.55E+00	1.95E+00	1.27E-01	8.61E-02	6.02E-03	2.35E-02
0.91	28	8	2.37E-03	5.63E-03	3.43E+00	2.02E+00	1.27E-01	9.88E-02	4.14E-03	1.67E-02
0.85	56	18	3.55E-03	1.37E-02	6.03E+00	3.66E+00	1.28E-01	9.59E-02	3.53E-03	2.24E-02
0.80	74	28	3.78E-03	2.00E-02	1.24E+01	4.36E-01	1.18E-01	9.74E-02	1.83E-03	2.75E-01
0.73	59	37	4.01E-03	2.62E-02	5.53E+00	7.25E+00	1.14E-01	9.89E-02	4.35E-03	2.17E-02
0.66	71	47	6.02E-03	3.01E-02	7.41E+00	9.83E+00	1.11E-01	9.25E-02	4.88E-03	1.84E-02
0.58	54	63	3.84E-03	4.34E-02	3.29E+00	1.26E+01	1.31E-01	9.19E-02	6.99E-03	2.07E-02
0.49	78	54	4.87E-03	5.06E-02	7.48E+00	9.44E+00	1.07E-01	1.13E-01	3.91E-03	3.21E-02
0.38	81	81	5.91E-03	5.78E-02	5.67E+00	1.26E+01	1.33E-01	1.25E-01	6.25E-03	2.75E-02
0.00	88	91	6.56E-03	5.90E-02	6.36E+00	1.25E+01	1.21E-01	1.19E-01	6.19E-03	2.83E-02

Table A.5: Values of local two-phase flow parameters at (a) z/D=1.7, (b) z/D=5.0 & (c) z/D=8.3; Run # 5

(a)

Radial Location	Number Of Drops		Dispersed Phase Fraction		Interfacial Area Concentration		Interface Velocity		Sauter Mean Diameter	
r/R	N_1	N_2	α_1	α_2	a_1	a_2	v_1	v_2	D_{sm1}	D_{sm2}
[-]	[-]	[-]	[-]	[-]	[1/m]	[1/m]	[m/s]	[m/s]	[m]	[m]
0.96	0	0	0.00E+00	0.00E+00	0.00E+00	0.00E+00	0.00E+00	0.00E+00	-	-
0.91	106	15	1.57E-02	1.86E-02	1.86E+01	4.62E+00	9.65E-02	8.45E-02	5.07E-03	2.41E-02
0.85	88	78	9.00E-03	8.41E-02	8.87E+00	2.11E+01	9.98E-02	7.20E-02	6.09E-03	2.39E-02
0.80	99	94	1.03E-02	9.98E-02	8.94E+00	1.99E+01	1.07E-01	8.22E-02	6.90E-03	3.01E-02
0.73	110	110	1.16E-02	1.16E-01	9.00E+00	1.87E+01	1.15E-01	9.24E-02	7.70E-03	3.72E-02
0.66	141	85	1.70E-02	7.70E-02	1.52E+01	2.14E+01	1.05E-01	9.12E-02	6.72E-03	2.16E-02
0.58	156	105	1.67E-02	8.90E-02	1.60E+01	2.19E+01	1.07E-01	9.73E-02	6.26E-03	2.44E-02
0.49	119	131	1.18E-02	1.14E-01	9.05E+00	2.43E+01	1.13E-01	9.78E-02	7.85E-03	2.81E-02
0.38	121	132	1.14E-02	1.13E-01	1.00E+01	2.51E+01	1.12E-01	9.91E-02	6.79E-03	2.71E-02
0.00	149	133	1.58E-02	1.05E-01	1.29E+01	2.59E+01	1.12E-01	1.03E-01	7.36E-03	2.43E-02

(b)

Radial Location	Number Of Drops		Dispersed Phase Fraction		Interfacial Area Concentration		Interface Velocity		Sauter Mean Diameter	
r/R	N_1	N_2	α_1	α_2	a_1	a_2	v_1	v_2	D_{sm1}	D_{sm2}
[-]	[-]	[-]	[-]	[-]	[1/m]	[1/m]	[m/s]	[m/s]	[m]	[m]
0.96	70	39	5.56E-03	4.27E-02	8.56E+00	1.44E+01	1.05E-01	5.38E-02	3.89E-03	1.79E-02
0.91	94	55	7.56E-03	6.09E-02	1.24E+01	1.51E+01	9.33E-02	7.24E-02	3.66E-03	2.42E-02
0.85	100	78	8.33E-03	8.70E-02	1.16E+01	1.75E+01	9.60E-02	8.39E-02	4.33E-03	2.98E-02
0.80	101	90	8.48E-03	9.11E-02	1.08E+01	1.80E+01	8.63E-02	7.58E-02	4.69E-03	3.03E-02
0.73	102	101	8.63E-03	9.52E-02	1.80E+01	1.87E+01	1.07E-01	6.77E-02	2.88E-03	3.05E-02
0.66	107	103	1.11E-02	9.32E-02	1.01E+01	1.85E+01	9.75E-02	8.35E-02	6.58E-03	3.02E-02
0.58	182	77	1.24E-02	1.02E-01	2.51E+01	1.94E+01	1.02E-01	9.20E-02	2.96E-03	3.15E-02
0.49	136	122	1.37E-02	1.11E-01	1.31E+01	2.48E+01	1.00E-01	7.95E-02	6.24E-03	2.68E-02
0.38	135	128	1.44E-02	1.20E-01	1.18E+01	2.36E+01	1.03E-01	9.71E-02	7.34E-03	3.04E-02
0.00	178	124	1.94E-02	1.00E-01	1.67E+01	2.27E+01	1.11E-01	1.04E-01	6.97E-03	2.65E-02

(c)

Radial Location	Number Of Drops		Dispersed Phase Fraction		Interfacial Area Concentration		Interface Velocity		Sauter Mean Diameter	
r/R	N_1	N_2	α_1	α_2	a_1	a_2	v_1	v_2	D_{sm1}	D_{sm2}
[-]	[-]	[-]	[-]	[-]	[1/m]	[1/m]	[m/s]	[m/s]	[m]	[m]
0.96	100	32	8.78E-03	3.12E-02	1.70E+01	2.53E+01	8.27E-02	3.74E-02	3.10E-03	7.39E-03
0.91	99	41	9.30E-03	4.34E-02	1.46E+01	1.31E+01	9.51E-02	4.72E-02	3.83E-03	1.98E-02
0.85	120	55	1.07E-02	5.57E-02	1.73E+01	1.90E+01	9.56E-02	5.50E-02	3.70E-03	1.75E-02
0.80	132	87	1.20E-02	8.71E-02	1.54E+01	2.37E+01	1.05E-01	7.24E-02	4.65E-03	2.20E-02
0.73	115	116	9.30E-03	1.19E-01	1.16E+01	2.47E+01	9.11E-02	7.64E-02	4.81E-03	2.89E-02
0.66	128	108	1.58E-02	1.15E-01	2.47E+01	3.17E+01	8.66E-02	7.54E-02	3.84E-03	2.17E-02
0.58	141	99	1.30E-02	1.02E-01	1.67E+01	2.73E+01	9.73E-02	5.84E-02	4.65E-03	2.24E-02
0.49	167	100	1.72E-02	8.75E-02	2.05E+01	2.78E+01	9.64E-02	7.06E-02	5.03E-03	1.89E-02
0.38	155	107	1.57E-02	9.95E-02	1.61E+01	2.43E+01	1.04E-01	8.88E-02	5.84E-03	2.46E-02
0.00	154	148	1.32E-02	1.27E-01	1.34E+01	3.47E+01	1.05E-01	8.49E-02	5.91E-03	2.20E-02

Table A.6: Values of local two-phase flow parameters at (a) z/D=1.7, (b) z/D=5.0 & (c) z/D=8.3; Run # 6

(a)

Radial Location	Number Of Drops		Dispersed Phase Fraction		Interfacial Area Concentration		Interface Velocity		Sauter Mean Diameter	
r/R	N_1	N_2	α_1	α_2	a_1	a_2	v_1	v_2	D_{sm1}	D_{sm2}
[-]	[-]	[-]	[-]	[-]	[1/m]	[1/m]	[m/s]	[m/s]	[m]	[m]
0.96	0	0	0.00E+00	0.00E+00	0.00E+00	0.00E+00	0.00E+00	0.00E+00	-	-
0.91	32	37	3.14E-03	5.32E-02	3.27E+00	8.01E+00	1.09E-01	9.57E-02	5.77E-03	3.99E-02
0.85	42	61	3.89E-03	7.55E-02	4.01E+00	1.59E+01	1.04E-01	9.70E-02	5.82E-03	2.85E-02
0.80	74	55	7.87E-03	6.39E-02	1.01E+01	1.71E+01	1.09E-01	9.74E-02	4.67E-03	2.24E-02
0.73	106	48	1.18E-02	5.22E-02	1.62E+01	1.83E+01	1.15E-01	9.79E-02	4.39E-03	1.71E-02
0.66	102	74	1.40E-02	8.24E-02	1.29E+01	1.92E+01	1.10E-01	1.03E-01	6.48E-03	2.57E-02
0.58	89	108	8.50E-03	1.20E-01	8.21E+00	2.34E+01	1.18E-01	1.02E-01	6.21E-03	3.08E-02
0.49	96	105	1.04E-02	1.07E-01	9.00E+00	2.37E+01	1.18E-01	1.06E-01	6.93E-03	2.71E-02
0.38	103	101	1.15E-02	1.00E-01	1.02E+01	2.16E+01	1.22E-01	1.12E-01	6.80E-03	2.78E-02
0.00	108	112	1.12E-02	1.03E-01	1.05E+01	2.67E+01	1.24E-01	1.16E-01	6.42E-03	2.32E-02

(b)

Radial Location	Number Of Drops		Dispersed Phase Fraction		Interfacial Area Concentration		Interface Velocity		Sauter Mean Diameter	
r/R	N_1	N_2	α_1	α_2	a_1	a_2	v_1	v_2	D_{sm1}	D_{sm2}
[-]	[-]	[-]	[-]	[-]	[1/m]	[1/m]	[m/s]	[m/s]	[m]	[m]
0.96	20	29	1.46E-03	3.28E-02	2.61E+00	1.25E+01	6.11E-02	6.29E-02	3.37E-03	1.57E-02
0.91	53	45	4.73E-03	5.02E-02	7.01E+00	1.29E+01	9.91E-02	6.98E-02	4.04E-03	2.33E-02
0.85	45	68	2.44E-03	8.52E-02	4.14E+00	1.86E+01	1.12E-01	8.59E-02	3.54E-03	2.75E-02
0.80	50	70	4.40E-03	8.33E-02	4.19E+00	2.71E+01	1.21E-01	7.85E-02	6.31E-03	1.84E-02
0.73	55	71	6.36E-03	8.13E-02	4.23E+00	3.56E+01	1.29E-01	7.11E-02	9.02E-03	1.37E-02
0.66	58	87	4.36E-03	1.05E-01	5.92E+00	2.06E+01	9.43E-02	8.25E-02	4.42E-03	3.06E-02
0.58	63	98	5.36E-03	1.12E-01	3.31E+01	1.35E+01	1.01E-01	8.72E-02	9.72E-04	4.99E-02
0.49	68	109	6.36E-03	1.20E-01	5.69E+00	2.74E+01	1.08E-01	7.92E-02	6.71E-03	2.62E-02
0.38	104	79	6.36E-03	1.20E-01	1.28E+01	2.11E+01	1.18E-01	9.72E-02	2.99E-03	3.42E-02
0.00	229	7	6.36E-03	1.20E-01	4.81E+01	1.47E+00	1.14E-01	0.00E+00	7.93E-04	4.89E-01

(c)

Radial Location	Number Of Drops		Dispersed Phase Fraction		Interfacial Area Concentration		Interface Velocity		Sauter Mean Diameter	
r/R	N_1	N_2	α_1	α_2	a_1	a_2	v_1	v_2	D_{sm1}	D_{sm2}
[-]	[-]	[-]	[-]	[-]	[1/m]	[1/m]	[m/s]	[m/s]	[m]	[m]
0.96	83	9	8.46E-03	8.62E-03	2.04E+01	1.44E+01	9.27E-02	8.96E-03	2.49E-03	3.60E-03
0.91	94	14	1.06E-02	1.22E-02	1.86E+01	4.82E+00	1.13E-01	8.33E-02	3.43E-03	1.52E-02
0.85	122	48	1.29E-02	4.76E-02	2.15E+01	1.82E+01	1.10E-01	8.41E-02	3.61E-03	1.57E-02
0.80	108	67	1.17E-02	6.88E-02	1.65E+01	2.06E+01	9.67E-02	5.32E-02	4.25E-03	2.01E-02
0.73	94	85	1.05E-02	9.01E-02	1.15E+01	2.29E+01	1.00E-01	8.21E-02	5.44E-03	2.36E-02
0.66	105	92	1.26E-02	8.92E-02	1.27E+01	2.47E+01	1.10E-01	9.20E-02	5.94E-03	2.16E-02
0.58	85	111	9.13E-03	1.17E-01	9.27E+00	3.58E+01	9.19E-02	8.33E-02	5.91E-03	1.95E-02
0.49	154	78	1.12E-02	1.16E-01	2.30E+01	2.13E+01	1.10E-01	9.73E-02	2.91E-03	3.27E-02
0.38	143	88	1.12E-02	1.16E-01	1.77E+01	2.21E+01	1.15E-01	1.07E-01	3.79E-03	3.15E-02
0.00	112	120	1.32E-02	1.16E-01	1.11E+01	2.53E+01	1.10E-01	1.04E-01	7.14E-03	2.75E-02

Table A.7: Values of local two-phase flow parameters at (a) z/D=1.7, (b) z/D=5.0 & (c) z/D=8.3; Run # 7

(a)

Radial Location	Number Of Drops		Dispersed Phase Fraction		Interfacial Area Concentration		Interface Velocity		Sauter Mean Diameter	
r/R	N_1	N_2	α_1	α_2	a_1	a_2	v_1	v_2	D_{sm1}	D_{sm2}
[-]	[-]	[-]	[-]	[-]	[1/m]	[1/m]	[m/s]	[m/s]	[m]	[m]
0.96	0	0	0.00E+00	0.00E+00	0.00E+00	0.00E+00	0.00E+00	0.00E+00	-	-
0.91	36	16	3.60E-03	1.72E-02	4.32E+00	4.33E+00	1.12E-01	7.93E-02	5.00E-03	2.38E-02
0.85	26	44	1.72E-03	4.31E-02	1.77E+00	7.86E+00	1.08E-01	7.33E-02	5.86E-03	3.29E-02
0.80	37	59	2.32E-03	5.34E-02	2.46E+00	1.01E+01	1.11E-01	8.24E-02	5.65E-03	3.19E-02
0.73	48	74	2.92E-03	6.38E-02	3.16E+00	1.23E+01	1.14E-01	9.15E-02	5.54E-03	3.12E-02
0.66	60	76	3.69E-03	6.72E-02	4.50E+00	1.33E+01	1.07E-01	1.04E-01	4.92E-03	3.04E-02
0.58	85	76	5.80E-03	6.62E-02	6.69E+00	1.41E+01	1.20E-01	9.03E-02	5.20E-03	2.81E-02
0.49	69	104	4.09E-03	8.21E-02	4.32E+00	1.78E+01	1.24E-01	1.05E-01	5.67E-03	2.78E-02
0.38	79	118	5.27E-03	9.30E-02	4.43E+00	1.77E+01	1.25E-01	1.12E-01	7.13E-03	3.14E-02
0.00	139	146	9.32E-03	1.14E-01	7.26E+00	1.77E+01	1.66E-01	3.65E-02	7.71E-03	3.84E-02

(b)

Radial Location	Number Of Drops		Dispersed Phase Fraction		Interfacial Area Concentration		Interface Velocity		Sauter Mean Diameter	
r/R	N_1	N_2	α_1	α_2	a_1	a_2	v_1	v_2	D_{sm1}	D_{sm2}
[-]	[-]	[-]	[-]	[-]	[1/m]	[1/m]	[m/s]	[m/s]	[m]	[m]
0.96	30	21	2.83E-03	1.77E-02	2.85E+00	6.18E+00	1.05E-01	5.25E-02	5.95E-03	1.72E-02
0.91	39	42	2.72E-03	3.08E-02	2.85E+00	7.83E+00	1.34E-01	7.98E-02	5.72E-03	2.36E-02
0.85	37	87	1.45E-03	6.93E-02	1.60E+00	1.32E+01	1.23E-01	9.61E-02	5.44E-03	3.15E-02
0.80	57	90	3.14E-03	7.15E-02	4.83E+00	1.49E+01	1.19E-01	8.82E-02	3.90E-03	2.88E-02
0.73	76	92	4.82E-03	7.37E-02	6.45E+00	1.57E+01	1.14E-01	8.03E-02	4.49E-03	2.81E-02
0.66	95	88	7.57E-03	6.76E-02	8.06E+00	1.66E+01	1.14E-01	9.20E-02	5.63E-03	2.45E-02
0.58	159	49	7.04E-03	8.13E-02	2.07E+01	1.12E+01	1.11E-01	1.04E-01	2.04E-03	4.36E-02
0.49	91	119	6.51E-03	9.50E-02	5.27E+00	1.82E+01	1.20E-01	9.14E-02	7.41E-03	3.13E-02
0.38	111	116	9.23E-03	8.36E-02	8.33E+00	1.98E+01	1.17E-01	1.10E-01	6.65E-03	2.54E-02
0.00	135	125	1.16E-02	8.57E-02	9.24E+00	1.62E+01	1.29E-01	1.16E-01	7.54E-03	3.16E-02

(c)

Radial Location	Number Of Drops		Dispersed Phase Fraction		Interfacial Area Concentration		Interface Velocity		Sauter Mean Diameter	
r/R	N_1	N_2	α_1	α_2	a_1	a_2	v_1	v_2	D_{sm1}	D_{sm2}
[-]	[-]	[-]	[-]	[-]	[1/m]	[1/m]	[m/s]	[m/s]	[m]	[m]
0.96	79	6	6.94E-03	4.63E-03	1.33E+01	3.40E+00	1.03E-01	4.58E-02	3.14E-03	8.17E-03
0.91	63	25	5.33E-03	1.83E-02	7.44E+00	6.50E+00	1.12E-01	8.38E-02	4.30E-03	1.68E-02
0.85	116	55	9.64E-03	4.29E-02	6.03E+00	1.28E+01	1.19E-01	8.52E-02	9.60E-03	2.00E-02
0.80	96	79	7.11E-03	6.56E-02	5.33E+00	1.60E+01	1.18E-01	8.19E-02	8.01E-03	2.46E-02
0.73	75	103	4.57E-03	8.83E-02	4.62E+00	1.92E+01	1.21E-01	8.73E-02	5.93E-03	2.76E-02
0.66	106	84	8.54E-03	7.19E-02	8.91E+00	1.72E+01	1.24E-01	8.26E-02	5.75E-03	2.51E-02
0.58	85	106	6.91E-03	8.45E-02	5.97E+00	2.41E+01	1.13E-01	9.04E-02	6.95E-03	2.10E-02
0.49	152	81	9.15E-03	8.48E-02	1.54E+01	1.62E+01	1.20E-01	1.01E-01	3.56E-03	3.15E-02
0.38	147	121	1.14E-02	8.51E-02	1.04E+01	2.05E+01	1.37E-01	1.08E-01	6.58E-03	2.49E-02
0.00	130	155	9.97E-03	1.02E-01	9.09E+00	2.42E+01	1.19E-01	1.13E-01	6.58E-03	2.53E-02

Table A.8: Values of local two-phase flow parameters at (a) z/D=1.7, (b) z/D=5.0 & (c) z/D=8.3; Run # 8

(a)

Radial Location	Number Of Drops		Dispersed Phase Fraction		Interfacial Area Concentration		Interface Velocity		Sauter Mean Diameter	
r/R	N_1	N_2	α_1	α_2	a_1	a_2	v_1	v_2	D_{sm1}	D_{sm2}
[-]	[-]	[-]	[-]	[-]	[1/m]	[1/m]	[m/s]	[m/s]	[m]	[m]
0.96	0	0	0.00E+00	0.00E+00	0.00E+00	0.00E+00	0.00E+00	0.00E+00	-	-
0.91	3	1	6.37E-03	1.23E-02	0.00E+00	0.00E+00	0.00E+00	0.00E+00	-	-
0.85	63	97	3.18E-03	8.14E-02	4.19E+00	1.57E+01	1.19E-01	8.17E-02	4.55E-03	3.10E-02
0.80	85	102	4.95E-03	8.10E-02	5.92E+00	1.67E+01	1.26E-01	9.36E-02	5.02E-03	2.91E-02
0.73	107	107	6.73E-03	8.06E-02	7.65E+00	1.77E+01	1.34E-01	1.06E-01	5.28E-03	2.73E-02
0.66	159	99	1.36E-02	6.57E-02	1.47E+01	1.63E+01	1.31E-01	1.13E-01	5.55E-03	2.41E-02
0.58	211	144	1.18E-02	9.58E-02	1.80E+01	2.29E+01	1.26E-01	1.12E-01	3.93E-03	2.51E-02
0.49	170	130	1.20E-02	8.91E-02	1.29E+01	2.33E+01	1.31E-01	1.06E-01	5.58E-03	2.29E-02
0.38	186	159	1.31E-02	9.81E-02	1.33E+01	2.49E+01	1.34E-01	1.24E-01	5.89E-03	2.37E-02
0.00	270	172	2.45E-02	1.04E-01	2.09E+01	2.70E+01	1.47E-01	1.31E-01	7.04E-03	2.32E-02

(b)

Radial Location	Number Of Drops		Dispersed Phase Fraction		Interfacial Area Concentration		Interface Velocity		Sauter Mean Diameter	
r/R	N_1	N_2	α_1	α_2	a_1	a_2	v_1	v_2	D_{sm1}	D_{sm2}
[-]	[-]	[-]	[-]	[-]	[1/m]	[1/m]	[m/s]	[m/s]	[m]	[m]
0.96	63	41	2.60E-03	3.81E-02	5.89E+00	1.01E+01	1.27E-01	6.45E-02	2.65E-03	2.27E-02
0.91	80	81	4.01E-03	6.90E-02	6.15E+00	1.41E+01	1.22E-01	7.58E-02	3.91E-03	2.93E-02
0.85	157	94	7.96E-03	7.11E-02	1.53E+01	1.93E+01	1.25E-01	7.68E-02	3.11E-03	2.21E-02
0.80	122	114	5.96E-03	8.51E-02	1.03E+01	3.47E+01	1.22E-01	7.74E-02	3.49E-03	1.47E-02
0.73	87	134	3.96E-03	9.91E-02	5.18E+00	5.01E+01	1.19E-01	7.80E-02	4.59E-03	1.19E-02
0.66	247	33	1.23E-02	9.31E-02	3.86E+01	8.81E+00	1.08E-01	6.76E-02	1.90E-03	6.34E-02
0.58	205	107	1.64E-02	9.00E-02	2.44E+01	1.67E+01	1.23E-01	8.81E-02	4.03E-03	3.23E-02
0.49	183	143	2.06E-02	8.70E-02	1.73E+01	2.07E+01	1.15E-01	9.57E-02	7.11E-03	2.52E-02
0.38	162	180	1.11E-02	1.12E-01	1.02E+01	2.47E+01	1.34E-01	1.08E-01	6.52E-03	2.73E-02
0.00	248	133	2.25E-02	8.18E-02	2.36E+01	2.60E+01	1.27E-01	1.07E-01	5.72E-03	1.89E-02

(c)

Radial Location	Number Of Drops		Dispersed Phase Fraction		Interfacial Area Concentration		Interface Velocity		Sauter Mean Diameter	
r/R	N_1	N_2	α_1	α_2	a_1	a_2	v_1	v_2	D_{sm1}	D_{sm2}
[-]	[-]	[-]	[-]	[-]	[1/m]	[1/m]	[m/s]	[m/s]	[m]	[m]
0.96	327	10	1.00E-02	7.90E-03	5.60E+01	6.18E+00	1.07E-01	7.66E-02	1.07E-03	7.66E-03
0.91	305	29	1.20E-02	1.72E-02	2.51E+01	8.02E+00	1.24E-01	6.60E-02	2.87E-03	1.28E-02
0.85	282	47	1.77E-02	3.49E-02	1.64E+01	1.27E+01	1.18E-01	7.01E-02	6.46E-03	1.64E-02
0.80	345	22	1.21E-02	5.43E-02	1.21E+01	1.51E+01	1.16E-01	9.38E-02	5.99E-03	2.16E-02
0.73	260	67	6.46E-03	7.37E-02	7.79E+00	1.75E+01	1.21E-01	8.01E-02	4.98E-03	2.53E-02
0.66	174	111	1.32E-02	7.17E-02	1.69E+01	2.12E+01	1.12E-01	8.22E-02	4.68E-03	2.03E-02
0.58	135	141	1.00E-02	1.00E-01	9.18E+00	3.11E+01	1.32E-01	8.85E-02	6.56E-03	1.94E-02
0.49	180	127	1.45E-02	8.04E-02	1.56E+01	2.57E+01	1.23E-01	9.89E-02	5.56E-03	1.88E-02
0.38	257	128	1.68E-02	8.01E-02	2.54E+01	2.41E+01	1.27E-01	1.15E-01	3.97E-03	2.00E-02
0.00	191	159	1.63E-02	9.74E-02	1.46E+01	2.38E+01	1.25E-01	1.07E-01	6.72E-03	2.45E-02

Table A.9: Values of local two-phase flow parameters at (a) z/D=1.7, (b) z/D=5.0 & (c) z/D=8.3; Run # 9

(a)

Radial Location	Number Of Drops		Dispersed Phase Fraction		Interfacial Area Concentration		Interface Velocity		Sauter Mean Diameter	
r/R	N_1	N_2	α_1	α_2	a_1	a_2	v_1	v_2	D_{sm1}	D_{sm2}
[-]	[-]	[-]	[-]	[-]	[1/m]	[1/m]	[m/s]	[m/s]	[m]	[m]
0.96	0	0	0.00E+00	0.00E+00	0.00E+00	0.00E+00	0.00E+00	0.00E+00	-	-
0.91	29	27	1.01E-02	1.37E-01	1.61E+01	3.41E+01	6.37E-02	7.90E-02	3.78E-03	2.40E-02
0.85	31	29	1.10E-02	1.38E-01	6.47E+00	2.75E+01	1.21E-01	6.65E-02	1.02E-02	3.02E-02
0.80	27	31	8.85E-03	1.48E-01	6.98E+00	2.92E+01	1.02E-01	7.64E-02	7.61E-03	3.04E-02
0.73	22	33	6.66E-03	1.57E-01	7.48E+00	3.09E+01	8.37E-02	8.62E-02	5.34E-03	3.05E-02
0.66	27	32	8.76E-03	1.60E-01	1.15E+01	4.66E+01	7.47E-02	5.87E-02	4.58E-03	2.06E-02
0.58	36	29	1.26E-02	1.43E-01	1.34E+01	3.17E+01	9.43E-02	6.20E-02	5.63E-03	2.71E-02
0.49	23	42	5.80E-03	2.18E-01	5.65E+00	3.66E+01	9.05E-02	7.02E-02	6.16E-03	3.57E-02
0.38	48	51	1.74E-02	2.03E-01	1.15E+01	4.66E+01	1.01E-01	7.20E-02	9.06E-03	2.62E-02
0.00	43	82	1.30E-02	2.96E-01	6.65E+00	5.26E+01	1.24E-01	1.05E-01	1.18E-02	3.37E-02

(b)

Radial Location	Number Of Drops		Dispersed Phase Fraction		Interfacial Area Concentration		Interface Velocity		Sauter Mean Diameter	
r/R	N_1	N_2	α_1	α_2	a_1	a_2	v_1	v_2	D_{sm1}	D_{sm2}
[-]	[-]	[-]	[-]	[-]	[1/m]	[1/m]	[m/s]	[m/s]	[m]	[m]
0.96	20	28	5.03E-03	1.08E-01	7.97E+00	3.38E+01	6.36E-02	6.46E-02	3.79E-03	1.91E-02
0.91	37	34	1.29E-02	1.26E-01	1.33E+01	3.11E+01	1.05E-01	7.30E-02	5.81E-03	2.43E-02
0.85	32	53	9.10E-03	2.18E-01	6.87E+00	5.15E+01	9.93E-02	6.51E-02	7.95E-03	2.54E-02
0.80	39	49	1.28E-02	1.86E-01	9.23E+00	6.74E+01	1.01E-01	6.74E-02	8.33E-03	1.66E-02
0.73	45	45	1.65E-02	1.55E-01	1.16E+01	8.33E+01	1.02E-01	6.96E-02	8.56E-03	1.11E-02
0.66	62	60	2.50E-02	2.08E-01	1.60E+01	5.75E+01	1.02E-01	8.99E-02	9.39E-03	2.17E-02
0.58	104	35	1.79E-02	2.22E-01	1.27E+01	5.30E+01	9.89E-02	1.02E-01	8.46E-03	2.51E-02
0.49	39	69	1.08E-02	2.36E-01	9.41E+00	4.85E+01	1.02E-01	7.86E-02	6.88E-03	2.92E-02
0.38	60	39	1.90E-02	2.04E-01	2.21E+01	3.85E+01	9.87E-02	8.90E-02	5.16E-03	3.18E-02
0.00	63	52	2.73E-02	1.72E-01	2.38E+01	4.54E+01	9.91E-02	9.49E-02	6.87E-03	2.28E-02

(c)

Radial Location	Number Of Drops		Dispersed Phase Fraction		Interfacial Area Concentration		Interface Velocity		Sauter Mean Diameter	
r/R	N_1	N_2	α_1	α_2	a_1	a_2	v_1	v_2	D_{sm1}	D_{sm2}
[-]	[-]	[-]	[-]	[-]	[1/m]	[1/m]	[m/s]	[m/s]	[m]	[m]
0.96	19	11	7.07E-03	5.07E-02	8.93E+00	1.95E+01	1.26E-01	7.23E-02	4.75E-03	1.56E-02
0.91	20	17	6.65E-03	6.68E-02	5.70E+00	1.99E+01	1.29E-01	8.03E-02	6.99E-03	2.02E-02
0.85	24	20	6.71E-03	7.71E-02	8.65E+00	2.40E+01	8.90E-02	7.20E-02	4.65E-03	1.93E-02
0.80	26	28	1.03E-02	1.16E-01	6.82E+00	2.63E+01	1.07E-01	8.48E-02	9.06E-03	2.66E-02
0.73	27	50	4.01E-03	1.80E-01	6.15E+00	3.39E+01	1.26E-01	8.91E-02	3.92E-03	3.19E-02
0.66	48	49	1.44E-02	1.60E-01	1.77E+01	4.92E+01	9.13E-02	7.23E-02	4.89E-03	1.96E-02
0.58	35	38	1.33E-02	1.34E-01	8.12E+00	3.90E+01	1.27E-01	9.14E-02	9.79E-03	2.06E-02
0.49	49	34	2.34E-02	1.27E-01	1.78E+01	3.09E+01	1.05E-01	8.72E-02	7.88E-03	2.47E-02
0.38	45	50	1.49E-02	1.62E-01	1.66E+01	4.07E+01	8.99E-02	9.28E-02	5.40E-03	2.38E-02
0.00	30	39	1.24E-02	1.26E-01	6.02E+00	2.91E+01	1.19E-01	9.04E-02	1.24E-02	2.60E-02

Table A.10: Values of local two-phase flow parameters at (a) z/D=1.7, (b) z/D=5.0 & (c) z/D=8.3; Run # 10

(a)

| Radial Location	Number Of Drops		Dispersed Phase Fraction		Interfacial Area Concentration		Interface Velocity		Sauter Mean Diameter	
r/R	N_1	N_2	α_1	α_2	a_1	a_2	v_1	v_2	D_{sm1}	D_{sm2}
[-]	[-]	[-]	[-]	[-]	[1/m]	[1/m]	[m/s]	[m/s]	[m]	[m]
0.96	0	0	0.00E+00	0.00E+00	0.00E+00	0.00E+00	0.00E+00	0.00E+00	-	-
0.91	35	67	3.53E-03	1.27E-01	2.61E+00	2.62E+01	1.44E-01	9.91E-02	8.13E-03	2.89E-02
0.85	71	86	8.96E-03	1.57E-01	1.03E+01	2.96E+01	1.09E-01	9.33E-02	5.22E-03	3.18E-02
0.80	76	96	9.69E-03	1.59E-01	1.06E+01	3.19E+01	1.16E-01	9.65E-02	5.47E-03	3.00E-02
0.73	81	106	1.04E-02	1.62E-01	1.09E+01	3.41E+01	1.22E-01	9.98E-02	5.71E-03	2.84E-02
0.66	97	99	1.56E-02	1.55E-01	1.53E+01	3.71E+01	1.17E-01	9.45E-02	6.12E-03	2.52E-02
0.58	100	107	1.52E-02	1.66E-01	1.35E+01	3.57E+01	1.24E-01	1.03E-01	6.74E-03	2.79E-02
0.49	103	120	1.57E-02	1.78E-01	1.27E+01	3.64E+01	1.26E-01	9.98E-02	7.45E-03	2.93E-02
0.38	105	133	1.63E-02	1.90E-01	1.19E+01	3.71E+01	1.27E-01	9.68E-02	8.27E-03	3.07E-02
0.00	72	155	8.18E-03	2.28E-01	6.37E+00	6.95E+01	1.17E-01	5.69E-02	7.71E-03	1.97E-02

(b)

Radial Location	Number Of Drops		Dispersed Phase Fraction		Interfacial Area Concentration		Interface Velocity		Sauter Mean Diameter	
r/R	N_1	N_2	α_1	α_2	a_1	a_2	v_1	v_2	D_{sm1}	D_{sm2}
[-]	[-]	[-]	[-]	[-]	[1/m]	[1/m]	[m/s]	[m/s]	[m]	[m]
0.96	24	41	2.21E-03	7.80E-02	3.51E+00	1.84E+01	8.11E-02	5.67E-02	3.77E-03	2.54E-02
0.91	32	57	2.90E-03	1.04E-01	4.40E+00	2.72E+01	9.04E-02	6.40E-02	3.95E-03	2.28E-02
0.85	52	84	5.06E-03	1.54E-01	7.51E+00	3.46E+01	1.02E-01	8.03E-02	4.05E-03	2.68E-02
0.80	63	87	7.63E-03	1.54E-01	1.64E+01	3.12E+01	1.05E-01	6.93E-02	2.79E-03	2.96E-02
0.73	73	89	1.02E-02	1.53E-01	2.53E+01	2.79E+01	1.08E-01	5.82E-02	2.42E-03	3.30E-02
0.66	144	38	1.35E-02	1.31E-01	4.31E+01	2.12E+01	9.96E-02	8.35E-02	1.88E-03	3.71E-02
0.58	101	77	1.68E-02	1.10E-01	2.00E+01	3.42E+01	1.12E-01	8.13E-02	5.02E-03	1.92E-02
0.49	90	85	1.46E-02	1.39E-01	1.44E+01	3.46E+01	1.04E-01	8.08E-02	6.09E-03	2.40E-02
0.38	100	82	1.78E-02	1.23E-01	1.56E+01	5.18E+01	1.12E-01	8.86E-02	6.84E-03	1.43E-02
0.00	100	82	1.78E-02	1.23E-01	9.23E+00	3.19E+01	1.20E-01	9.63E-02	1.16E-02	2.32E-02

(c)

Radial Location	Number Of Drops		Dispersed Phase Fraction		Interfacial Area Concentration		Interface Velocity		Sauter Mean Diameter	
r/R	N_1	N_2	α_1	α_2	a_1	a_2	v_1	v_2	D_{sm1}	D_{sm2}
[-]	[-]	[-]	[-]	[-]	[1/m]	[1/m]	[m/s]	[m/s]	[m]	[m]
0.96	38	31	5.71E-03	4.85E-02	7.83E+00	1.57E+01	9.78E-02	7.39E-02	4.38E-03	1.86E-02
0.91	47	42	5.69E-03	6.65E-02	8.69E+00	2.01E+01	1.16E-01	6.82E-02	3.93E-03	1.99E-02
0.85	68	69	7.12E-03	1.12E-01	1.20E+01	2.72E+01	1.04E-01	8.94E-02	3.56E-03	2.48E-02
0.80	55	75	7.44E-03	1.29E-01	6.75E+00	2.82E+01	1.15E-01	8.57E-02	6.62E-03	2.76E-02
0.73	67	84	8.40E-03	1.39E-01	9.46E+00	3.35E+01	1.14E-01	8.20E-02	5.33E-03	2.50E-02
0.66	78	92	9.37E-03	1.49E-01	1.22E+01	3.87E+01	1.13E-01	7.83E-02	4.62E-03	2.31E-02
0.58	77	77	1.35E-02	1.25E-01	1.32E+01	3.95E+01	1.07E-01	7.76E-02	6.12E-03	1.90E-02
0.49	84	92	1.15E-02	1.40E-01	1.27E+01	5.08E+01	1.08E-01	8.37E-02	5.41E-03	1.65E-02
0.38	109	98	1.63E-02	1.44E-01	1.86E+01	3.87E+01	1.08E-01	8.99E-02	5.24E-03	2.23E-02
0.00	65	97	8.29E-03	1.36E-01	8.30E+00	2.90E+01	1.17E-01	1.00E-01	5.99E-03	2.81E-02

Table A.11: Values of local two-phase flow parameters at (a) z/D=1.7, (b) z/D=5.0 & (c) z/D=8.3; Run # 11

(a)

| Radial Location	Number Of Drops		Dispersed Phase Fraction		Interfacial Area Concentration		Interface Velocity		Sauter Mean Diameter	
r/R	N_1	N_2	α_1	α_2	a_1	a_2	v_1	v_2	D_{sm1}	D_{sm2}
[-]	[-]	[-]	[-]	[-]	[1/m]	[1/m]	[m/s]	[m/s]	[m]	[m]
0.96	0	0	0.00E+00	0.00E+00	0.00E+00	0.00E+00	0.00E+00	0.00E+00	-	-
0.91	48	29	8.54E-03	5.33E-02	1.06E+01	1.37E+01	1.12E-01	9.69E-02	4.83E-03	2.34E-02
0.85	111	40	1.55E-02	5.79E-02	2.75E+01	2.43E+01	1.12E-01	9.25E-02	3.38E-03	1.43E-02
0.80	80	62	1.06E-02	9.45E-02	1.67E+01	2.60E+01	1.10E-01	9.25E-02	3.82E-03	2.19E-02
0.73	48	83	5.77E-03	1.31E-01	5.91E+00	2.76E+01	1.08E-01	8.81E-02	5.86E-03	2.85E-02
0.66	81	71	1.19E-02	1.11E-01	1.31E+01	2.84E+01	1.14E-01	8.12E-02	5.46E-03	2.33E-02
0.58	72	91	8.82E-03	1.33E-01	9.11E+00	2.64E+01	1.23E-01	1.03E-01	5.81E-03	3.01E-02
0.49	94	104	3.47E-02	1.09E-01	1.27E+01	3.17E+01	1.18E-01	1.01E-01	1.64E-02	2.06E-02
0.38	116	116	1.63E-02	1.52E-01	1.63E+01	3.71E+01	1.33E-01	1.14E-01	6.03E-03	2.47E-02
0.00	85	146	1.15E-02	1.96E-01	7.88E+00	5.76E+01	1.15E-01	8.02E-02	8.75E-03	2.05E-02

(b)

Radial Location	Number Of Drops		Dispersed Phase Fraction		Interfacial Area Concentration		Interface Velocity		Sauter Mean Diameter	
r/R	N_1	N_2	α_1	α_2	a_1	a_2	v_1	v_2	D_{sm1}	D_{sm2}
[-]	[-]	[-]	[-]	[-]	[1/m]	[1/m]	[m/s]	[m/s]	[m]	[m]
0.96	25	46	2.63E-03	8.05E-02	2.95E+00	1.73E+01	9.66E-02	5.95E-02	5.35E-03	2.79E-02
0.91	52	70	5.08E-03	1.06E-01	7.02E+00	3.10E+01	1.06E-01	8.43E-02	4.34E-03	2.05E-02
0.85	53	110	4.41E-03	1.76E-01	5.09E+00	3.58E+01	1.33E-01	9.19E-02	5.20E-03	2.95E-02
0.80	61	106	7.09E-03	1.59E-01	6.64E+00	2.97E+01	1.30E-01	8.27E-02	6.41E-03	3.22E-02
0.73	68	102	9.76E-03	1.43E-01	7.41E+00	2.66E+01	1.28E-01	7.35E-02	7.91E-03	3.22E-02
0.66	65	78	9.13E-03	1.18E-01	8.18E+00	2.36E+01	1.18E-01	9.38E-02	6.70E-03	3.00E-02
0.58	106	72	1.72E-02	9.91E-02	1.94E+01	2.57E+01	1.26E-01	9.63E-02	5.32E-03	2.31E-02
0.49	75	100	1.01E-02	1.41E-01	9.73E+00	3.45E+01	1.20E-01	9.73E-02	6.24E-03	2.45E-02
0.38	74	91	1.15E-02	1.17E-01	8.92E+00	4.81E+01	1.11E-01	9.89E-02	7.73E-03	1.46E-02
0.00	85	94	1.25E-02	1.26E-01	1.06E+01	2.47E+01	1.26E-01	1.01E-01	7.04E-03	3.06E-02

(c)

Radial Location	Number Of Drops		Dispersed Phase Fraction		Interfacial Area Concentration		Interface Velocity		Sauter Mean Diameter	
r/R	N_1	N_2	α_1	α_2	a_1	a_2	v_1	v_2	D_{sm1}	D_{sm2}
[-]	[-]	[-]	[-]	[-]	[1/m]	[1/m]	[m/s]	[m/s]	[m]	[m]
0.96	28	30	3.55E-03	4.79E-02	4.97E+00	1.50E+01	9.96E-02	7.28E-02	4.28E-03	1.91E-02
0.91	46	37	6.53E-03	5.53E-02	7.83E+00	1.64E+01	1.23E-01	6.39E-02	5.01E-03	2.02E-02
0.85	34	68	2.71E-03	1.10E-01	2.87E+00	2.13E+01	1.32E-01	7.00E-02	5.67E-03	3.11E-02
0.80	59	51	8.37E-03	8.10E-02	1.05E+01	1.95E+01	1.30E-01	8.60E-02	4.81E-03	2.49E-02
0.73	58	66	7.27E-03	1.03E-01	9.24E+00	2.47E+01	1.25E-01	8.13E-02	4.73E-03	2.49E-02
0.66	57	81	6.17E-03	1.25E-01	8.02E+00	3.00E+01	1.09E-01	7.66E-02	4.62E-03	2.49E-02
0.58	56	89	6.16E-03	1.27E-01	6.95E+00	4.21E+01	1.21E-01	9.13E-02	5.31E-03	1.81E-02
0.49	83	78	1.45E-02	1.11E-01	1.34E+01	4.19E+01	1.05E-01	8.11E-02	6.48E-03	1.59E-02
0.38	104	96	1.40E-02	1.32E-01	1.65E+01	3.25E+01	1.24E-01	9.45E-02	5.10E-03	2.44E-02
0.00	76	144	6.71E-03	1.75E-01	7.55E+00	4.16E+01	1.35E-01	1.02E-01	5.33E-03	2.53E-02

Table A.12: Values of local two-phase flow parameters at (a) z/D=1.7, (b) z/D=5.0 & (c) z/D=8.3; Run # 12

(a)

Radial Location	Number Of Drops		Dispersed Phase Fraction		Interfacial Area Concentration		Interface Velocity		Sauter Mean Diameter	
r/R	N_1	N_2	α_1	α_2	a_1	a_2	v_1	v_2	D_{sm1}	D_{sm2}
[-]	[-]	[-]	[-]	[-]	[1/m]	[1/m]	[m/s]	[m/s]	[m]	[m]
0.96	0	0	0.00E+00	0.00E+00	0.00E+00	0.00E+00	0.00E+00	0.00E+00	-	-
0.91	254	8	1.03E-02	1.61E-02	8.06E+01	4.50E+00	1.03E-01	6.99E-02	7.65E-04	2.14E-02
0.85	40	23	3.55E-03	4.56E-02	7.69E+00	1.09E+01	1.60E-01	6.81E-02	2.77E-03	2.50E-02
0.80	0	0	5.93E-03	5.85E-02	2.04E+01	2.07E+01	1.26E-01	7.83E-02	1.75E-03	1.70E-02
0.73	120	41	8.31E-03	7.14E-02	3.30E+01	3.04E+01	9.17E-02	8.86E-02	1.51E-03	1.41E-02
0.66	40	46	2.73E-03	1.00E-01	5.75E+00	1.80E+01	1.28E-01	9.01E-02	2.85E-03	3.34E-02
0.58	85	50	7.89E-03	8.81E-02	1.77E+01	2.10E+01	1.08E-01	7.99E-02	2.67E-03	2.52E-02
0.49	48	64	4.54E-03	1.00E-01	6.17E+00	2.01E+01	1.23E-01	9.59E-02	4.41E-03	3.00E-02
0.38	153	69	1.78E-02	9.36E-02	2.81E+01	2.45E+01	1.36E-01	1.12E-01	3.81E-03	2.29E-02
0.00	228	121	2.43E-02	1.61E-01	4.26E+01	4.52E+01	1.35E-01	1.17E-01	3.43E-03	2.14E-02

(b)

Radial Location	Number Of Drops		Dispersed Phase Fraction		Interfacial Area Concentration		Interface Velocity		Sauter Mean Diameter	
r/R	N_1	N_2	α_1	α_2	a_1	a_2	v_1	v_2	D_{sm1}	D_{sm2}
[-]	[-]	[-]	[-]	[-]	[1/m]	[1/m]	[m/s]	[m/s]	[m]	[m]
0.96	107	29	9.78E-03	4.51E-02	3.06E+01	1.72E+01	1.14E-01	4.68E-02	1.91E-03	1.58E-02
0.91	171	32	1.23E-02	4.22E-02	4.00E+01	1.40E+01	1.53E-01	8.78E-02	1.85E-03	1.81E-02
0.85	157	36	1.25E-02	5.32E-02	3.48E+01	1.60E+01	1.58E-01	9.39E-02	2.16E-03	2.00E-02
0.80	127	36	1.98E-02	6.84E-02	2.85E+01	1.78E+01	1.41E-01	9.06E-02	4.18E-03	2.31E-02
0.73	111	36	2.71E-02	8.36E-02	2.53E+01	1.87E+01	1.25E-01	8.74E-02	6.43E-03	2.69E-02
0.66	96	36	1.12E-02	6.03E-02	2.21E+01	1.95E+01	1.30E-01	8.43E-02	3.05E-03	1.85E-02
0.58	162	52	1.61E-02	6.71E-02	3.78E+01	2.14E+01	1.27E-01	1.06E-01	2.56E-03	1.88E-02
0.49	216	55	1.99E-02	7.61E-02	4.54E+01	2.09E+01	1.45E-01	9.87E-02	2.62E-03	2.18E-02
0.38	179	69	1.74E-02	8.89E-02	3.50E+01	3.04E+01	1.52E-01	1.04E-01	2.98E-03	1.75E-02
0.00	266	87	2.10E-02	1.19E-01	5.82E+01	3.54E+01	1.38E-01	1.10E-01	2.17E-03	2.02E-02

(c)

Radial Location	Number Of Drops		Dispersed Phase Fraction		Interfacial Area Concentration		Interface Velocity		Sauter Mean Diameter	
r/R	N_1	N_2	α_1	α_2	a_1	a_2	v_1	v_2	D_{sm1}	D_{sm2}
[-]	[-]	[-]	[-]	[-]	[1/m]	[1/m]	[m/s]	[m/s]	[m]	[m]
0.96	136	26	1.62E-02	4.44E-02	3.46E+01	1.55E+01	1.28E-01	7.60E-02	2.81E-03	1.72E-02
0.91	117	39	9.88E-03	6.51E-02	2.73E+01	2.37E+01	1.39E-01	8.74E-02	2.17E-03	1.65E-02
0.85	110	40	1.06E-02	6.37E-02	3.35E+01	2.03E+01	1.42E-01	9.85E-02	1.89E-03	1.88E-02
0.80	160	34	1.70E-02	5.05E-02	3.98E+01	1.70E+01	1.44E-01	9.78E-02	2.57E-03	1.78E-02
0.73	149	52	1.27E-02	6.65E-02	3.29E+01	2.35E+01	1.35E-01	9.46E-02	2.32E-03	1.70E-02
0.66	155	57	1.16E-02	7.52E-02	2.20E+01	2.63E+01	1.18E-01	9.51E-02	3.17E-03	1.72E-02
0.58	161	62	1.51E-02	7.66E-02	3.28E+01	3.18E+01	1.48E-01	9.95E-02	2.77E-03	1.45E-02
0.49	275	55	2.41E-02	7.34E-02	6.07E+01	2.51E+01	1.54E-01	1.00E-01	2.38E-03	1.76E-02
0.38	248	58	2.63E-02	8.00E-02	5.70E+01	2.51E+01	1.31E-01	1.02E-01	2.77E-03	1.91E-02
0.00	290	77	1.92E-02	8.91E-02	7.61E+01	3.70E+01	1.17E-01	1.23E-01	1.52E-03	1.44E-02

Appendix B: Plots of Local Data
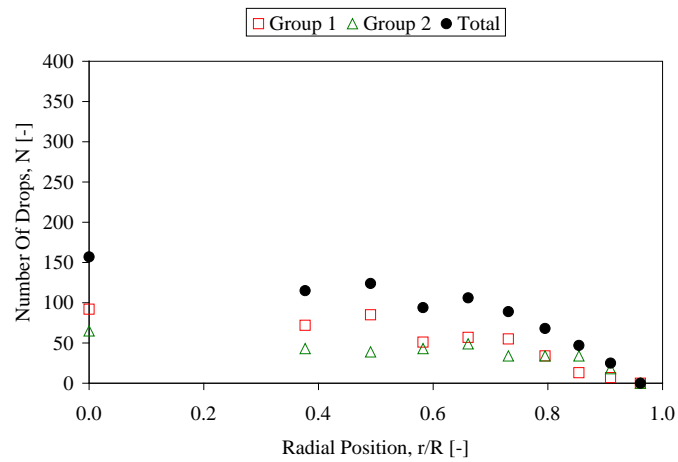
(a)
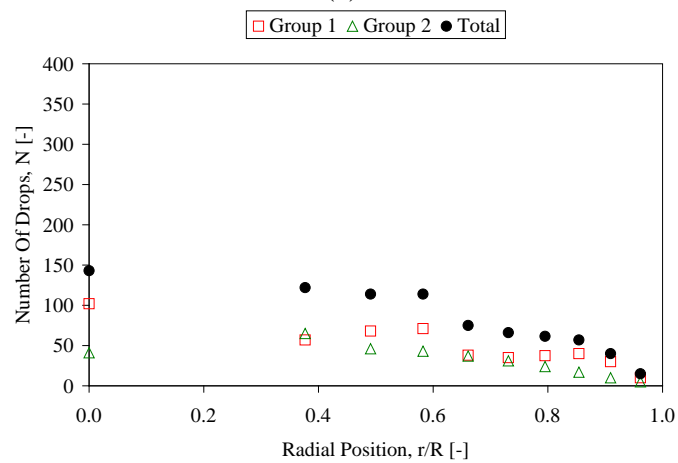
(b)
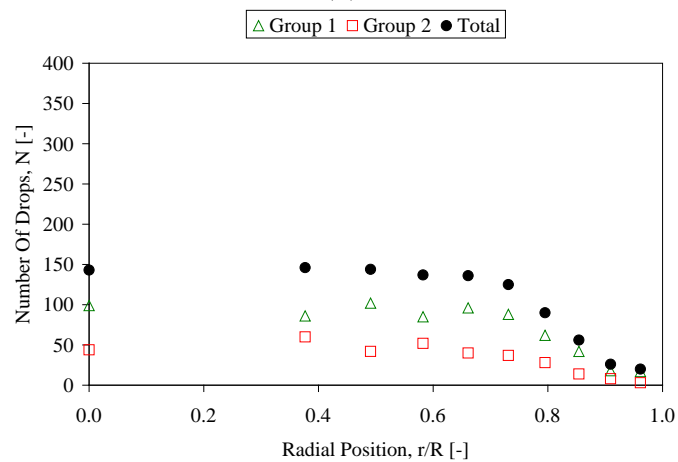
(c)

Figure B.1: Profiles of number of drops at (a) z/D=1.7, (b) z/D=5.0 & (c) z/D=8.3;
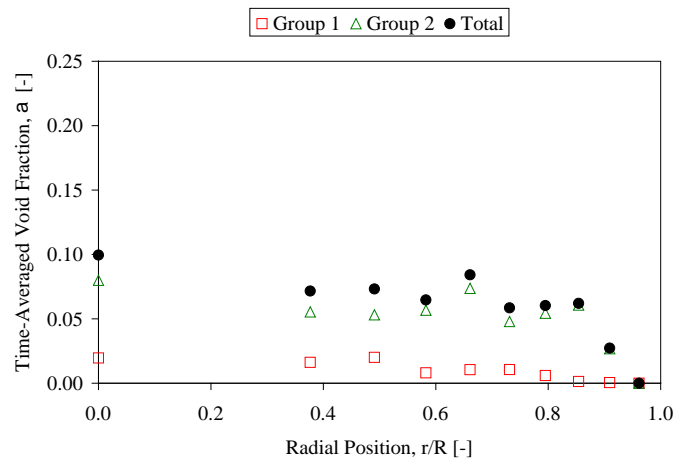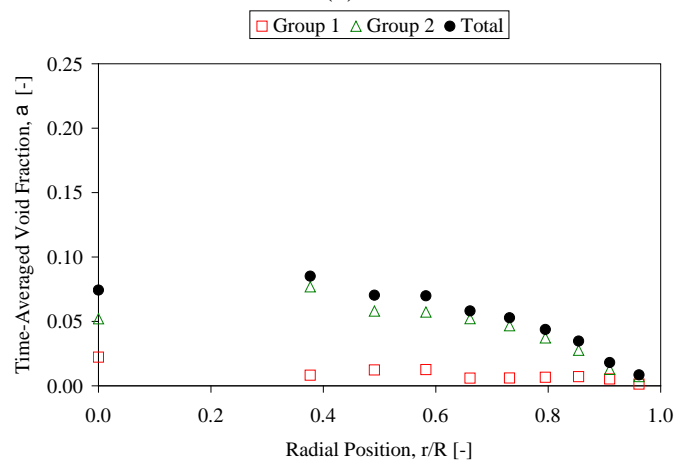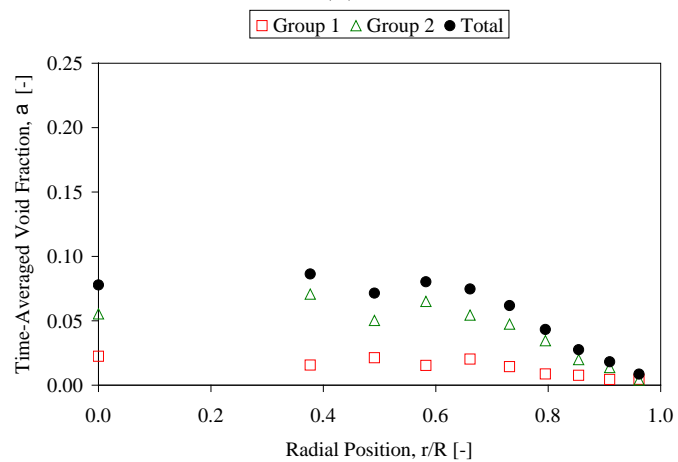
Run # 1

Figure B.2: Local void fraction profiles at (a) z/D=1.7, (b) z/D=5.0 & (c) z/D=8.3;
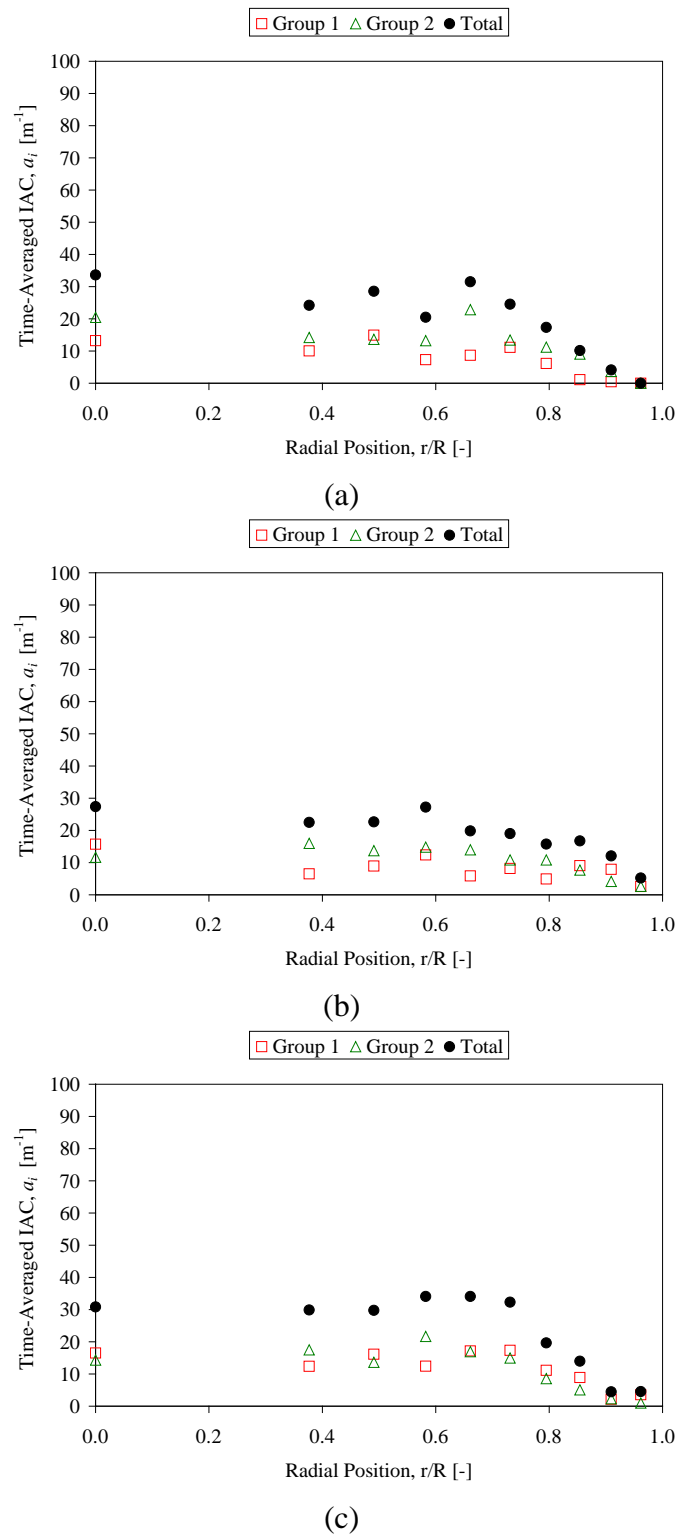
Run # 1
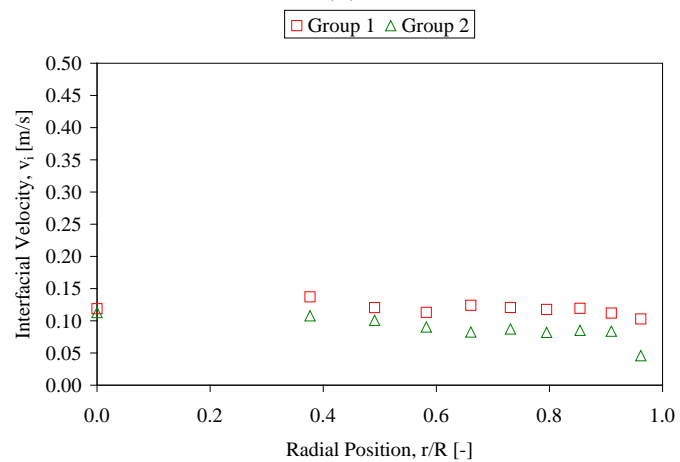
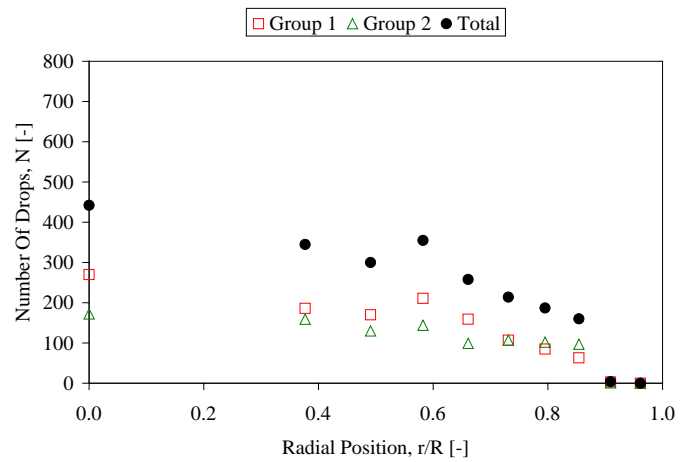Figure B.3: Local interfacial area concentration profiles at (a) z/D=1.7, (b) z/D=5.0 &
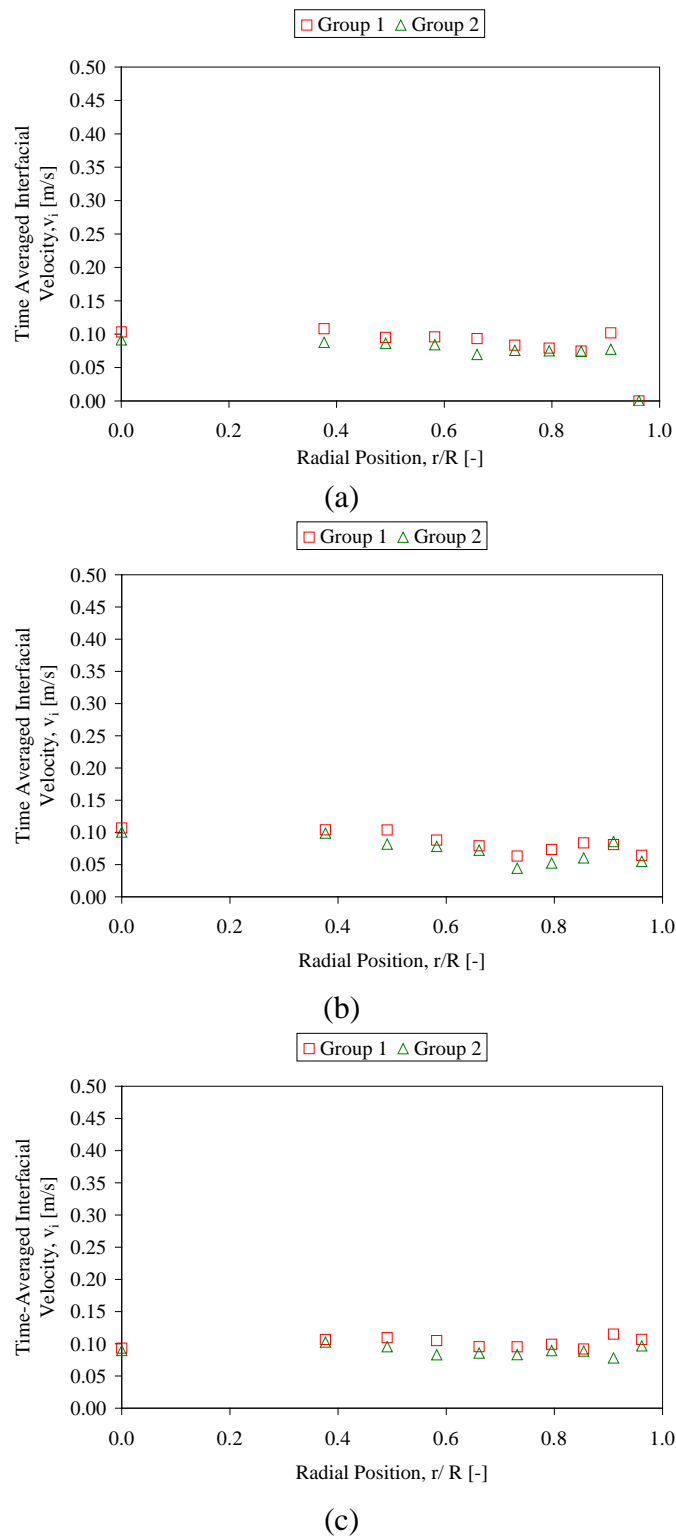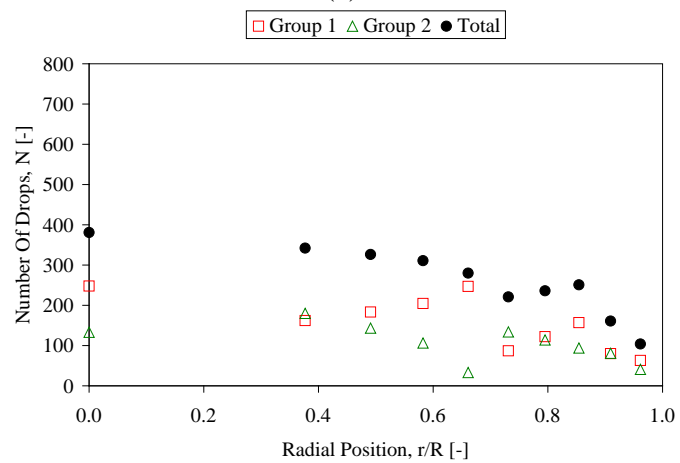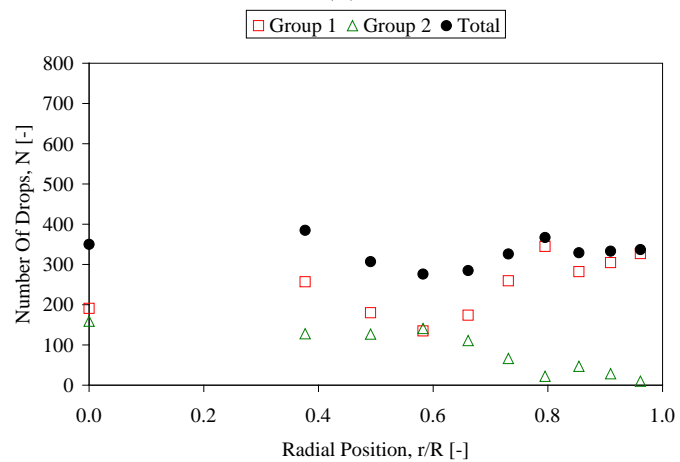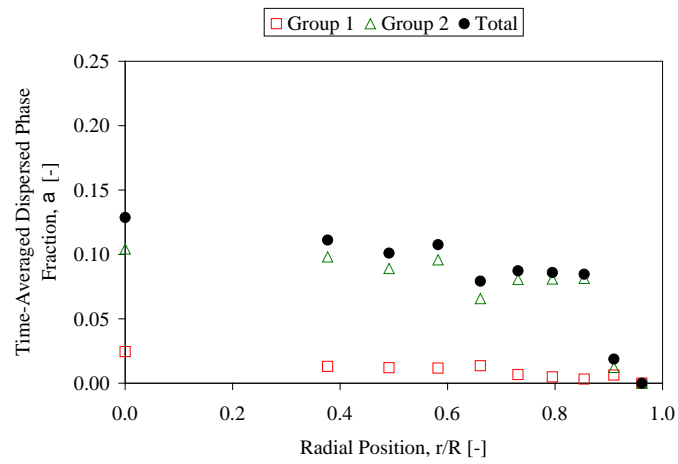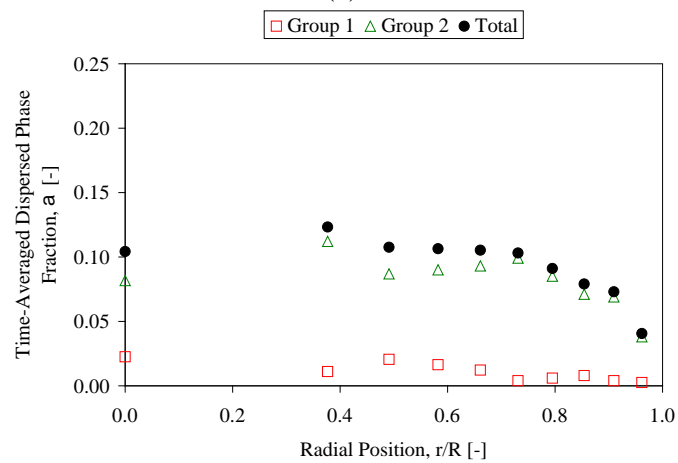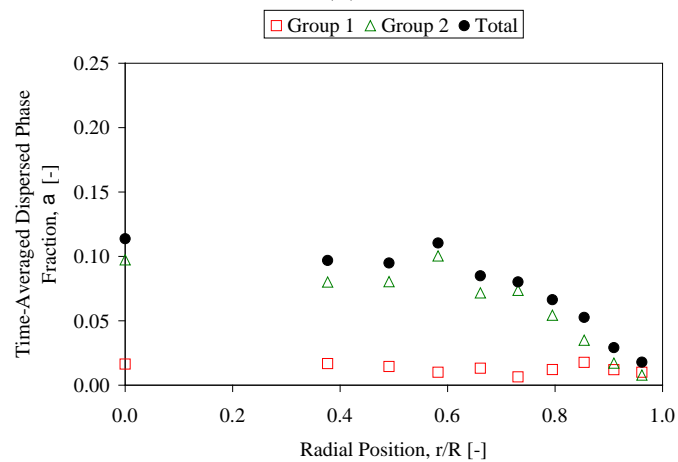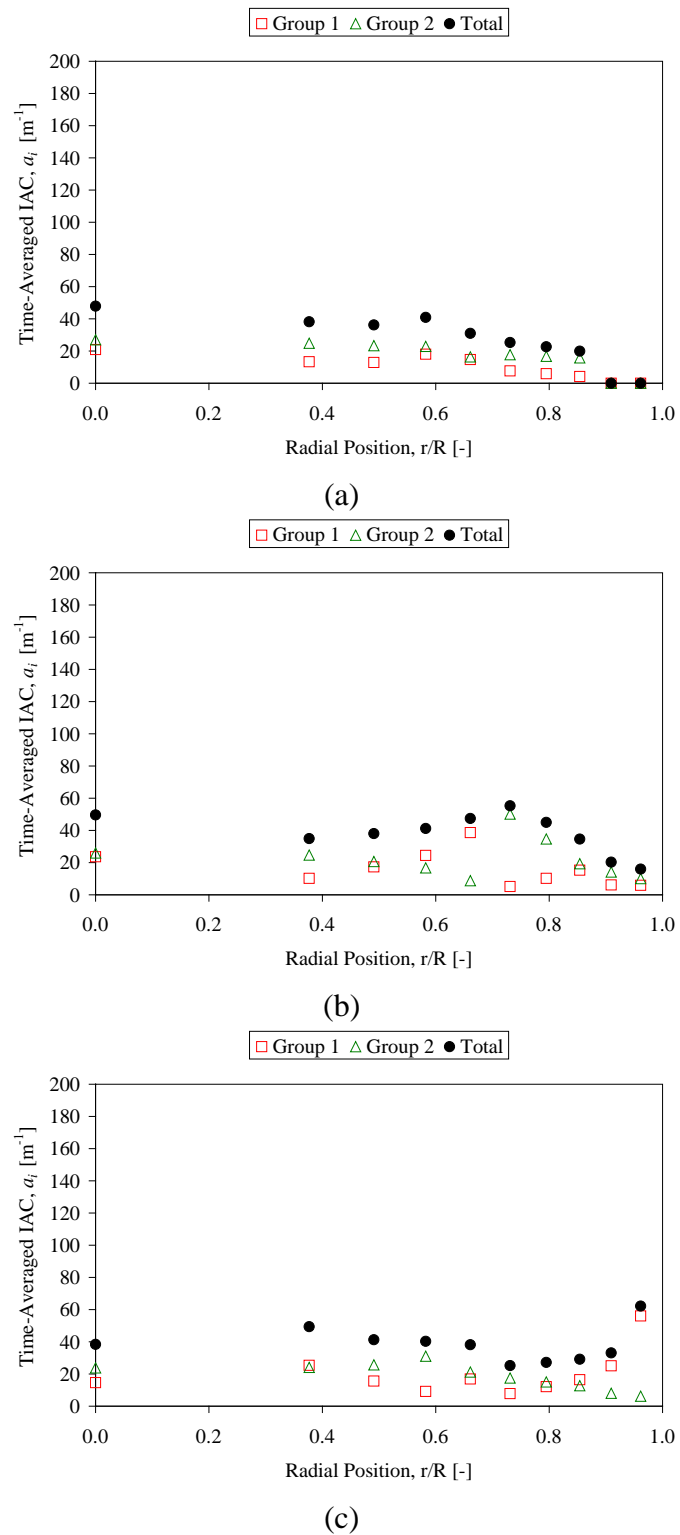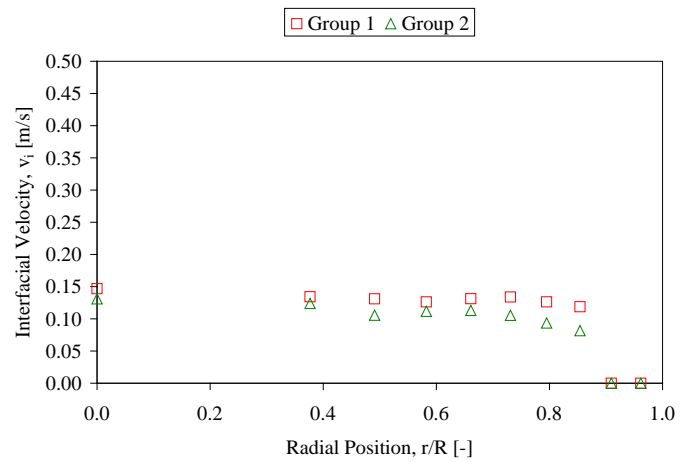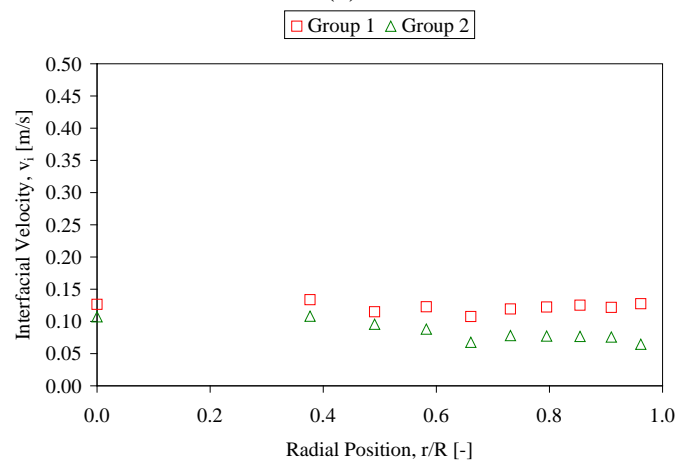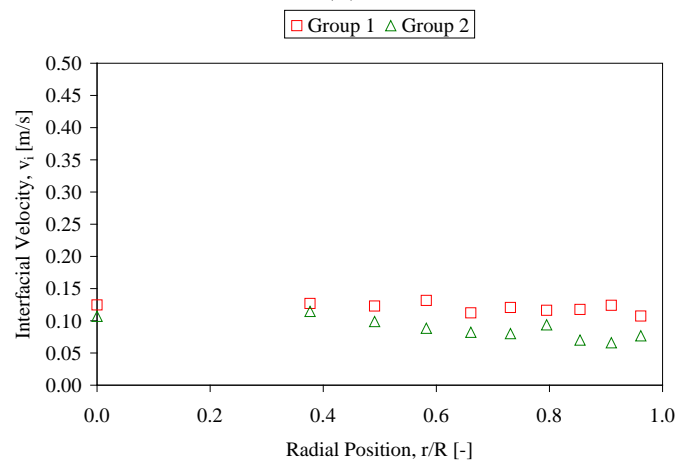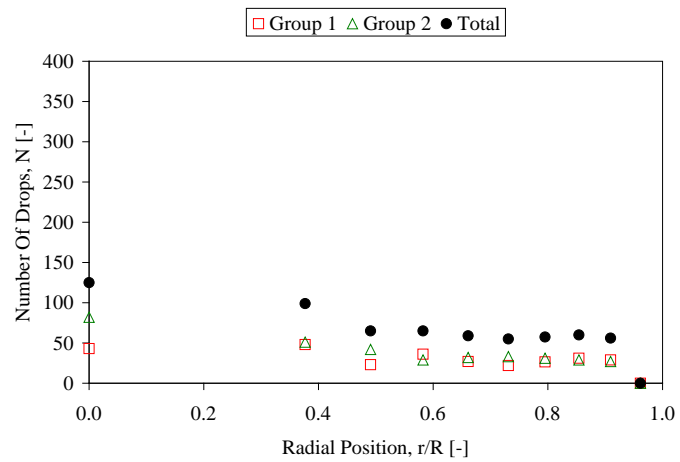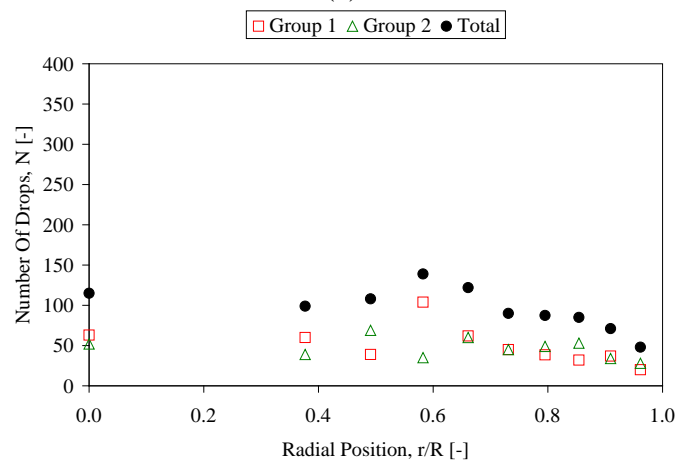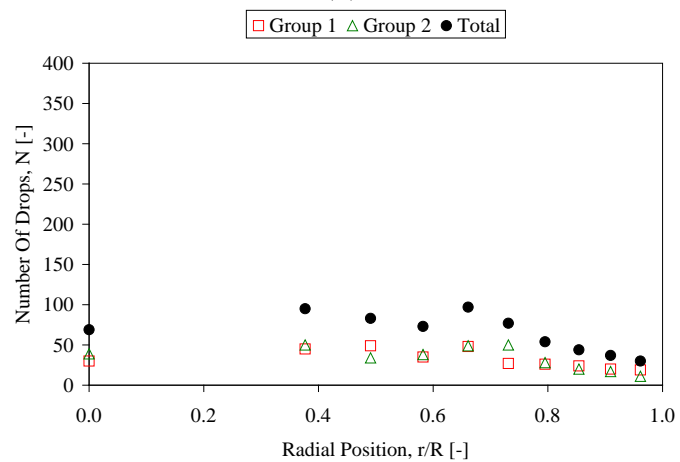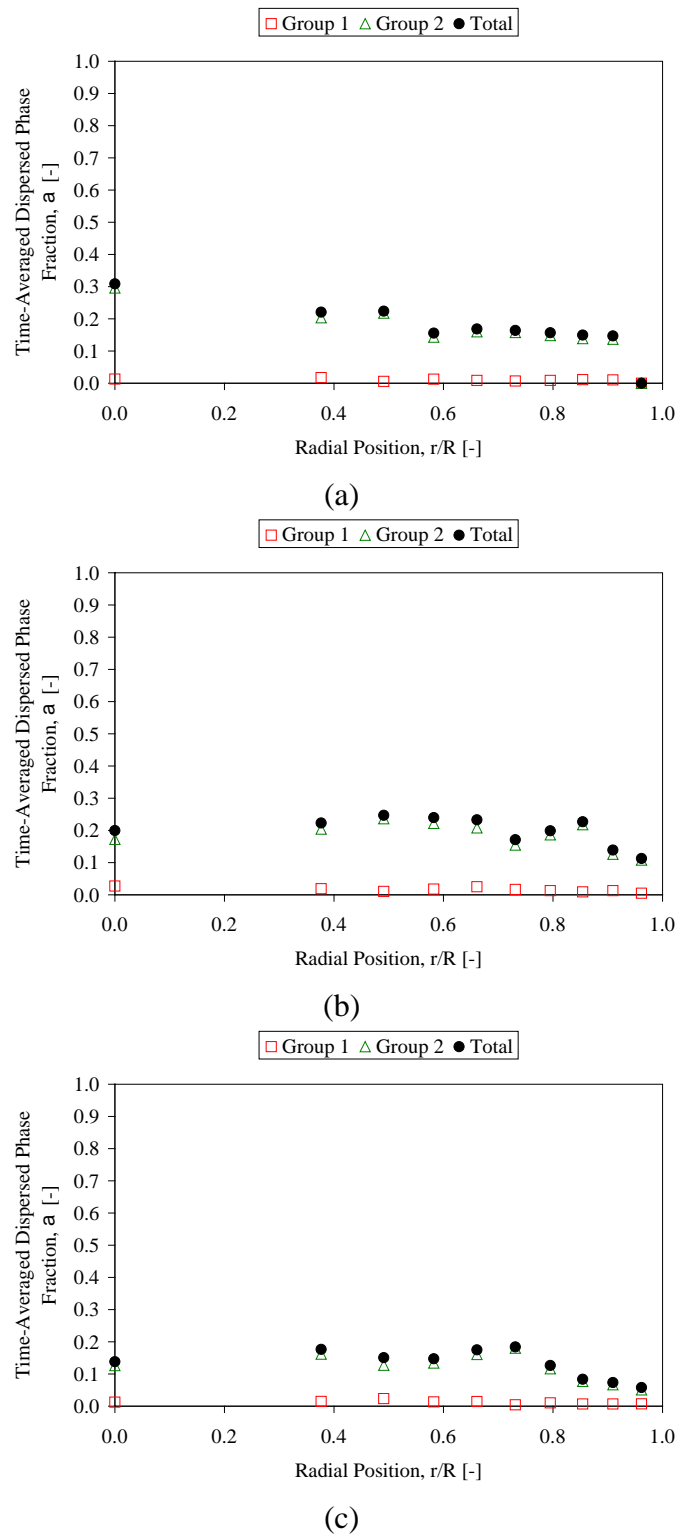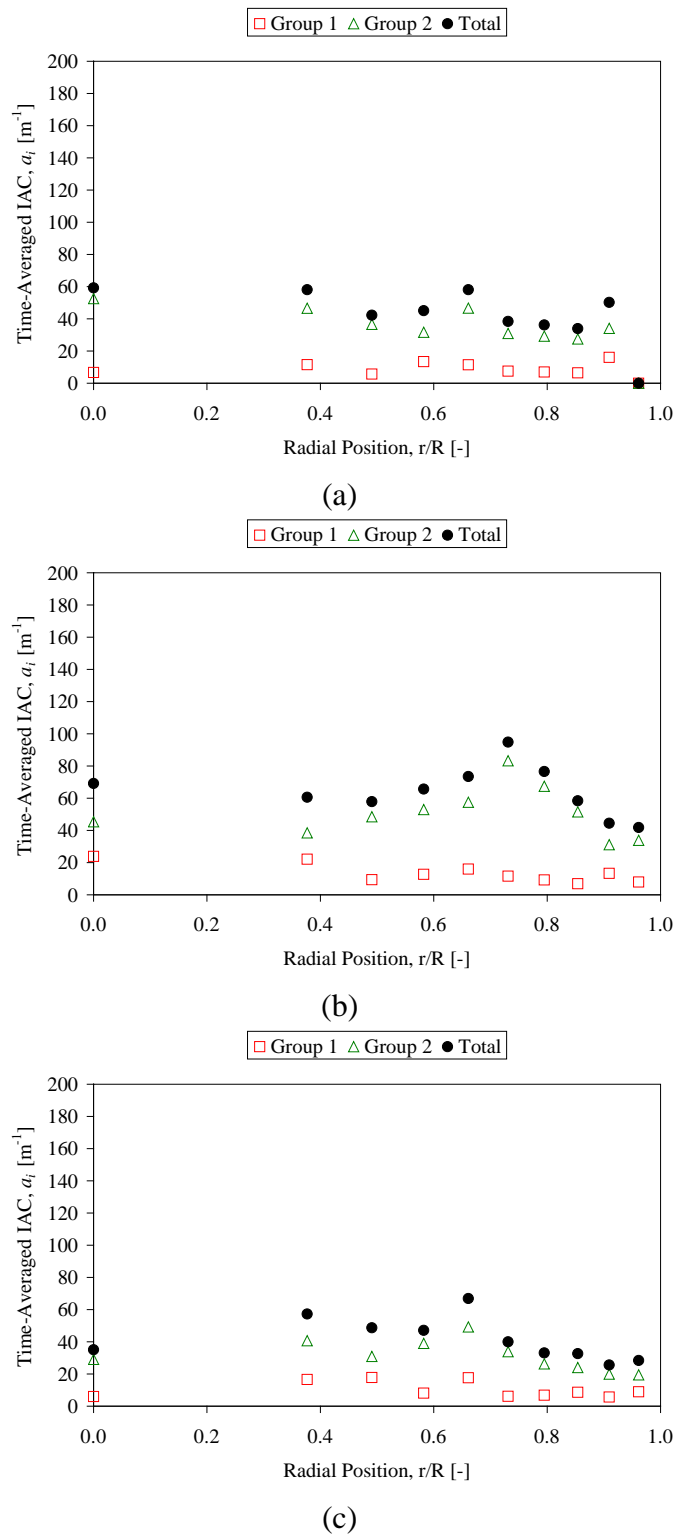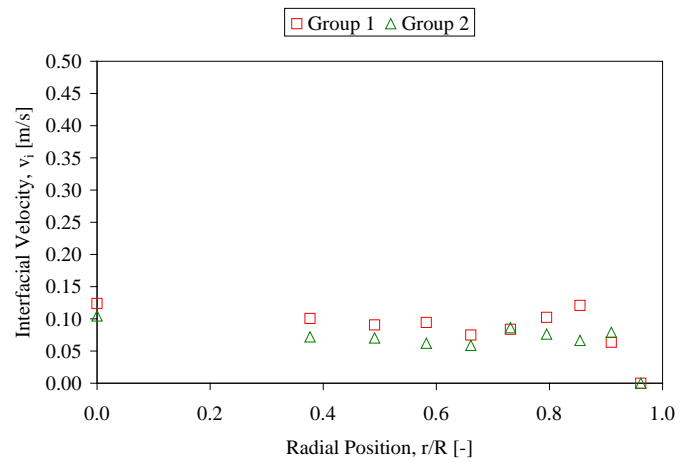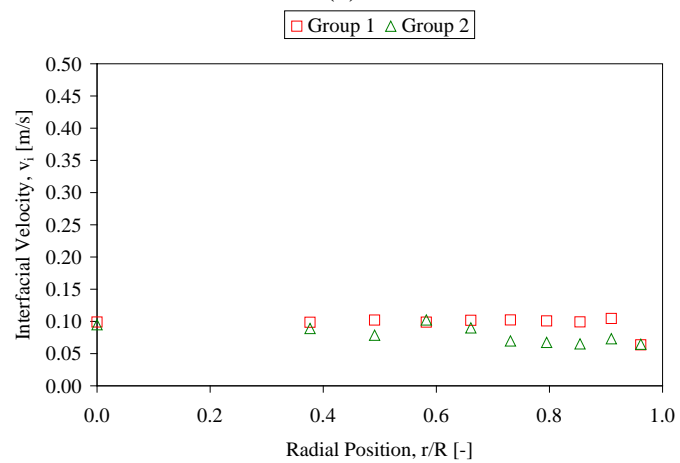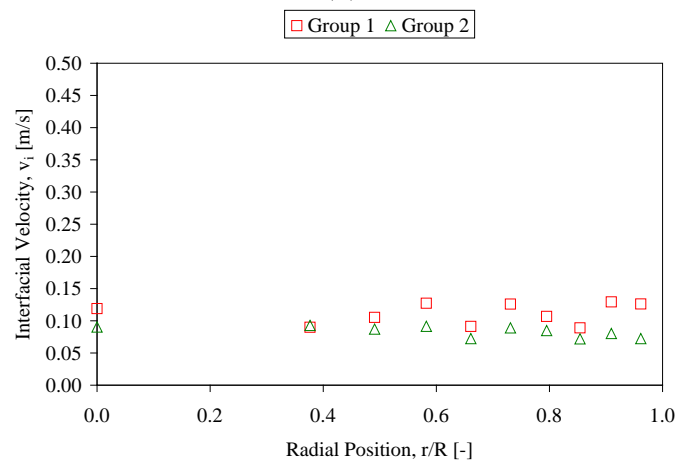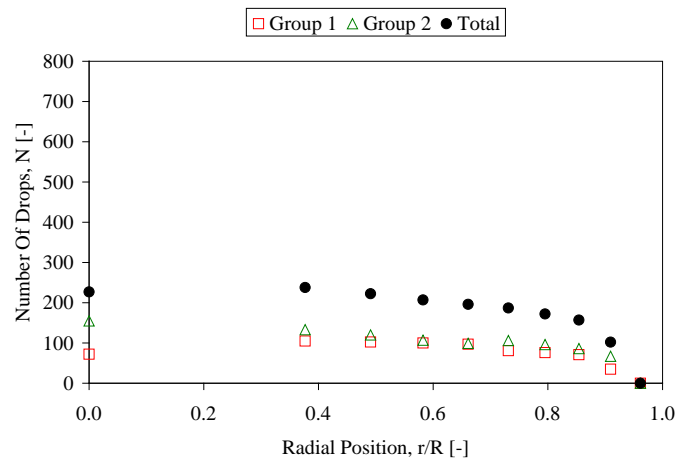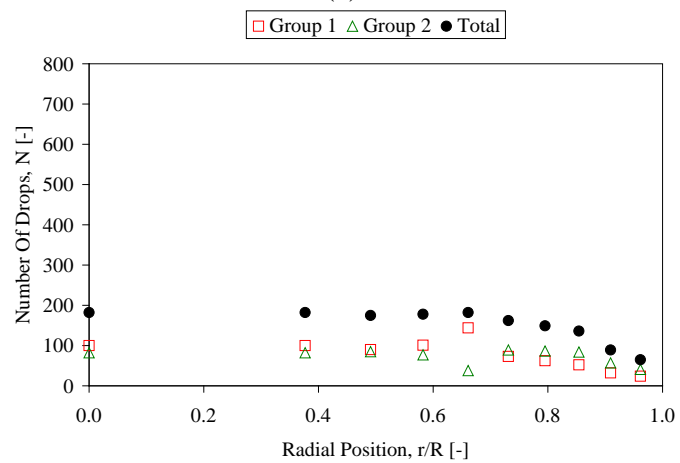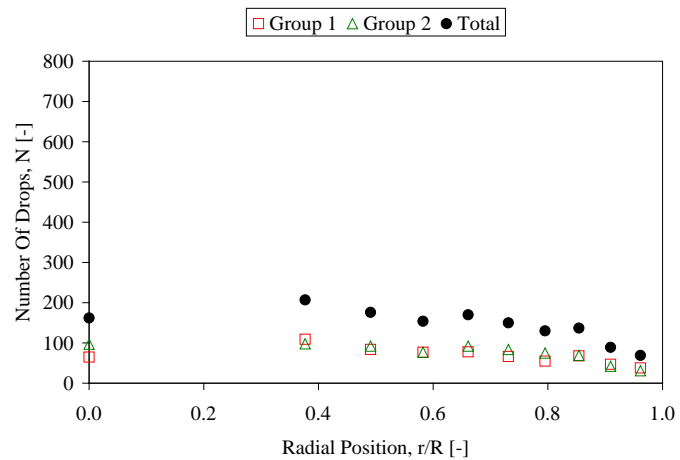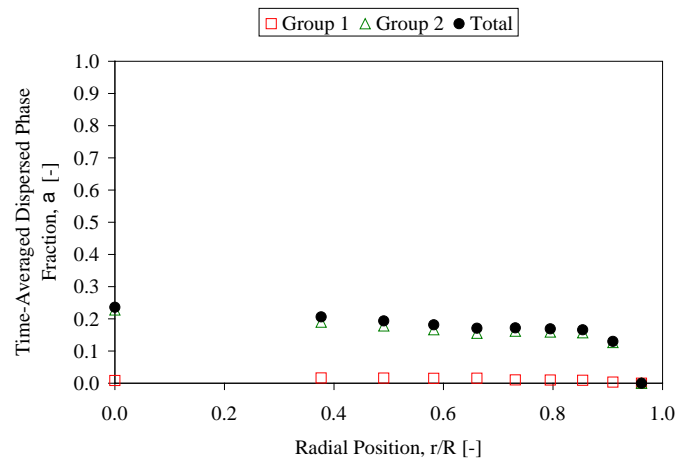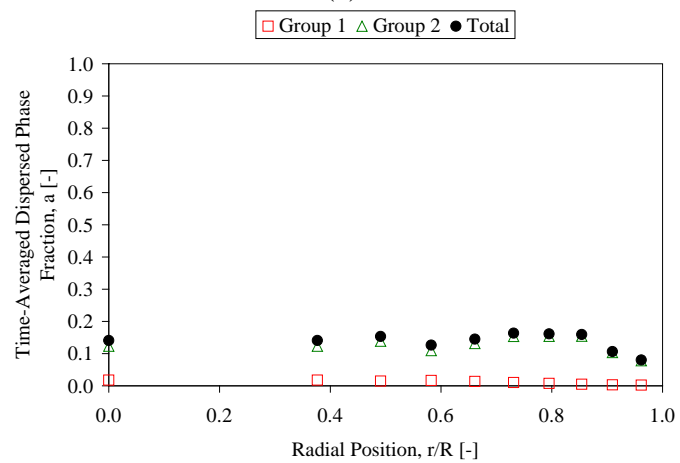
(c) z/D=8.3; Run # 1

Figure B.4: Local interfacial velocity profiles at (a) z/D=1.7, (b) z/D=5.0 &
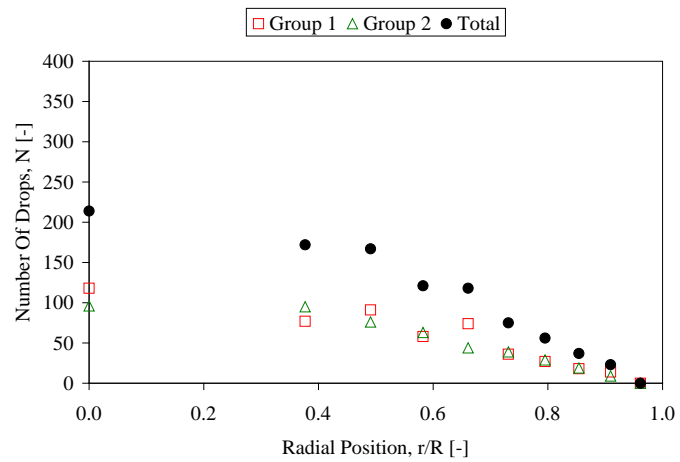
(c) z/D=8.3; Run # 1

(a)
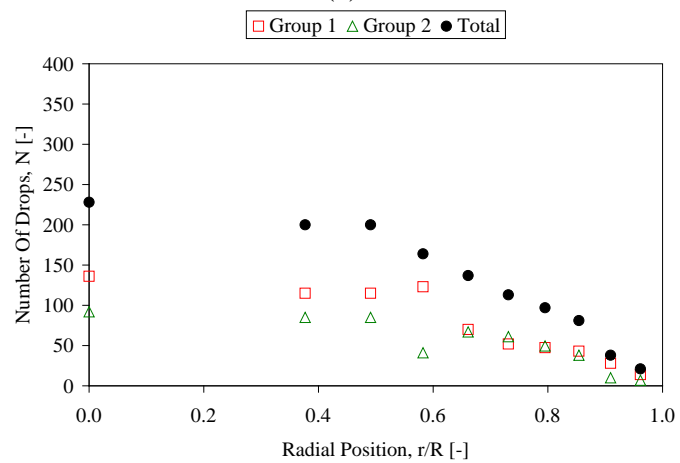
(b)
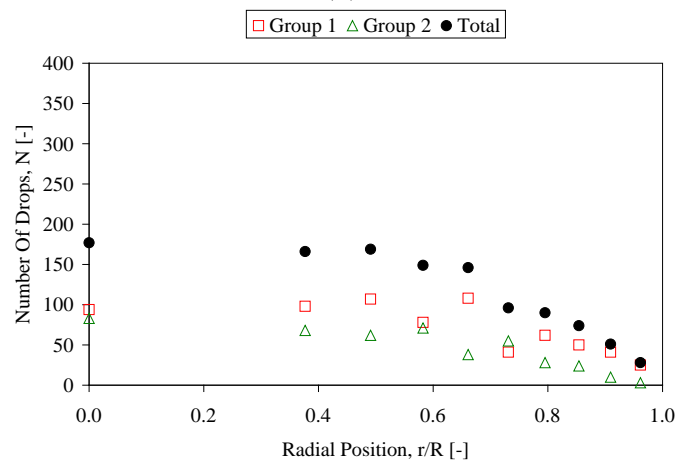
(c)

Figure B.5: Profiles of number of drops at (a) z/D=1.7, (b) z/D=5.0 & (c) z/D=8.3;
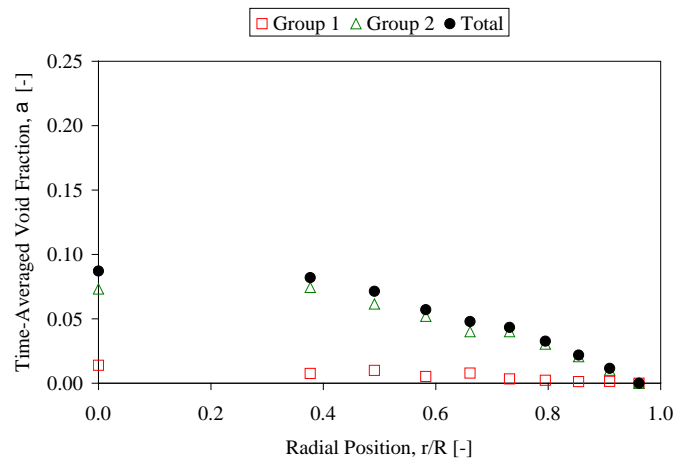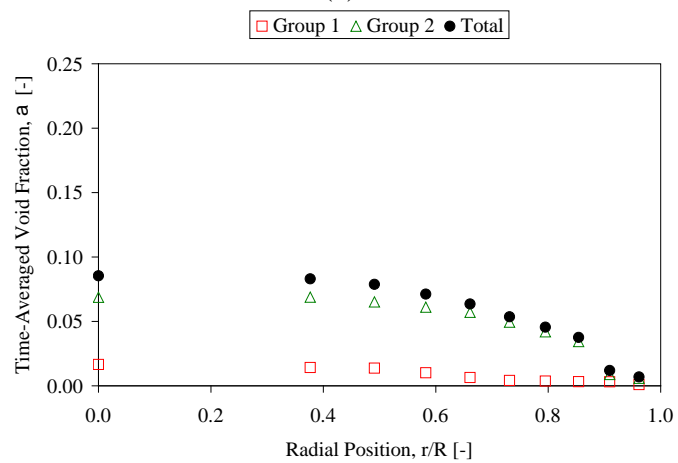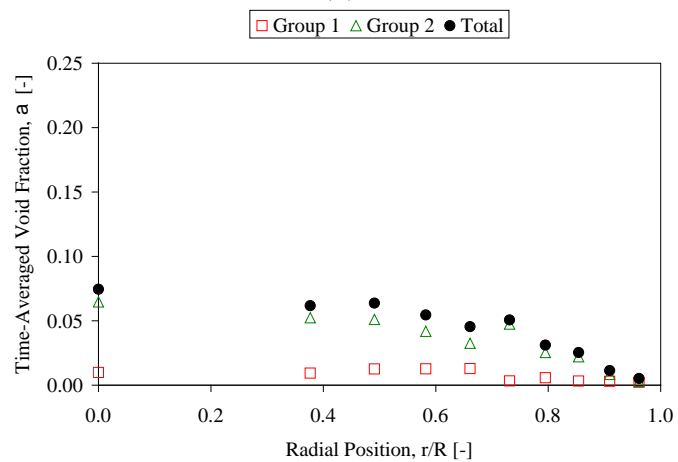
Run # 2
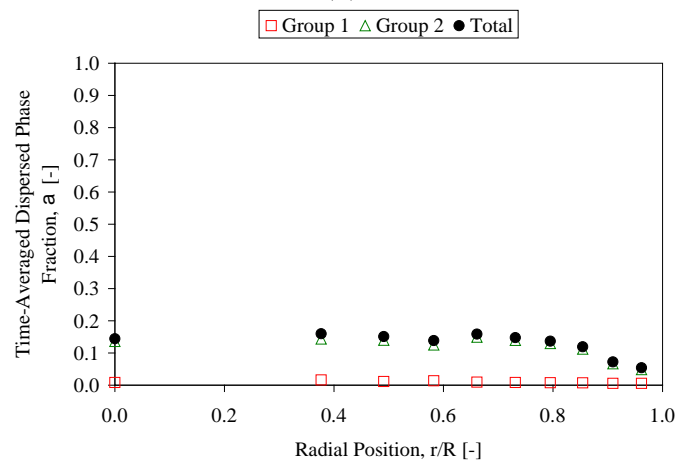
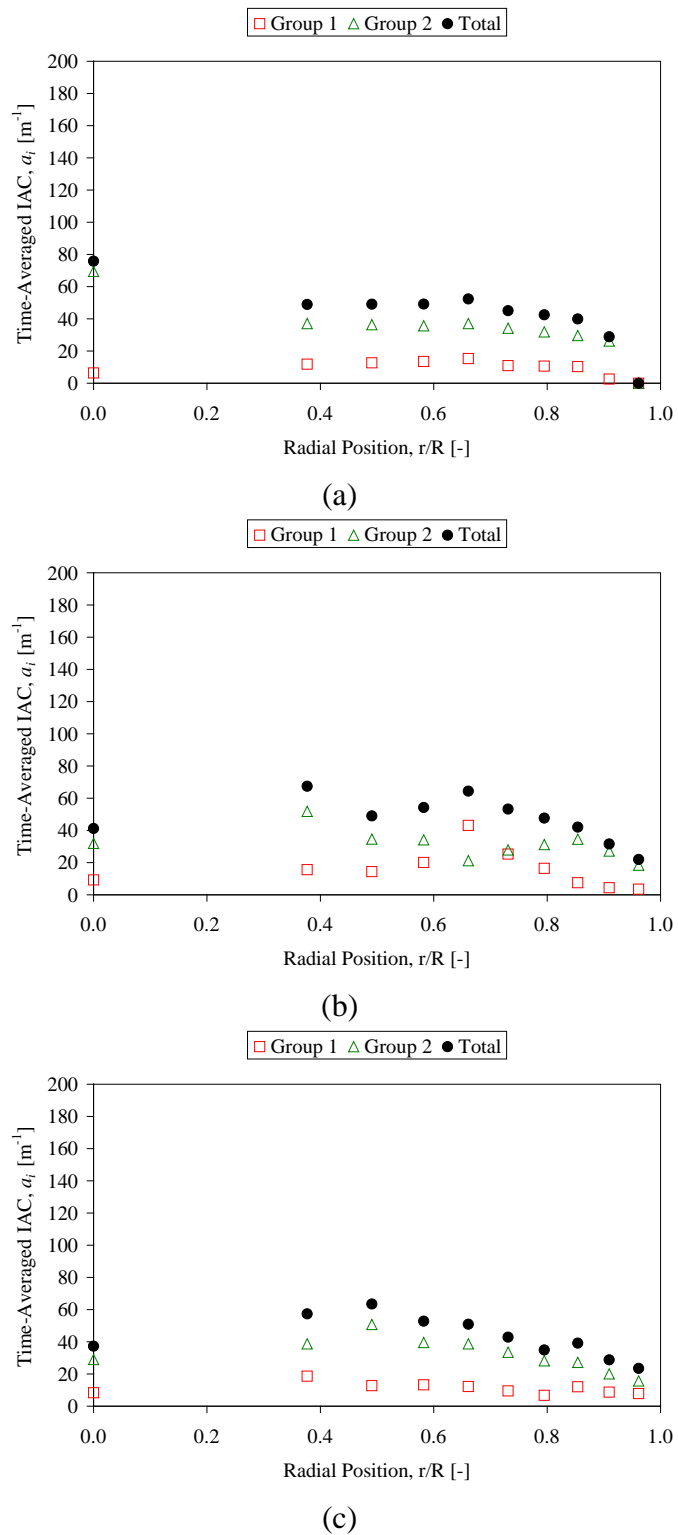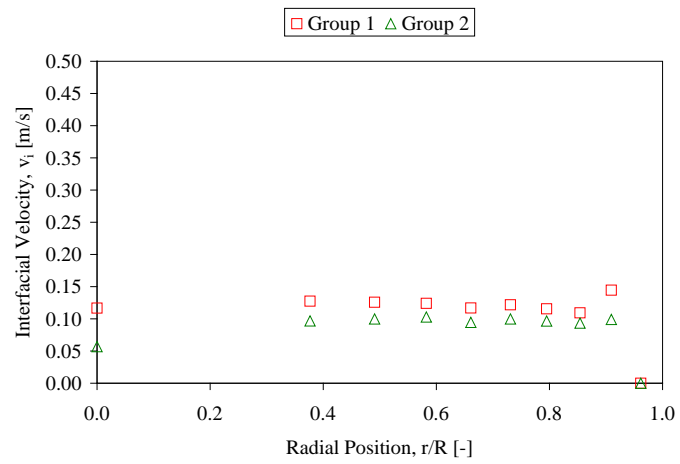Figure B.6: Local void fraction profiles at (a) z/D=1.7, (b) z/D=5.0 & (c) z/D=8.3;
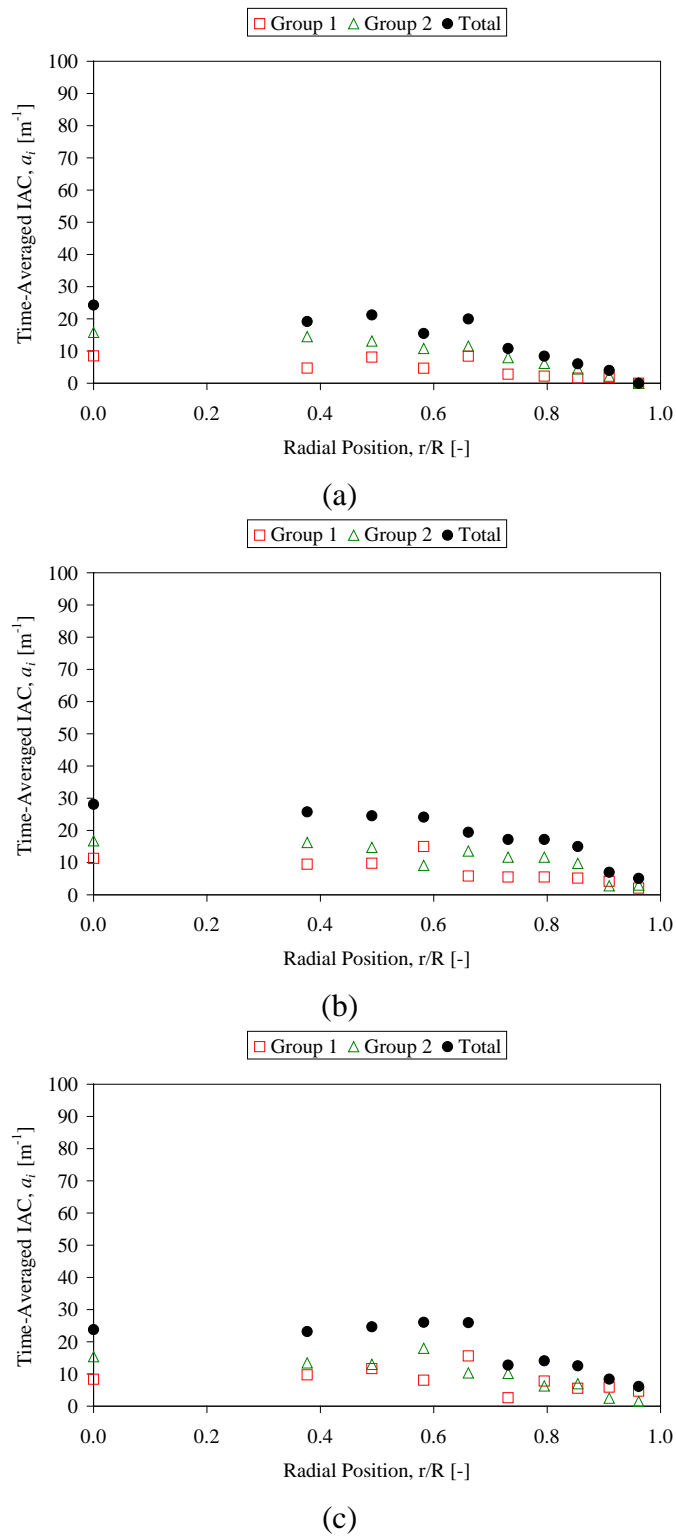
Run # 2

Figure B.7: Local interfacial area concentration profiles at (a) z/D=1.7, (b) z/D=5.0 &
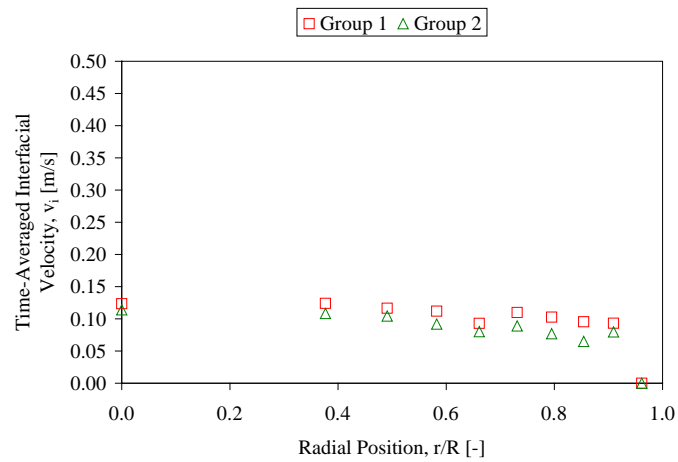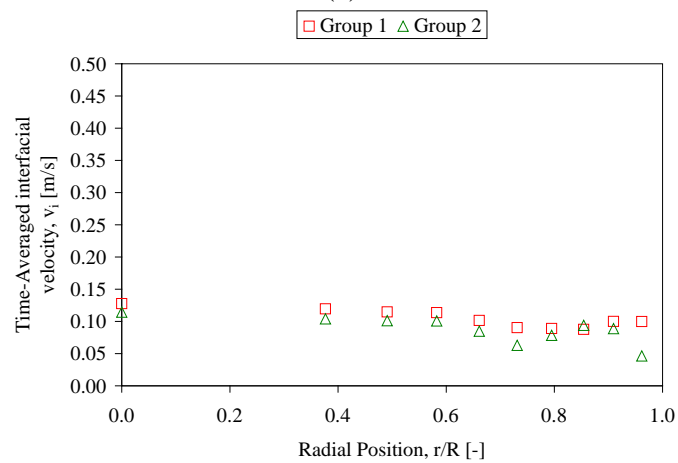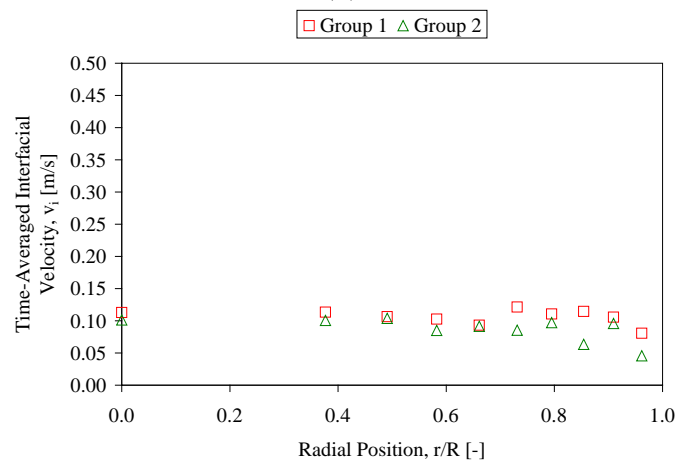
(c) z/D=8.3; Run # 2

Figure B.8: Local interfacial velocity profiles at (a) z/D=1.7, (b) z/D=5.0 &
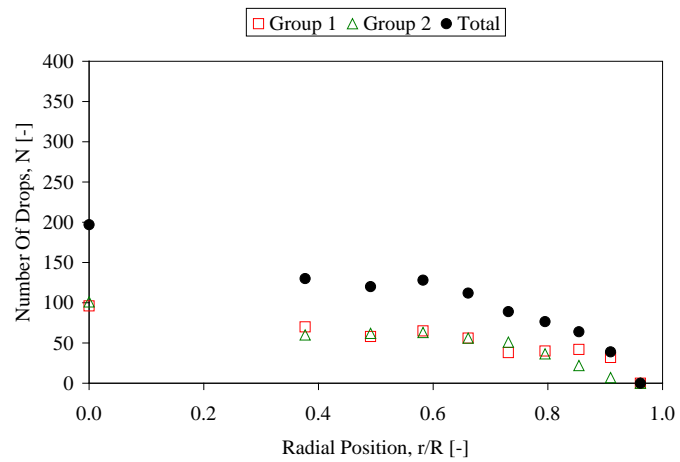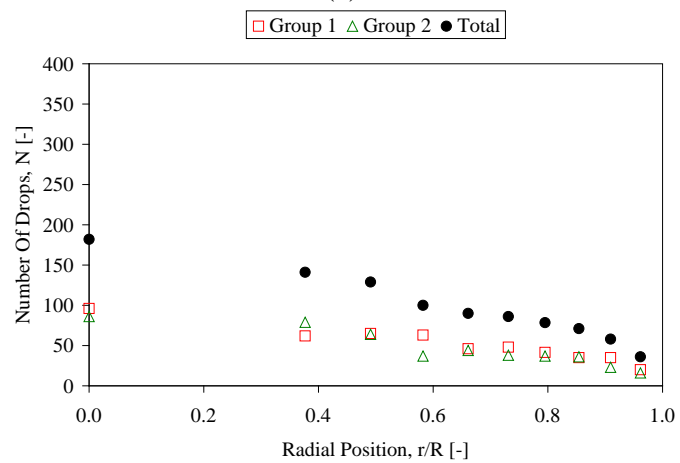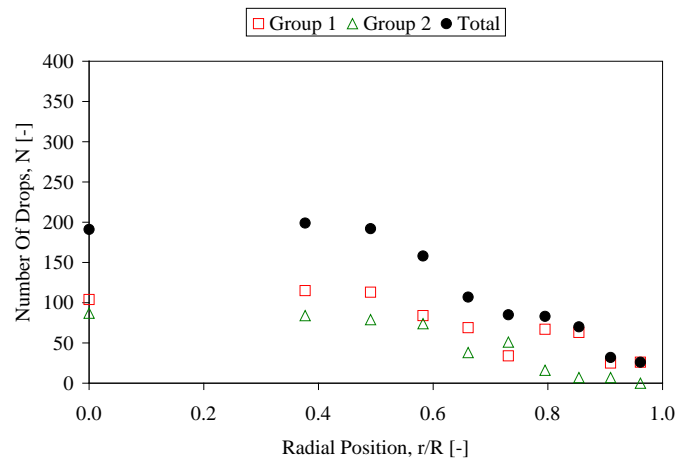
(c) z/D=8.3; Run # 2

Figure B.9: Profiles of number of drops at (a) z/D=1.7, (b) z/D=5.0 & (c) z/D=8.3;
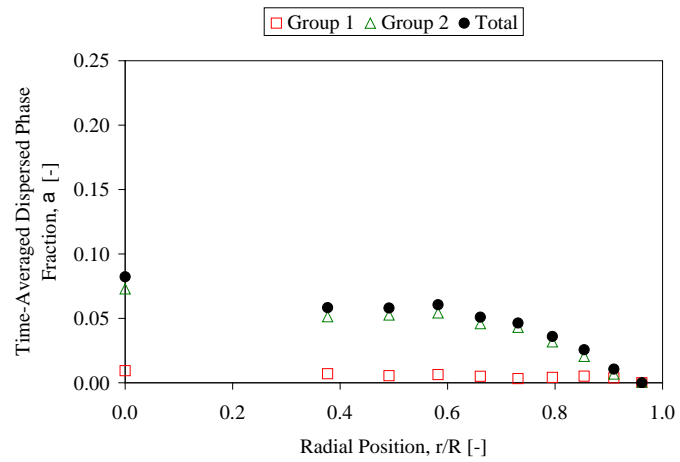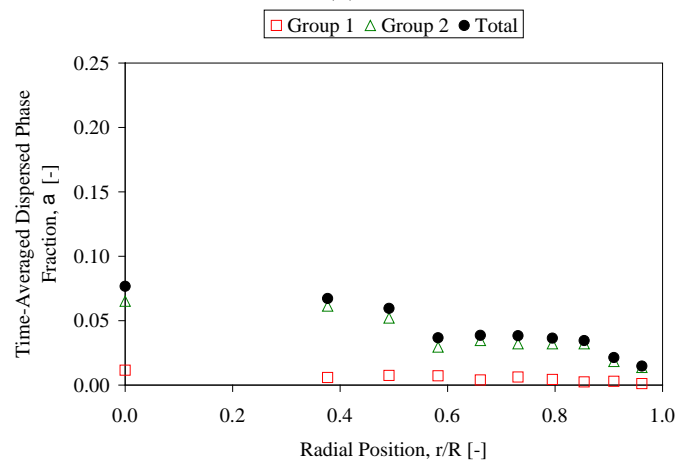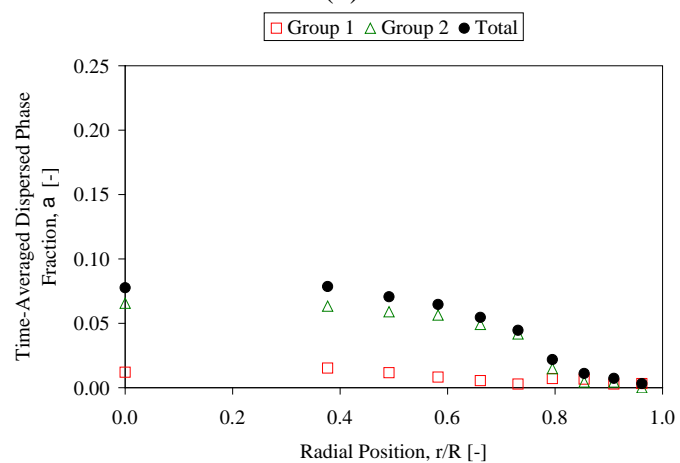
Run # 3

Figure B.10: Local void fraction profiles at (a) z/D=1.7, (b) z/D=5.0 & (c) z/D=8.3;
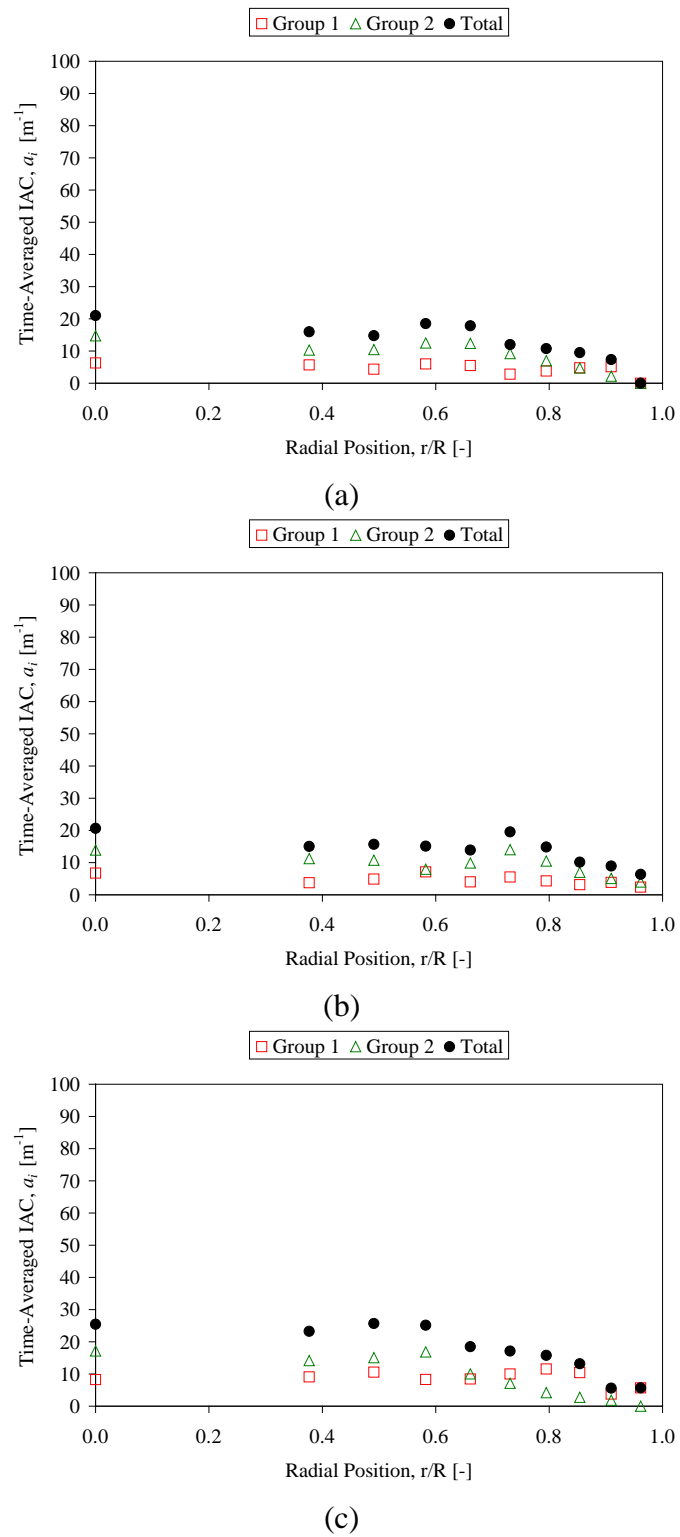
Run # 3
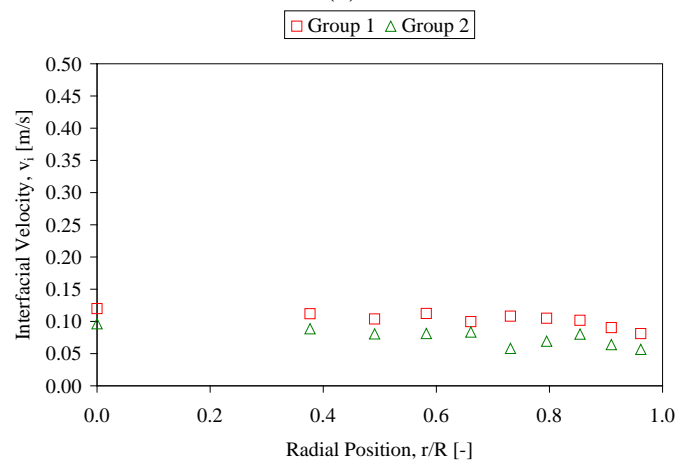
Figure B.11: Local interfacial area concentration profiles at (a) z/D=1.7, (b) z/D=5.0 & (c) z/D=8.3; Run # 3
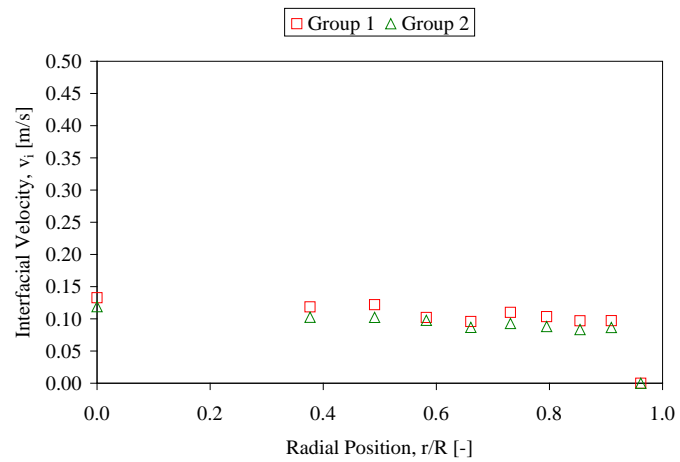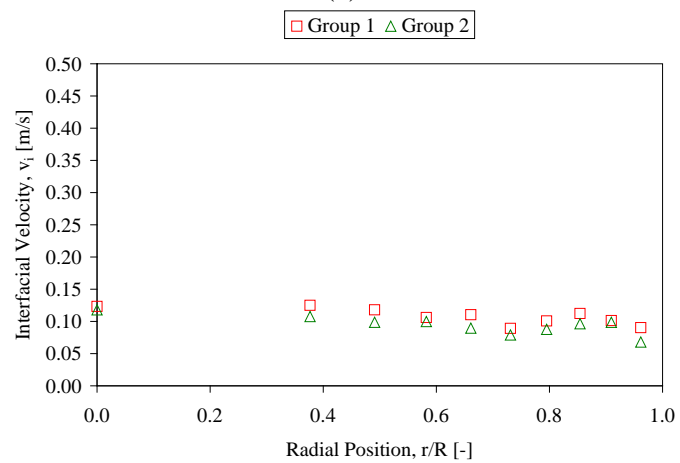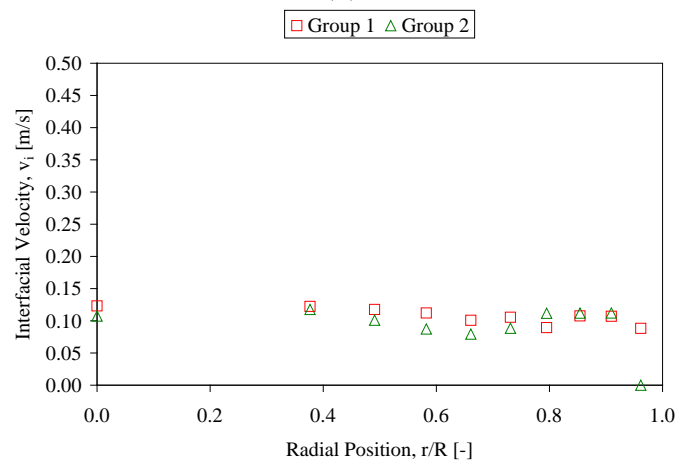
Figure B.12: Local interfacial velocity profiles at (a) z/D=1.7, (b) z/D=5.0 &
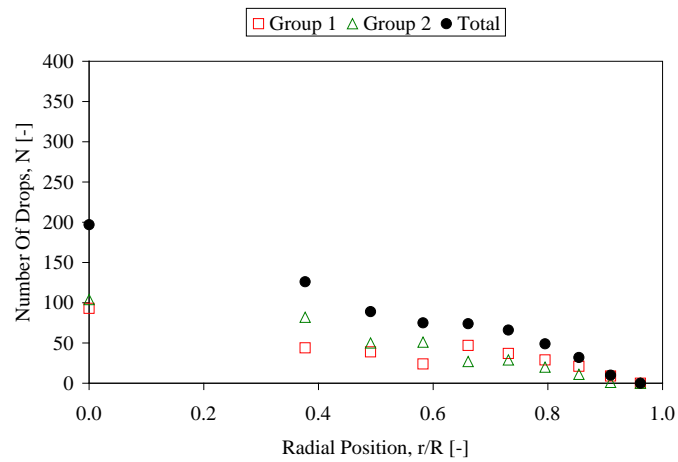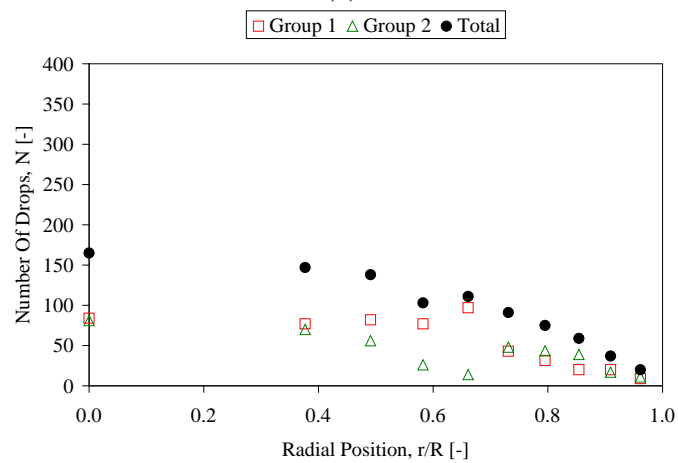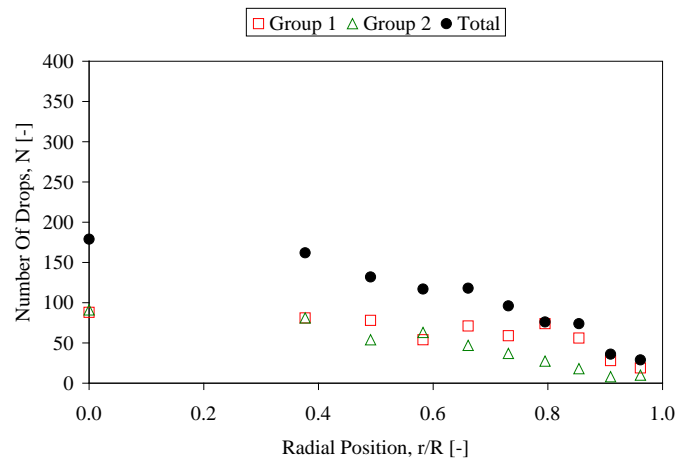
(c) z/D=8.3; Run # 3

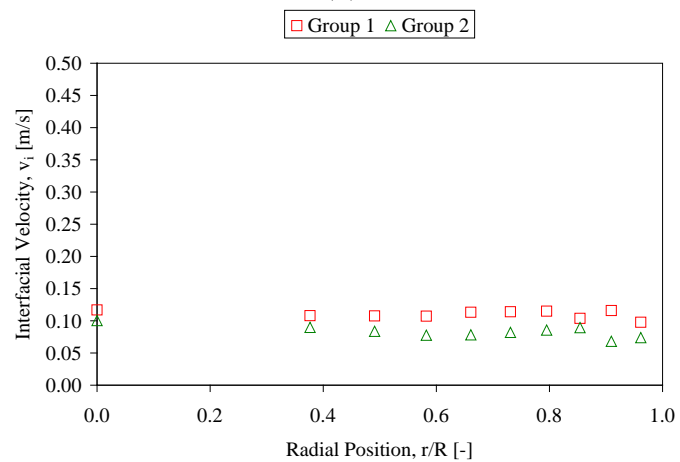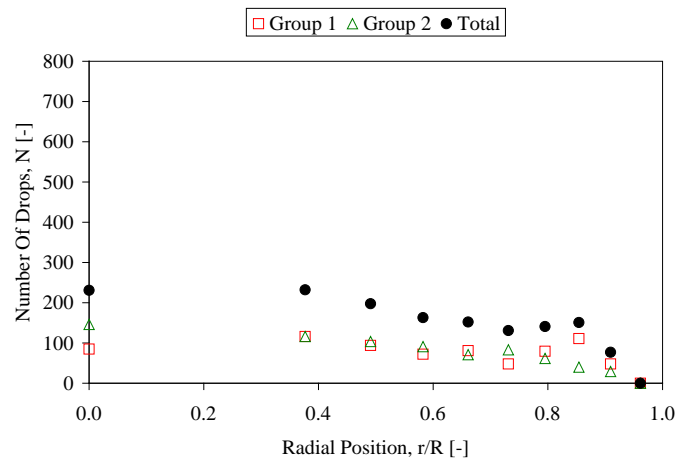Figure B.13: Profiles of number of drops at (a) z/D=1.7, (b) z/D=5.0 & (c) z/D=8.3;
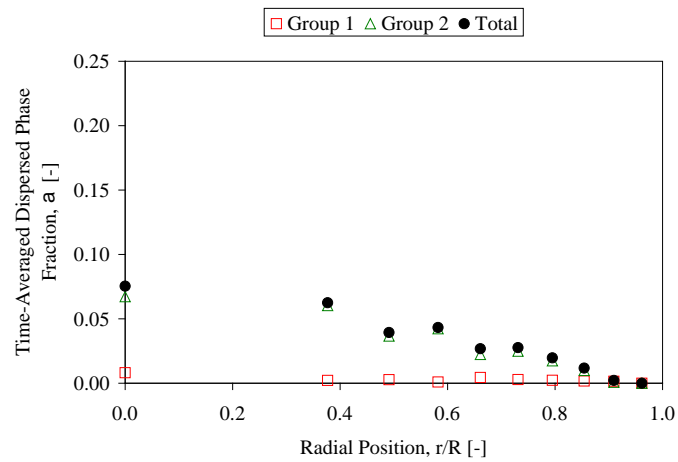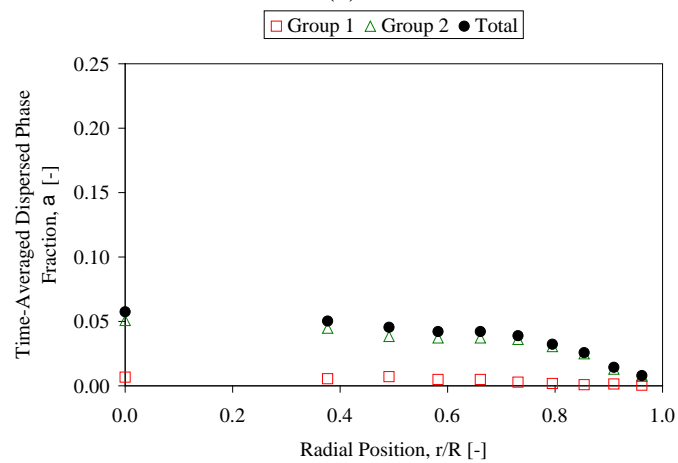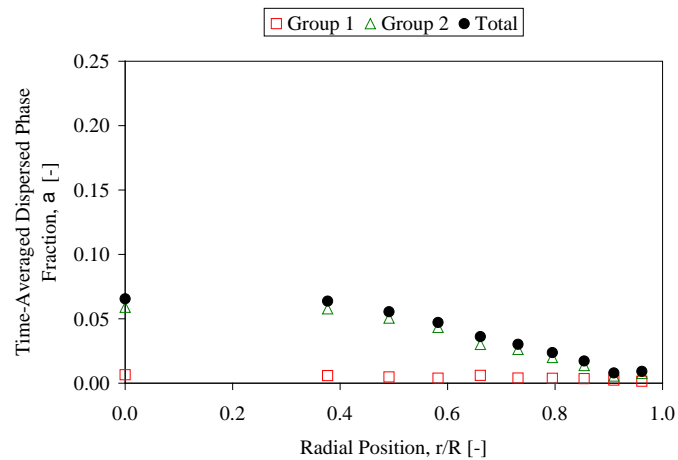
Run # 4

Figure B.14: Local void fraction profiles at (a) z/D=1.7, (b) z/D=5.0 & (c) z/D=8.3;
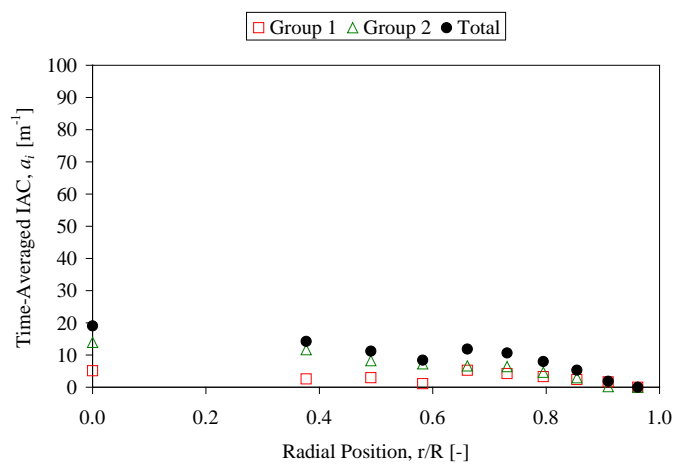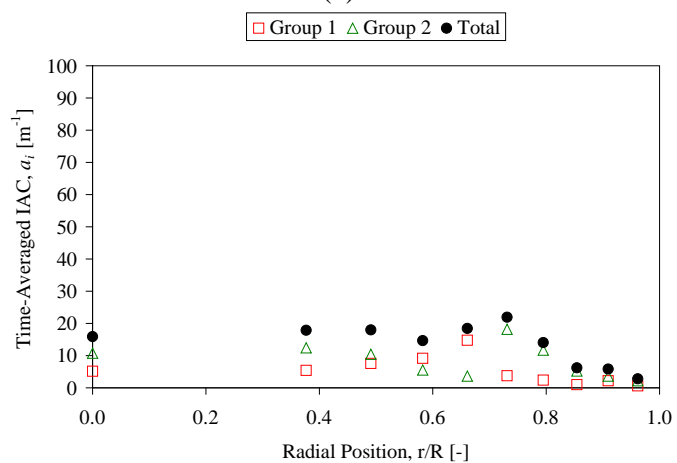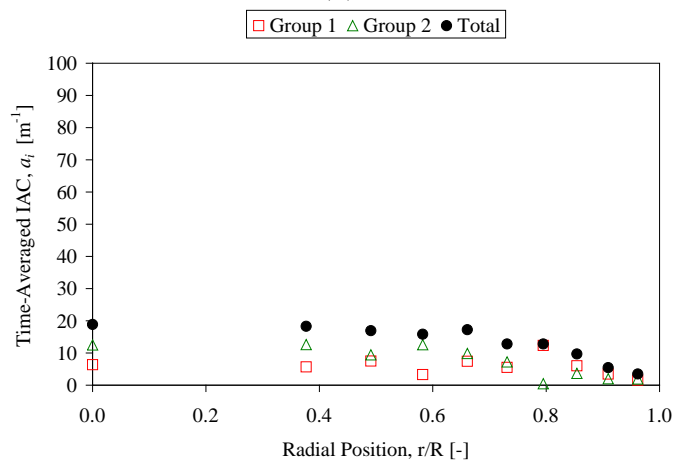
Run # 4

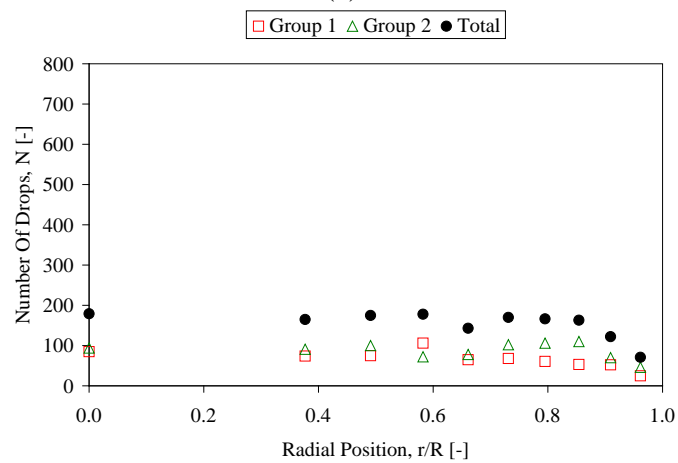Figure B.15: Local interfacial area concentration profiles at (a) z/D=1.7, (b) z/D=5.0 & (c) z/D=8.3; Run # 4
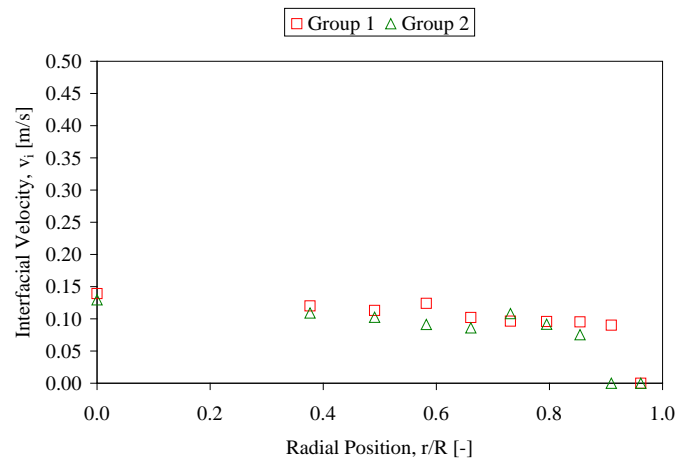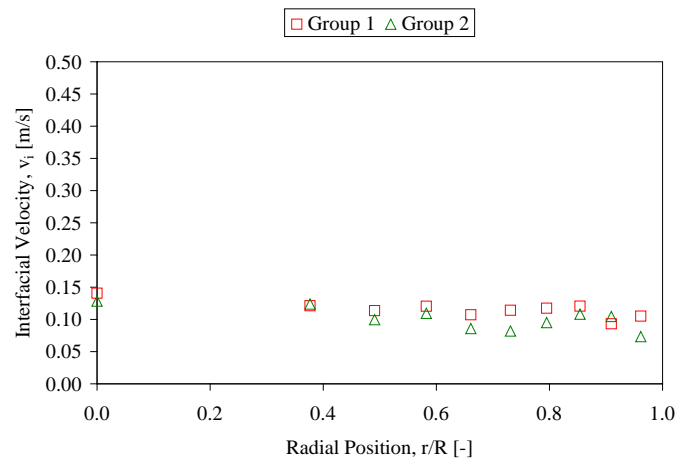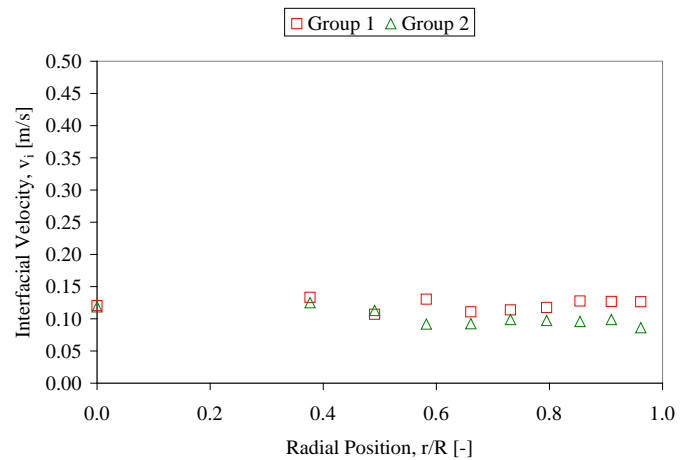
Figure B.16: Local interfacial velocity profiles at (a) z/D=1.7, (b) z/D=5.0 &
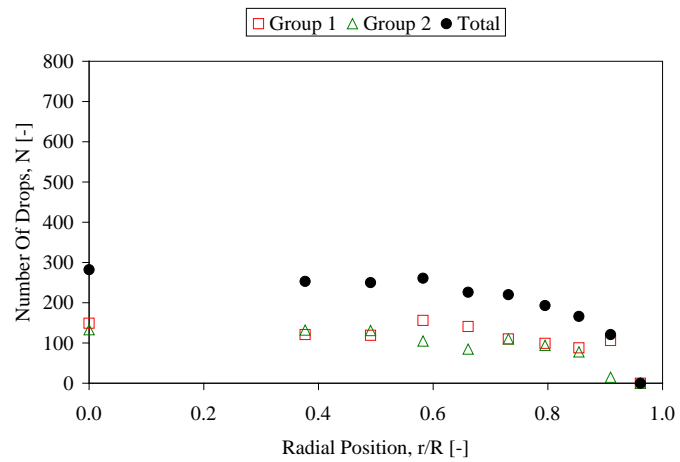
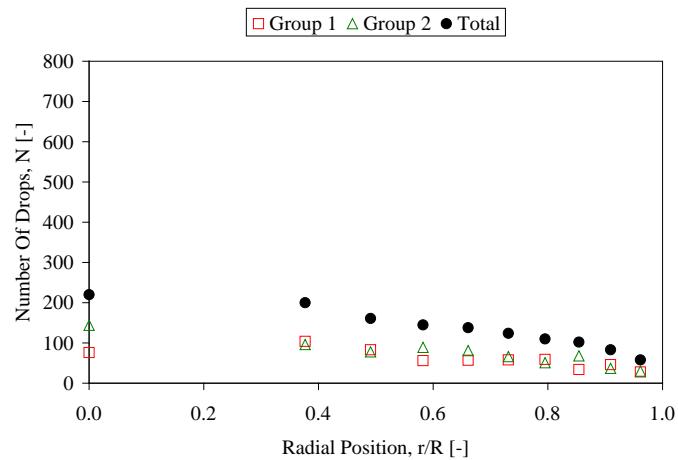(c) z/D=8.3; Run # 4

(a)
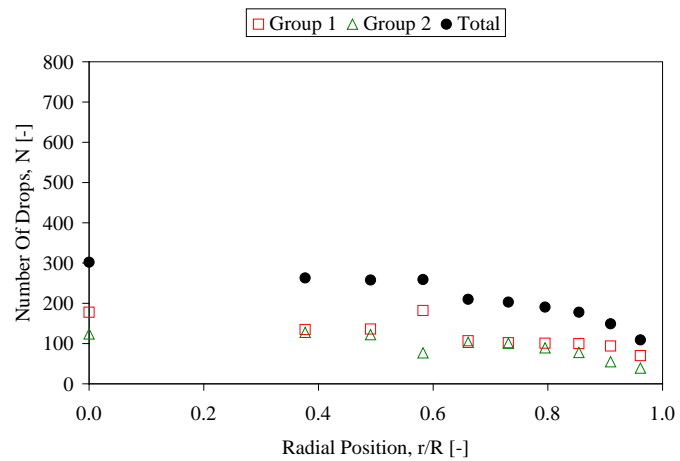
(b)
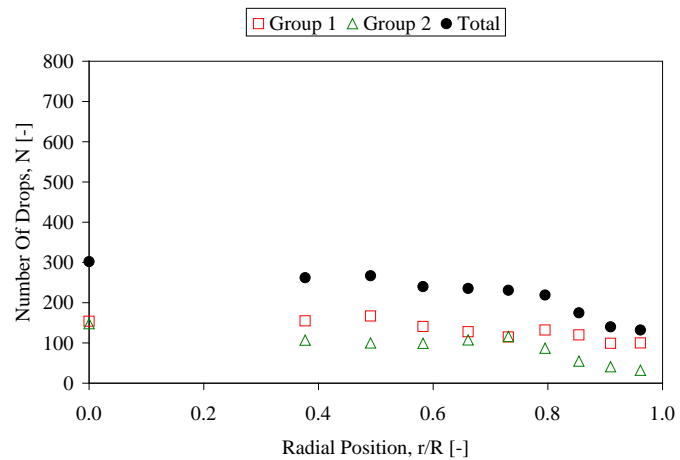
(c)

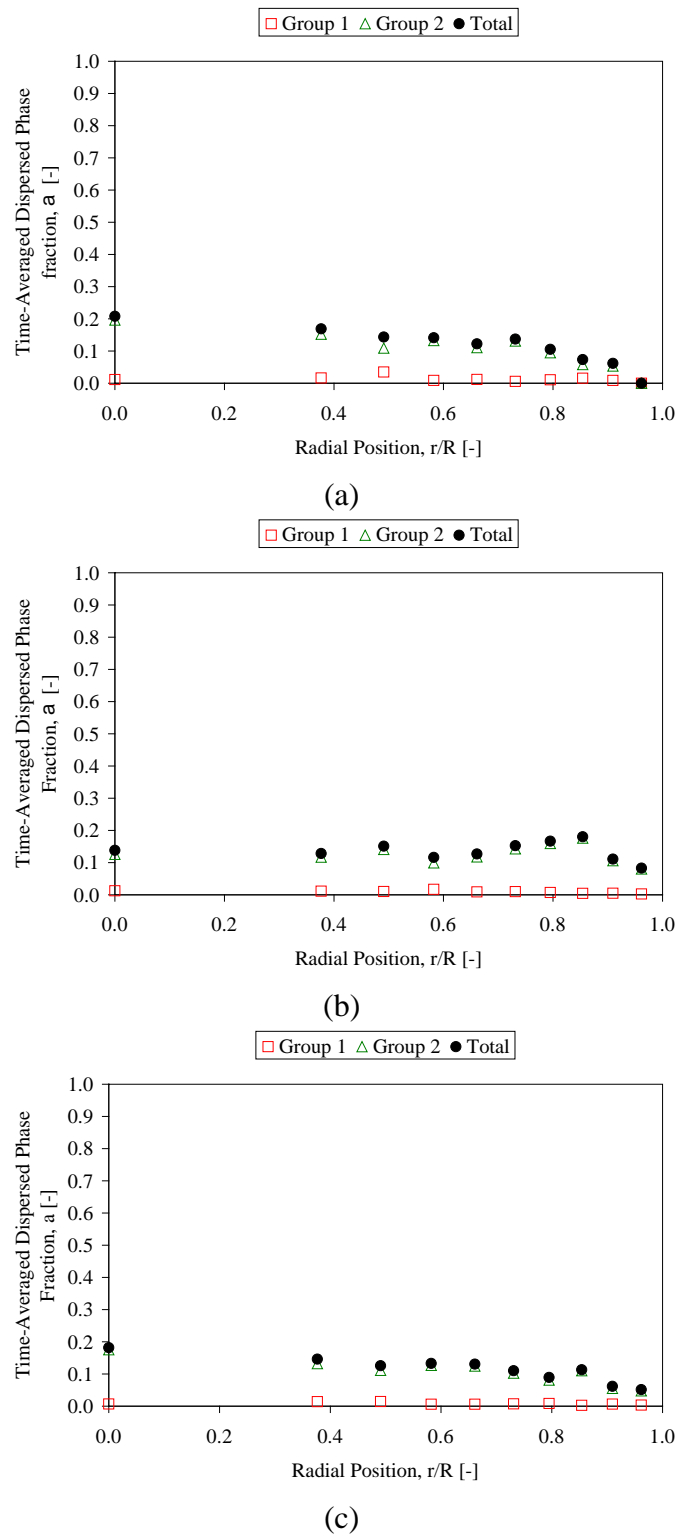Figure B.17: Profiles of number of drops at (a) z/D=1.7, (b) z/D=5.0 & (c) z/D=8.3;

Run # 5

(a)

(b)

(c)
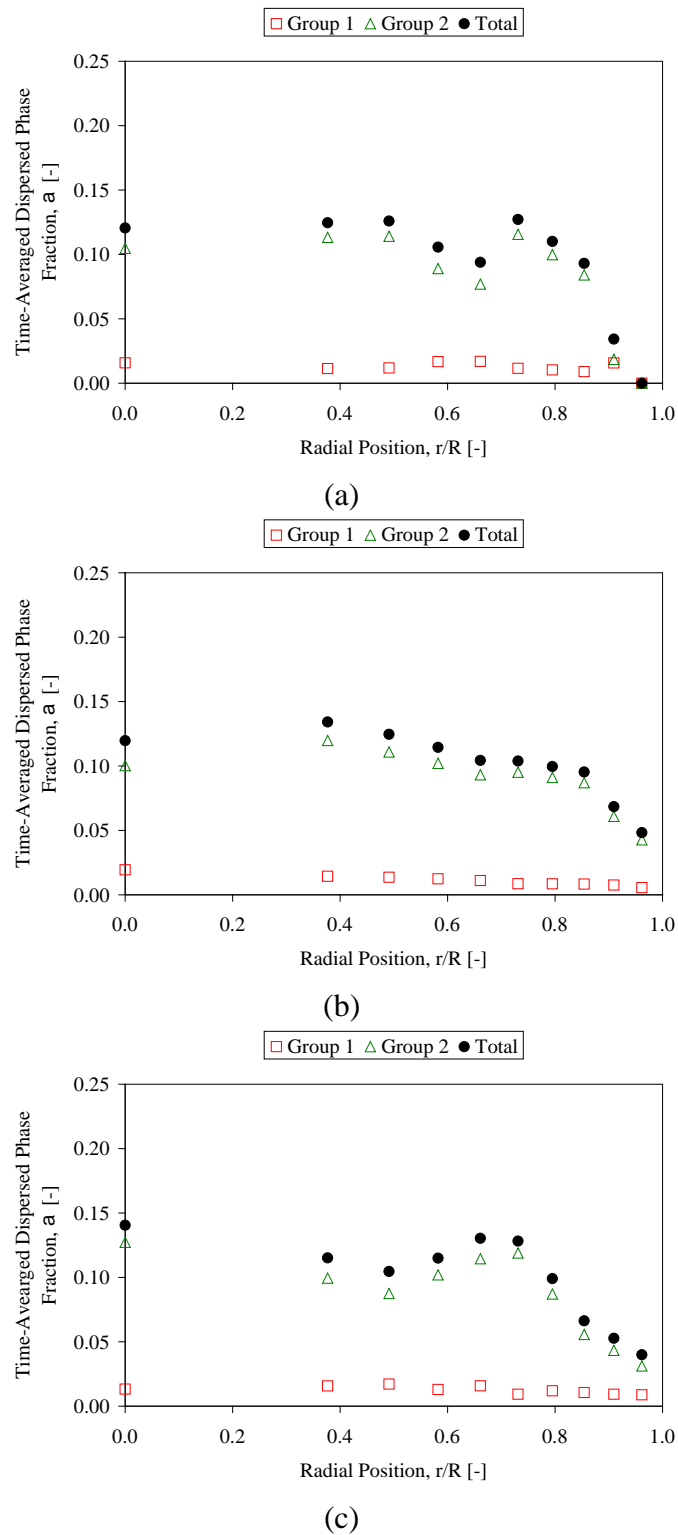
Figure B.18: Local void fraction profiles at (a) z/D=1.7, (b) z/D=5.0 & (c) z/D=8.3;
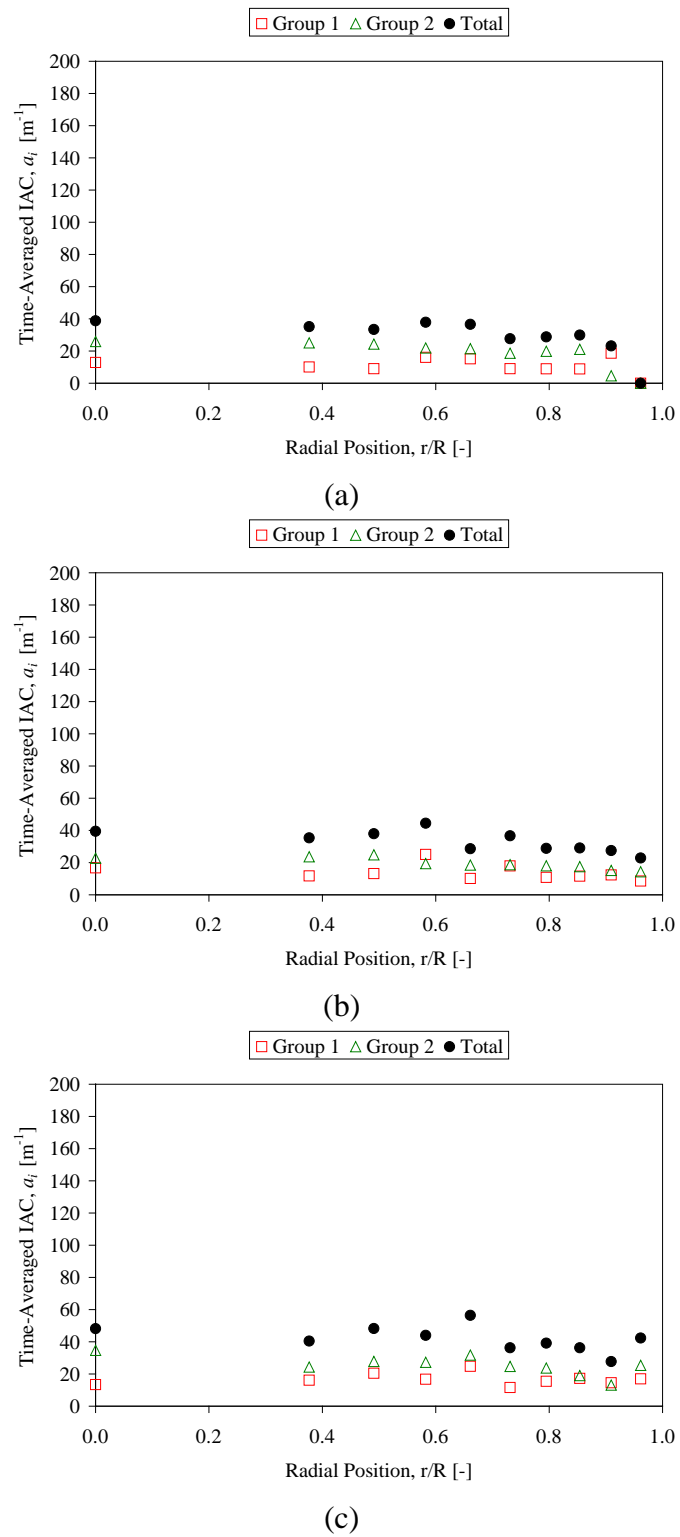
Run # 5

Figure B.19: Local interfacial area concentration profiles at (a) z/D=1.7, (b) z/D=5.0 & (c) z/D=8.3; Run # 5
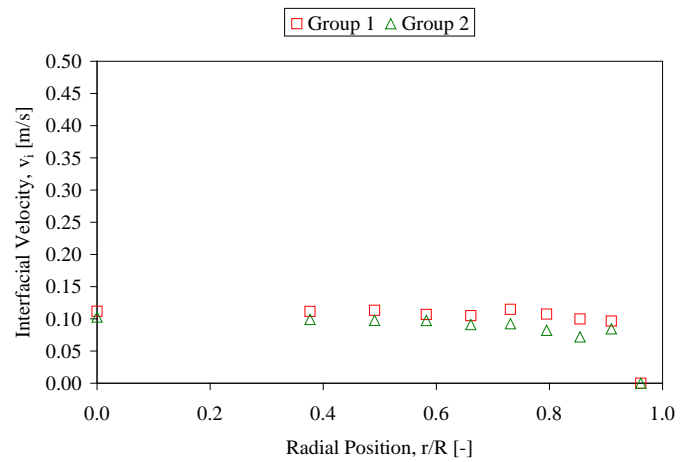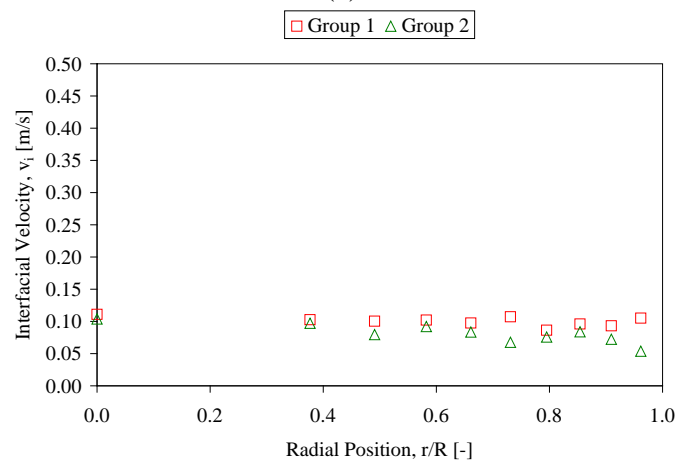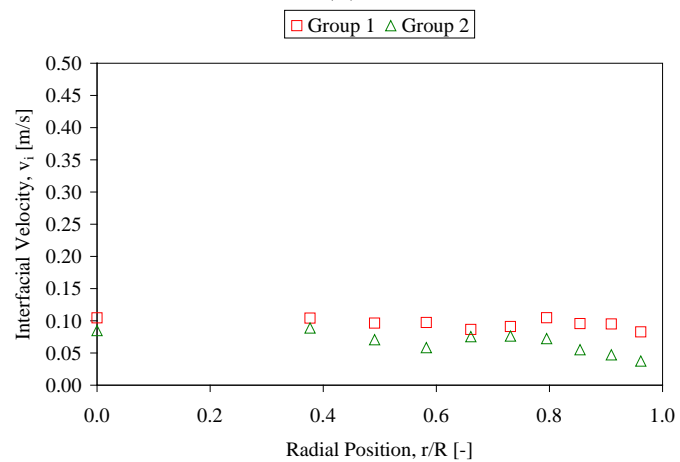
Figure B.20: Local interfacial velocity profiles at (a) z/D=1.7, (b) z/D=5.0 &
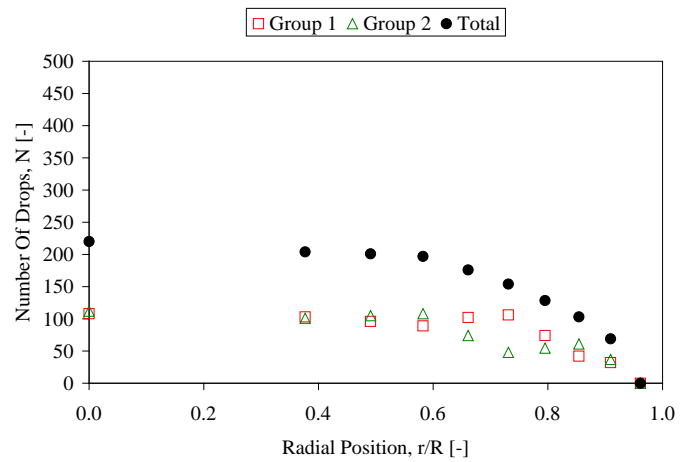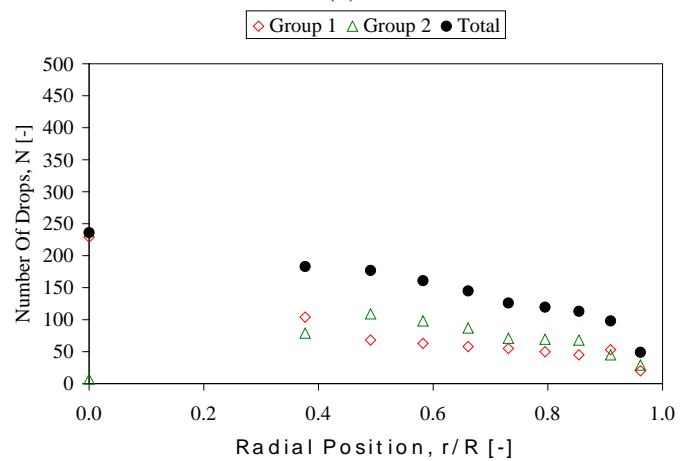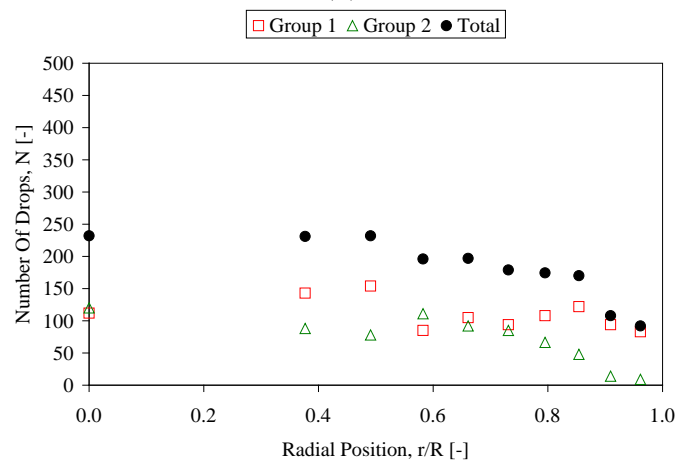
(c) z/D=8.3; Run # 5

Figure B.21: Profiles of number of drops at (a) z/D=1.7, (b) z/D=5.0 & (c) z/D=8.3;
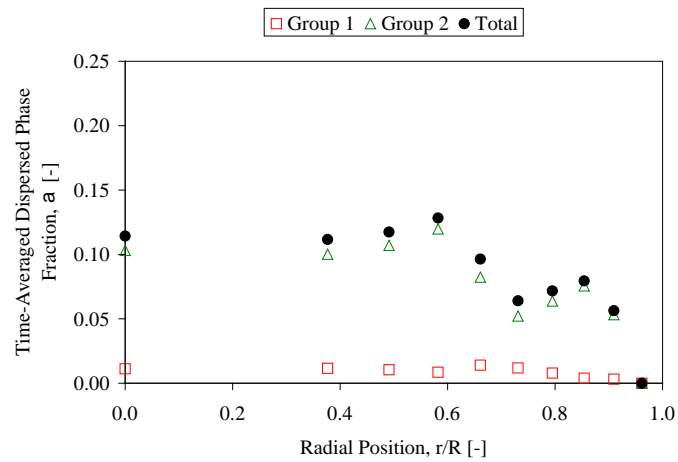
Run # 6

(a)
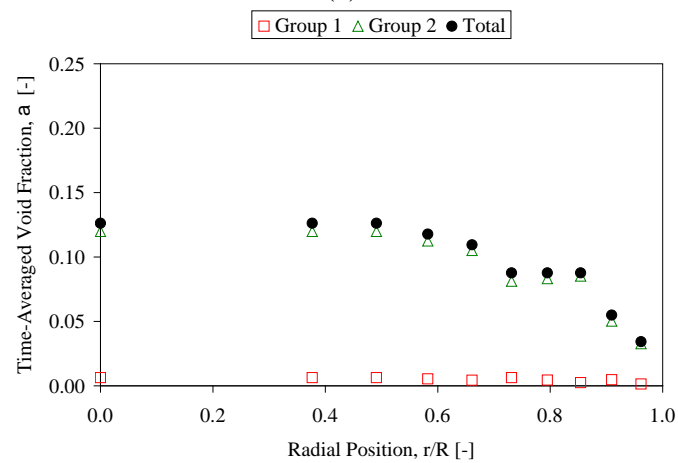
(b)
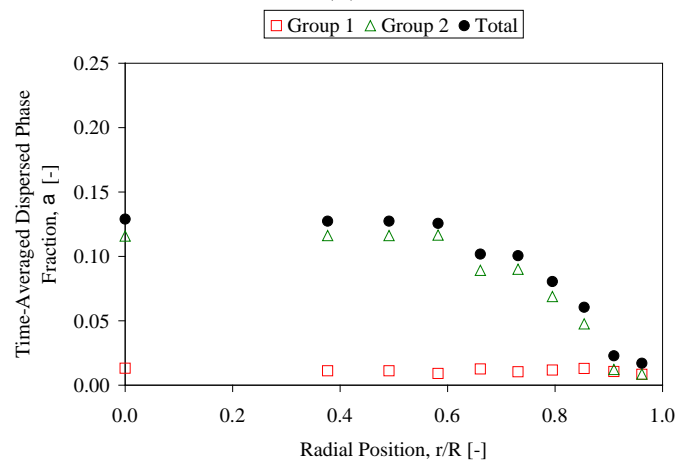
(c)

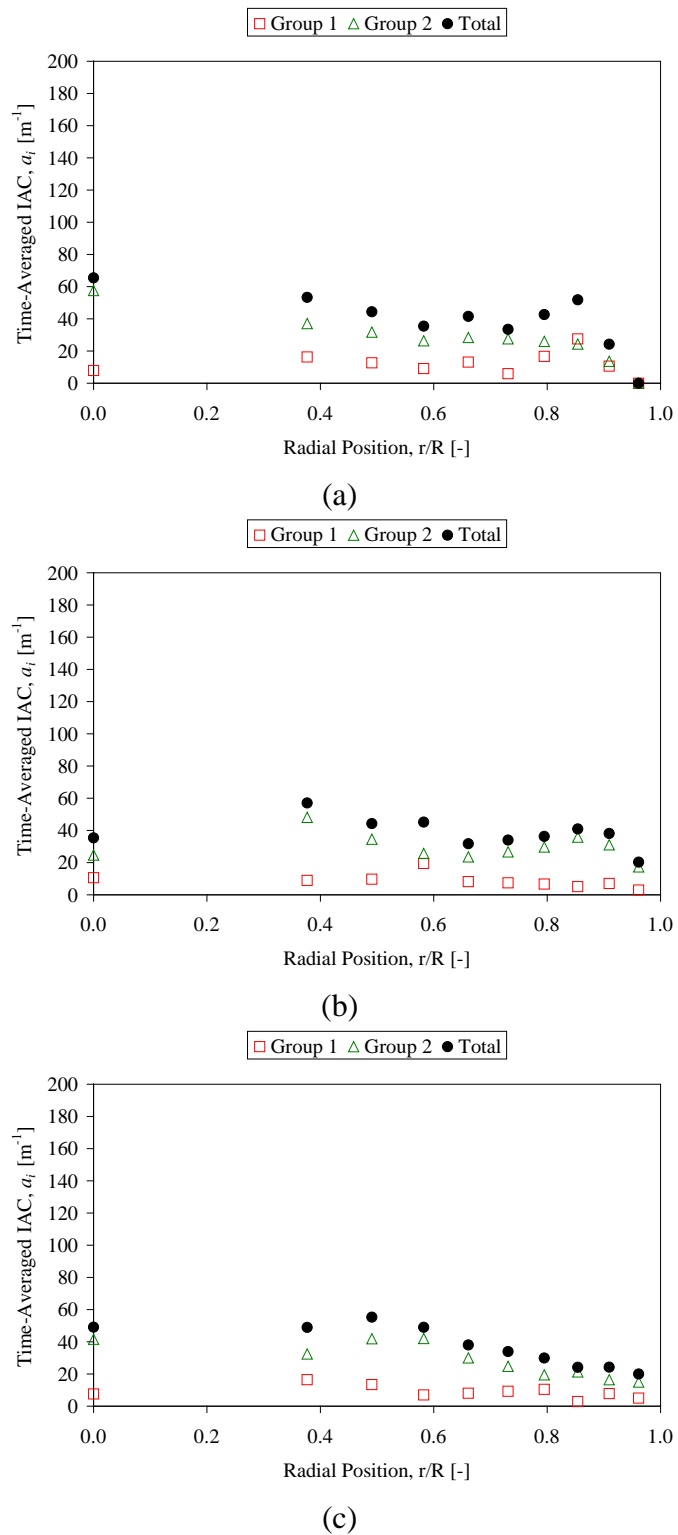Figure B.22: Local void fraction profiles at (a) z/D=1.7, (b) z/D=5.0 & (c) z/D=8.3;

Run # 6

(a)

(b)

(c)
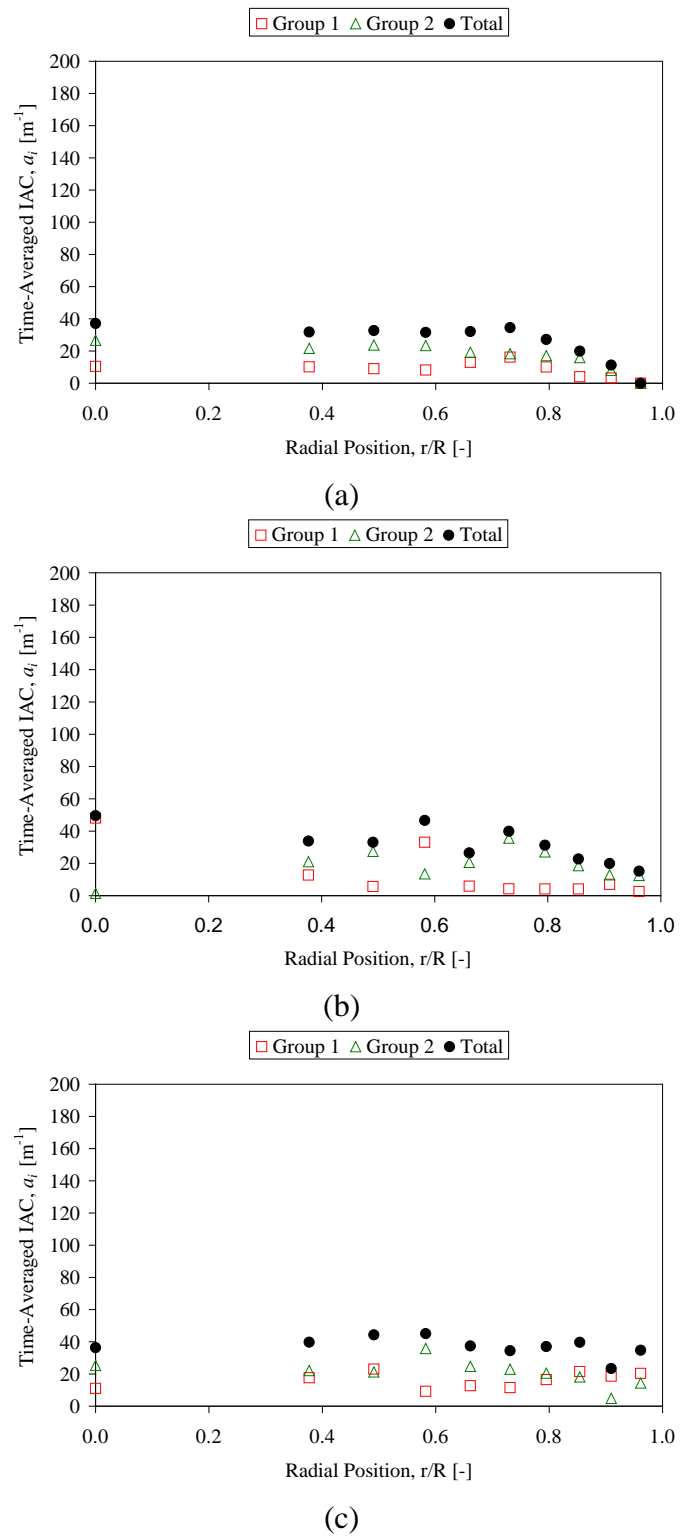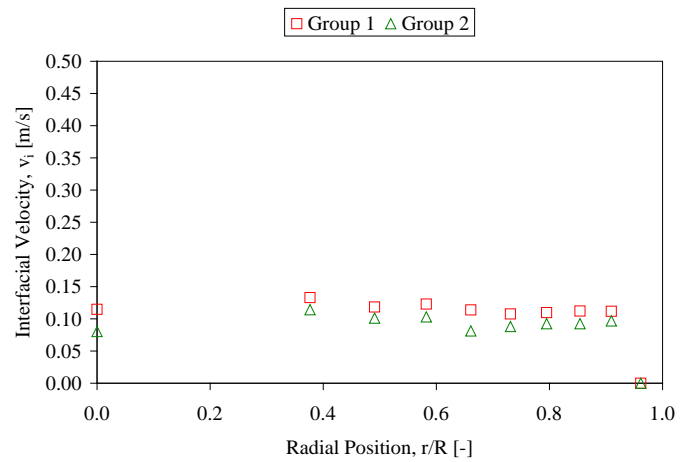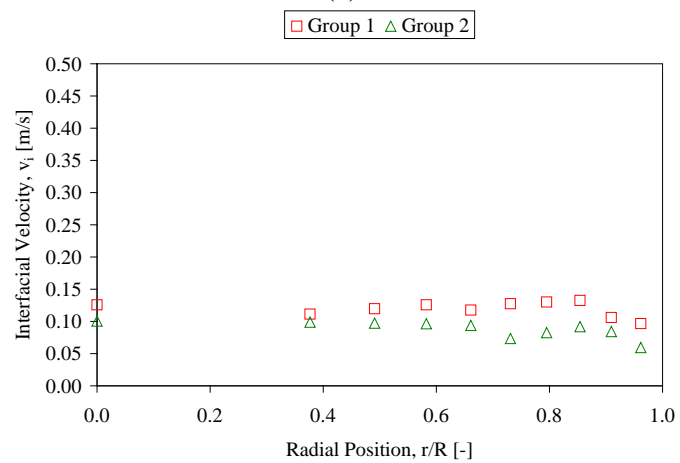
Figure B.23: Local interfacial area concentration profiles at (a) z/D=1.7, (b) z/D=5.0 &
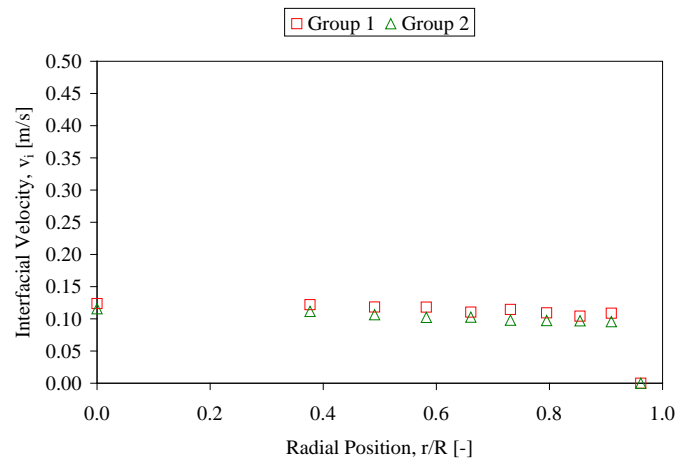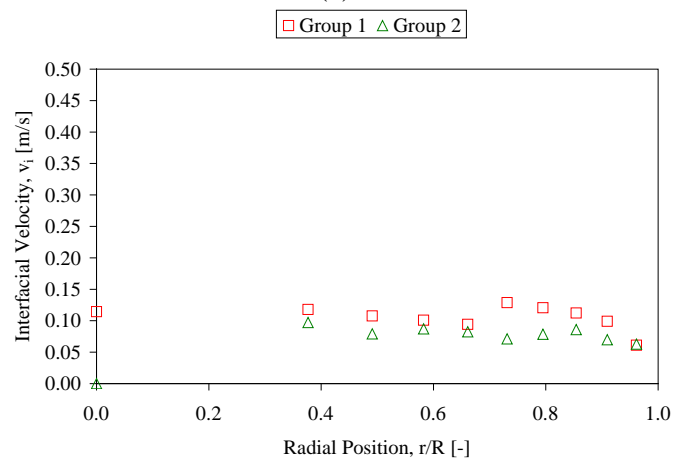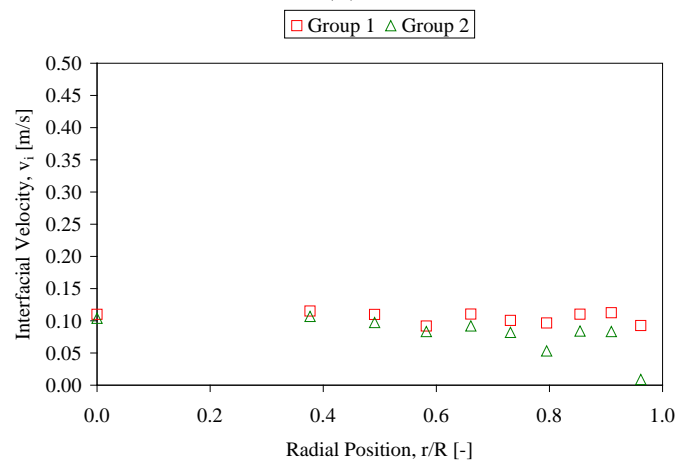
(c) z/D=8.3; Run # 6

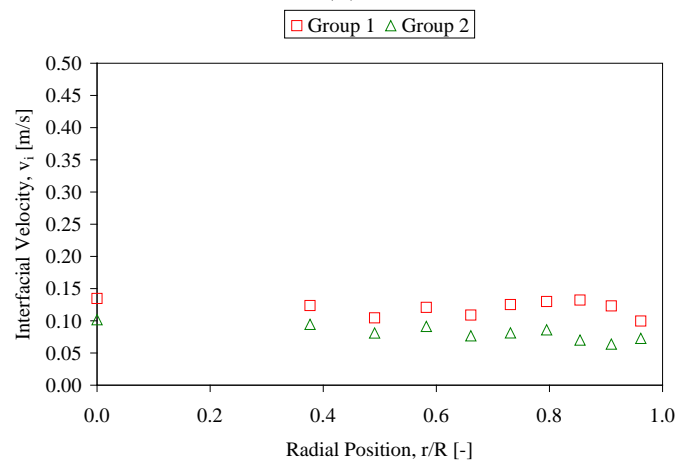Figure B.24: Local interfacial velocity profiles at (a) z/D=1.7, (b) z/D=5.0 & (c) z/D=8.3; Run # 6
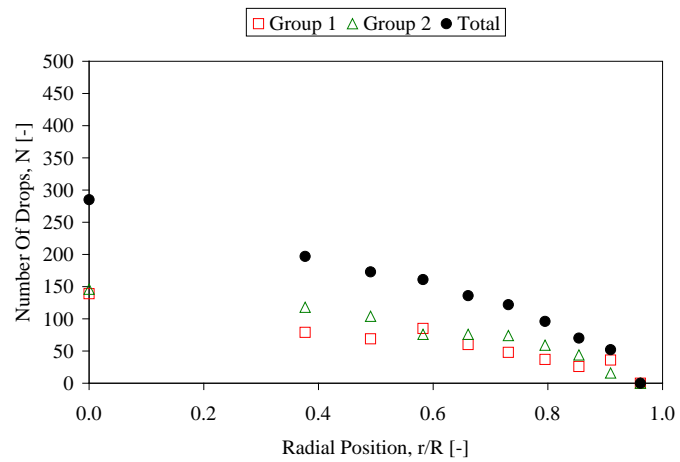
(a)
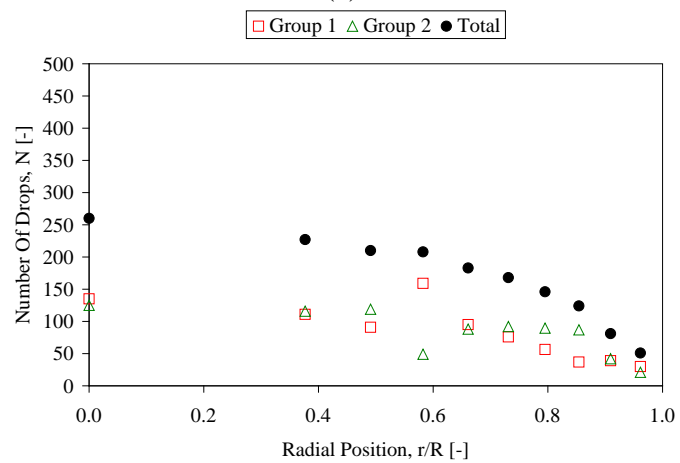
(b)
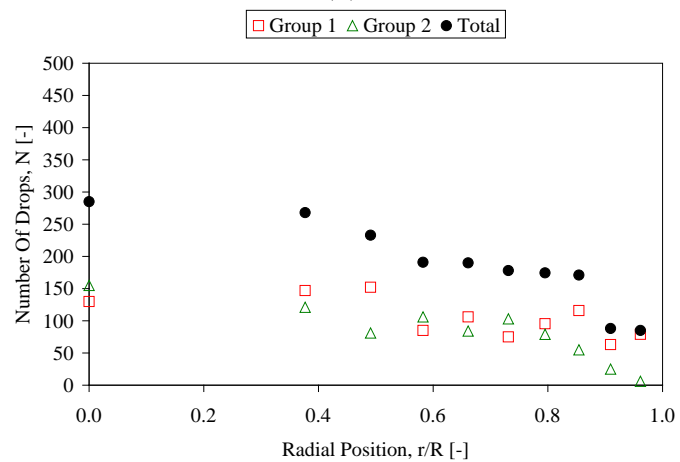
(c)

Figure B.25: Profiles of number of drops at (a) z/D=1.7, (b) z/D=5.0 & (c) z/D=8.3;
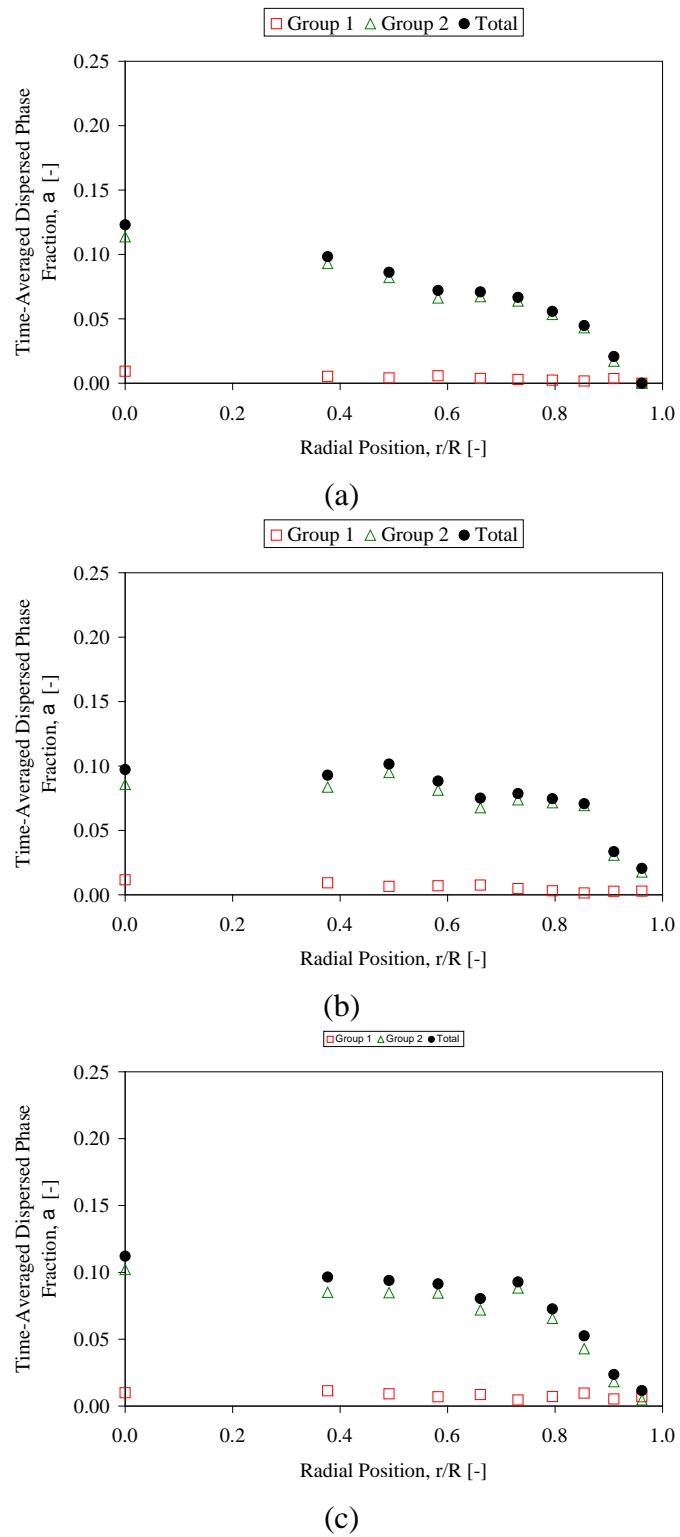
Run # 7

Figure B.26: Local void fraction profiles at (a) z/D=1.7, (b) z/D=5.0 & (c) z/D=8.3;

Run # 7

(a)

(b)

(c)
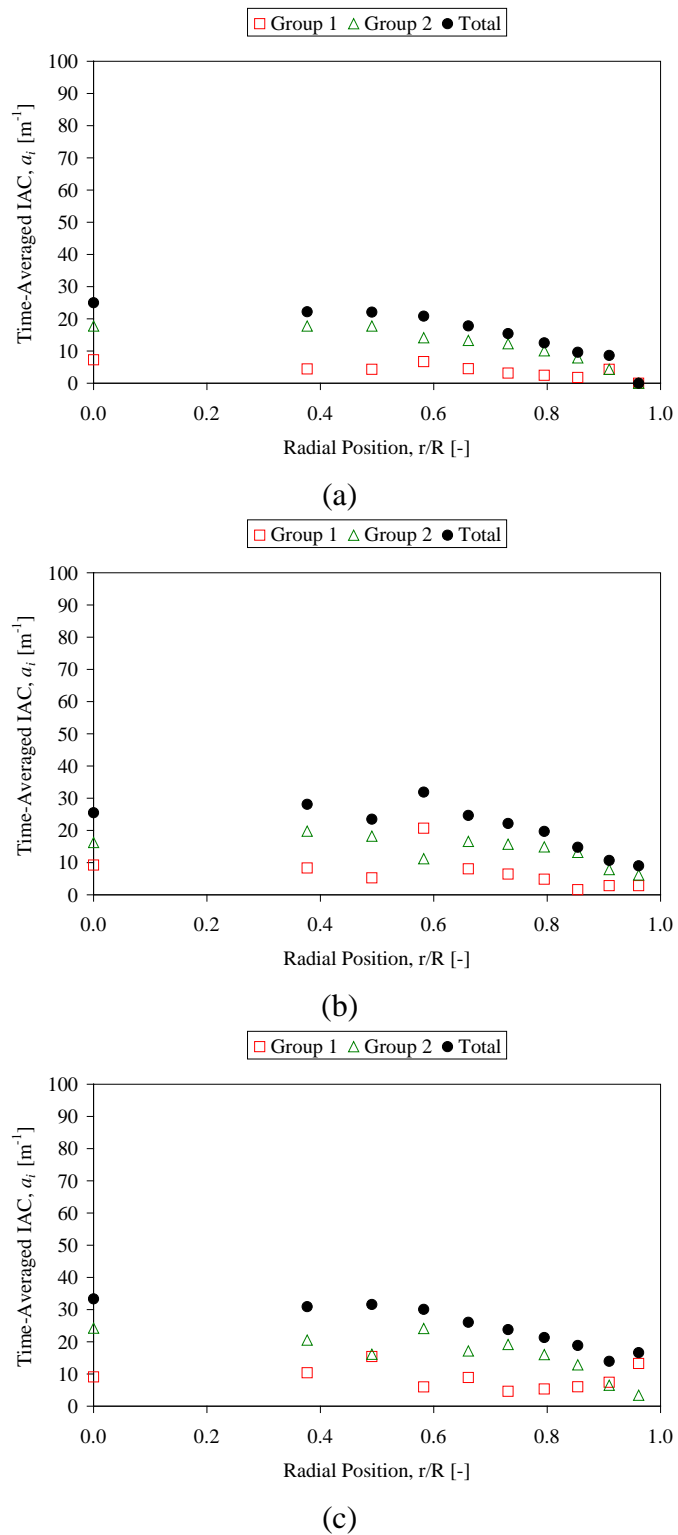
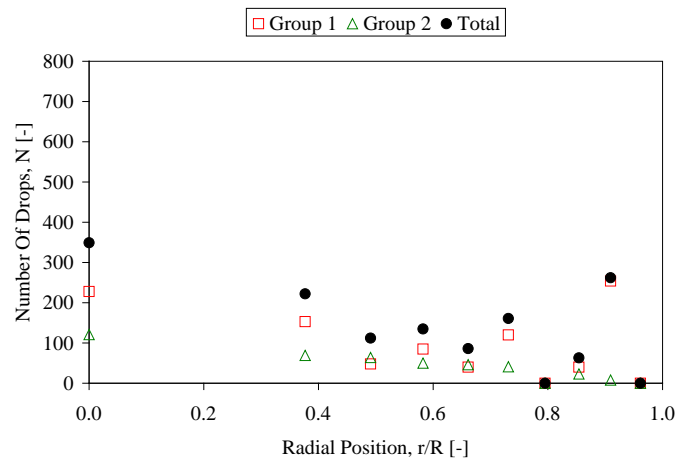Figure B.27: Local interfacial area concentration profiles at (a) z/D=1.7, (b) z/D=5.0 & (c) z/D=8.3; Run # 7
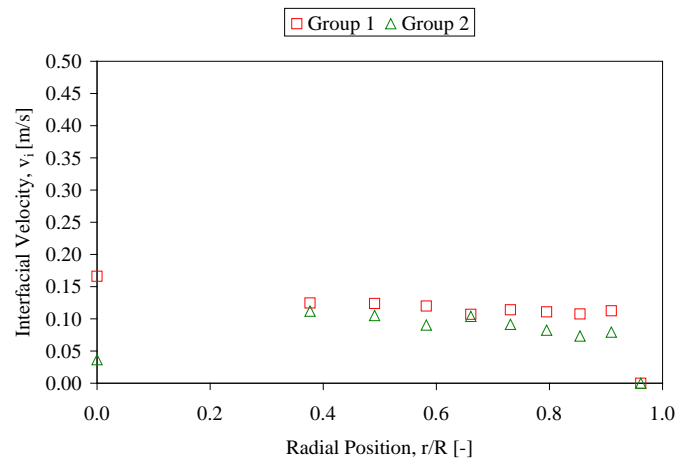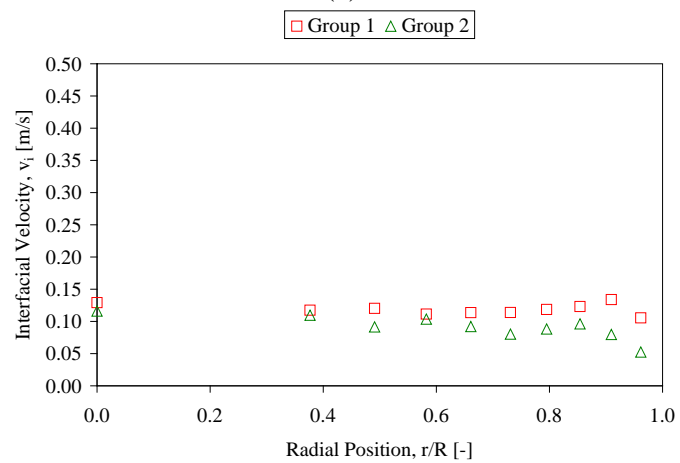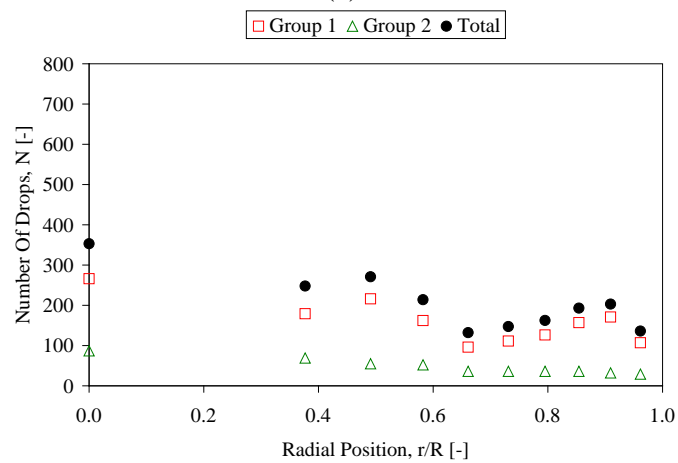
Figure B.28: Local interfacial velocity profiles at (a) z/D=1.7, (b) z/D=5.0 &

(c) z/D=8.3; Run # 7

Figure B.29: Profiles of number of drops at (a) z/D=1.7, (b) z/D=5.0 & (c) z/D=8.3;

Run # 8

Figure B.30: Local void fraction profiles at (a) z/D=1.7, (b) z/D=5.0 & (c) z/D=8.3;

Run # 8

Figure B.31: Local interfacial area concentration profiles at (a) z/D=1.7, (b) z/D=5.0 & (c) z/D=8.3; Run # 8
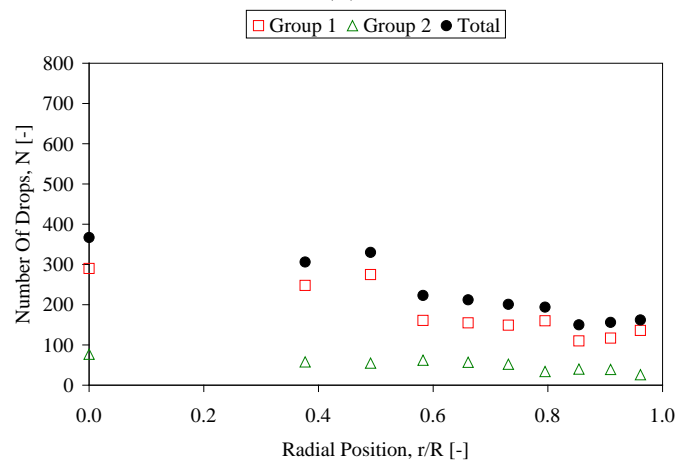
Figure B.32: Local interfacial velocity profiles at (a) z/D=1.7, (b) z/D=5.0 & (c) z/D=8.3; Run # 8
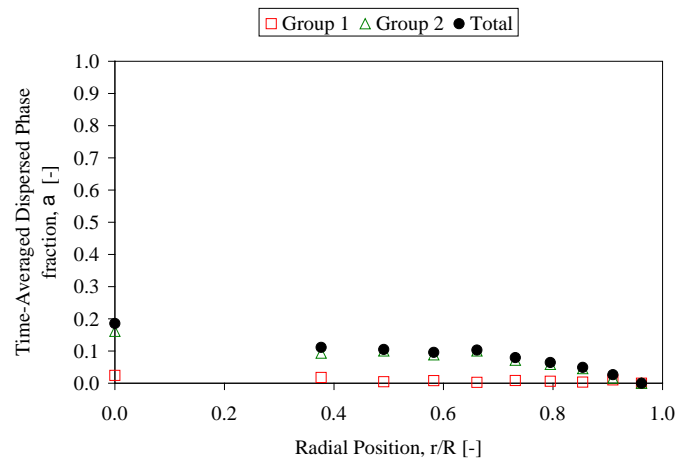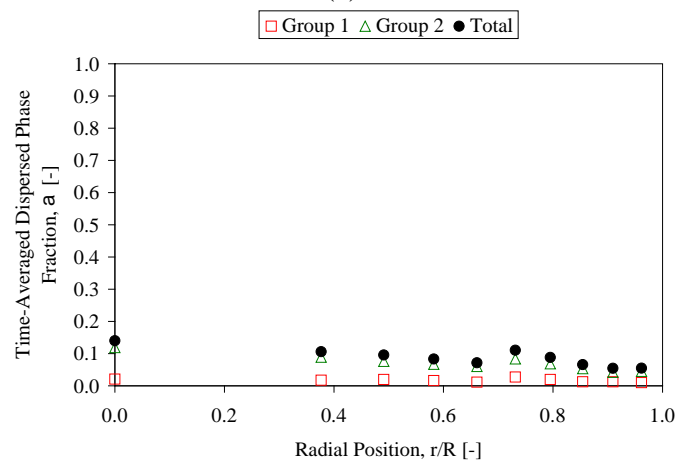
Figure B.33: Profiles of number of drops at (a) z/D=1.7, (b) z/D=5.0 & (c) z/D=8.3;

Run # 9

Figure B.34: Local void fraction profiles at (a) z/D=1.7, (b) z/D=5.0 & (c) z/D=8.3;

Run # 9

(a)

(b)

(c)

Figure B.35: Local interfacial area concentration profiles at (a) z/D=1.7, (b) z/D=5.0 & (c) z/D=8.3; Run # 9

Figure B.36: Local interfacial velocity profiles at (a) z/D=1.7, (b) z/D=5.0 &

(c) z/D=8.3; Run # 9

Figure B.37: Profiles of number of drops at (a) z/D=1.7, (b) z/D=5.0 & (c) z/D=8.3;

Run # 10

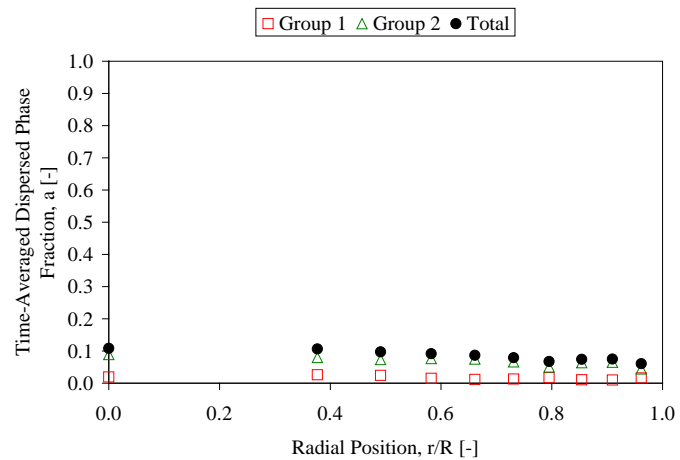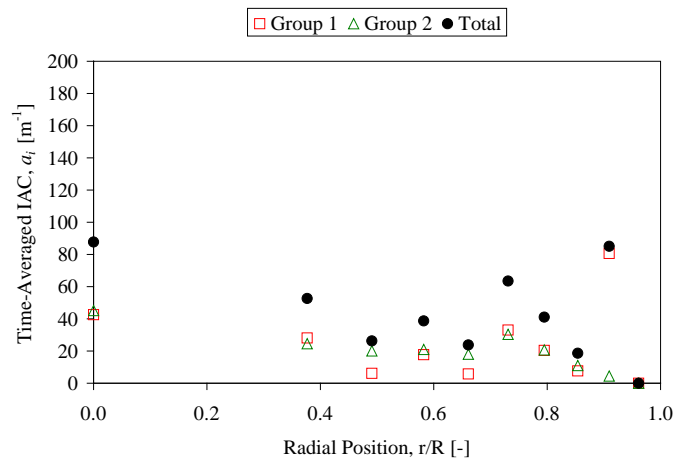Figure B.38: Local void fraction profiles at (a) z/D=1.7, (b) z/D=5.0 & (c) z/D=8.3;

Run # 10

Figure B.39: Local interfacial area concentration profiles at (a) z/D=1.7, (b) z/D=5.0 &

(c) z/D=8.3; Run # 10

Figure B.40: Local interfacial velocity profiles at (a) z/D=1.7, (b) z/D=5.0 &

(c) z/D=8.3; Run # 10

Figure B.41: Profiles of number of drops at (a) z/D=1.7, (b) z/D=5.0 & (c) z/D=8.3;

Run # 11
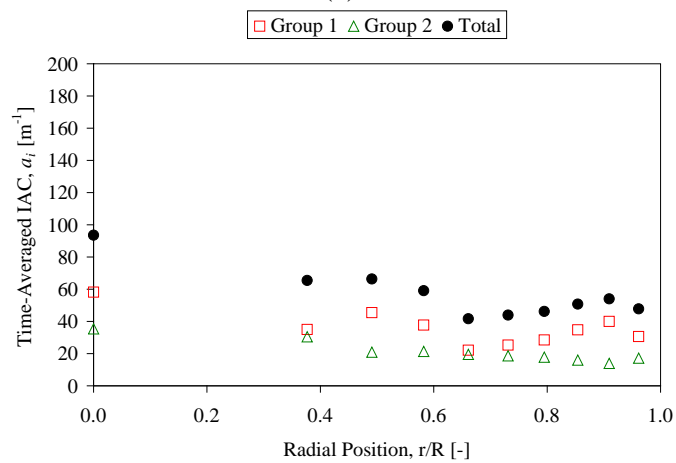
Figure B.42: Local void fraction profiles at (a) z/D=1.7, (b) z/D=5.0 & (c) z/D=8.3;
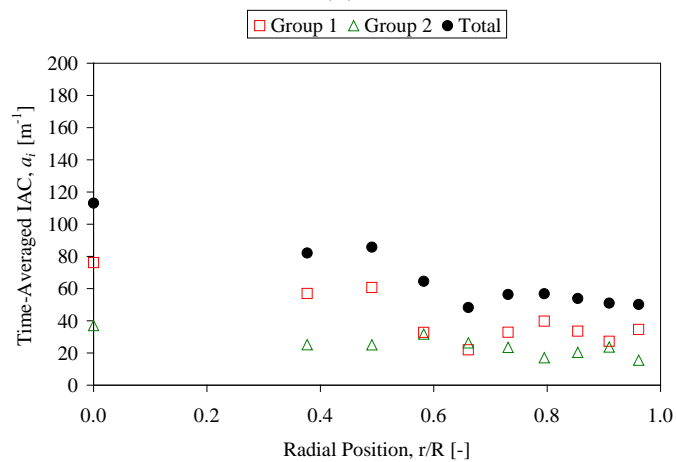
Run # 11
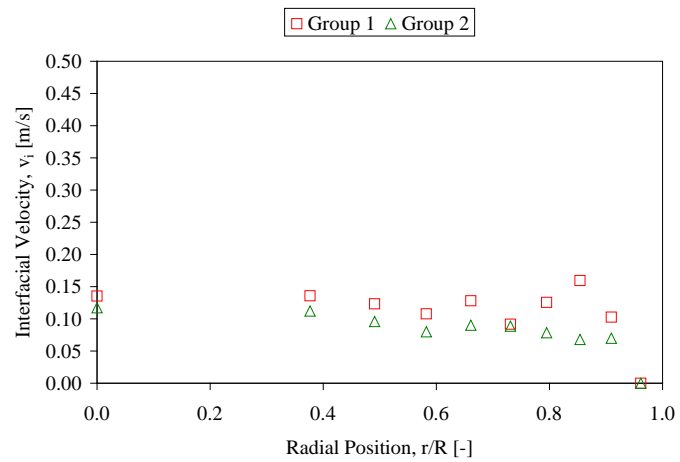
Figure B.43: Local interfacial area concentration profiles at (a) z/D=1.7, (b) z/D=5.0 &

(c) z/D=8.3; Run # 11

Figure B.44: Local interfacial velocity profiles at (a) z/D=1.7, (b) z/D=5.0 & (c) z/D=8.3; Run # 11

Figure B.45: Profiles of number of drops at (a) z/D=1.7, (b) z/D=5.0 & (c) z/D=8.3;

Run # 12

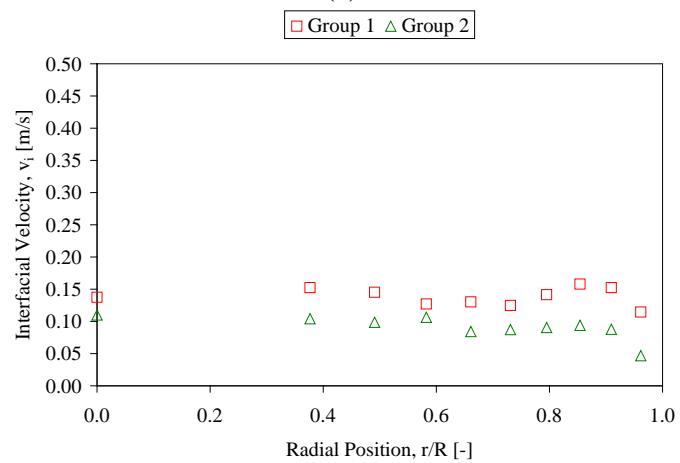Figure B.46: Local void fraction profiles at (a) z/D=1.7, (b) z/D=5.0 & (c) z/D=8.3;

Run # 12
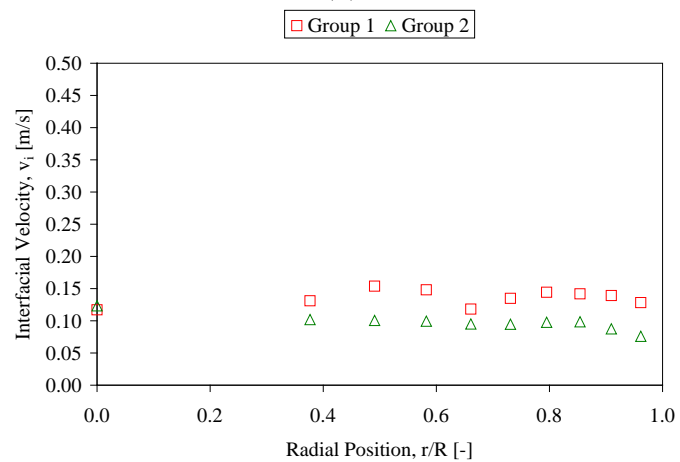
Figure B.47: Local interfacial area concentration profiles at (a) z/D=1.7, (b) z/D=5.0 & (c) z/D=8.3; Run # 12

Figure B.48: Local interfacial velocity profiles at (a) z/D=1.7, (b) z/D=5.0 &

(c) z/D=8.3; Run # 12

VITA

VITA

Tirthankar Roy was born in the city of Kolkata located in the state of West Bengal in India on May 22nd, 1980. He is the elder of two children of Mr. Timir Baran Roy and Mrs. Gouri Roy. Tirthankar received his elementary and high school education from Kendriya Vidyalaya. Following this, Tirthankar pursued engineering education at Jadavpur University, Kolkata, India and received his Bachelor's degree in chemical engineering in July 2001. Thereafter, he joined the Master of Technology program in Energy Systems Engineering at the Indian Institute of Technology, Bombay, India and received his degree in July 2004. Thereafter he went to the USA to join the Doctor of Philosophy program under the supervision of Prof. M. Ishii in The School of Nuclear Engineering at Purdue University, West Lafayette, Indiana. He finished research on his thesis in July 2010 and has been working as a post-doctoral researcher at The Flow Assurance Center in Trondheim, Norway since then.